

Integrating Thermal and Coastal Dynamics in Modelling Permafrost Erosion

A Case Study at Barter Island

CIEM0500: MSc Thesis

Kevin de Bruijn



Integrating Thermal and Coastal Dynamics in Modelling Permafrost Erosion

A Case Study at Barter Island

by

Kevin de Bruijn

Student number:	4863976
Project duration:	April 22, 2024 – January 15, 2025
Thesis committee:	Dr. ir. S. G. Pearson, Prof. dr. ir. W. S. J. Uijttewaal, Dr. ir. R. McCall, Dr. C. Seyfert, Dr. ir. K. Nederhoff, Prof. dr. T. Ravens, Dr. L. Erikson,
	Delft University of Technology, chair Delft University of Technology Deltares Deltares Deltares USA University of Alaska Anchorage United States Geological Survey

Cover: Barter Island, Alaska (2018). Photo by Shawn Harrison.
Style: TU Delft Report Style, with modifications by Daan Zwanenveld

Preface

Before you lies my final work to obtain the title Master of Science at the faculty of Civil Engineering and Geosciences at Delft University of Technology in the field of Hydraulic Engineering. Before presenting the contents of my thesis I would like to share a few words.

I started my Master studies almost 2.5 years ago. The relaxation of COVID-19 measures finally allowed me to physically go back to university, after having just switched study programmes. While taking courses, I was captivated by the Coastal Systems course and when I got an invitation to apply as a teaching assistant, I immediately accepted. It was through that position that I first met Stuart, my supervisor and chair, which ultimately led to my introduction to the topic of permafrost erosion, and to Kees, Robert, and Carola from Deltares who were looking for a student to work on a model to describe permafrost erosion.

During the following months, I started my thesis on permafrost erosion with Deltares. I worked with different parties from California and Alaska, and I was even given the opportunity to travel to Santa Cruz (California) to work on my model, for which I am incredibly grateful. Afterwards, I presented my work at a Deltares-hosted conference "Exploring Coastal Hazards". Working on this fascinating topic has presented me with great opportunities, and I hope that my work will benefit future research.

I would like to thank Stuart for his excellent supervision and positive energy. Your lectures are what first got me into coastal hydrodynamics, and I am here to stay! I look forward to continuing our collaboration during my PhD. I would also like to thank Wim for his critical questions that kept me grounded while working on a topic in which it is very easy to get lost.

From Deltares, I would like to thank Carola for asking me all the questions that I had forgotten to ask me myself. The help you gave me with this project was invaluable. To Robert, I am grateful for your constructive feedback and insights that have elevated my work to a higher level. I am also grateful to Kees. Thank you for hosting me in the U.S., your relentless pragmatism pushed me to make the decisions I put off for too long.

I would also like to thank Li and her colleagues for welcoming me at the USGS. You have made my stay an excellent experience, and your knowledge and experience made our discussions of invaluable worth to this project. To Tom, thank you for your previous work on this topic and for helping me to continue your work. Your insights provided me with the knowledge and direction to complete my project.

I also want to express my gratitude to my friends and family for supporting me through my studies. To my parents and aunt, thank you for nurturing my curiosity and creativity. To my partner, thank you for travelling half a world to support me and go on adventures together. To my younger brother, thank you for the laughs and company. Finally, to my twin brother, thank you for your wisdom and support throughout my academic career. We will be colleagues soon and I look forward to confusing people by publishing in the same field.

*Kevin de Bruijn
Delft, January 2025*

Abstract

Over 30% of the world's coastline consists of permafrost and large sections of these coasts are subject to erosion. In the Arctic, unlike with temperate low-latitude coastlines, thermal processes affect erosion mechanisms. There is a lack of long-term predictive capability of morphodynamics for Arctic coastlines, which results in a knowledge gap regarding the coastal processes inducing permafrost erosion and how these processes will change under the effects of climate change. Previously developed parametric morphodynamic permafrost models lack generalizability because they either do not include all erosion mechanisms or were calibrated for specific eroding coastlines. Comprehensive morphodynamic models that include permafrost dynamics are too computationally expensive to perform long-term analysis and are thus applied to storm time scales only.

This study implements a novel method that integrates thermodynamics, hydrodynamics, and morphodynamics to predict the morphodynamic evolution of a permafrost-affected coastline. We developed and validated a process-based numerical model for Barter Island (North Slope, Alaska). This model showed skill in predicting the ground temperature distribution and the erosion of a permafrost bluff. Sensitivity analyses indicated that the environmental drivers affected by climate change (i.e., air and sea temperatures, water level) are expected to accelerate the erosion of permafrost-affected coastlines under the effects of climate change, confirming the findings of previous work. Rising temperatures will compound with diminishing sea ice to widen the annual window during which erosion can occur, which will increase the number of storm events that lead to erosion. Lower bluffs composed of finer sands are especially vulnerable.

The low computation costs mean that the model can be used to predict coastal erosion for larger regions, potentially benefiting strategic coastal management and policy-making. Additionally, the developed model will improve global climate models. It can facilitate the mapping of permafrost degradation and organic carbon release, with the release of organic carbon through permafrost erosion being one of the greatest unknown drivers of global warming. Though further calibration is required, the developed model can be used as a tool to research the quantitative effects of climate change on the erosion of Arctic coastlines and gain a deeper understanding of how climate change affects the processes that ultimately lead to the erosion of permafrost bluffs.

Nomenclature

The tables below contain overviews of abbreviations and symbols used in this research. Symbols are ordered alphabetically and categorized by Greek and Latin notation.

Abbreviations

Abbreviation	Definition
BLUE	Best Linear Unbiased Estimator
ECMWF	European Centre for Medium-Range Weather Forecasts
ERA5	ECMWF Reanalysis v5
FTCS	Forward Time Central Space
GSC	Geological Survey of Canada
MAE	Mean Absolute Error
MSL	Mean Sea Level
OAT	One-At-a-Time (method for varying parameters in sensitivity analysis)
PCMSC	Pacific Coastal and Marine Science Center
RMSE	Root Mean Squared Error
USGS	United States Geological Survey

Symbols

Symbol	Definition	Unit
A	Altitude angle (angle off of the horizontal with which the sun's rays strike a horizontal surface)	[°]
AZ	Azimuth counter-clockwise from south	[°]
c_w	Volumetric heat capacity of seawater	[m]
C_s	Specific heat capacity for solid material	[J/K/kg]
C_l	Specific heat capacity for liquid material	[J/K/kg]
d_r	Representative depth	[m]
d_{thaw}	Depth that needs to be frozen before being treated as non-erodible	[m]
D_{50}	Mean sediment diameter	[m]
D_p	Main wave angle (i.e., the direction of propagation)	[°]
E	parameter depending on whether the turbulent boundary layer flow is hydraulically smooth or fully rough	[‐]
fac_{ua}	XBeach factor governing onshore transport through wave asymmetry	[‐]
f_{nyq}	Nyquist frequency (i.e., the highest frequency used to generate the JONSWAP spectrum)	[s ^{‐1}]
f_p	Peak frequency of the wave spectrum	[s ^{‐1}]
f_w	Wave friction factor at melting surface	[m]
h	Enthalpy	[J/kg]
h	Hour angle	[°]

Symbol	Definition	Unit
$h_{c,\text{air}}$	Convective heat transfer coefficient for a soil-air interface	[W/m ² /K]
$h_{c,\text{water}}$	Convective heat transfer coefficient for a soil-water interface	[W/m ² /K]
H_0	Offshore significant wave height	[m]
H_{m0}	Significant wave height of the wave spectrum	[m]
H_r	Representative wave height	[m]
I	Solar intensity	[W/m ²]
I_0	Solar constant (radiation at the top of the atmosphere normal to the sun)	[W/m ²]
k	Thermal conductivity	[W/m/K]
k_{frozen}	Thermal conductivity of frozen (solid) material	[W/m/K]
k_{unfrozen}	Thermal conductivity of unfrozen (liquid) material	[W/m/K]
k_r	Representative wave number	[rad/m]
k_s	Equivalent sand roughness of the melting surface	[m]
L	Latent heat of fusion	[J/kg]
L_0	Offshore wave length	[m]
L_c	Convective length scale	[m]
m	Superscript denoting the m^{th} grid cell in z direction	[\cdot]
n	Superscript denoting the n^{th} (sub-grid) time step	[\cdot]
n_b	Soil water content	[\cdot]
N	Current day of the year	[m]
N_{thermal}	Number of nodes in 1D enthalpy models	[m ⁻¹]
Pr	Prandtl number	[\cdot]
$q_{\text{convective}}$	Convective heat flux	[W/m ²]
q_{latent}	Latent heat flux	[W/m ²]
$q_{\text{radiation}}$	Radiation eat flux	[W/m ²]
$q_{\text{radiation, long-wave}}$	Long-wave radiation heat flux	[m]
$q_{\text{radiation, short-wave}}$	Short-wave radiation heat flux	[m]
r	Enhancement factor	[m]
r	Pearson correlation coefficient	[\cdot]
R^2	Coefficient of determination	[\cdot]
$R_{2\%}$	2% run-up	[m]
s	Directional spreading coefficient	[m]
t	Time	[s]
T	Temperature	[K]
T_0	Temperature at the ground surface	[K]
T_m	Melting temperature	[K]
T_r	Representative wave period	[s]
u_b	Representative fluid velocity immediately outside the boundary layer	[m/s]
u_*	Shear velocity associated with the shear stress at the melting surface	[m/s]
v_w	Wind speed	[m/s]
x	Cartesian coordinate direction	[m]
y	Cartesian coordinate direction	[m]
z	Cartesian coordinate direction	[m]
Z	Azimuth counter-clockwise from east	[$^{\circ}$]
α	Empirical parameter for determining convective heat transfer for a soil-water interface	[\cdot]
$\alpha_{\text{surface flux}}$	Calibration coefficient	[\cdot]

Symbol	Definition	Unit
β_f	Average slope of the bed level over a region of $\pm 2\sigma$ around the mean water level [-], with σ the standard deviation of the continuous water level record, which can be predicted from the offshore significant wave height	[-]
γ	Peak enhancement factor in the JONSWAP expression	[-]
δ	Declination angle	[°]
Δf_j	Step size frequency used to generate the JONSWAP spectrum	[s ⁻¹]
Δz	Grid spacing	[m]
Δt	Time step	[s]
θ	Angle between surface and radiation	[°]
ν_{air}	Air kinematic viscosity	[m ² /s]
ν_{water}	Water kinematic viscosity	[m ² /s]
ρ	Density	[kg/m ³]
ϕ	Latitude	[°]

Contents

Preface	ii
Abstract	iii
Nomenclature	iv
1 Introduction	1
1.1 Research Context	1
1.2 Problem Definition	1
1.3 Research Objective and Questions	2
1.4 Report Outline	3
2 Literature Review	5
2.1 Coastal setting	5
2.1.1 Geological Characteristics	5
2.1.2 Coastal Characteristics	7
2.2 Drivers of Arctic Erosion	8
2.2.1 Waves	8
2.2.2 Water Level	8
2.2.3 Sea Ice	8
2.2.4 River Sediments	9
2.2.5 Salinity	9
2.2.6 Heat Fluxes	9
2.2.7 Snow	9
2.3 Erosion Mechanisms	10
2.4 Climate Sensitivity	12
2.4.1 Air Temperature	13
2.4.2 Sea Temperature	13
2.4.3 Open Water Period	13
2.4.4 Wave Climate	14
2.4.5 Sea Level	14
2.4.6 Future Perspectives	14
2.5 Impacts of Arctic Erosion	15
2.5.1 Natural Environment	15
2.5.2 Human Environment	15
2.6 Modelling of Arctic Erosion	15
2.6.1 Thermal Abrasion	16
2.6.2 Thermal Denudation	16
2.6.3 Thermal Abrasion and Denudation	17
2.6.4 Other	17
2.6.5 Physical Modelling	17
2.6.6 Data	17
2.7 Research Gap	18
3 Methodology	19
3.1 Main Approach	19
3.2 Methods	20
4 Model formulation	21
4.1 Python Wrapper	21
4.1.1 Integration of XBeach and Thermal Module	22

4.2 XBeach Module	23
4.2.1 Introduction	23
4.2.2 Hydrodynamics and Waves	24
4.2.3 Sediment Transport and Morphology	24
4.3 Thermal Module	24
4.3.1 Enthalpy	24
4.3.2 Grid	26
4.3.3 Sub-grid Time step	26
4.3.4 Thaw Depth	27
4.3.5 Boundary Conditions	28
5 Case Study at Barter Island	33
5.1 Site Description	33
5.2 Data	36
5.2.1 Initial Conditions	36
5.2.2 Forcing	39
5.2.3 Physical and Calibration Parameters	40
5.2.4 Calibration and Validation data	42
5.3 Calibration and Validation	47
5.3.1 Thermal Module Calibration	47
5.3.2 Thermal Module Validation	48
5.3.3 Thermo-morphological Model Calibration	52
5.3.4 Thermo-morphological Model Validation	53
5.4 Sensitivity Analysis	58
5.4.1 Description and Model Setup	58
5.4.2 Results	60
6 Discussion	68
6.1 Climate Change	68
6.1.1 Air and Sea Temperature	68
6.1.2 Relative Sea Level Rise	69
6.1.3 Storm Intensity and Timing	69
6.1.4 Future Perspectives and Societal Impact	71
6.2 Generalizability of Thermo-morphological Model	71
6.2.1 Erosion Mechanism: Thermal Denudation and Thermal Abrasion	71
6.2.2 Missing Physical Parameters	72
6.2.3 Schematization Challenges	73
6.2.4 Opportunities for Improved Calibration and Validation	74
7 Conclusions and Recommendations	76
7.1 Conclusions	76
7.1.1 Key Findings	76
7.2 Recommendations	77
7.2.1 Model Improvements	77
7.2.2 Data Collection Priorities	79
7.2.3 Practical Applications	79
7.2.4 Future Research Directions	79
References	81
A Differences with Arctic XBeach	96
B Thermo-morphological Model Flow Chart	97
C Thermo-morphological Model Public Repository	99
D Hydrodynamic Boundary Conditions	100
E Challenge of Modelling Long-term Morphology	101
F Calibrated Model Configuration	102

G Base Configuration	108
H Ordered Sensitivity Analysis	114
I Discussion of New Numeric Parameters	116
J Computation Times	118
K Alongshore Transport	120

1

Introduction

1.1. Research Context

Over 30% of the world's coastline consists of permafrost (Lantuit et al., 2012). Large sections of these coasts are subject to erosion (Jones et al., 2020). Especially unlithified Arctic coastlines, which consist of granular material, are experiencing large rates of erosion, with some sites retreating at 2 - 10 meters per year (Jones et al., 2009; Lantuit et al., 2012; Günther et al., 2015). Additionally, erosion rates have been increasing for the past decades (Jones et al., 2020). Arctic erosion poses a severe threat to both the human and natural environment (Fritz et al., 2017).

In the Arctic, erosion mechanisms differ from conventional low-latitude coastlines due to the importance of thermal processes (Ravens et al., 2017). This is because sediment can only be eroded when thawed (Lantuit et al., 2013). Therefore, sea ice, permafrost, and ground ice all affect the Arctic coastal morphodynamics (Overeem et al., 2011; Lim et al., 2020; Nielsen et al., 2020). Additionally, ground ice thawing leads to substantial subsidence in the littoral zone (Nairn et al., 1998). Furthermore, wave action and storm surges are highly seasonal due to the presence of sea ice (Ravens et al., 2023). Erosion mechanisms that include thermal processes unaccounted for in conventional morphological models become important. The two most important mechanisms are thermal abrasion (Figure 1.1) and thermal denudation (Figure 1.2) (Ravens et al., 2023). Modelling efforts have been made to include thermal abrasion (Barnhart et al., 2014b) and thermal denudation (Rolph et al., 2022), some including both (Islam and Lubbad, 2022).

1.2. Problem Definition

The effects of climate change are expected to further intensify erosion along the majority of permafrost coasts (Irrgang et al., 2022). Global surface temperatures are expected to increase the most in the Arctic, facilitating erosion, and changing seasonal sea ice coverage (Kattsov et al., 2005; Dmitrenko et al., 2011; Timmermans and Labé, 2020). Furthermore, (relative) sea level rise and changes in timing and intensity of storms are both associated with increased erosion (Atkinson, 2005; Manson and Solomon, 2007; Meyssignac and Cazenave, 2012). Arctic erosion is a threat to coastal communities (Brady and Leichenko, 2020), infrastructure (Radosavljevic et al., 2016), and cultural heritage (Irrgang et al., 2019), and it releases organic material and nutrients into the environment (Terhaar et al., 2021). The rapid erosion highlights the need for policy and strategic coastal management, for which accurate predictions are required.

Extensive process-based models have been developed to help predict coastal morphology. However, they lack applicability to long-term (decadal) morphodynamic modelling, which is a prerequisite for modelling climate change, engineering, and management time scales. Morphodynamic models have been developed for specific (eroding) coastlines, either by calibrating to a single coastline (Islam and Lubbad, 2022) or by not including all erosion mechanisms (Hoque and Pollard, 2009; Barnhart et al., 2014b). Comprehensive morphodynamic models are run on the time scale of storms only, as they are too computationally expensive to perform long-term analysis (Bull et al., 2020).

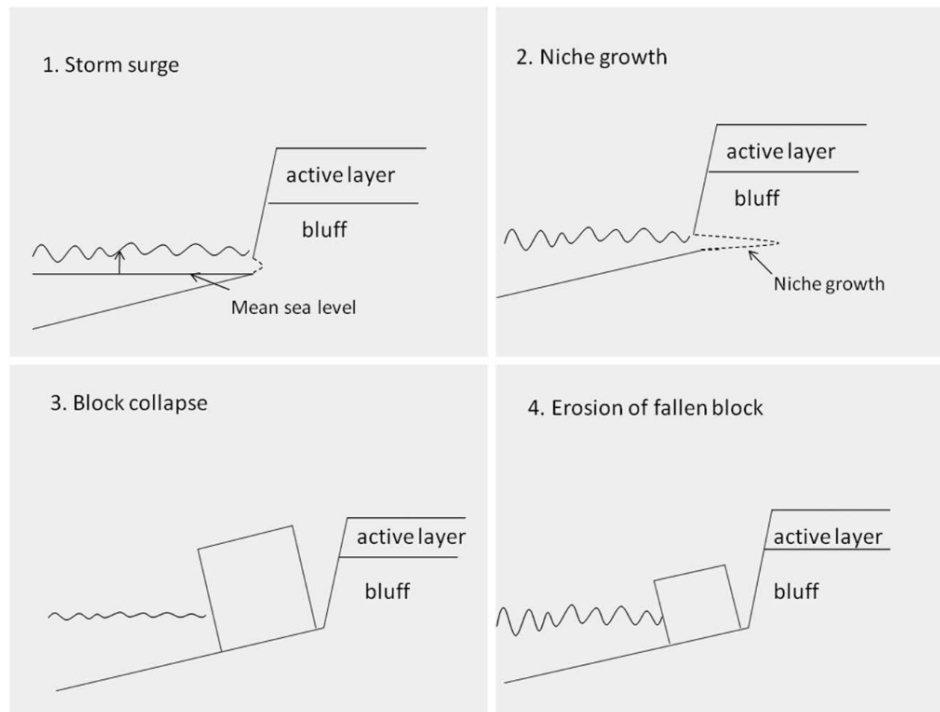


Figure 1.1: Conceptual model of thermal abrasion (also referred to as niche/block collapse), which includes 1) the thawing of (part of) the bluff face, followed by 2) the formation of a niche eroded by waves in combination with storm surge, 3) the block collapsing into the sea, and 4) erosion of the fallen block. Reprinted from Ravens et al., 2012.

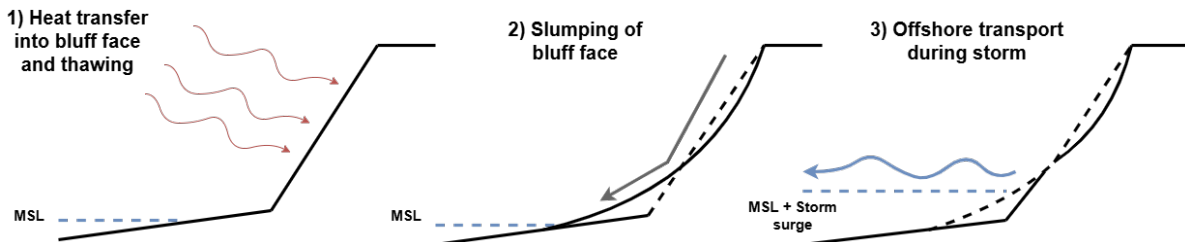


Figure 1.2: Conceptual model of thermal denudation (also referred to as bluff face thaw/slump), which includes 1) the thawing of the bluff face, followed by 2) the slumping and deposition on the beach face, followed by 3) the offshore transport due to storm surge and waves.

Ravens et al. (2017) developed a promising method for modelling Arctic erosion, which is called "Arctic XBeach". This method uses the thermal model by Hu and Argyropoulos (1996), and the well-established XBeach model (Roelvink et al., 2009) is used to model hydrodynamics and simulate coastal morphology. The thermal module predicts a thaw depth, which XBeach uses as the erodible layer. They built a thermal module into XBeach's morphodynamic module. However, the XBeach model is too computationally expensive to perform long-term (decadal) analysis.

1.3. Research Objective and Questions

There is a lack of long-term predictive capability of morphodynamics for Arctic coastlines affected by thermal denudation. This is especially problematic due to the effects of climate change, which are likely to enhance Arctic erosion further. This study aims to research the effects of climate change on Arctic coastal morphology by improving our long-term predictive capability of Arctic coastal morphological changes and using this predictive capability to research the effects of climate change on Arctic erosion, specifically for the erosion mechanism of thermal denudation.

With this goal in mind, we pose the following main research question:

How can the morphodynamics of permafrost coastlines be efficiently modelled at seasonal to yearly time scales to inform the analysis of climate change impacts?

To answer this question, we first developed a decoupled thermal and coastal morphological model. The less computationally expensive thermal model runs continuously to predict thaw depth, while the coastal morphological model is only active when erosion is expected to occur, for example during storms. This research builds on the Arctic XBeach model (Ravens et al., 2017) and therefore also employs the thermal model by Hu and Argyropoulos (1996), as well as the XBeach model (Roelvink et al., 2009) to simulate hydrodynamics and morphodynamics.

Secondly, we use the model to research the effects of climate change on coastal erosion in a case study of Barter Island, which is located on the northern coast of Alaska, US. Specifically, we research the importance of storm timing with respect to permafrost bluff erosion, the increase of air- and water temperature on coastal erosion processes, and the effect of relative sea level rise. These are the main drivers of Arctic erosion and are all likely to change in the future due to the climate crisis.

To develop the decoupled thermo-morphological model, we require data for calibration and validation. We use morphological, meteorological, and hydrodynamic data from Barter Island (Alaska) to calibrate the model. This research focuses on unlithified permafrost-affected coastlines, specifically Barter Island.

To answer the main research question, we pose the following sub-questions:

1. **To what extent can coastal morphology at Barter Island be predicted using a decoupled thermo-morphological model?**
 - i) *What are the dominant processes to be modelled for permafrost-affected coastlines?*
 - ii) *How can the processes and erosion mechanisms that are important for permafrost-affected coastal morphology be modelled accurately?*
 - iii) *How does the model perform for the case study of Barter Island, Alaska, US?*
2. **How sensitive is the thermo-morphological model to site characteristics and changes in forcing related to climate change?**
 - i) *Which site characteristics are most important for controlling erosion?*
 - ii) *Which environmental drivers are most important for controlling erosion rates?*
 - iii) *To what extent does storm timing affect seasonal erosion?*
 - iv) *How will climate change affect the Barter Island coastline?*
 - v) *To what extent can this method be applied to other study sites?*

1.4. Report Outline

This report is outlined as follows:

Chapter 1: Introduction

Chapter 2: Literature Review

This chapter presents a literature review regarding the (modelling of) Arctic erosion. We discuss previous studies of (geological) site characteristics, environmental drivers, erosion mechanisms, climate sensitivity, and impacts on the human and natural environment. Additionally, previous modelling efforts are described. Finally, this chapter outlines the research gap.

Chapter 3: Methodology

This chapter outlines the methodology that we applied in this study.

Chapter 4: Model Formulation

This chapter presents the theoretical framework used in this research, and how we implemented this framework in a process-based numerical model.

Chapter 5: Case study at Barter Island

This chapter describes the application of the developed model to the study site of Barter Island. The chapter contains a site and data description, a description of the calibration and validation effort, and results of the sensitivity analysis we performed with the developed thermo-morphological model.

Chapter 6: Discussion

This chapter discusses the results of the study.

Chapter 7: Conclusions

This chapter provides the conclusions drawn during this study and discusses recommendations for future research.

References**Appendix**

2

Literature Review

This chapter reviews the existing literature on the topic of Arctic erosion. First, we discuss the site-specific coastal settings. Subsequently, we explain the drivers of Arctic erosion, i.e., the environmental drivers. Afterwards, we discuss erosion mechanisms. Next we discuss climate sensitivity, followed by the impacts of Arctic erosion. Afterwards, we describe previous modelling efforts. Finally, the research gap is identified and discussed.

2.1. Coastal setting

Each coastline is unique in terms of its geology and morphology. The interaction of environmental drivers with the coastline determines its evolution, and, in case of erosion, the dominant erosion mechanisms. This section discusses the coastal setting. Specifically, we discuss geological characteristics and morphology.

2.1.1. Geological Characteristics

When considering a coastline, it is important to first know about its sedimentary features. Together with permafrost and ground-ice, which are typical for the Arctic (Overduin et al., 2014), these sedimentary features determine the response of a system to the forcing provided by environmental drivers (Günther et al., 2013; Barnhart et al., 2014a; Kroon et al., 2017; Sinitsyn et al., 2020).

Similar to temperate coasts, Arctic coastlines are highly geologically variable. Perhaps most distinctly, Arctic coastlines can be classified as lithified or unlithified (Overduin et al., 2014). A lithified coast refers to a coast consisting of lithified material, i.e., solid rock. An unlithified coast refers to a coastline consisting of sediment clasts (i.e., granular sand and mud particles). The north-Alaskan coast is mostly unlithified and characterized by frozen bluffs with high ground-ice content (Lantuit et al., 2012).

Arctic coasts are characterized by the presence of permafrost (Lantuit et al., 2012). This refers to the physical state of the lithosphere. Permafrost is defined as "ground (i.e., soil and rock) that remains at or below 0 degrees Celsius for at least two years" (Harris et al., 1988). An active layer is identified, which refers to a layer of ground subject to seasonal freezing and thawing (Dobinski, 2011). The thickness of the active layer depends on (most importantly) the temperature of the ground surface, thermal properties of the ground and its cover, soil moisture content, and snow cover (French, 2017), and on the presence of vegetation (Kelley et al., 2004). A much thicker permanently frozen layer lies beneath the active layer.

For unlithified systems in particular, the volume and distribution of ground ice (i.e., ice formed within the frozen ground, Harris et al., 1988) within the permafrost influence the behaviour of the system, especially with respect to thermal and mechanical erosion (Lim et al., 2020; Smith et al., 2022). More specifically, the erodibility of a coastal section depends on ground ice content. We discuss this further in section 2.3.

Furthermore, ice wedges may form primarily due to cryosuction (Doré, 2004; Woo, 2012). Cryosuction

occurs when temperatures drop and a freezing front forms, which induces a pressure difference and causes water to migrate towards the freezing front. The spatial scale of block failure, which is one of the dominant erosion mechanisms for Arctic coastlines (Section 2.3), depends on the spatial distribution of ice wedges (Ravens et al., 2012). Furthermore, ground-ice content is important in the context of coastal flooding as it may result in significant subsidence when thawed, which results from the reduced volume of the thawed water (O'Neill et al., 2023). This is enhanced further by large parts of the Arctic (unlithified) coast containing excess ice, where the ice volume exceeds the total pore volume. Ground-ice content also partly determines the cohesion of (thawed) sediments (Lantuit et al., 2012). Figure 2.1 provides an example of a permafrost soil, with an active layer and ice wedge present.

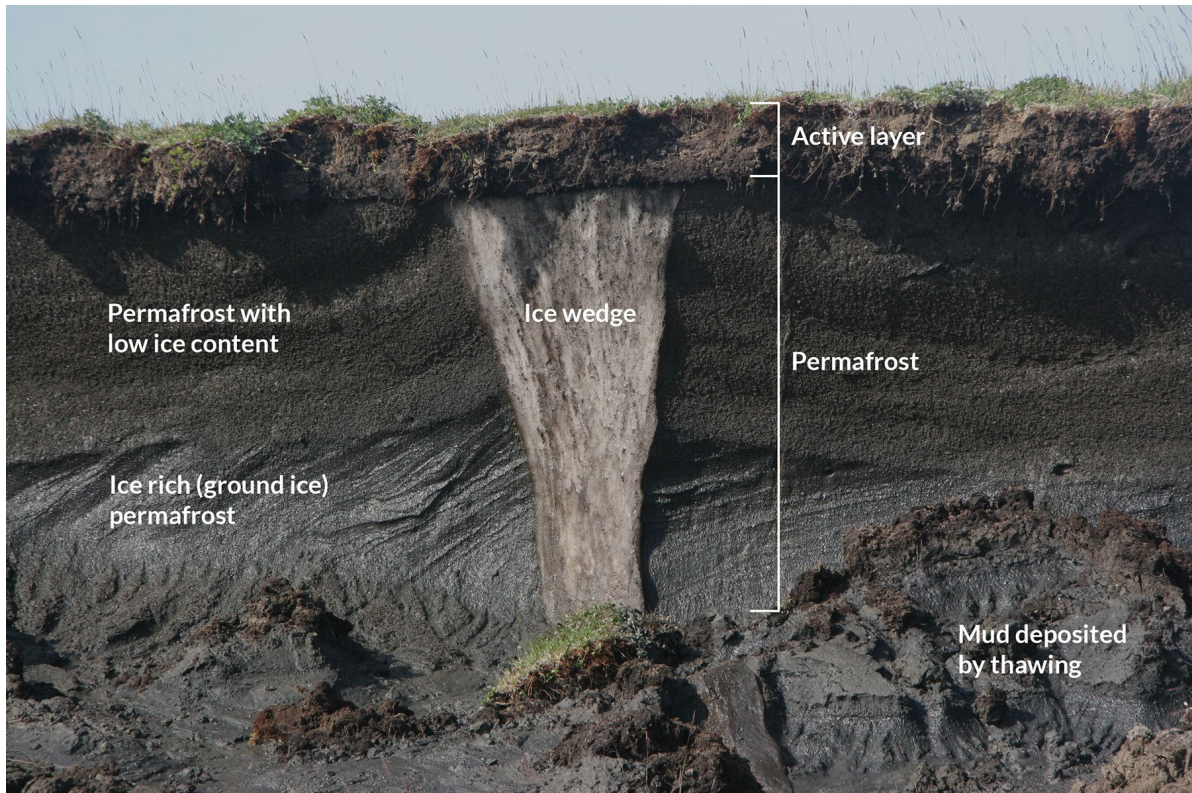


Figure 2.1: Photograph of an unlithified permafrost bluff at Herschel Island (Yukon, Canada). We can identify an active layer, as well as an ice wedge. Photo from Wallace (2019).

There is a high variability in sediment properties in the Arctic with respect to size, distribution, material, etc. (Rawlinson, 1990). Bluffs may be poorly consolidated and consist of a wide distribution of materials (dense clay, interbedded sand and gravel, massive sand), which is complicated further by the presence of ground ice in the form of ice wedges, segregated ice layers, massive ice, and thermokarst ice (Rawlinson, 1990; Jorgenson and Brown, 2005; Kanevskiy et al., 2013; Gibbs et al., 2019). The erodibility of cohesive sediments is determined by the interaction of both physical sediment properties (e.g., particle size distribution, bulk density, water content, temperature, salinity, chemical composition, etc.) and environmental processes (e.g., bioturbation and biogenic substances) (Grabowski et al., 2011). The relative importance of these properties varies for each site and is not fully understood (Grabowski et al., 2011). Arctic beaches are often characterized by a bi-modality with a coarse and a fine fraction (Moore, 1961, Rex, 1964, Owens and McCann, 1970). While fines are transported offshore from the beach during storms, coarser sediments remain on the beach (Rolph et al., 2022).

Typically, the upper layer of the Arctic soil consists of a few centimeters of moss (Gonzalez Martinez et al., 2023), followed by approximately 10 centimeters of organic soil (peat) (Hinzman et al., 1991). This peat can absorb large amounts of water when dried, allowing it to rapidly increase in size (Hinzman et al., 1991). The organic soil attenuates both thermal and hydrological fluctuations in the soil below it (Hinzman et al., 1991). This peat layer, as well as thawed sediment being deposited on the beach, can be seen in Figure 2.2.

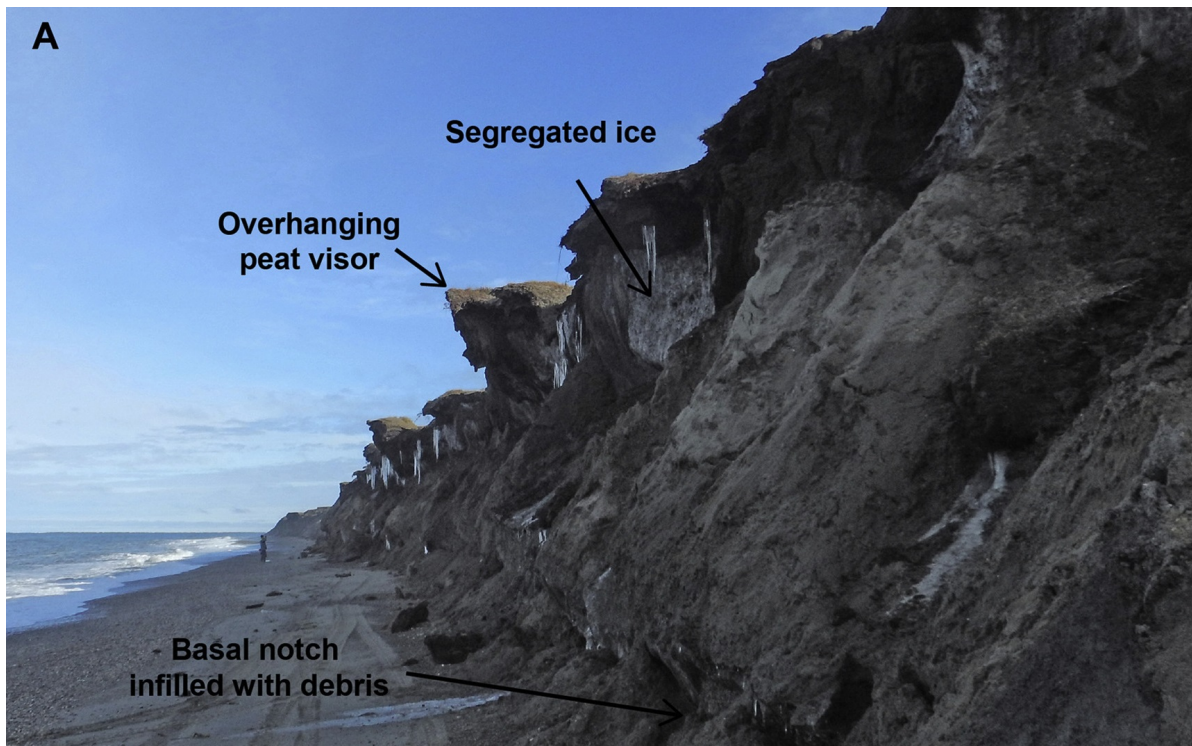


Figure 2.2: Photograph of the bluffs at Barter Island showing overhanging peat visors at the top of the bluffs underlain by a thick layer of segregated ice and unconsolidated sand and gravel that are notched at their base and partially infilled with debris; the bluff height is approximately 8 meters (Photo A. Gibbs, Sept. 2016). Reprinted from Gibbs et al. (2019).

2.1.2. Coastal Characteristics

Bluffs are common occurrences on Arctic coastlines. Bluff height can reach over 10 meters (for example, at Barter Island, Gibbs et al., 2019). Bluff height, bluff inclination, and bluff orientation relative to the north all influence the active layer depth (Ravens et al., 2023). Bluff height in combination with angle determines the exposure length to either air or seawater during extreme setup (Rolph et al., 2022). A large bluff height (and thus large exposure length) increases the total convective heat transfer, which increases thaw depth (Rolph et al., 2022). Additionally, a lower bluff inclination increases solar intensity as the angle between the bluff surface area and the incoming radiation increases (Buffo et al., 1972; Ravens et al., 2023). Even though larger bluff faces facilitate more heat transfer, it is found that higher cliffs take longer to retreat because of the larger volumes to be eroded (Lantuit et al., 2012). Low-lying coasts can erode more quickly (Kobayashi et al., 1999; Lantuit et al., 2011; Rolph et al., 2022). Additionally, low-lying coasts are more vulnerable to inundation (Barnhart et al., 2014a).

Short (1973) researched the nearshore morphology of northeastern Alaskan coasts. He found that beach properties, such as nearshore slope, width, and height are determined by sediment response to the environmental forcing during the sea ice-free season. During the sea ice-free period, beach response is directly related to wave conditions. Due to variability in wave conditions, two different regimes are distinguishable: accretive and erosive. This is reflected in 1) a high-frequency beach response, and 2) the formation of outer bars. Sediments are noted to be fine seaward of the swash bar, bi-modal on the bar, and finer landward of the bar. Inner bars are generally not formed due to the relatively low waves. The bathymetric profile of the shoreface in the Arctic generally does not differ from that in sea ice-free seas (Are et al., 2008).

Coastal orientation is important for determining incoming wave height, as refraction and diffraction impact the incoming waves (Penney and Price, 1952; Komar, 1998). Additionally, wave conditions are highly dependent on fetch and thus on the location of sea ice (Short, 1973). This further enhances the importance of coastal orientation for the wave regime. Barrier islands are also prominent, especially along the northeastern coast of Alaska, which influences local wave climates (Short, 1973). Offshore islands reduce wave energy, which restricts erosion rates (Frederick et al., 2016).

Permafrost is also present below the waterline. Submarine permafrost may be partially frozen, depending on temperature, salt content, sediment grain size, and composition (Overduin et al., 2019). Degradation of submerged permafrost leads to thaw subsidence of the land surface onshore (Grosse et al., 2007) or the sea bed offshore (Overduin et al., 2012). Offshore subsidence leads to local changes in the bathymetry, which are smoothed out by wave action (Are et al., 2008). The eroded profile may serve as accommodation space for sediments eroded from the coast (Hequette and Barnes, 1990). The nearshore sediment is predominantly silt (Ping et al., 2011), which may increase salinity locally, leading to the thawing of permafrost (Overduin et al., 2012), thereby increasing permafrost degradation. Subsidence of the nearshore allows larger waves to reach the coast. Aré (2003) correlated the rate of submarine permafrost degradation with coastal erosion rates. Submarine permafrost degradation may be controlled by sea level rise and coastal erosion, sea bottom temperature, salinity regimes, geothermal heat flux, and heat and mass diffusion within the sediment column (Overduin et al., 2012). At Barrow, Alaska, the mean submarine permafrost degradation rate in the nearshore is 1-4 cm/year (Overduin et al., 2012). However, the effect of the thawing of submarine permafrost in the nearshore zone on coastal erosion is considered to be small (Reimnitz et al., 1988; Are et al., 2008).

2.2. Drivers of Arctic Erosion

2.2.1. Waves

Waves are one of the main drivers of Arctic erosion. The wave climatology determines how much wave energy can be transmitted to the shore (Irrgang et al., 2022). The Arctic is characterized by a low mean annual wave energy (Frederick et al., 2016). Wave energy is directly controlled by (peak) wave period and height (Thomson et al., 2016).

Environmental controls on the wave climate further include sea-ice coverage, and the duration, frequency, and seasonal timing of storms (Thomson et al., 2016; Ahmad et al., 2019), as well as wind speed and direction, fetch, and nearshore bathymetry (Ogorodov et al., 2016; Shabanova et al., 2018). Wave energy in the Arctic greatly depends on fetch, which is controlled by sea ice coverage and wind direction (Short, 1973; Barnhart et al., 2014a).

Therefore, the timing of freeze-up and break-up of the sea ice with respect to storm timing determines the wave energy affecting the coast (Shabanova et al., 2018). The strongest Arctic storms typically occur in autumn (Atkinson, 2005; Manson et al., 2005), towards the end of the sea ice-free season. This timing coincides with maximum active layer thickness (Brown et al., 2000; Nicolsky et al., 2017), which makes the coast vulnerable to high erosion rates. Storms occurring at the beginning of the sea ice-free period have minimal impact because the soil has not thawed (Ravens et al., 2023). During the sea ice-free season, currents generated by wave action are important drivers for the redistribution of sediments (Hume and Schalk, 1967).

2.2.2. Water Level

Storms increase the sea level through storm surge, which further increases wave energy transmission to the coast (Irrgang et al., 2022). Besides, an increased sea level allows waves to directly impact the coastal bluffs (Irrgang et al., 2022), which enhances thermal abrasion (Gibbs et al., 2019). A large (temporary) increase in sea level may also induce flooding and subsequently thawing of permafrost in affected areas (Sinitsyn et al., 2020; Kim et al., 2021).

Most of the Arctic coast is characterized by a micro-tidal regime (ESA, 2019). This means that (daily) tidal processes have little effect on coastal dynamics (Irrgang et al., 2022). However, relative sea level rise due to glacial isostatic adjustment, tectonic activity, and thaw subsidence may have large long-term effects (Lambeck et al., 2014; Farquharson et al., 2018; Horton et al., 2018). In this context, glacial isostatic adjustment refers to the adjustment of the Earth's solid mass, gravitational field, and oceans to the growth or decay of global ice sheets (Whitehouse, 2018).

2.2.3. Sea Ice

Sea ice directly influences Arctic coasts both in the nearshore and the offshore. In the nearshore, sea ice restricts erosion, suspension and transport of sediment through wave action (Barnhart et al., 2014a). Furthermore, convective heat transport from the sea to the coast is also limited by sea ice (Barnhart

et al., 2014a). The local albedo is increased by the presence of sea ice, which leads to a lower water temperature (Kashiwase et al., 2017).

Sea ice can also transport sediment offshore through sea ice drifts (Eicken et al., 2005), damage the coast through ice pile-up and ride-up (Kovacs and Sodhi, 1980), or induce resuspension and transport of shelf sediments (Rearic et al., 1990; Héquette et al., 1995). However, these transport rates are considerably smaller than transport induced by hydrodynamic processes in the nearshore (Barnhart et al., 2014a).

Therefore, sea ice is generally associated with reducing wave energy transmitted to the coast, both by reducing storm intensity through limiting fetch (Ogorodov et al., 2016) and by protecting the nearshore (Barnhart et al., 2014a). During the sea ice-free season, sea ice may be blown to shore from higher latitudes (Kempama et al., 1989). This sea ice protects the shore through wave attenuation (Manson et al., 2016). Land-fast ice may also serve as a form of protection for the coast, while also blocking the sediment transport mechanisms described above (Barnhart et al., 2014a).

2.2.4. River Sediments

River sediments compose a large part of the nearshore coastal sediment budget for most of the Arctic (Irgang et al., 2022). Due to freeze-up, sediment delivery to the coast shows large seasonal variations (Wegner et al., 2015). Rivers are frozen during the winter months, which limits sediment transport (Bendixen and Kroon, 2017).

2.2.5. Salinity

During summer months, large rivers affect sea surface salinity (Kuzin et al., 2010; Bauch et al., 2013; Golubeva et al., 2019). Salinity influences the thawing temperature, as higher salinity induces the thawing of frozen sediment (Guimond et al., 2021). Furthermore, saltwater intrusion, which is increased for an increased sea level, drives permafrost thaw (Guimond et al., 2021).

2.2.6. Heat Fluxes

Sediments can only be eroded when thawed (Lantuit et al., 2013). Heat fluxes impacting the thaw of sediment consist of shortwave (solar) radiation, longwave radiation (emitted from the earth's surface and downward from the atmosphere), sensible heat fluxes, and latent heat fluxes (Ravens et al., 2023).

Solar radiation varies seasonally due to diurnal variations and insolation. The sensible heat flux consists of convective heat transfer (Incropera et al., 2013) from air and water, which occurs if air/water temperatures are different from soil temperatures. Latent heat fluxes occur due to phase changes of a material (Incropera et al., 2013), e.g., due to the thawing of pore water in permafrost-affected soil.

Due to the importance of both temperature and phase changes, a standard heat conduction model is not suitable (Hu and Argyropoulos, 1996). Instead, heat balance equations in terms of *enthalpy* may be used (Ravens et al., 2023), where enthalpy is defined as the sum of thermal energy and flow work (Incropera et al., 2013).

2.2.7. Snow

Snow cover impacts the ground thermal regime (Zhang, 2005). Snow has a high albedo, ranging from 0.60 to 0.85 (with 1 being perfect reflection), depending on the weather and snow conditions (Wendler and Kelley, 1988; Zhang et al., 1996). This high albedo reduces the amount of absorbed solar energy and thus lowers the snow temperature (Zhang, 2005).

Snow cover may insulate a bluff which temporarily protects the bluff face from incoming radiation (Zhang, 2005). This reduces the impact of thermal denudation, which influences the relative importance of different erosion mechanisms (Vasiliev et al., 2005; Günther et al., 2012). However, the cooling effect of the snow surface temperature is limited because the solar elevation is limited at high (Arctic) latitudes during the months in which snow is present (Zhang, 2005).

Snow also has high emissivity and absorptivity, which leads to surface cooling during clear-sky conditions, but surface warming during cloudy-sky conditions when there is a higher intensity of incoming longwave radiation (Zhang, 2005). Due to its low thermal conductivity, seasonal snow cover functions

as an insulator between the air and soil (Zhang, 2005). Since snow cover occurs mostly during winter months, the snow insulation effect prevents the soil from cooling due to sensible heat fluxes from the colder air (Zhang, 2005).

The effect of latent heat from snow is not well understood, though it is known that the melting of snow initially functions as an energy sink, requiring additional energy and keeping the soil temperature low (Zhang, 2005). For Arctic coastlines, snow melt induces thaw in frozen bluffs (Guegan and Christiansen, 2016). Additionally, runoff from melting snow can erode frozen sediments through a process called nivation, which is induced by alternated freezing and thawing of the soil (French, 2007; Guegan and Christiansen, 2016).

2.3. Erosion Mechanisms

The main erosion mechanisms include thermal abrasion, thermal denudation (Ravens et al., 2023), retrogressive thaw slumps (Jones et al., 2019), and surface wash (Gibbs et al., 2013). Thermal abrasion (also referred to as niche erosion or block collapse) and retrogressive thaw slumps occur mostly where coastal bluffs are ice-rich (Ping et al., 2011; Jones et al., 2019).

Thermal abrasion refers to the formation of a wave cut niche in the permafrost bluff, usually formed during storm conditions, which may result in block collapse (Kobayashi, 1985; Aré, 1988). During a (temporary) increase in sea level, due to for example storm surge, waves reach the bluff face and convective heat transfer in combination with mechanical wave action leads to niche formation, which can finally result in block collapse when the weight of the overhang exceeds the strength of the bluff (Ravens et al., 2023). Most erosion occurs below the waterline (Aré, 1988), and erosion rates are negligible when the water level does not reach the base of the bluff (Barnhart et al., 2014b). Furthermore, the formation of the niche is controlled by the duration of the sea ice-free season, and the (sea) water temperature (Barnhart et al., 2014b). Figure 2.3 provides an example of thermal abrasion resulting in block collapse, which is conceptualized by Figure 1.1.



Figure 2.3: Example of thermal abrasion from Drewpoint, Alaska, US. Adapted from Jones (2017).

Thermal denudation (also called bluff face thaw/slump) refers to the thawing of frozen material at the bluffs and slumping of the material due to gravity, followed by offshore transport by wave action, possibly during storm conditions (Razumov, 2001; Baranskaya et al., 2021; Ravens et al., 2023). The bluff face is heated by a combination of heat fluxes: solar (shortwave) radiation, longwave radiation emission

from the Earth's surface, absorption of downward longwave radiation from the atmosphere, a sensible heat flux, and a latent heat flux (Westermann et al., 2009; Ravens and Ullgren, 2020; Ravens et al., 2023). Material from the bluff face slumps down to the beach. From there it is transported offshore by relatively small storms (Ravens et al., 2011). This process is important at Barter Island (Ravens et al., 2011; Panchang and Kaihatu, 2018). Fines and ground ice do not contribute to the sediment balance in the littoral zone when eroded (Nairn et al., 1998; Rolph et al., 2022). The ground ice melts during transport by seawater, and fines are transported offshore. This means that after a storm, which transports deposited fines offshore, the fines are not transported onshore again. Figure 2.4 gives an example of thermal denudation, which Figure 1.2 conceptualizes.

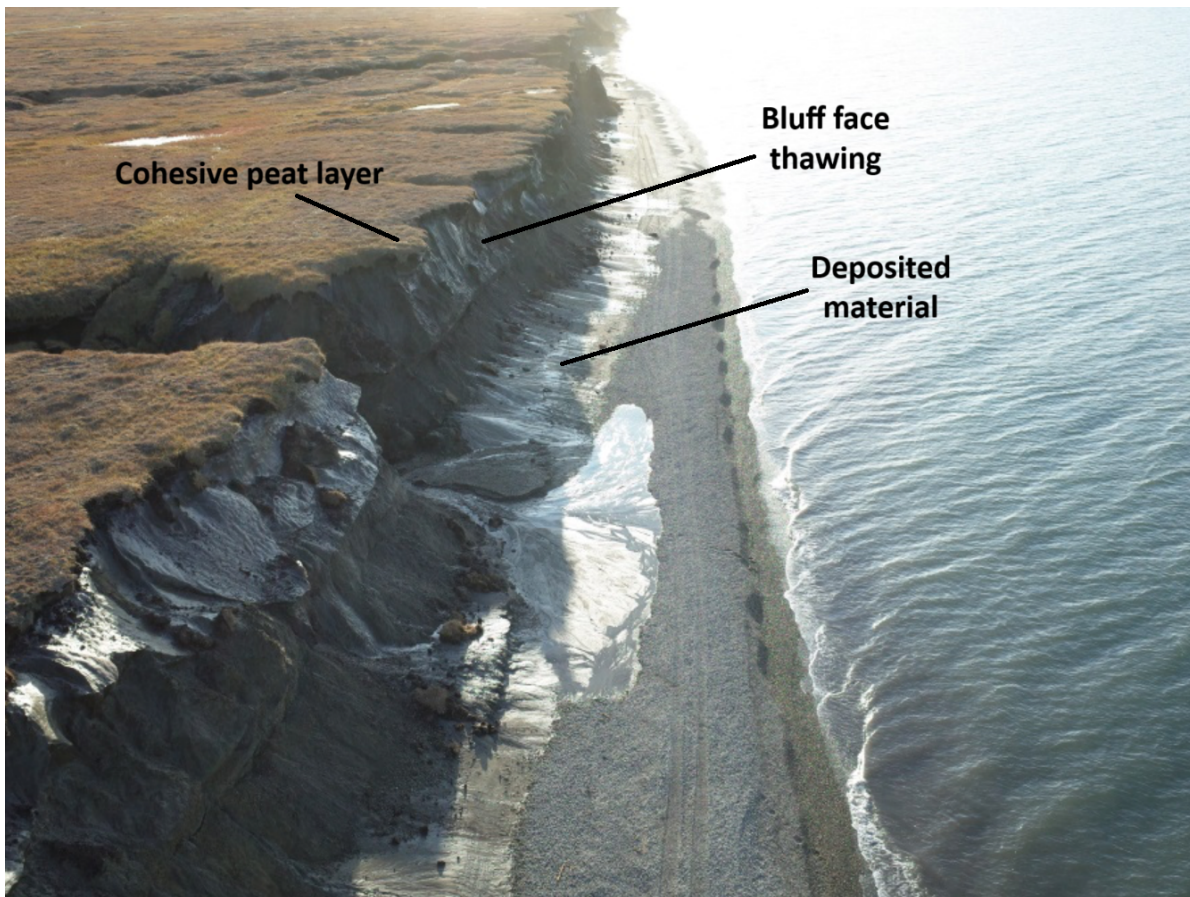


Figure 2.4: Example of thermal denudation occurring at Barter Island, Alaska, US. Adapted from Pacific Coastal and Marine Science Center (2019).

Ravens and Peterson (2021) identify a single parameter that determines whether thermal abrasion or thermal denudation is the dominant erosion mechanism: the **coarse sediment areal density**. The coarse sediment areal density is defined as "the dry mass of coarse sediment (sand and gravel) contained in a column of bluff sediment/soil per unit horizontal area (g cm^{-2})" (Ravens and Peterson, 2021). In general, thermal abrasion is the dominant erosion mechanism where there are few coarse sediments present in the coastal bluffs, and there is frequent contact between the sea and the bluff. A low beach elevation below the bluff further facilitates this. Conversely, thermal denudation is dominant where sediments are coarse, resulting in a high beach elevation, which means contact between sea and bluff is less frequent (Ravens et al., 2011; Ravens and Peterson, 2021).

Retrogressive thaw slumps are a form of thermokarst. Thermokarst is defined as "the process by which characteristic landforms result from the thawing of ice-rich permafrost" (Harris et al., 1988). Retrogressive thaw slumps form at ice wedges and refer to a flow of fluidized sediment moving downslope (Kokelj and Jorgenson, 2013; Jones et al., 2019). These slumps can grow by several meters per year and cause large erosion (Lantuit and Pollard, 2008; Grosse et al., 2011). Retrogressive thaw slumps

are associated with high, steep bluffs (>8 m) containing icy sediments (Gibbs et al., 2013; Zwieback et al., 2018). They commonly form adjacent to streams, (thermokarst) lakes, or coastlines where ice-rich permafrost is exposed through erosion (Lantuit and Pollard, 2008; Gibbs et al., 2013; Jorgenson, 2013). Figure 2.5 provides an example of a retrogressive thaw slump.



Figure 2.5: Example of a retrogressive thaw slump from the Beaufort Sea coast, Northwest Territories, Canada. Photo by GSC (2021).

Surface wash is a form of mechanical erosion driven by surface runoff, or by the melting of (ground) ice wedges (Gibbs et al., 2013). Melting may occur due to convective heat transfer from warmer surface runoff or exposure to warm air temperatures. This mechanical erosion leads to the formation of gullies (Figure 2.6).

Depending on the relative importance of the erosion mechanisms described above, total erosion may be a combination of each. Sediment can only be eroded when thawed (Lantuit et al., 2013), which is why thermal effects are important for Arctic erosion. This makes erosion highly seasonal. Erosion therefore mostly occurs during the summer months.

In case of thermal denudation, which is the main failure mechanism at Barter Island (Section 5.1), thawed sediments first slump to the beach. Material from the beach is transported offshore during episodic events. These episodic events may also cause thermal abrasion (i.e., niche formation resulting in block failure) (Gibbs et al., 2019).

2.4. Climate Sensitivity

The erosion mechanisms described in Section 2.3 are sensitive to the effects of climate change. This highlights the need for a long-term morphological model, for time scales of the same order of magnitude as the changing climate. This section describes how different effects of climate change might influence erosion mechanisms.



Figure 2.6: Example of surface wash in Greenland. Photo by Shone (2023).

2.4.1. Air Temperature

The air temperature in the Arctic has experienced a greater increase relative to global means, with increases being up to 2-3 times as large (Ballinger et al., 2022; Chylek et al., 2022; Rantanen et al., 2022). For example, air temperatures at Utqiagvik (Alaska) have increased by over 1.5 degrees Celsius since 1921 (Wendler et al., 2014). Air temperature influences ground temperature and thus active layer thickness, sea temperature, sea ice coverage, and duration of the sea ice-free season (Irrgang et al., 2022). An increase in ground temperatures allows for deeper development of the active layer, which induces permafrost degradation and thaw-induced subsidence (Günther et al., 2015; Lim et al., 2020). This increases erosion rates and salt intrusion (Günther et al., 2015; Lim et al., 2020).

Furthermore, air temperature is one of the main drivers of sediments thawing in bluff faces (Jones et al., 2018; Irrgang et al., 2022). These sediments slump to the bluff toe when thawed, thereby increasing erosion rates for higher air temperatures. Therefore, coasts that are susceptible to thermal denudation have an increased sensitivity to rises in air temperature. Rises in air temperature are associated with an increased erosion rate for these coasts (Günther et al., 2013; Günther et al., 2015; Shabanova et al., 2018; Baranskaya et al., 2021). Finally, an increase in air temperature induces an increase in sea temperature and a reduction of sea ice coverage, as well as a lengthening of the sea ice-free season (Irrgang et al., 2022).

2.4.2. Sea Temperature

Sea surface temperatures are rising throughout the Arctic (Carvalho and Wang, 2020). This increase is controlled by solar radiation, air temperature, sea ice coverage and distribution, cloud coverage, and advection from lower latitudes (Timmermans and Labe, 2020). An important effect is the lengthening of the sea ice-free season (Timmermans and Labe, 2020) (Section 2.4.3). Furthermore, an increase in sea temperature enhances the potential of thermo-mechanical erosion, with higher sea temperatures leading to higher erosion along coasts with high ground-ice content and increased submarine permafrost degradation (Dmitrenko et al., 2011).

2.4.3. Open Water Period

Due to climate change, Arctic sea ice coverage has declined (Maslanik et al., 2007; Kwok et al., 2022; Perovich et al., 2020). The average yearly sea ice coverage of the entire Beaufort Sea has reduced from 83 % to 69% over the period 1979 to 2012 (Wendler et al., 2014). Furthermore, the sea ice-free season (or open water period) has increased in length, having doubled in length for the north Alaskan

coast from 45 days to 95 days over the period 1979 to 2009 (Overeem et al., 2011).

Especially important is the lengthening of the open water period into the autumnal storm season (Barnhart et al., 2015; Box et al., 2019). Storms at the end of the open water period induce high erosion because that is when the depth of the active layer (i.e., thawing depth) is at a maximum (Ravens et al., 2023).

Additionally, for intermediate sea ice coverage, increased wind friction can induce an increased storm surge height (Joyce et al., 2019). A decrease in sea ice cover results in a larger fetch, which results in more frequent and more intense storms. This is enhanced further by the lengthening of the sea ice-free season resulting in a larger expected frequency of storm conditions (Vermaire et al., 2013; Barnhart et al., 2014a; Thomson et al., 2016; Casas-Prat and Wang, 2020; Nielsen et al., 2020).

Finally, a decrease in sea ice coverage results in a lower albedo. This increases radiation absorption and leads to higher sea temperatures, which accelerates the decline in sea ice coverage (Kashiwase et al., 2017).

2.4.4. Wave Climate

Due to climate change, mean near-surface wind speeds over the Arctic Ocean are expected to increase (Mioduszewski et al., 2018). Extreme wave events are projected to occur more frequently (Vermaire et al., 2013). Increased fetch and lengthening of the sea ice-free season induce the generation of long swell waves and an increased wave height, which increases both the intensity and frequency of storm conditions (Vermaire et al., 2013; Barnhart et al., 2014a; Thomson et al., 2016; Casas-Prat and Wang, 2020; Nielsen et al., 2020). An increase in wave height leads to higher wave setup which, together with an increase in wave energy, enhances thermal abrasion (Gibbs et al., 2019).

Nederhoff et al. (2022) report an increase in cumulative yearly wave power of 400% for the period 1979 to 2019, mostly due to an increase in the length of the open water period for the Beaufort Sea coast. Additionally, simulations show that the number of rough wave days (defined as days when maximum wave heights exceed 2.5 meters) has increased from 1.5 to 13.1 days over that same period (Nederhoff et al., 2022).

2.4.5. Sea Level

The relative sea level in the Arctic has been increasing since at least 1990, with the most rapid increases of up to 10 to 15 millimeters per year occurring in the Beaufort Sea, off the coast of northern Alaska (Jin et al., 2023). Annual means are subject to variability due to the Arctic Oscillation (which is associated with wind-induced Ekmann transport) and the Arctic dipole anomaly (which results from a wind anomaly) (Jin et al., 2023). Relative sea level rise due to glacial isostatic adjustment, tectonic activity, and thaw subsidence may have large long-term effects (Lambeck et al., 2014; Farquharson et al., 2018; Horton et al., 2018).

An increase in sea level enhances thermal abrasion, and induces flooding resulting in the thawing of permafrost in the affected area (Section 2.2). Additionally, a (temporary) increase in sea level due to e.g., wave setup or wind-driven surge, allows higher waves to reach the coast, enhancing thermal abrasion (Gibbs et al., 2019).

2.4.6. Future Perspectives

Effects of climate change include an increased active layer depth, a lengthening of the open water period, increased storm intensity and frequency, and an increase in sea level (Irrgang et al., 2022). Each of these factors is associated with increased erosion rates along permafrost-affected coastlines, which implies that climate change will further intensify erosion along Arctic coasts. As coastal erosion induces a positive feedback loop through global warming (Irrgang et al., 2022), negative effects of climate change (e.g., sea level rise) both accelerate and are accelerated by Arctic coastal erosion. An effective response to climate change in the polar region needs to include both short-term response and long-term planning (Intergovernmental Panel On Climate Change (Ipcc), 2022).

2.5. Impacts of Arctic Erosion

This section discusses the impacts of Arctic erosion. Impacts are categorized by whether they (mainly) affect the natural or the human environment.

2.5.1. Natural Environment

Huge amounts of organic carbon (Hugelius et al., 2014; Couture et al., 2018; Friedlingstein et al., 2020), nitrogen/nutrients (Terhaar et al., 2021), and contaminants (Schaefer et al., 2020) are present in permafrost soils. The fluxes of these materials into the Arctic Ocean are highly dependent on the coastal erosion rate (Irrgang et al., 2022). The impact of Arctic coastal erosion on the natural environment is twofold.

Firstly, the primary production in the Arctic Ocean is likely to change as a result of these fluxes (Dunton et al., 2006). A change in nutrient availability or bio-turbidity (which determines light intrusion) may cause large-scale alterations in the marine food web, and thus the Arctic ecosystems (Dunton et al., 2012).

Secondly, the organic matter released from the permafrost soil may be emitted directly as a greenhouse gas (Abbott and Jones, 2015; Tanski et al., 2021; Miner et al., 2022). These emissions are directly linked to the erosion of a permafrost bluff (Vonk et al., 2012). The release of greenhouse gasses results in a global feedback loop which further enhances climate change (Irrgang et al., 2022) and Arctic coastal erosion (Section 2.4).

2.5.2. Human Environment

Erosion is a direct threat to people living in close proximity to the coast (Jaskólski et al., 2018), particularly subsistence-based lifestyles (Brady and Leichenko, 2020). Furthermore, coastal erosion threatens cultural heritage (Radosavljevic et al., 2016; Nyland et al., 2017; Dawson et al., 2018; Irrgang et al., 2019), among which archaeological sites (O'Rourke, 2017; Irrgang et al., 2019), and infrastructure (Hjort et al., 2018; Hjort et al., 2022). Coastal settlements are susceptible to permafrost degradation, coastal erosion, and flooding (Ramage et al., 2021). Relocation of people is one of the proposed solutions but often faces problems with high costs, cultural and social objections, or geotechnical issues with new locations (Landauer and Juhola, 2019). Furthermore, changes in the marine ecosystems mentioned in the previous subsection affect the food web, which is especially troublesome for local subsistence-based communities (Dunton et al., 2012), because of hunting areas being lost (Gorokhovich et al., 2014).

The decline of Arctic sea ice coverage and permafrost can also provide opportunities. Human presence in the Arctic is increasing (Jaskólski, 2021). Natural resources that were previously inaccessible or avoided can become accessible (Ermida, 2014; Stephen, 2018; Irrgang et al., 2022), new shipping routes can become available (Smith and Stephenson, 2013; Mudryk et al., 2021), and the cruise ship tourism sector is expected to profit (Stewart et al., 2015). However, exploitation of natural resources comes at the risk of pollution of the natural environment or permafrost degradation, thereby further intensifying coastal erosion (Irrgang et al., 2022). Tourism also adversely affects the environment through tundra trampling, pollution, and increased sea and air traffic (Dawson et al., 2017; Jaskólski, 2021). The changing geopolitical climate also increases the pressure on the Arctic environment and highlights the need for a better understanding of the Arctic coastline and the processes that affect it (Brimmer, 2023).

2.6. Modelling of Arctic Erosion

This section discusses previous efforts to model Arctic erosion.

A wide range of models exist that describe the morphology of a temperate coastline. However, these are usually not applicable to permafrost coastlines (due to the processes described in Section 2.3). Models that simulate the erosion of permafrost bluffs exist. These were mostly developed in the past decades (Irrgang et al., 2022). Models consider varying spatial and temporal scales and resolutions, use varying empirical or physical formulations for different erosion mechanisms, and include different forcing variables.

2.6.1. Thermal Abrasion

One of (if not) the first modelling efforts to describe niche erosion was made by Kobayashi (1985), and it remains widely used. They derive a semi-empirical analytical solution to describe niche depth during a storm surge event as a function of time. Their solution includes seawater temperature, salinity, sediment concentration, and horizontal cross-shore fluid velocity. It is expanded upon by Kobayashi and Aktan (1986), who analyze heat conduction through frozen sediment exposed to wave action for conditions where a niche does not form.

Kobayashi and Virdrine (1995) couple an analytical solution for a (partially) frozen beach to a coastal morphological model, the COSMOS-2D model (Southgate and Nairn, 1993; Nairn and Southgate, 1993). Barnhart et al. (2014b) show that the formulation by Kobayashi (1985) is not applicable for modelling longer (decadal) periods.

The formulation by Kobayashi (1985) was used by Hoque and Pollard (2009) to assess the stability of predefined failure planes (in the bluff). Hoque and Pollard (2016) determine failure criteria for block failure as a function of niche depth, ice wedge distance, and ice-wedge depth for bluffs of a given height and with a given soil strength. The work by Hoque and Pollard (2009) was expanded upon by Ravens et al. (2012), who also propose an empirical formulation for the erosion of the fallen block (after failure) assuming thermal abrasion. This formulation was adapted by Barnhart et al. (2014b) to better agree with field observations. Ravens et al. (2012) also include wind characteristics to predict water levels by employing the cross-shore equation of motion (Freeman et al., 1957; Dean and Dalrymple, 2004). Model calibration was done using historic coastal retreat rates. A similar study was performed by Islam et al. (2020) and included a probabilistic model to determine the effects of uncertainty in the input parameters.

Conversely, Wobus et al. (2011) treat erosion of the fallen block as a purely thermal process and use the power-law model by Holland et al. (2008) to determine the melt rate of the block, which itself is based on the melting of free-drifting icebergs (Russell-Head, 1980). A different approach was taken by Ahmad et al. (2019), who employ the incompressible Reynolds-Averaged Navier-Stokes (RANS) equations to model seawall erosion, as a proxy for thermal abrasion. However, this approach does not include thermal processes and does not apply to the modelling of longer periods due to its high computational costs. This limits its pan-Arctic applicability.

Frederick et al. (2021) employ a coupled thermal-mechanical model. A solid mechanics model calculates the three-dimensional stress, strain, and displacement fields of the permafrost, and a thermal model determines the three-dimensional heat conduction and phase changes in the permafrost. This approach eliminates empirical formulations for failure modes by using a finite element model to represent constitutive relations, and it models erosion by dynamically removing elements from the mesh. This thermo-mechanical model is part of the Arctic Coastal Erosion (ACE) model developed by Bull et al. (2020) and is highly specialized for small-scale (i.e., single-failure-event) calculations. Though the computational cost is large, this model is one of (if not) the most comprehensive and physically sound existing models.

Rolph et al. (2022) employ a different implementation which utilizes heat and sediment balance equations to predict horizontal cliff retreat and vertical erosion of a fronting beach. They use cliff and beach erosion formulations by Kobayashi et al. (1999), which they couple with a bathystrophic storm surge model (Freeman et al., 1957; Dean and Dalrymple, 2004). However, they do no model thermal processes explicitly. Slumping is also not included. Guégan (2015) derived equations that describe temperature-dependent slope stability and slump failure, but they do not include progressive failure or cross-shore beach profile development.

2.6.2. Thermal Denudation

The modelling efforts described so far consider thermal abrasion as the main erosion mechanism. In recent years, attention has shifted towards thermal denudation (Frederick et al., 2016). An early effort by Ravens et al. (2017) employs a two-step model referred to as 'Arctic XBeach'.

During the first step, a heat transfer module determines thaw depth (or active layer depth) by computing the temperature and phase of the sediment and water in the soil using the 1D time-dependent heat balance equation in terms of enthalpy (Hu and Argyropoulos, 1996). Since sediment can only be

eroded when thawed (Lantuit et al., 2013), this active layer depth is then given to the conventional (2D) XBeach model (Roelvink et al., 2009). During the second step, XBeach is activated.

XBeach was developed for temperate coasts (e.g., the test cases in Roelvink et al., 2009). However, since permafrost does not significantly affect the shape of the shoreface profile (Are et al., 2008), it may also be used to simulate morphological change in the Arctic.

The XBeach model includes a subroutine to determine the slumping of unfrozen material. The heat transfer module includes convective heat transfer from water (Kobayashi et al., 1999) and air (Ravens et al., 2017). Ravens et al. (2023) further expanded the thermal module by including a solar radiation flux calculator (Section 4.3.5). The heat transfer module and solar flux calculator alternate with the XBeach model, meaning both modules must run continuously. This limits its application to the modelling of longer periods due to its high computational costs.

A solution to this problem could be to decouple the thermal module and hydrodynamic/morphodynamic module. The thermal module, which has a relatively low computational cost, is run continuously, whereas the more costly morphodynamic module is active only during periods of high expected morphological change (e.g., during storm events). This is done by Kupilik et al. (2020), who employ an empirical formulation for erosion as a function of longshore and cross-shore transport, sea level, and thermo-erosion alongside Delft3D to model the wave climate (but not sea level as a result of storm surge). Storm timing is determined using wind speeds and directions. However, this approach does not explicitly model the process of thermal denudation.

2.6.3. Thermal Abrasion and Denudation

Efforts have been made to include both thermal abrasion and thermal denudation in a single model. Islam and Lubbad (2022) implement different sub-modules within XBeach for the different erosion mechanisms. They use 'permafrost thaw' and 'slumping' modules for thermal denudation, and they use 'niche growth', 'bluff collapse', and 'degradation of collapsed bluff' modules to simulate thermal abrasion. These subroutines feature empirical relationships.

2.6.4. Other

A completely different approach was taken by Nielsen et al. (2022). Their work assumes that coastal erosion is a linear combination of Arctic-mean yearly-accumulated daily-mean positive 2 m air temperatures and Arctic-mean yearly-accumulated daily significant wave heights. This simplified erosion model allows the modelling of multiple climate scenarios on a large (pan-Arctic) spatial scale.

2.6.5. Physical Modelling

Understanding of Arctic erosion may also be improved through physical modelling. Korte et al. (2020) present a framework for experimental model generations to analyze permafrost in coastal environments. However, the reconstruction of a homogeneous soil specimen with accurate temperature control remains challenging. Scaling issues also arise due to the lack of comparable scale series data. This limits the current applicability.

2.6.6. Data

Modelling of Arctic erosion is dependent on permafrost and sea-ice distribution. These are often simplified in coastal erosion models. However, the modelling of permafrost and ground temperature distribution has seen recent progress through Nicolsky et al. (2017). Regarding sea ice, studies typically implement a threshold value for sea ice coverage of 15-30% above which waves are assumed to be completely attenuated (Overeem et al., 2011; Islam and Lubbad, 2022; Rolph et al., 2022; Engelstad et al., 2023).

The numerical modelling of Arctic erosion is constrained by a lack of consistent high-spatiotemporal-resolution shoreline change data and local coastal characteristics data. Measurements of environmental drivers such as waves are also limited (Irrgang et al., 2022). However, sensitivity analyses of permafrost bluff models show that erosion is driven by the length of the open-water season, time-varying water levels, wave conditions, and air and sea temperature (Barnhart et al., 2014a; Casas-Prat et al., 2018). This highlights the need for data on these variables. Earth System Models (ESMs) present a

solution through the hindcasting and forecasting of these forcing variables (Irrgang et al., 2022).

2.7. Research Gap

This literature review highlights the need for predicting coastal erosion, and the processes which might be important for doing so. The effects of climate change will likely further enhance erosion rates, and being able to quantitatively predict coastal erosion is required to facilitate policy-making and strategic coastal management (Irrgang et al., 2022).

Morphodynamic models have been developed in previous studies for specific (eroding) coastlines, either by calibrating to a single coastline (Islam and Lubbad, 2022) or by not including all erosion mechanisms (Hoque and Pollard, 2009; Barnhart et al., 2014b). Comprehensive morphodynamic models can be run on storm time scales only as they are too computationally expensive to perform long-term analysis (Bull et al., 2020). There is a lack of long-term predictive capability of morphodynamics for Arctic coastlines, which results in a knowledge gap regarding the coastal processes inducing permafrost erosion and how these will change under the effects of climate change.

Especially coasts subject to thermal denudation are under-studied (Section 2.6). The few process-based models that do exist are difficult to run on longer time scales (i.e., several years) due to the high computational costs. This study expands on the work done by Ravens et al. (2017) to model thermal denudation by decoupling the thermal module from 'Arctic XBeach' and implementing a wrapper that determines when to activate XBeach. This allows the thermal module to run continuously without needing XBeach to be continuously active.

3

Methodology

This chapter describes the methods used in the current study. Firstly, we outline the goal of the study and relate it to the main approach adopted for this study. Subsequently, the methods are explained on a high level.

3.1. Main Approach

This study aims to advance our understanding of the long-term morphological development of Arctic coastlines by integrating thermal and coastal processes through the development of a process-based numerical model. We developed the model to simulate thermal denudation (Section 2.3). We adopted a process-based modelling approach to research the effect of varying environmental drivers on the process of thermal denudation. Climate change will lead to a change in environmental drivers (Section 2.4) and the effects of climate change on thermal denudation are not yet understood.

To simulate the process of thermal denudation, a process-based model should be able to simulate at least the following physics (Figure 1.2):

- thawing of the bluff face,
- slumping and deposition on the beach face,
- and offshore transport (during storm conditions).

Ravens et al. (2017) used XBeach to simulate the latter two processes. They included a thermal module in XBeach to simulate the thawing of a bluff face (also referred to as 'Arctic XBeach'). This study aimed to decouple the thermal module from XBeach to improve computational efficiency, which enables the modelling of the morphodynamics of a permafrost coastline for longer periods (i.e., several years). To this end, we implemented a Python wrapper to determine when XBeach should be activated (Section 4.1).

The thermal module simulates the thawing of the bluff face by modelling enthalpy of the soil (Section 4.3). This is done by computing surface heat fluxes which serve as a Neumann-type boundary condition and performing a numerical update with a discretized subsurface soil domain. Heat exchange at the ground surface is a continuous process. We therefore model it continuously using the thermal module.

Slumping and offshore transport are event-driven and therefore do not need to be modelled continuously. Hence, XBeach is not continuously active. Instead, a Python wrapper (Section 4.1) determines when XBeach is active based on different criteria (Section 4.1.1). XBeach specifications are discussed in Section 4.2.

The modelling of morphodynamics on longer time scales brings additional complications that are less relevant to shorter (i.e., storm) timescales. As a result, the developed model (also referred to as the 'integrated thermo-morphological model') varies significantly from the model developed by Ravens et al. (2017). Appendix A summarizes the added features compared to the Arctic XBeach (Ravens et al., 2017). The exact model formulation is described in Chapter 4.

3.2. Methods

Firstly, we developed a decoupled version of Arctic XBeach (Ravens et al., 2017) (Chapter 4). We collected data to use as boundary and initial conditions (Section 5.2). We obtained data on boundary conditions from global climate models and hydrodynamic models. The latter was down-scaled from global climate models by Engelstad et al. (2023) and Nederhoff et al. (2022). The thermal module of the developed model requires an initial ground temperature, which we obtained from global climate models (and improved through multi-linear regression, Section 5.2.1). The XBeach module requires an initial bathymetry, which we obtained from existing bed measurements.

We then calibrated and validated the decoupled thermal module using measured ground temperature data (Section 5.3.1 and 5.3.2). We assessed the ability of the thermal module to accurately predict the ground temperature distribution over time using the Root Mean Squared Error (RMSE).

Next, we calibrated and validated the integrated thermo-morphological model using measured coastal retreat data (Section 5.3.3 and 5.3.4). Again, the RMSE was used to assess the model skill. Additionally, we used the Mean Absolute Error (MAE), the coefficient of determination (R^2), bias, and Pearson correlation coefficient (r) to assess the quality of the model prediction against the measured values. Definitions of the RMSE, MAE, R^2 , bias, and r are given below.

- $\text{RMSE}(y, \hat{y}) = \sqrt{\frac{\sum_{i=0}^{N-1} (y_i - \hat{y}_i)^2}{N}}$, where y and \hat{y} are the measured and modelled data points respectively, and N represents the total amount of data points.
- $\text{MAE}(y, \hat{y}) = \frac{\sum_{i=0}^{N-1} |y_i - \hat{y}_i|}{N}$
- $R^2 = 1 - \frac{\sum_{i=0}^{N-1} (y_i - \hat{y}_i)^2}{\sum_{i=0}^{N-1} (y_i - \bar{y})^2}$, where \bar{y} is the mean of the observed data defined as $\bar{y} = \frac{\sum y}{N}$.
- bias = $\bar{y} - \hat{y}$, where the overbars denotes averaging.
- $r = \sqrt{\frac{\sum_{i=0}^{N-1} (y_i - \bar{y})(\hat{y}_i - \bar{y})^2}{\sum_{i=0}^{N-1} (y_i - \bar{y})^2}}$

Using the validated model, we performed a sensitivity study (Section 5.4). We considered the sensitivity of upper bluff erosion to changes in coastal geometry, sediment characteristics, and environmental drivers. We also tested the sensitivity of the model to newly introduced parameters. Finally, we assessed the relevance of the thermal module in simulating bluff erosion. Model prediction results may be used as indicators of the relative importance of different effects of climate change.

Figure 3.1 provides an overview fo the workflow used in this study.

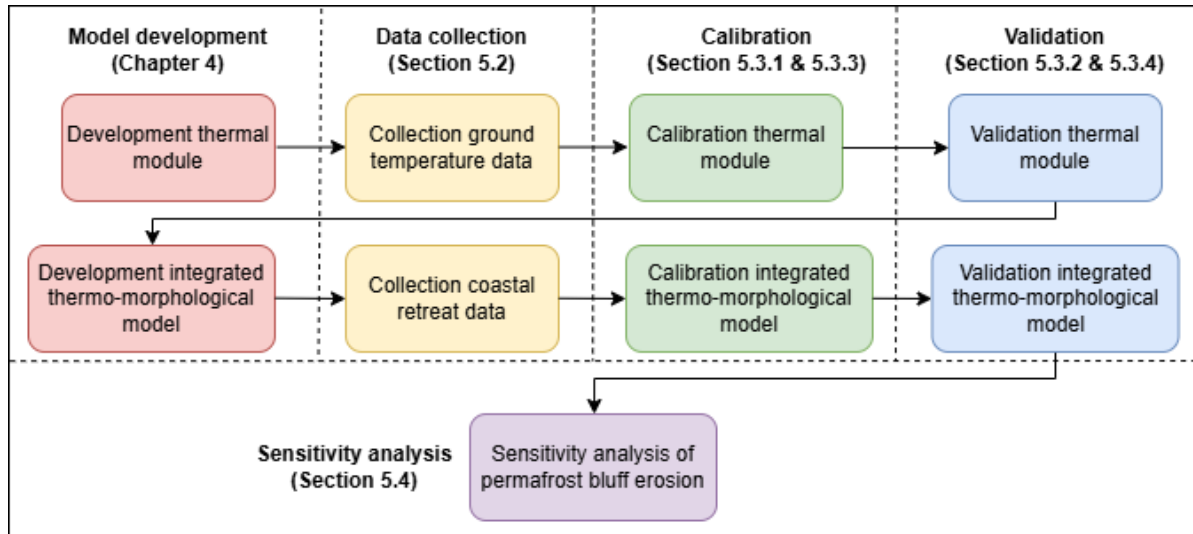


Figure 3.1: Flowchart of the workflow adopted for this study.

4

Model formulation

This chapter describes the formulation of the thermo-morphological model. The model consists of a Python wrapper (Section 4.1) that alternates an XBeach module (Section 4.2) with a thermal module (Section 4.3). The thermal module runs continuously, whereas the wrapper activates XBeach only during periods with expected morphodynamic activity (Section 4.1.1). Figure 4.1 provides a conceptualization of this process. For a complete conceptualization of a simulation in the form of a flowchart, see Appendix B. The model is publicly available (Appendix C).

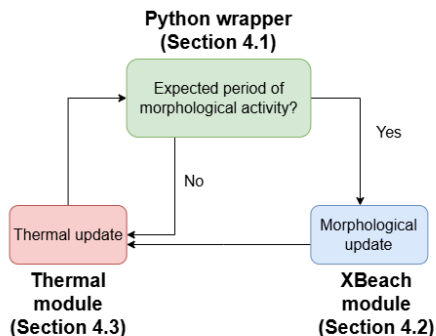


Figure 4.1: Flowchart depicting how the Python wrapper alternates the thermal and XBeach modules.

4.1. Python Wrapper

Python is a high-level, object-oriented programming language, which comes with the drawback of being slow relative to low-level programming languages (Srinath, 2017). This makes Python less suitable for computationally demanding tasks. Additionally, porting existing code to Python is a cumbersome task.

We used a Python wrapper to circumvent this. It extends the functionality of existing code, without necessarily modifying it. It calls some specialized code when required, without executing computationally expensive tasks from Python directly. For example, a Python wrapper can call high-performance routines written in a faster language like Fortran (Peterson, 2001).

The current research used a Python Wrapper to alternate between a thermal module and an XBeach module. The thermal module was written in Python and is less computationally expensive. We developed it specifically for this research. The XBeach module consists of some wrapper functions written in Python and a pre-compiled XBeach executable written in Fortran. XBeach requires more computational resources and (moreover) has already been developed. Therefore, we used a Python wrapper to avoid having to redevelop existing XBeach code in Python and also facilitate higher computational efficiency through the use of a pre-compiled Fortran executable.

4.1.1. Integration of XBeach and Thermal Module

To avoid running XBeach every time step, we decoupled the thermal module from XBeach. The thermal module is less computationally expensive, so it can run every time step of a simulation. The Python wrapper determines for which time steps XBeach should be activated. It uses three criteria to make this decision.

1. *Storms:*

The storm timing is readily available at the start of the simulation. During storms, a period of high morphological activity is expected which means that XBeach should be activated. Beachface hydro- and morphodynamics are mainly driven by run-up (Elfrink and Baldock, 2002; Senechal et al., 2011). This makes the 2% run-up ($R_{2\%}$), which is defined as the run-up height that is exceeded by two per cent of run-up values, a suitable parameter to use as an indicator for periods of high morphological activity. We used the formulation by Stockdon et al. (2006) to predict $R_{2\%}$ based on existing morphology and offshore wave statistics. The formulation is given in Equation 4.1.

$$R_{2\%} = 1.1 \left(0.35\beta_f (H_0 L_0)^{0.5} + \frac{[H_0 L_0 (0.563\beta_f^2 + 0.004)]^{0.5}}{2} \right) \quad (4.1)$$

where,

- β_f = average slope of the bed level over a region of $\pm 2\sigma$ around the mean water level [-], with σ the standard deviation of the continuous water level record, which can be predicted from the offshore significant wave height,
- H_0 = offshore significant wave height [m],
- L_0 = offshore wave length [m].

Different values may be used as the threshold value for the $R_{2\%}$. A lower value resulted in the identification of more periods of high morphological activity, and thus more XBeach activations, i.e., longer simulation times. Choosing a threshold value that leads to enough XBeach activations while maintaining low computational costs is an optimization problem (Section 5.2.3).

2. *Sea ice:*

XBeach was only activated during storms whenever the fraction of sea ice coverage is lower than some threshold. Above this threshold, we assumed that wave action is fully attenuated. In practice, since global climate models are used for forcing, a sea ice coverage of 30% of an offshore 2D horizontal grid cell is often used as the threshold value (above which global climate models do not provide hydrodynamic data). This also limits data availability to periods during which sea ice coverage is 30% or less (Section 5.2). For the current application, hydrodynamic forcing is set to zero above a 30% sea ice coverage, leading to zero run-up, which blocks XBeach from activating.

Measured and modelled timeseries of offshore hydrodynamic boundary conditions often already include sea ice. Wave parameters are set to zero when the sea ice threshold is exceeded. Together with the first described criteria, this results in the XBeach module not being activated when sea ice coverage is high. However, explicitly including a threshold value allows for sensitivity testing with this threshold as long as the threshold is set to some value below the threshold used in the boundary conditions. For this reason, we included the sea ice threshold in the model.

3. *Inter-storm activation:*

We ensured that XBeach was activated regardless of storm timing and sea ice at some fixed inter-storm interval. This interval was set to one week (or 168 time steps of one hour). We used the XBeach module to simulate sediment transport processes including avalanching (Section 4.2.3). Therefore, we used the inter-storm interval to ensure that XBeach is activated also during prolonged periods without storms. That way, thawed material from the bluff face slumps to the beach and does not remain on the bluff face where it might insulate the frozen material below.

By only running the XBeach module when the above-described criteria are met, the ratio of XBeach to thermal time steps reduces from 1:1 to about 1:100 - 1:20, depending on the threshold chosen for the

$R_{2\%}$. At the start of the simulation, a start time, end time, time step and sub-grid time (Section 4.3.3) step were provided to the model. The wrapper generated a range of time steps from the given start and end times. The model then looped through the time steps while determining whether or not XBeach should be active for each time step. Figure 4.2 provides a flow chart visualizing how the model decides whether or not to run XBeach.

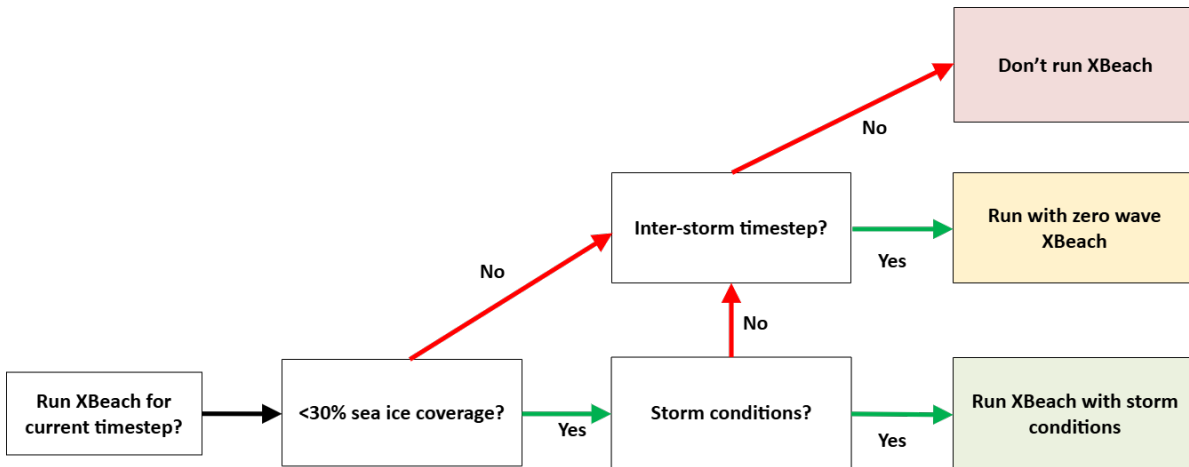


Figure 4.2: Flowchart depicting how the model decides when to activate the XBeach module based on the three criteria (Section 4.1.1).

Erosion of permafrost-affected soil is only possible when the active layer is thawed (Section 2.2). Whenever the XBeach module was activated, the wrapper updated the thaw depth and passed it to XBeach to function as the erodible layer. An XBeach executable was then activated, which outputted a morphological update and water level. The morphological update and water level were then passed back to the thermal module. The thermal module used the water level to determine the convective heat transport of water (potentially during storm setup).

4.2. XBeach Module

This section provides a short description of the XBeach model to argue its applicability to the modelling of Arctic erosion. Further details can be found in the XBeach manual, or in Roelvink et al. (2009).

4.2.1. Introduction

XBeach is a numerical model used to compute and simulate nearshore hydrodynamics and morphodynamic response to storm events (Roelvink et al., 2009). Similar to other modelling software, it requires input data (consisting of initial conditions, physical/numerical parameters, and forcing data) to generate output. The required initial conditions consist of an initial bathymetry, i.e., a series of grid points with associated elevation representing a cross-shore transect. The physical parameters range from sediment parameters (e.g., D_{50} , angle of repose) to the density of water and other physical constants. Numerical parameters include for example a bin width for directional spreading, a computational time step, and a morfac (morphological acceleration factor). Finally, forcing data refers to hydrodynamic forcing such as wave heights, wave periods, and storm surge (through water level), but also include non-hydrodynamic forcing such as wind speeds and direction. This forcing data can be defined as a timeseries, which lets XBeach dynamically vary values throughout the simulation.

Though XBeach facilitates the usage of a 2D horizontal domain, the current thermo-morphological model employed (1D horizontal) transects as a first step towards understanding long-term Arctic erosion. XBeach numerically solves horizontal equations for wave propagation, flow, sediment transport and bottom changes, and varying (spectral) wave and flow boundary conditions (Roelvink et al., 2009).

XBeach uses a staggered grid with bed levels, water levels, water depths, and concentrations being defined at the center of each cell (i.e., grid point), and velocities and sediment transports being defined at cell borders (Roelvink et al., 2009).

4.2.2. Hydrodynamics and Waves

Barter Island is subject to relatively low wave heights and storm surges (Section 5.1). Due to the high bluffs (i.e., higher than ten meters), most regimes can be categorized as 'swash' (during normal conditions) or 'collision' (during storm conditions) following the 'Impact Levels' defined by Sallenger (2000).

XBeach employs the wave action balance (including a roller energy balance) to solve for the radiation stresses over the computational domain, from which the wave force can be determined. Low-frequency oscillations and mean flows are solved using the shallow-water equations.

The hydrodynamic boundary conditions (and other boundary conditions used in XBeach) are explained in Appendix D.

4.2.3. Sediment Transport and Morphology

In general, XBeach employs the depth-averaged advection-diffusion equation by Galappatti and Vreugdenhil (1985). This formulation uses an equilibrium sediment concentration in combination with an adaptation time that depends on local water depth and sediment properties. The equilibrium sediment concentration is computed using either the Soulsby-Van Rijn equations (Van Rijn, 1984; Soulsby, 1997), or the Van Thiel-Van Rijn equations (Van Rijn, 2007; Van Thiel de Vries, 2009). The latter of these formulations is the default and separates critical velocity for currents and waves, and foregoes the computation of the drag coefficient.

Morphological updates are based on sediment transport gradients throughout the computational domain and a morphological acceleration factor (*morfac*). The avalanching module checks the bed slope between adjacent grid cells. If this slope exceeds a critical slope, sediment is exchanged between the grid cells until the slope is below critical. The critical slope is defined separately for dry and wet sediment (Roelvink et al., 2009). The physical processes of slumping followed by offshore transport are the important drivers of thermal denudation at the study site, and XBeach's ability to simulate both avalanching and surfbeat makes it suitable for capturing these processes.

Decoupling Arctic XBeach induces a problem with sediment transport. XBeach is only activated during storm events, leading to sediment transport only occurring during storms (i.e., erosive conditions). Long-term sediment transport processes, which tend to rebuild beaches in between storms, are neglected. The result is severe beach erosion during storms but no accretion during calmer conditions (for XBeach's default parameter settings). To reduce beach erosion, onshore transport through wave asymmetry can be increased artificially in XBeach. Therefore, we selected the governing parameter (*fac_{ua}*) as one of the calibration parameters. We discuss alternative solutions to the problem of neglecting long-term sediment transport processes in Appendix E.

4.3. Thermal Module

This section describes the thermal module implemented as part of the thermo-morphological model.

4.3.1. Enthalpy

The purpose of the thermal module was to provide a thaw depth to the XBeach module (Section 4.1). Since both temperature and phase distribution were important, a standard heat conduction model was not suitable. Instead, we used the heat balance equations in terms of enthalpy (Hu and Argyropoulos, 1996; Kasper et al., 2023; Ravens et al., 2023), where we defined enthalpy as the sum of thermal energy and flow work per unit mass (Incropera et al., 2013). A conceptualization of temperature versus enthalpy is given in Figure 4.3. The heat balance in terms of enthalpy is:

$$\rho \frac{\partial h}{\partial t} = \frac{\partial}{\partial z} \left(k \frac{\partial T}{\partial z} \right) \quad (4.2)$$

where,

ρ = density of soil [kg/m³]

h = enthalpy [J/kg],

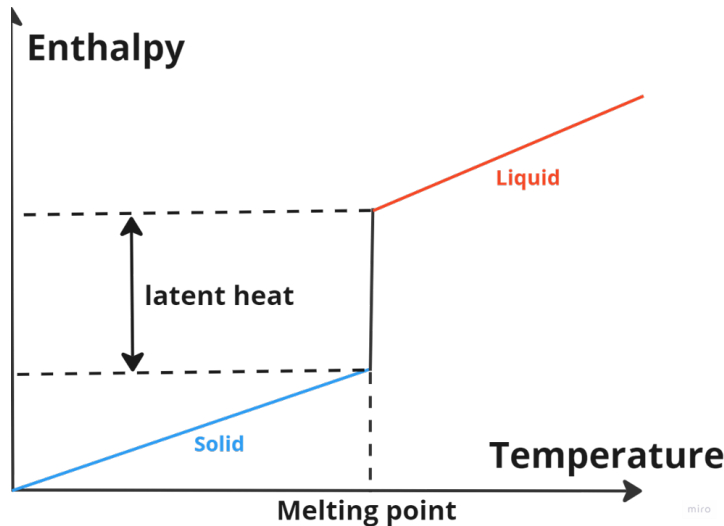


Figure 4.3: Conceptualization of temperature and enthalpy. Temperature increases linearly with enthalpy until the melting temperature is reached. This approach assumes a constant temperature at the melting point (i.e., isothermal phase change). Once the threshold of latent heat has been overcome, temperature can increase further.

- t = time [s],
- k = thermal conductivity of soil [W/m/K],
- T = temperature [K],
- z = Cartesian coordinate direction [m].

Equation 4.3 gives the discretization of this equation through the finite differences method. This method (Forward Time Central Space or FTCS) is second-order-accurate in space and first-order-accurate in time. We employed a sub-grid time step to adhere to the CFL (Courant-Friedrich-Lowy) condition (Section 4.3.3). When alternating the XBeach and thermal modules, the thermal module was executed for each sub-grid time step for each simulated time step.

$$h_m^{n+1} = h_m^n + \frac{k}{\rho \Delta z^2} \left(T_{m-1}^n - 2T_m^n + T_{m+1}^n \right) \quad (4.3)$$

where,

- m = m^{th} cell in z direction [-],
- n = n^{th} (sub-grid) time step [-].

Once the model computed the new enthalpy, it was able to determine the associated new temperature distribution. Assuming isothermal phase change (i.e., constant temperature during phase transition), the enthalpy as a function of temperature is given in Equation 4.4.

$$h = \begin{cases} C_s T, & T < T_m \\ C_l T + (C_s - C_l)T_m + L n_b, & T > T_m \end{cases} \quad (4.4)$$

where,

- h = enthalpy [J/kg],
- C_s, C_l = specific heat capacity for frozen and unfrozen soil [J/K/kg], given by c_s/ρ and c_l/ρ respectively, where c_s and c_l are the volumetric heat capacity for frozen and unfrozen soil [J/K/m³],
- T = temperature [K],
- T_m = melting temperature [K],

$$\begin{aligned} L &= \text{latent heat of fusion for water-ice [J/kg]}, \\ n_b &= \text{soil water content [-] (or [m}^3/\text{m}^3\text{])}. \end{aligned}$$

The conversion from enthalpy to temperature is phase-dependent. We therefore rewrote Equation 4.4 to Equation 4.5.

$$T = \begin{cases} \frac{h}{C_s}, & \frac{h}{C_s} < T_m \\ T_m, & \frac{h}{C_s} \geq T_m \text{ and } \frac{h-(C_s-C_l)T_m-Ln_b}{C_l} < T_m \\ \frac{h-(C_s-C_l)T_m-Ln_b}{C_l}, & \frac{h-(C_s-C_l)T_m-Ln_b}{C_l} \geq T_m \end{cases} \quad (4.5)$$

We then used the new temperature distribution to determine the new phase distribution (and hence, thaw depth).

4.3.2. Grid

The model required an initial bathymetry to be provided (Section 5.2). Using the XBeach Python toolbox (de Ridder, 2023), we generated a spatially-varying x -grid. We then interpolated the initial bathymetry to the x -grid. To determine the thaw depth, we modelled the ground temperature distribution. This was done by implementing a series of 1D models (one for each grid point) perpendicular to the bathymetry. Each 1D model consists of a series of grid points extending until some maximum distance from the current surface (e.g., Figure 4.4).

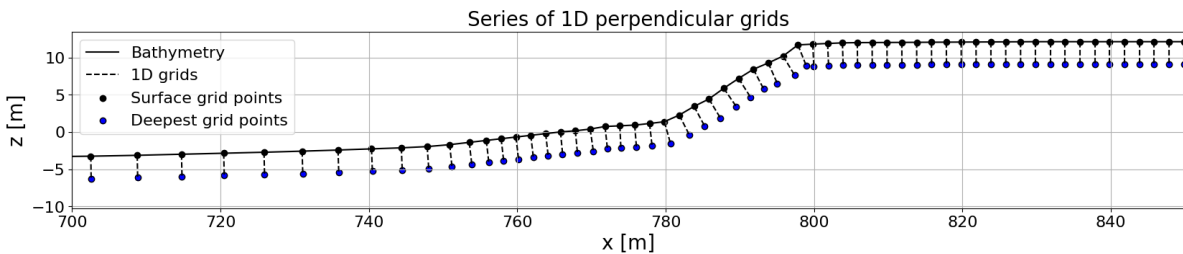


Figure 4.4: Example of a bathymetric grid, with a series of 1D perpendicular models. This example uses a length of 3 meters for each 1D model, though we use a length of 15 meters in the current studies.

After a morphological update is performed by XBeach, some of the 1D models included grid points located above the ground surface. Additionally, some 1D models were no longer oriented perpendicular to the surface after a morphological update. We dealt with this by generating a new perpendicular grid after each XBeach activation, for which the first node was always placed at the ground surface.

The ground enthalpy distribution needed to be determined for this new grid. We did this by selecting the nearest surface node from the old grid, and subsequently using the associated perpendicular model. We computed values for enthalpy through interpolation based on only z -coordinates.

When a new grid point was located above the old bed level, we assumed that sedimentation had occurred and that the deposited material had the same temperature as the seawater. In that case, we computed the enthalpy from the seawater temperature. When a new grid point was located below the lowest old grid point (e.g., due to erosion), the enthalpy of the new grid point was set to that of the nearest old grid point, i.e., the deepest old grid point.

Generating a new x -grid after each morphological update ensured that a high model resolution was maintained where necessary due to shorter wavelengths, i.e., in the surf zone.

4.3.3. Sub-grid Time step

The enthalpy formulation required the discretization of a second-order derivative. This was done through the use of the (explicit) second-order finite differences method, which requires a CFL coeffi-

cient of lower than 0.5 (Burkhardt, 2012). We achieved this by running the thermal module on a sub-grid time step. The CFL is given by Equation 4.6.

$$\text{CFL} = \frac{k}{\rho} \frac{\Delta t}{\Delta z^2} \quad (4.6)$$

where,

- k = thermal conductivity of soil [W/m/K],
- ρ = density of soil [kg/m³],
- Δt = time step [s],
- Δz = grid spacing [m].

The model used a default time step of one hour, and a default sub-grid time step of two seconds. In practice, this resulted in a thermal update being performed 1800 times for each model time step.

For example, using a thermal conductivity of 2 W/m/K, a density of 1500 kg/m³, a sub-grid time step of 2 s, and a grid spacing of 0.1 m, a CFL of $\frac{2}{1500} \frac{2}{0.1^2} \approx 0.27$ is found, which is not far below the CFL-threshold. This demonstrates the requirement for a sub-grid time step.

4.3.4. Thaw Depth

The phase distribution of the ground not only governs the thickness of the erodible layer given to XBeach. The phase of a material also governs its thermal properties. Specifically, the thermal conductivity k and the heat capacity C are phase-dependent. Therefore, the thermal module computed the phase distribution to obtain a spatial distribution of thermal properties regardless of whether or not XBeach was activated. The phase distribution was computed through Equation 4.5.

From this phase distribution, the thickness of the erodible layer was computed. This was done by the Python wrapper, though we explain it here for clarity. XBeach defines the erodible layer as vertical from each grid cell. However, the thermal module used a series of 1D models perpendicular to the ground surface. Hence, the thaw depth needed to be converted from the perpendicular grid to a vertical grid.

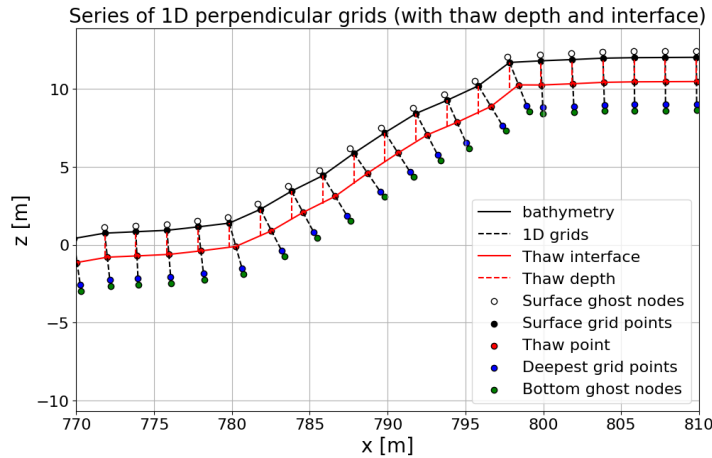


Figure 4.5: Example of how we obtained the thaw depth from the thaw interface. For each 1D grid, we identified a perpendicular thaw depth. Each of these points is then connected with straight lines. For each surface grid point, we compute the thaw depth as the vertical distance to the piecewise linear function representing the thaw interface.

We did this by finding the first grid point (starting from the surface) in each 1D model with a temperature lower than the melting temperature T_m . Connecting these points resulted in a piecewise linear function below the ground surface. This represented the thaw interface. The vertical distance between each grid point and this thaw interface was used as a representative thaw depth (Figure 4.5).

Though the erodible layer can be obtained this way, the question arises whether or not this formulation is valid for the refreezing of the upper soil layer. When the upper soil layer refreezes, the potentially

thawed layer below that may still erodible be erodible to some extend. For example, if a fully thawed soil is covered by a thin sheet of ice, it may still be erodible.

To account for erodibility during refreezing, we introduced a 'thaw threshold'. This threshold represents a thickness starting from the surface that needed to be frozen before being treated as non-erodible. The soil was still treated as erodible if the thickness of the frozen layer did not exceed the thaw threshold.

4.3.5. Boundary Conditions

Each 1D thermal model required a boundary condition at both the ground surface and the maximum modelled depth. Figure 4.6 represents a conceptualized ground temperature distribution for permafrost soil. At depth, the temperature gradient was assumed to be equal to the geothermal gradient, which typically equals $25 \text{ K/km} = 0.025 \text{ K/m}$ (Lowell and Rona, 2005).

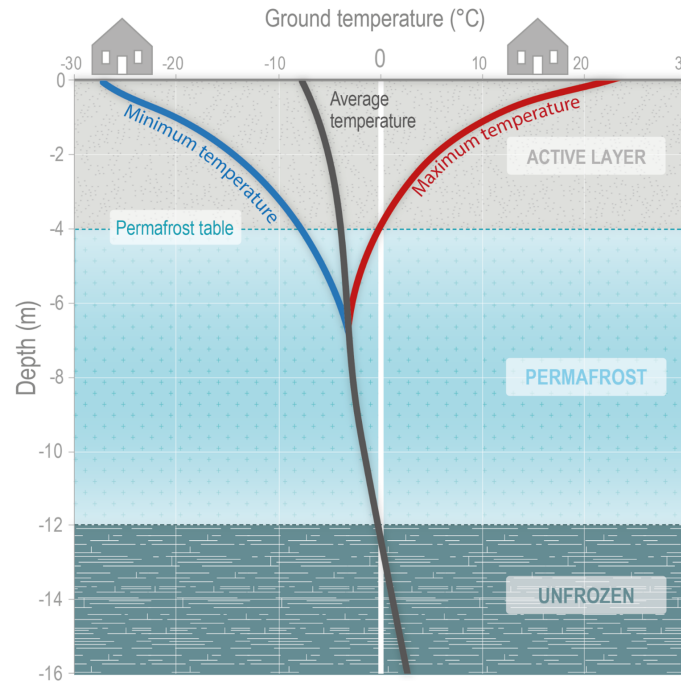


Figure 4.6: Example of the yearly oscillation of the ground temperature distribution for a permafrost-affected soil (Tom Ravens, personal communication, 02-05-2024). Both temperatures and active layer depth are exaggerated. The thaw depth at Barter Island typically does not exceed 1 meter (Figure 5.20).

Ghost Nodes

At the ground surface, we imposed a flux-type boundary condition (Ravens et al., 2017). The heat flux at the surface is the sum of convective heat transfer in/out of the soil, diffusive heat transfer from deeper in the ground, incoming/outgoing radiation, and incoming/outgoing latent heat.

We used a ghost node approach to implement the flux-type boundary condition (Coco et al., 2014; Tom Ravens, personal communication, 02-05-2024). We introduced a superficial 'ghost' node (exterior to the modelling domain and bordering the surface node), which we also included in the finite differences scheme. We determined the temperature of the ghost node at the start of each time step through Equation 4.7.

$$T_{\text{ghost, top}}^n = T_0^n + q_{\text{convective}}^n + q_{\text{radiation}}^n + q_{\text{latent}}^n \quad (4.7)$$

where,

T_0^n = temperature of the surface nodes [K],

- $q_{\text{convective}}^n$ = convective heat flux at the soil surface [W/m²],
 $q_{\text{radiation}}^n$ = radiation heat flux at the soil surface [W/m²],
 q_{latent}^n = latent heat flux at the soil surface [W/m²].

We used the temperature of the surface node from the previous time step (T_0^n) to compute the temperature of the ghost node. Furthermore, convective heat is a function of some convective heat transport coefficient, which depends on whether or not the soil surface is submerged, and the temperature difference between the soil surface and the exterior medium.

We calculated the heat flux from radiation as the sum of shortwave and longwave radiation. These are both readily available from the forcing data, as is the latent heat flux.

Subsequently, we used the temperature of the ghost node as a fixed boundary condition for the current sub-grid time step. In practical terms, the ghost node approach takes a Neumann-type (i.e., flux-type) boundary conditions and converts it to a Dirichlet-type boundary condition.

At the bottom boundary of the grid, we defined the boundary condition as the geothermal gradient. To include this Neumann boundary condition, we added another ghost node at the bottom of the grid. The temperature of this ghost node is defined as $T_{\text{ghost, bottom}}^n = T_M^n + \Delta z \frac{\partial T}{\partial z}$, where M indicates the bottom grid point, Δz is the grid spacing, and $\frac{\partial T}{\partial z}$ is the geothermal gradient.

Convective Heat

The convective heat transfer is a function of some convective heat transport coefficient, denoted by coefficient h_c , and the temperature difference between the soil and the exterior medium at the interface. The method for determining h_c depends on the external medium, which is either water or air. For air, the approach is much simpler and is given by Equation 4.8 (Man, 2023).

$$h_{c,\text{air}} = \frac{0.0296 \left(v_w \frac{L_e}{\nu_{\text{air}}} \right)^{4/5} Pr^{1/3} k_{\text{air}}}{L_e} \quad (4.8)$$

where,

- $h_{c,\text{air}}$ = convective heat transfer coefficient for a soil-air interface [W/m²/K],
 v_w = wind speed at 10 m height [m/s],
 L_e = convective length scale [m], 0.003 m is used,
 ν_{air} = air kinematic viscosity [m²/s], 1.33×10^{-5} is used,
 Pr = Prandtl number [-], 0.71 is used,
 k_{air} = thermal conductivity of air [W/m/K], 0.024 W/m/K is used.

Determining convective heat transfer through a soil-water interface subject to waves is less straightforward. We used the formulation by Kobayashi et al. (1999) (Equation 4.9). These formulations were developed for breaking waves inducing thermal abrasion of a cliff.

$$h_{c,\text{water}} = \frac{\alpha f_w c_w u_b}{1 + E \sqrt{0.5 f_w}} \quad (4.9)$$

where,

- $h_{c,\text{water}}$ = convective heat transfer coefficient for a soil-water interface [W/m²/K],
 α = empirical parameter [-], 0.5 is used for uni-directional flow,
 f_w = wave friction factor at the melting surface,
 c_w = volumetric heat capacity of seawater [J/K/m³], 3989 is used (Fischer, 1979),
 u_b = representative fluid velocity immediately outside the boundary layer [m/s],
 E = parameter depending on whether the turbulent boundary layer flow is hydraulically smooth or fully rough.

The representative fluid velocity is uncertain and affects the value of α . The maximum particle velocity at the bed is commonly used for wave boundary layer analysis outside the surf zone (Jonsson, 1966), and can also be applied in the surf zone (Cox et al., 1996). This velocity can be computed through Equation 4.10.

$$u_b = \frac{\pi H_r}{T_r \sinh k_r d_r} \quad (4.10)$$

where,

- H_r = representative wave height [m],
- T_r = representative wave period [s],
- k_r = representative wave number [rad/m].
- d_r = representative depth [m].

The wave friction factor f_w depends on the Reynolds number close to the bed, the amplitude of the particle displacement, and the wave number. Jonsson (1966) presents a diagram to determine f_w , which typically ranges from 0.01 to 1. Since using the diagram to determine values for f_w for every horizontal grid point and every (sub-grid) time step is unfeasible, we chose a representative value of 0.05, which we based on the Reynolds number, the maximum surface elevation, and the wave number.

Finally, the turbulent boundary layer flow parameter E is described by Kobayashi and Aktan (1986), and given in Equation 4.11.

$$E = \begin{cases} 5(Pr - 1 + \ln 1 + \frac{5}{6}(Pr - 1)), & \frac{u_* k_s}{\nu_{\text{water}}} < 5 \\ 0.52 \left(\frac{u_* k_s}{\nu_{\text{water}}}\right)^{0.45} Pr^{0.8}, & \frac{u_* k_s}{\nu_{\text{water}}} > 70 \end{cases} \quad (4.11)$$

where,

- u_* = shear velocity associated with the shear stress at the melting surface [m/s] = $u_b \sqrt{0.5 f_w}$,
- k_s = equivalent sand roughness of the melting surface [m] $\approx 2.5 \times D_{50}$ (Nielsen, 1992),
- ν_{water} = water kinematic viscosity [m^2/s], 1.848×10^{-6} is used (ITCC, 2011).

With the low data availability in the Arctic and the high computational cost of the above-described computations, we made a pragmatic assumption for the convective heat transfer coefficient at the soil-water interface, and chose a value of 500 W/m²/K.

When the convective heat transfer coefficient was obtained (either for an interface of soil and air or soil and water), we computed the convective heat flux through Equation 4.12.

$$q_{\text{convective}} = h_{c,\text{air/water}} (T_{\text{soil}} - T_{\text{air/water}}) \quad (4.12)$$

Solar Flux Calculator

The radiation flux is the sum of the net influx of shortwave and longwave radiation (Equation 4.13).

$$q_{\text{radiation}} = q_{\text{radiation, shortwave}} + q_{\text{radiation, longwave}} \quad (4.13)$$

The shortwave radiation flux on a surface depends on the angle that the incoming radiation makes with that surface. Shortwave radiation heat flux data are available for flat surfaces. However, data are not available for an inclined surface (such as a permafrost bluff). To account for bluff inclination, we used a 'solar flux calculator' to scale radiation from a flat surface to an inclined surface (Kasper et al., 2023; Ravens et al., 2023). For an inclined surface, the amount of incoming radiation was determined using Equation 4.14 (Buffo et al., 1972; Duffie and Beckman, 2013).

$$I = I_0 p^{1/\sin A} \sin \theta \quad (4.14)$$

where,

- I = solar intensity [W/m^2] (equals $q_{\text{radiation, shortwave}}$ in Equation 4.13),
 I_0 = solar constant [W/m^2] (radiation at the top of the atmosphere normal to the sun),
 p = atmospheric transmission coefficient (depending on altitude, weather, etc.),
 A = altitude angle [$^\circ$] (angle off of the horizontal with which the sun's rays strike a horizontal surface) = $\arcsin \sin \phi \sin \delta + \cos \phi \cos \delta \cos h$,
 ϕ = latitude [$^\circ$],
 δ = declination angle [$^\circ$] = $23.5 \times \frac{2\pi}{360} \cos \frac{2\pi}{365} (284 + N)$ (Yıldız, 2018),
 N = current day of the year [-],
 h = hour angle [$^\circ$] (varies daily, equaling 0 at 12:00 and π at 00:00, local time),
 θ = angle between surface and radiation [$^\circ$] = $\sin A \cos \alpha - \cos A \sin \alpha \sin Z - \beta$,
 Z = azimuth counter-clockwise from east [$^\circ$] = $AZ + \frac{1}{2}\pi$,
 AZ = azimuth counter-clockwise from south [$^\circ$] = $\arcsin \cos \delta \frac{\sin h}{\cos A}$,

Near the solstices, the sun sometimes crosses the east-west line. This happens when $\cos h < \frac{\tan \delta}{\tan \phi}$. If this condition is satisfied, the equation for AZ is modified through Equation 4.15.

$$AZ = \begin{cases} -\pi + |AZ|, & h < 0 \text{ (before 12:00)} \\ \pi - AZ, & h > 0 \text{ (after 12:00)} \end{cases} \quad (4.15)$$

The shortwave solar radiation data we used to force the model is defined on the Earth's surface for zero inclination. Equations 4.16 and 4.17 respectively represent the intensity of solar radiation on a flat surface, I_{flat} , and intensity of solar radiation on an inclined surface, I_{inclined} .

$$I_{\text{flat}} = I_0 p^{1/\sin A} \sin \theta_{\text{flat}} \quad (4.16)$$

$$I_{\text{inclined}} = I_0 p^{1/\sin A} \sin \theta_{\text{inclined}} \quad (4.17)$$

The atmospheric transmission coefficient is not affected by surface inclination. Hence, we related I_{flat} and I_{inclined} through Equation 4.18.

$$I_{\text{inclined}} = I_{\text{flat}} \frac{\sin \theta_{\text{inclined}}}{\sin \theta_{\text{flat}}} = I_{\text{flat}} r \quad (4.18)$$

where,

$$r = \text{enhancement factor.}$$

We used Equation 4.18 to compute the intensity of shortwave radiation on an inclined surface based on the intensity of shortwave radiation on a flat surface. The enhancement factor r is a function of surface inclination, day of the year, latitude, etc. (Equations 4.14 - 4.17). Figure 4.7 visualizes the enhancement factor r for several surface inclinations throughout the year for an (almost) north-facing bluff at a latitude of 70° . This represents conditions at Barter Island.

We conclude that solar radiation on a north-facing (positively) inclined surface should be reduced for most of the year. Conversely, a negative slope (i.e., a south-facing bluff) leads to a more perpendicular angle between incoming radiation and the surface. This means rays of solar radiation are distributed over a smaller area, which relates to higher solar intensity, and hence an enhancement factor larger than one.

Since longwave radiation is not incident from the sun but from the entire atmosphere, we assumed that surface angle does not influence the net flux of heat related to longwave radiation. We assumed the same for the surface latent heat flux. Finally, we assumed that the surface fluxes due to shortwave radiation, longwave radiation, and latent heat did not affect the submerged domain.

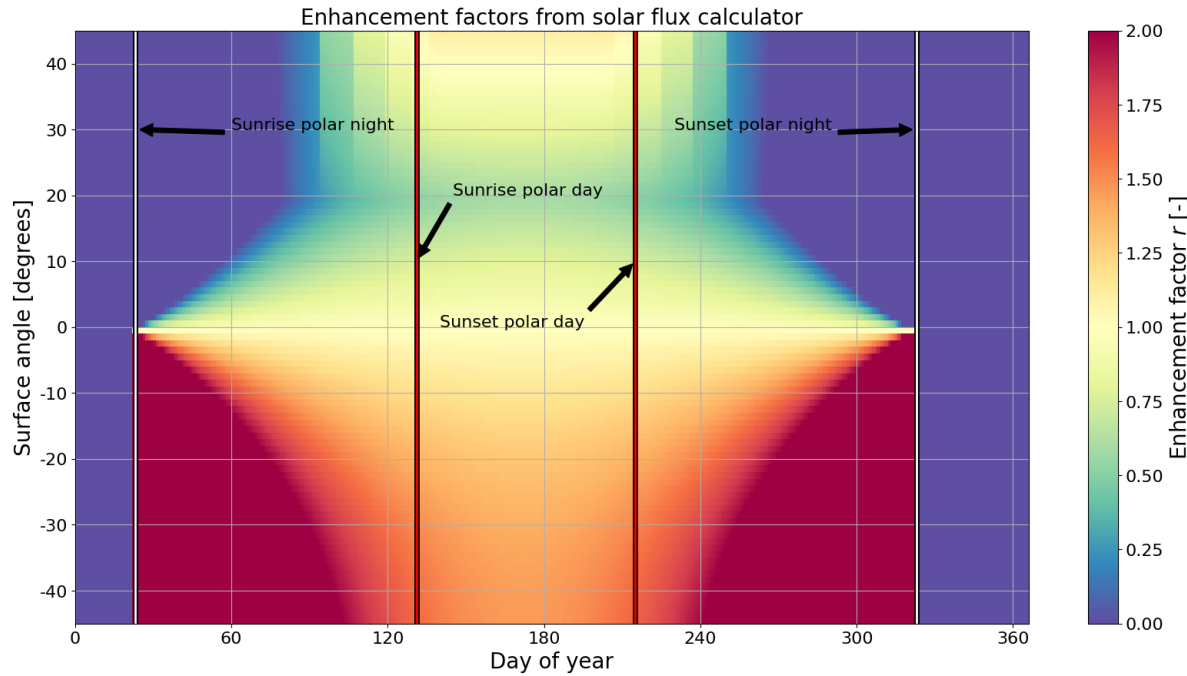


Figure 4.7: Enhancement factor r (Equation 4.18) for a bluff facing 88° (clockwise from east) at a latitude of 70° . This direction and latitude is typical for a bluff at Barter Island (Section 5.1). We computed the enhancement factors for a range of different bluff inclinations, for an entire year.

Finally, we include a calibration coefficient ($\alpha_{\text{surface flux}}$, also referred to as 'surface flux factor'). We implemented this calibration coefficient to implicitly account for a reduction of the surface heat flux due to the presence of a peat layer (Hinzman et al., 1991). Since this only applies to horizontal surfaces and not the bluff itself, this factor is only applied to non-horizontal surfaces (i.e., making an angle of 20° degrees or more with the horizontal, also referred to as the 'surface flux angle').

5

Case Study at Barter Island

We calibrated and validated the thermo-morphological model described in Chapter 4 through a case study of Barter Island (Alaska, United States). This chapter first provides a general site description. Next, it describes the data used for initial conditions, physical parameters, forcing, calibration, and validation. After that, a description of the model calibration and validation effort is given. Finally, we provide a description and the results of the sensitivity analysis we performed with the developed model.

5.1. Site Description

Barter Island is an island off the northern coast of Alaska . It is located in Borough County, North Slope, at a latitude of approximately 70.1° (USGS, 2000) (Figure 5.1 and Figure 5.2). Most inhabitants reside in the Kaktovik village, which has a population of 283 (as of 2020), with 80-90% being of Native American descent (USCB, 2020).

The coast of Barter Island is unlithified, i.e., consists of granular material (Lantuit et al., 2012; Overduin et al., 2014). This limits the generalizability of the developed numerical model to coasts similar to the northern coast of Barter Island, such as the Yukon Territory (Canada) and Western Russia (Overduin et al., 2014), where the coastal setting and relevant erosion mechanisms are similar to Barter Island.

Beach sediment at Barter Island is classified as coarse sand, with a diameter of 1.9 mm (Lantuit et al., 2012; Erikson et al., 2020a). However, Arctic coasts are often characterized by a bi-modal sediment composition (Section 2.1.1). A mean sediment diameter of 0.036 mm (i.e., coarse silt) is found at the bluff crest (Ferdinand Oberle, personal communication).

The presence of (large amounts of) coarse sediment in a permafrost bluff has been used as an indicator of the dominant erosion mechanism, which in that case is thermal denudation (bluff face thaw/slump) (Ravens et al., 2011; Panchang and Kaihatu, 2018; Ravens and Peterson, 2021). This allows the use of the XBeach model, which can not explicitly simulate (thermo-erosional) niches but can simulate (the convex upward) bathymetry relevant for thermal denudation. Though the main erosion mechanism at Barter Island is thermal denudation, some thermal abrasion events do occur, e.g., in 2008 (Ravens and Peterson, 2021).

Barter Island is one of the few Arctic sites where extensive observational data exists. Between 1947 and 2020, the Northern coastline has (on average) retreated a total of 114 meters, which averages to 1.6 m/year (Gibbs et al., 2021). Some years (e.g., 2012-2013) are characterized by erosion rates of up to 6.6 m/year (Gibbs et al., 2021). With significant permafrost impact, as well as seasonal sea ice coverage (Gibbs et al., 2021), Barter Island represents Arctic coastline conditions well. Moreover, the availability of data makes this site an attractive choice for model validation.

We used data from Barter Island for the model's initial conditions, forcing, calibration, and validation.



Figure 5.1: Map of Alaska, United States. Adapted from Nations Online Project (2016).



Figure 5.2: Map of Barter Island, Alaska, United States. Adapted from USGS (1955)

5.2. Data

5.2.1. Initial Conditions

The developed model required two types of initial conditions. Firstly, it needed a bathymetric transect (including orientation). For this transect, the XBeach module was used to simulate hydrodynamics and morphological processes, and the thermal module was used to simulate the ground temperature to obtain the thickness of the erodible layer (Section 4.3.4). Secondly, we required the initial ground temperature distribution, i.e., a temperature for each of the grid points of each 1D thermal model.

Bathymetric Transect

Bathymetric data are available from Erikson et al. (2020b). Erikson et al. (2020b) performed bathymetric surveys in 2010 and 2011, resulting in a series of depth measurements. Additionally, they measured beach elevation profiles along 29 different shore-normal transects, also in 2010 and 2011. Figure 5.3a visualizes a map of the northern coastline of Barter Island, which includes the bluff edge, shoreline, bathymetric survey, and beach profiles measured.

The thermo-morphological model required a 1D transect. In order to obtain it, a number of points that somewhat resemble a transect were selected, which were later connected to one of the beach transects. Four different depth profiles were generated (Figure 5.3a).

For each of these profiles, linear regression was used to draw a straight line through the points in a two-dimensional horizontal plane. The measurement points were then cast onto this line, which resulted in a 1D depth profile (Figure 5.3b). This gave a 1D grid of depth measurements for each of the considered transects (Figure 5.3c). Transects were in reasonable agreement, but show some variability, adding to the uncertainty in finding a representative profile.

Finally, for the profile that extended furthest offshore, we selected the nearest beach elevation profile (BTI-T5b) and attached it to the depth measurements, which resulted in a 1D transect (Figure 5.4). This profile provided a first estimate of what a transect might look like. However, data availability is limited, so this profile could not be assumed to be representative of the entire region.

Therefore, we used a schematized profile to allow easier consideration of different transects with varying geometries instead of the measured profile. This schematized profile consisted of a flat section, followed by a bluff, a beach, a nearshore slope, an offshore slope, and another flat section. An artificial flat was introduced at the offshore boundary to ensure the correct implementation of the equilibrium long wave in XBeach.

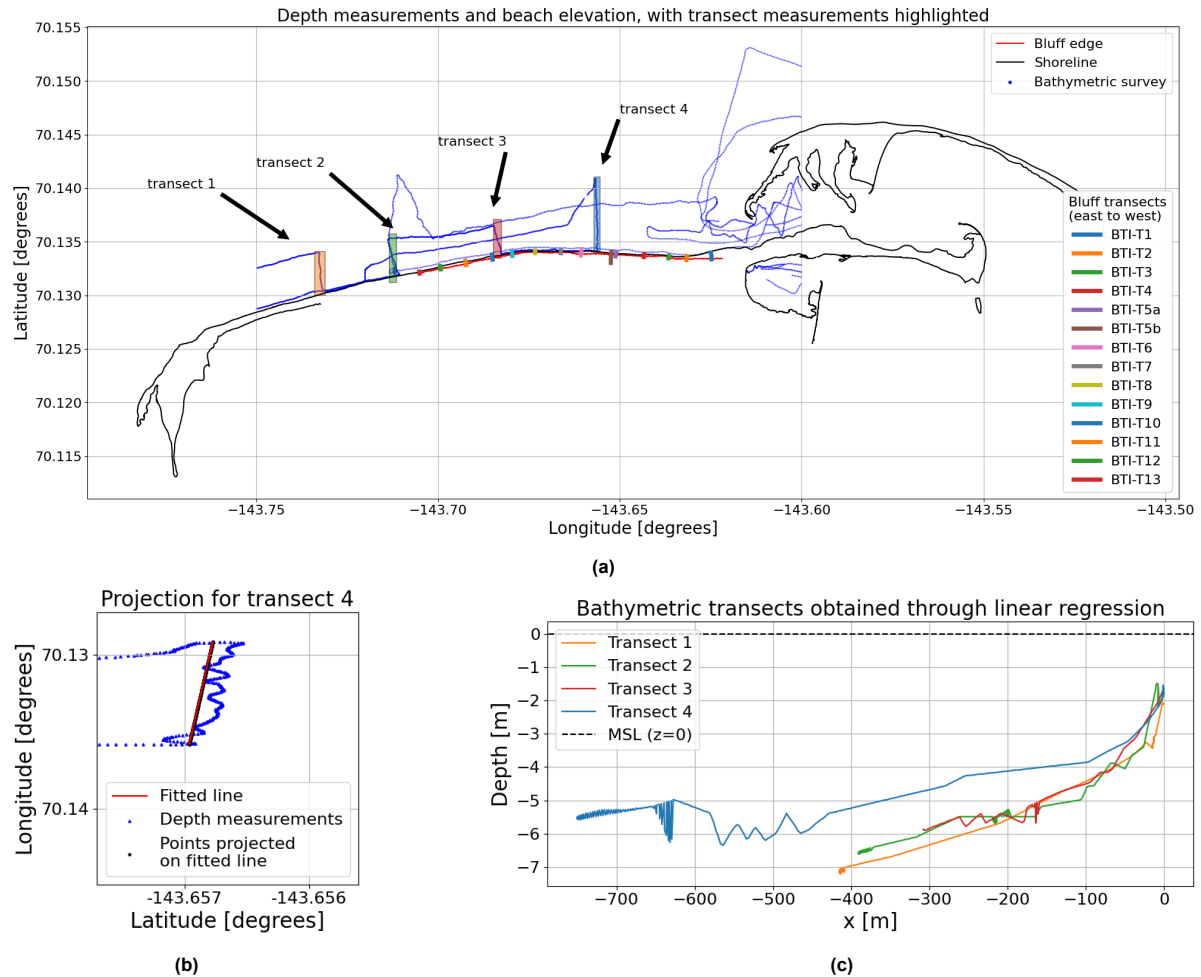


Figure 5.3: Beach transects, shoreline, and bluff edge at the northern coastline of Barter Island, with the depth measurements used to generate four different beach transects (i.e., points in the respective shaded regions) (Figure 5.3a), an example of depth measurement points being cast onto a line that is obtained through linear regression for the most eastward shaded region in Figure 5.3a, i.e., transect 4 (Figure 5.3b), and four bathymetric transects generated from the points within the shaded region from Figure 5.3a (Figure 5.3c).

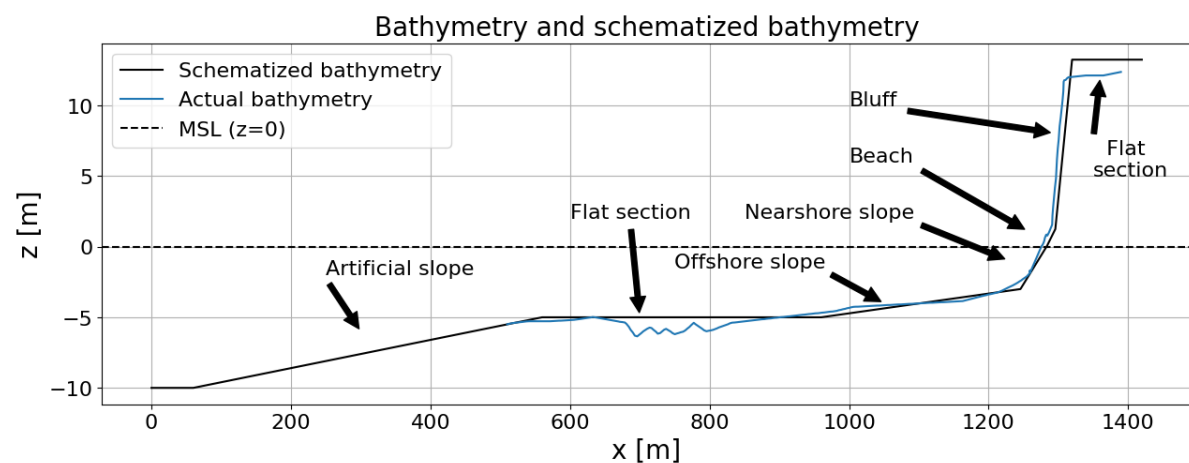


Figure 5.4: Bathymetric transect of the most eastward transect from Figure 5.3a (or 'Transect 4' in Figure 5.3c), and an annotated schematized version. The schematized transect consists of a flat section, bluff, beach, nearshore slope, offshore slope, another flat section, and an optional artificial slope.

Ground Temperature Distribution

Initial conditions for the soil temperature were obtained from ERA5. ERA5 is a climate reanalysis product from the European Centre for Medium-Range Weather Forecasts (ECMWF). It provides data on climate variables on regular longitude-latitude grids with a resolution of 0.25 by 0.25 degrees (Hersbach et al., 2020). We used the ERA5 dataset to obtain values for different heat fluxes, air and sea temperatures, and sea ice coverage. We used each of these variables to force the model.

ERA5 models the soil temperature at four different layers, being 0 to 7, 7 to 28, 28 to 100, and 100 to 289 centimeters. For the initial conditions, the center of each layer was assumed to be the respective temperature corresponding to that layer. We used linear interpolation to fill in the temperature conditions between these center points.

It should be noted that data regarding initial conditions is limited. The only historical data with sufficiently high temporal coverage is ERA5. Especially the timeseries with soil temperatures at different layers, which we used for initial conditions in the current studies, are unreliable (Cao et al., 2020).

Improving soil temperature data

The influence of initial conditions on the modelling result was reduced by including a spin-up time in simulations. This spin-up time can be reduced by improving initial conditions. In an effort to improve initial conditions for the ground temperature distribution, we compared the ERA5 ground temperature data with ground temperature data from Barter Island (Erikson et al., 2020b). The temperature measurements from this dataset span the period of 2011-07-08 to 2011-09-27.

Plotting the measured data against ERA5 data results in Figure 5.5a. We applied multi-linear regression (also referred to as Best Linear Unbiased Estimator or "BLUE") to fit the ERA5 data points to the measured points (Figure 5.5b).

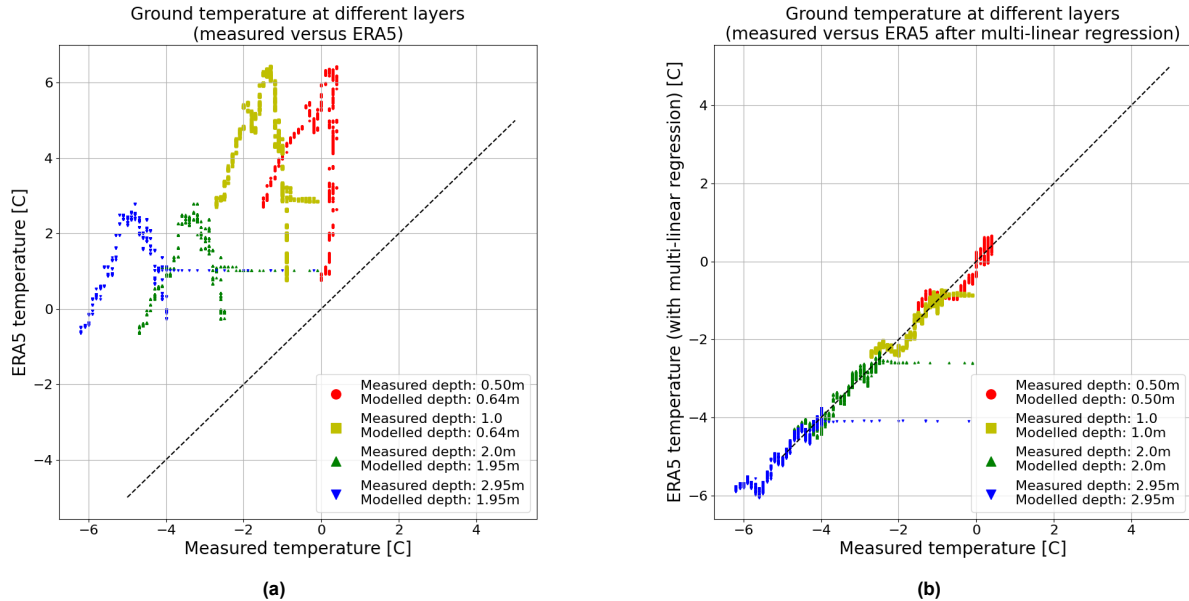


Figure 5.5: Measured data from Erikson et al. (2020a) plotted against modelled data from ERA5 spanning the same time period of 2011-07-08 to 2011-09-27. Figure 5.5a shows a direct comparison, and Figure 5.5b plots ERA5 data that was modified through multi-linear regression.

Spin-up time

Finally, we needed an estimate of the required spin-up time. To obtain that, we repeated a simulation of the ground temperature ten times for the year 2011. We then compute the absolute difference between the last (i.e., tenth) iteration and the previous years (Figure 5.6). This gives an indication of how much the predicted ground temperature for different layers changes after each year.

The convergence of initial conditions for the ground temperature at deeper layers does not vary much between using initial conditions without multi-linear regression (Figure 5.6a) and initial conditions with

multi-linear regression (Figure 5.6b). This means that the convergence of initial conditions is not sped up by using the modified initial conditions.

Instead, the convergence of initial conditions is governed by the depth of a node beneath the ground surface. However, we still applied the multi-linear regression to the initial conditions throughout this study to better represent measured ground temperatures at the onset of simulations.

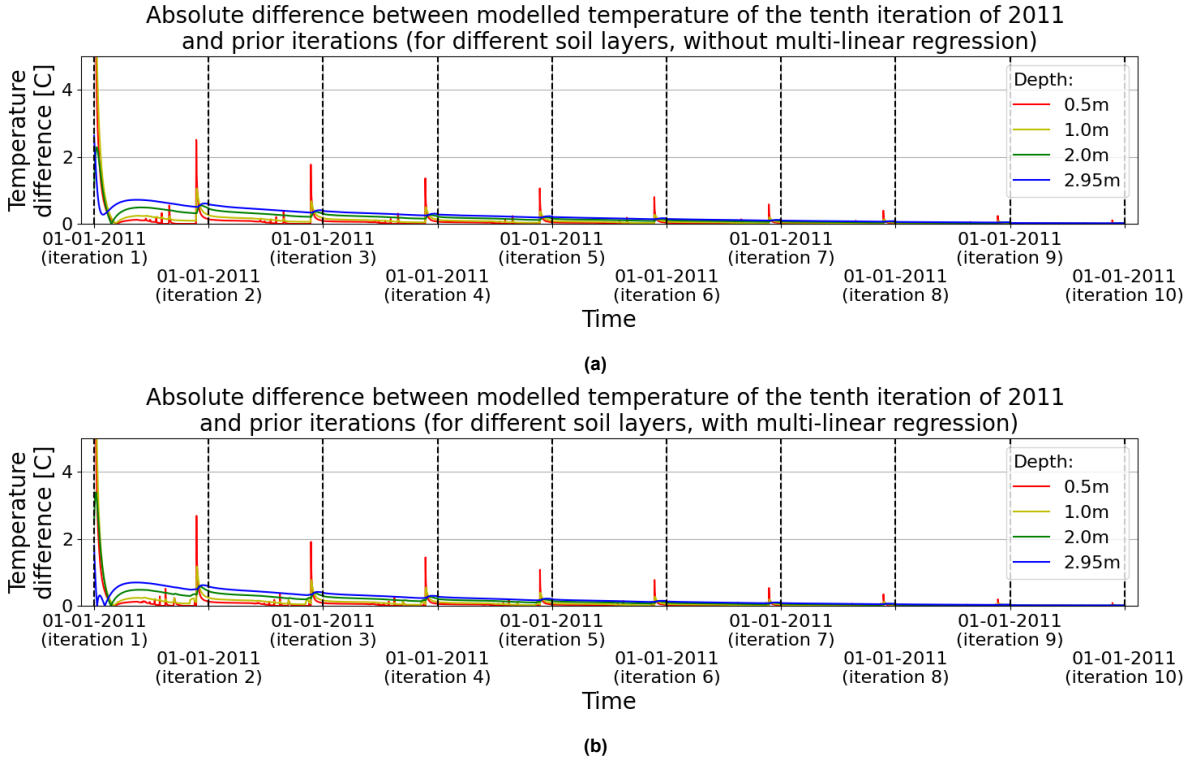


Figure 5.6: The absolute difference between the modelled ground temperature after ten years of repeated simulation of 2011 and the prior years (i.e., iterations). We computed the absolute difference when using initial conditions that were not recomputed using multi-linear regression (Figure 5.6a) and initial conditions that were recomputed using multi-linear regression (Figure 5.6b). For both cases, the difference between the final iteration and previous iterations decreases over time. These figures are not analogous with spin-up time, but can be used to make a first estimate of the required spin-up time before initial conditions converge and the ground temperature reaches a stable oscillation.

5.2.2. Forcing

The forcing of the thermo-morphological model consists of two parts, being hydrodynamic forcing and thermal forcing.

The hydrodynamic forcing is subdivided into wave conditions and water levels. We obtained wave conditions from the dataset published by Engelstad et al. (2023), which contains wave conditions that were hindcast for a period from 1979 to 2019, and are based on down-scaled ERA5 sea states through SWAN (Booij et al., 1997). This dataset supplies offshore wave height, peak period, and peak direction. ERA5 does not supply conditions for a sea ice coverage larger than 30%, which limits available wave data to periods with low sea ice coverage. We computed water levels as the sum of tides and storm surge (Kees Nederhoff, personal communication) and the sea level anomaly, which occurs due to geostrophic flows, salinity differences, and temperature-related expansion of water (Li Erikson, personal communication; Enfield and Allen, 1980).

We forced the thermal module of the thermo-morphological model using ERA5 datasets. These datasets have large spatial and temporal coverage, but low resolution. The spatial grid size of ERA5 is 0.25° , with an hourly temporal coverage. We obtained the following variables from ERA5 (categorized):

- Surface heat fluxes
 - mean surface latent heat flux [W/m^2]

- Mean surface net longwave radiation flux [W/m²]
- Mean surface net shortwave radiation flux [W/m²]
- **Computation of convective heat flux**
 - 10m u-component of wind [m/s]
 - 10m v-component of wind [m/s]
 - 2m temperature [K]
 - sea surface temperature [K]
- **Other**
 - Sea-ice cover [-]

5.2.3. Physical and Calibration Parameters

The thermo-morphological model uses over a hundred different parameters. To keep the workload manageable, we distinguished between fixed parameters and calibratable parameters. We kept fixed parameters constant throughout the calibration of the model. We used the calibratable parameters to calibrate the thermo-morphological model. We describe the most important parameters related to the thermal module, the XBeach module, and the Python wrapper below.

Thermal Module

For the thermal module, fixed physical parameters mostly consist of the thermal properties of water and soil. We set the melting temperature of water to 273.15 K. We assumed the latent heat of fusion of water to be 334 kJ/kg, and the geothermal gradient to be 0.025 K/m.

We obtained initial values for the calibratable parameters from Ravens et al. (2023). We tuned these further during the calibration process. Calibratable parameters included the soil's water/ice content n_b and thermal conductivity of frozen and unfrozen soil (k_{frozen} and k_{unfrozen} respectively). Furthermore, we included a calibratable factor $\alpha_{\text{surface flux}}$ (Section 4.3.5). This factor artificially reduces the surface heat flux at the top of the bluff to account for the behavior of the insulating peat layer, which is present landward of the bluff.

Finally, we used the number of nodes of each of the one-dimensional ground enthalpy models (N_{thermal}) to calibrate the integrated thermo-morphological model.

XBeach Module

XBeach has been extensively validated (e.g., Roelvink et al., 2009). Since this research aimed to integrate thermal processes into XBeach, most parameters related to XBeach are counted among fixed parameters. These include the water density, particle density, and bed friction coefficient.

The mean grain size at Barter Island was measured to be 0.036 millimetres at the bluff crest (Ferdinand Oberle, personal communication) and 1.9 millimetres at the bluff toe (Erikson et al., 2020b), which shows a clear bi-modality. This study sets the mean sediment diameter to 0.036 millimetres. This allowed XBeach to more efficiently transport the fine material offshore, which is an essential part of the thermal denudation process.

This study aimed to simulate thermal denudation. This erosion mechanism depends on the slumping of thawed material, followed by offshore transport. It therefore includes morphological parameters in its calibration parameters that relate to the sediment transport formulations used in XBeach to model these two processes.

Firstly, we used the critical dry slope to calibrate the model. We extracted initial estimates for the critical wet and dry slope from topographic measurements of the bluff. The wet and dry slopes were computed as the average slope of the beach and bluff face respectively (Figure 5.7). We used values of 0.6 and 0.1 for the critical dry and wet slopes respectively.

Secondly, we used the parameterized time-averaged current due to wave skewness/asymmetry in XBeach to calibrate the model. This parametrization uses the parameter fac_{ua} , which artificially enhances onshore transport when its value is increased. We used XBeach's default setting of 0.175 as a starting point.

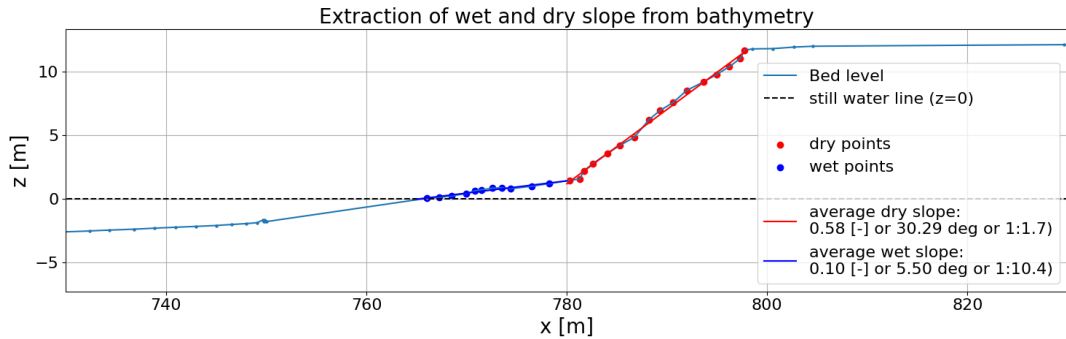


Figure 5.7: Topography as measured by Erikson et al. (2020a), with wet and dry slope highlighted. We computed the wet slope as the average beach slope, and the dry slope as the average slope of the bluff face.

Python Wrapper

We introduced several new parameters within the Python wrapper. These include the $R_{2\%}$ -threshold, the number of inter-storm XBeach activations (Section 4.1.1), and minimum thaw depth (Section 4.3.4). We found initial values for the latter two through preliminary sensitivity testing (Section 5.3.3). We set the initial value for the number of inter-storm XBeach activations to 168 hours, and the value for the minimum thaw depth to 30 centimeters.

However, choosing an initial value for the $R_{2\%}$ -threshold was not as straightforward. A threshold value had to be chosen that determines whether or not XBeach is activated for certain hydrodynamic conditions (Section 4.1.1). Based on wave and tide data (Section 5.2.2), and the formulation for 2% run-up by Stockdon et al. (2006), we performed a first analysis of expected run-up for hydrodynamic conditions between 1979 and 2018. For each year, we computed the number of hours with 2% run-up exceeding different thresholds (Figure 5.8), and also included the number of hours that total 1, 5, and 10 % of the number of hours in a year.

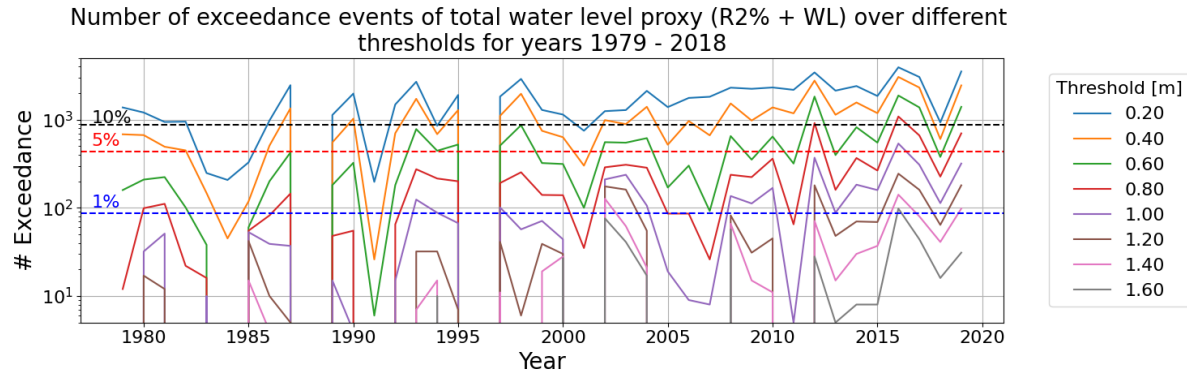


Figure 5.8: The number of hours per year that the total water level proxy ($R_{2\%}$ + water level) exceeds for different $R_{2\%}$ -thresholds. The number of hours per year that amount to 1%, 5%, and 10% (87.6, 438, and 876 respectively) of the total number of hours in a year are also plotted. These percentages should give an indication of how the number of hours that XBeach is active relates to the total number of hours modelled. Ideally, XBeach is activated as few times as possible while still maintaining an accurate description of morphological change.

To get more insight into the effects of different thresholds for a single year, we repeated the analysis for the year 2009 (Figure 5.9a). We computed the number of hours that exceed the total water level proxy (i.e., $R_{2\%}$ + water level) per threshold for the year 2009. Approximately three large storm events occur in 2009. In order to model only these storms, a threshold ranging between 0.7 meters to 0.9 meters should be chosen (Figure 5.9b).

To keep computational costs reasonable while still modelling all relevant storms and maintaining a ratio of hours with XBeach versus hours without XBeach of about 1/100 (i.e., 1%), we first set the threshold for the total water level proxy at 1.0 meters above mean sea level, resulting in simulation times of about 4 hours for a simulation describing 2012 - 2016.

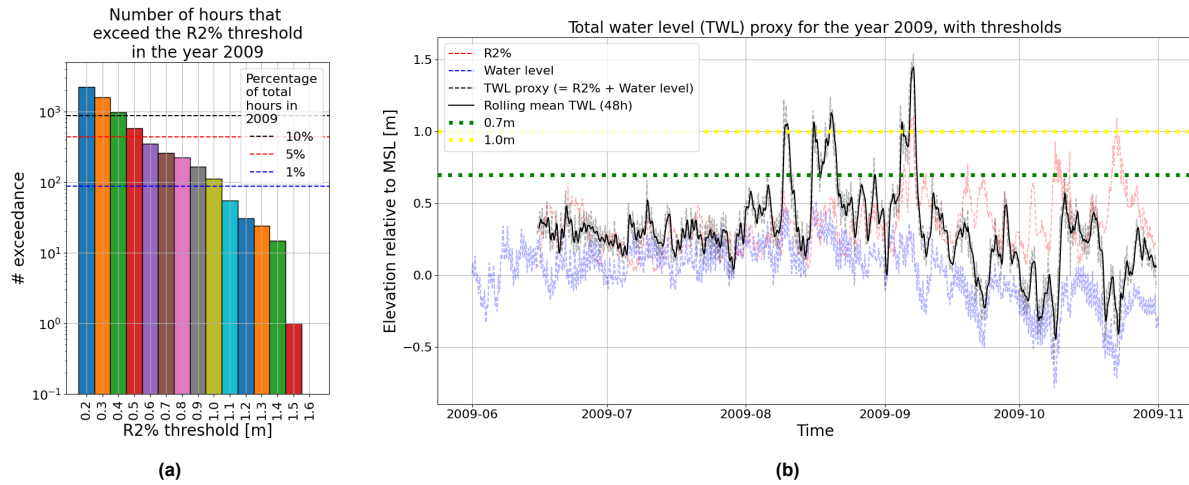


Figure 5.9: The number of hours for the year 2009 that the total water level proxy ($R2\% +$ water level) exceeds different thresholds (Figure 5.9a), with the number of hours that amount to 1%, 5%, and 10% (87.6, 438, and 876 respectively) of the total number of hours in that year, and a timeseries of the total water level proxy (smoothed using the rolling mean with a window size of 48 hours) within the sea ice-free period of the year 2009 to visualize which thresholds facilitate the modelling of the large storm events within that period (Figure 5.9b).

We also attempted threshold values as low as 0.7 meters, but these thresholds resulted in too long computation times (e.g., 48 hours for a simulation describing 2012 - 2016). Since the sensitivity analysis (Section 5.4) included approximately 90 two-year simulations, we deemed a simulation time of 48 hours to be unacceptable.

5.2.4. Calibration and Validation data

The calibration and validation of the thermo-morphological model consisted of two parts.

The first part of the calibration and validation used ground temperature data. We used the thermal module to simulate ground temperature through enthalpy. During calibration and validation, the thermal module aimed to reproduce measured soil temperature. We used two datasets containing ground temperature measurements. Both datasets were obtained from Barter Island and or the surrounding area (5.10).

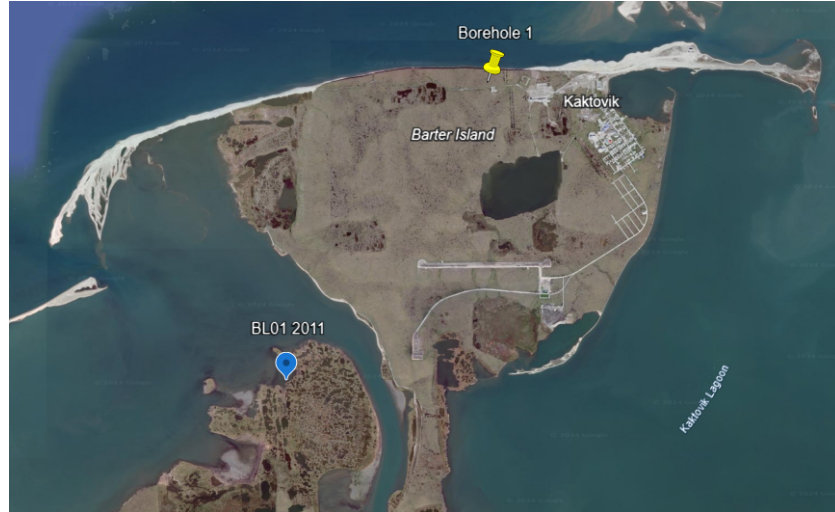


Figure 5.10: Locations where the datasets for calibration ('Borehole 1') and validation ('BL01 2011') of the thermal module were obtained (Google Earth, 2024).

The first dataset contains the soil temperature at 17 different soil layers (Figure 5.11a) and we used

this dataset for calibration. We obtained this dataset from Li Erikson (personal communication).

The second dataset contains the soil temperature at 4 different soil layers (Figure 5.11b). We used this dataset for validation. This dataset was obtained from Erikson et al. (2020a). The anomaly in Figure 5.11b likely results from a temporary removal of the measuring equipment from the soil (Li Erikson, personal communication).

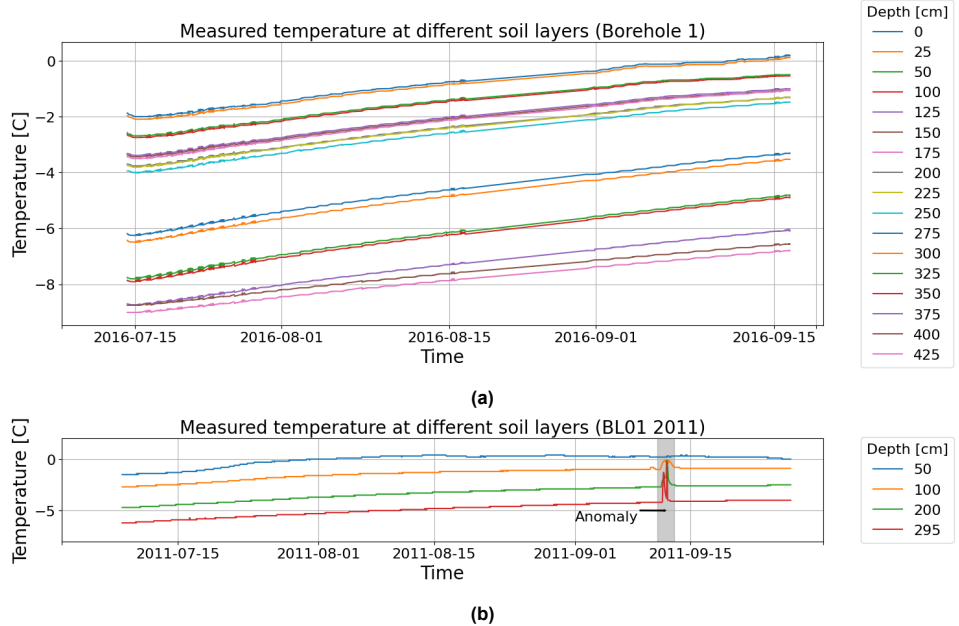


Figure 5.11: Measured ground temperature for different soil layers. The calibration dataset (Figure 5.11a) was obtained from Borehole 1 (Figure 5.10). The validation dataset (Figure 5.11b) was obtained from BL01 2011 (Figure 5.10).

We calibrated and validated the integrated thermo-morphological model with historic shoreline and bluff edge locations. We obtained a timeseries of shorelines and bluff edge locations from Gibbs et al. (2020). Using the same transect from Figure 5.4, we determined the exact distance to the same offshore baseline for each historical observation. This resulted in a timeseries of shore line and bluff edge locations for a 1D transect (Figure 5.12).

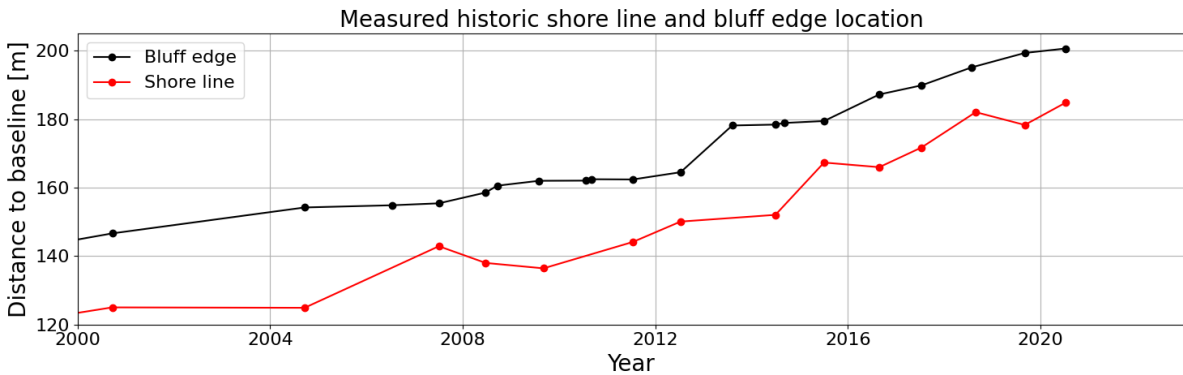
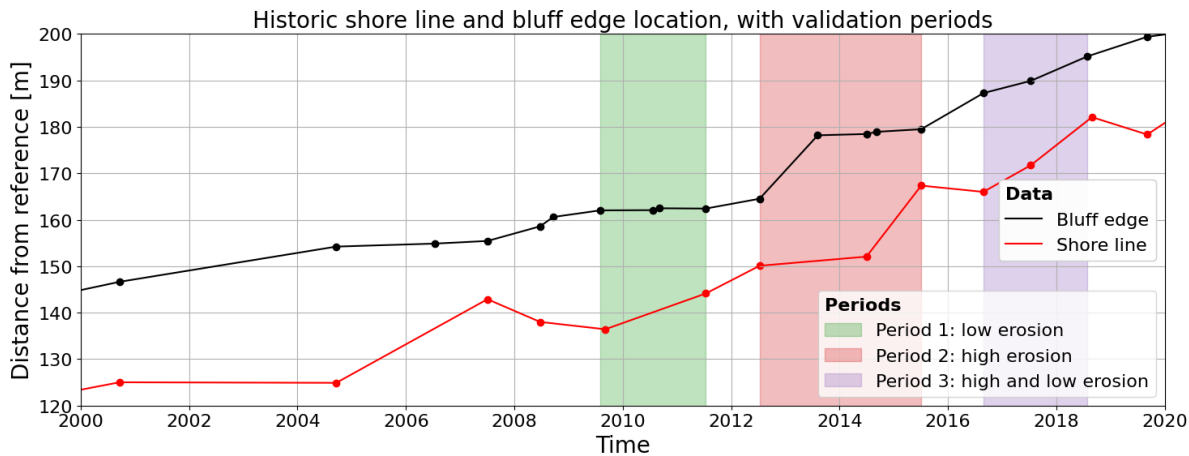


Figure 5.12: Distances of bluff edge and shore line of 'Transect 4' (Figures 5.3a and 5.3c) to an offshore baseline, based on data from Gibbs et al. (2020).

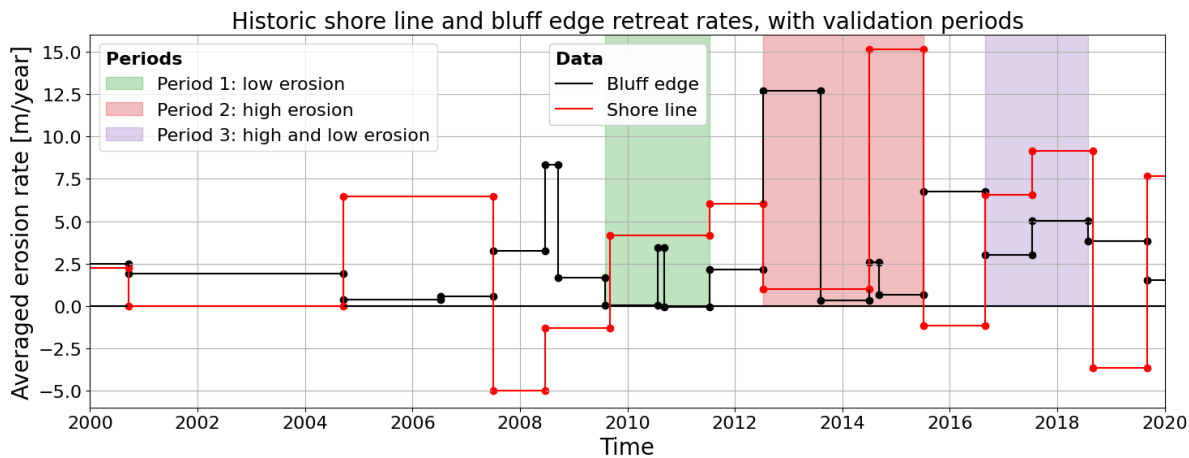
We selected three time periods from the erosion data (5.1). We chose these periods such that there is one period with low erosion, one period with high erosion, and one period with high erosion followed by low erosion (Figure 5.13a and Figure 5.13b). The exact starting and end dates of these periods depend on the erosion data. We used the second period (i.e., the period with high erosion followed by low erosion) for calibration, and the other two periods (i.e., period 1 and period 3) for validation.

Table 5.1: Periods used for model validation. Periods are chosen based on erosion rates during those periods (Figure 5.13b).

Description	Start time	End time	Average erosion rate [m/year]
Period 1: low erosion	2009-08-02	2011-07-15	0.2
Period 2: High and low erosion	2012-07-11	2015-07-05	5.0
Period 3: High erosion	2016-08-27	2018-07-30	4.1



(a)



(b)

Figure 5.13: Cumulative erosion (Figure 5.13a) and average erosion rate (Figure 5.13b) obtained from Gibbs et al. (2021). We used the highlighted periods for calibration and validation (Table 5.1). We computed erosion rates as the average erosion between two consecutive measurements.

Erosion rates have a high correlation with environmental drivers such as wave power, positive degree days (for both air and sea temperature), and duration of the sea ice-free period (Gibbs et al., 2021). Environmental drivers vary inter-annually (Figure 5.14). Wave power and the number of positive degree days are relatively low for the low erosion period (mid 2009 to mid 2011). For the high erosion followed by low erosion period (mid 2012 to mid 2015), the number of positive degree days is high first, followed by a period of moderate wave power. For the high erosion period (mid 2016 to mid 2018), the length of the sea ice-free period is long, the number of positive degree days is high, and wave power is also moderately high.

Since the thermo-morphological model is process-based, variations in environmental drivers resulted in variations in erosion rates. Figure 5.14 reveals variations in environmental drivers for the different validation periods, and Figure 5.13b indicates differences in erosion rates. Using the three different

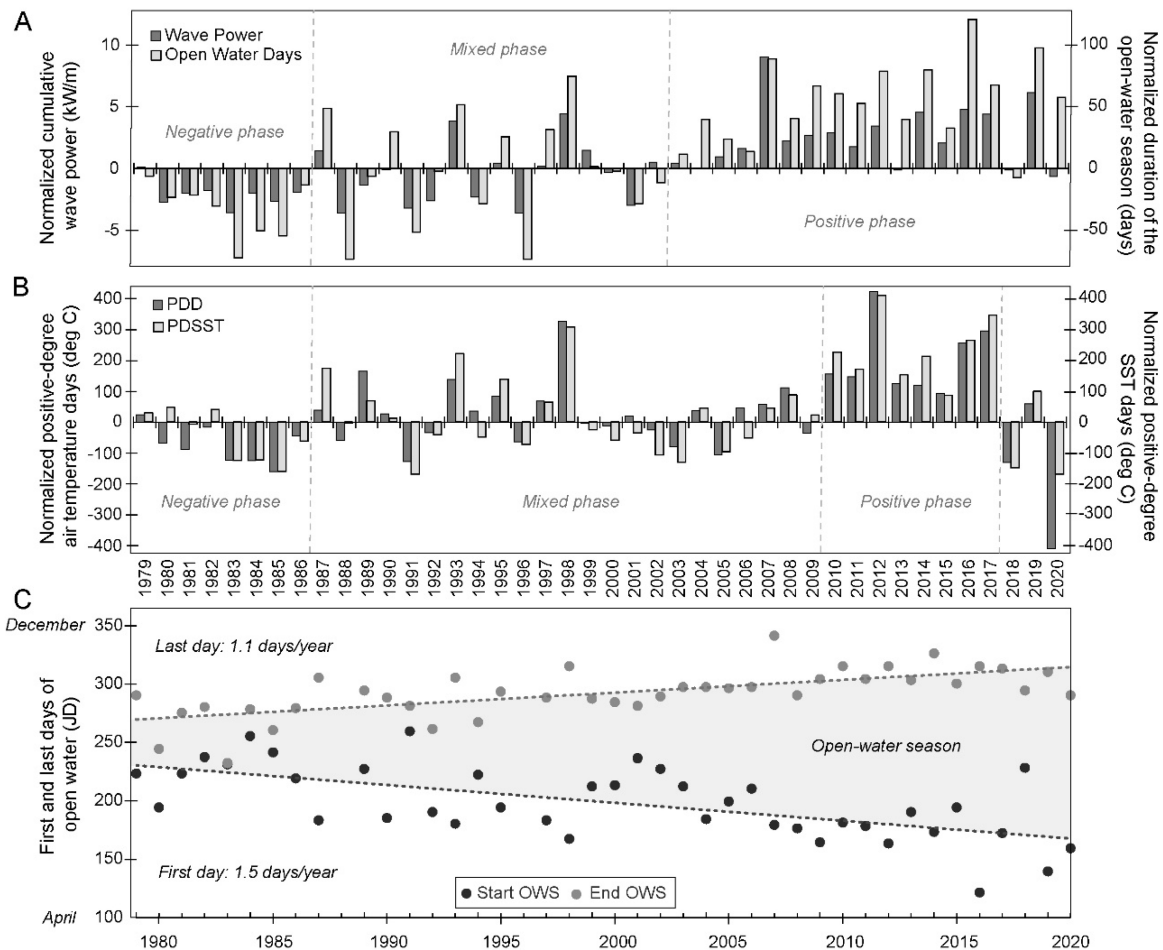


Figure 5.14: "(A) Cumulative wave power (WP) and the duration of the open-water season (OWS) normalized to the 1979–2009, 30 year mean; (B) positive degree day air and sea surface temperature (PDD and PDSST) conditions normalized to the 1979–2009, 30 year mean; (C) First and last days of open water between 1979 and 2020 and linear trends of their rate of expansion" Figure 9, Gibbs et al. (2021). Gibbs et al. (2021) correlated these environmental drivers with bluff retreat. Reprinted from Gibbs et al. (2021).

periods made it possible to assess the skill of the model in reproducing varying erosion rates when forced by varying environmental drivers.

To compare modelling results against measured bluff retreat, we required a method for extracting the bluff edge from a given bathymetric transect. Palaseanu-Lovejoy et al. (2016) present a method for detecting bluff edges. This method connects an onshore and offshore point with a line and defines the bluff edge coordinate as the point with the largest (positive) perpendicular distance to this line (Figure 5.15).

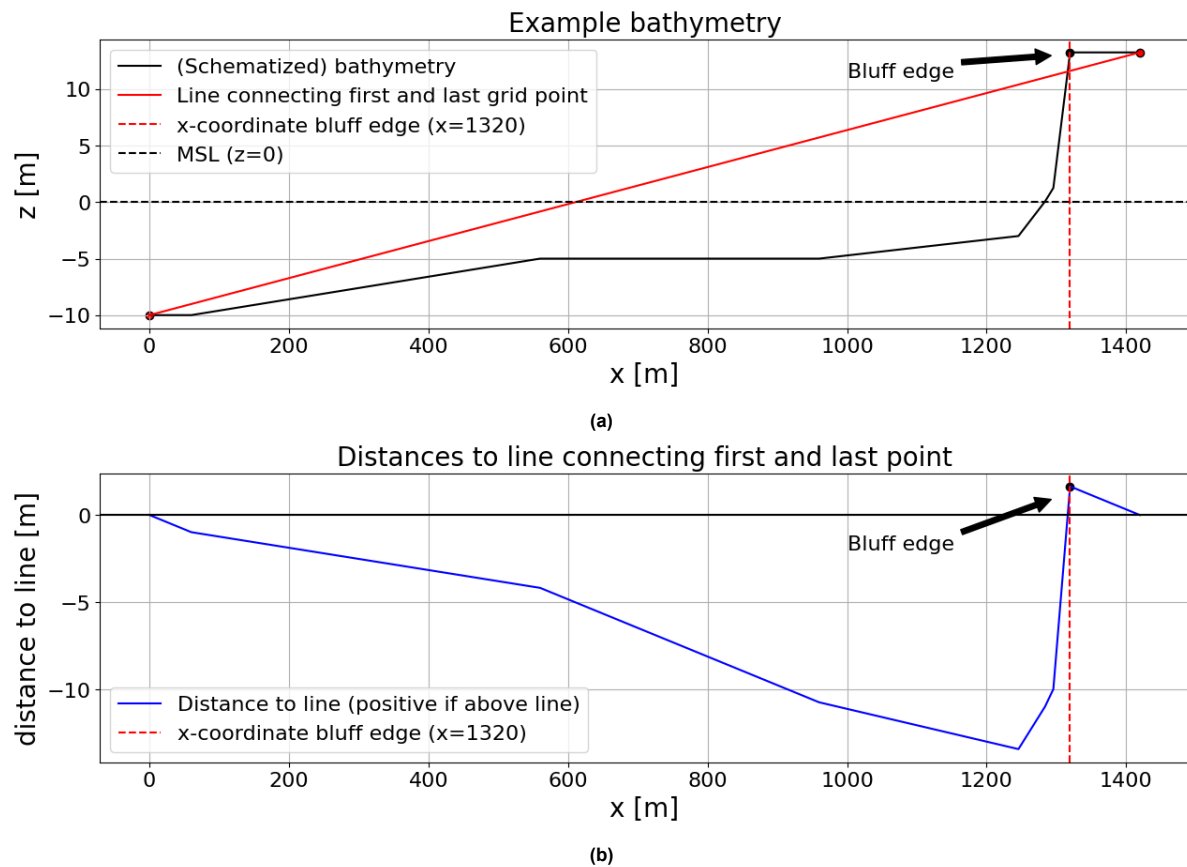


Figure 5.15: Example of determination of the bluff edge location for a schematized bathymetry, where the first and last point are connected with a red line (Figure 5.15a). Figure 5.15b plots the distance to this red line for the entire transect. We define the bluff edge coordinate as the point with the largest positive distance to the red line (Palaseanu-Lovejoy et al., 2016).

5.3. Calibration and Validation

The thermo-morphological model consists of two modules (Chapter 4): the thermal module and the XBeach module. Hence, the calibration and validation of the thermo-morphological model consisted of two parts. Firstly, we calibrated and validated the thermal module separately using ground temperature data. Secondly, we calibrated and validated the integrated thermo-morphological model using bluff retreat data.

The morphological module uses the physics-based model XBeach, which has been validated extensively and has shown accurate results in a number of test cases (Roelvink et al., 2009). However, the current case study varies from standard XBeach applications at temperate latitudes and (moreover) we require the accurate modelling of long-term morphodynamics while only simulating short-term hydrodynamics. We thus re-calibrated some XBeach settings (i.e., critical dry slope and fac_{ua}). This re-calibration occurred as part of the calibration of the integrated thermo-morphological model.

5.3.1. Thermal Module Calibration

We developed the thermal module to predict the ground temperature distribution to determine the thickness of the erodible layer (Section 4.3). We assessed the ability of the thermal module to accurately predict ground temperature using timeseries of ground temperature (Section 5.2.4).

For the calibration of the thermal module, we varied four different parameters (Section 5.2.3). These parameters include the frozen and unfrozen thermal conductivity, the water/ice content, and the surface flux factor. During preliminary testing, we found that the thermal module was sensitive to the values of these parameters. Since no data are available for these parameters, we selected them as calibration parameters.

Intuitively, we expected that a lower surface flux factor results in a lower heat flux into the soil, which reduces active layer depth. However, the complexity of the system makes it difficult to predict the response of the system to varying parameters. The response of the system to a change in heat conductivity and water/ice content is difficult to predict (Figure 5.16). Therefore, a brute force method is adopted. We tried three different values for each parameter (Table 5.2), resulting in a total of $3^4 = 81$ simulations during this calibration.

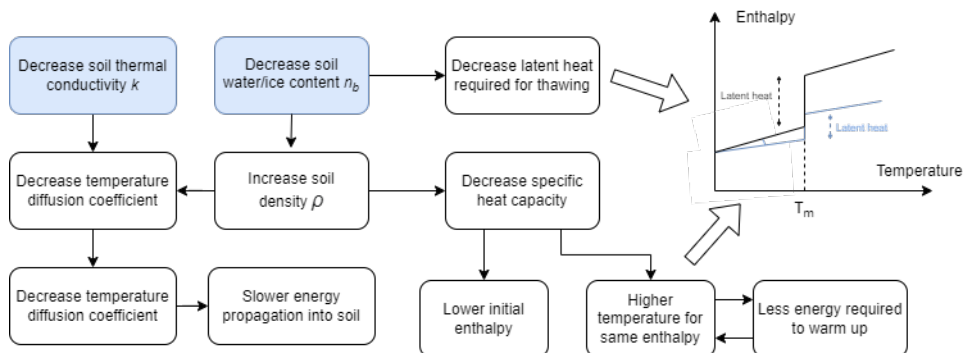


Figure 5.16: Diagram of the processes being affected by changes in parameters. This diagram shows an overview of first-order responses of the system to changes in water/ice content and thermal conductivity, and does not include complex feedback loops.

Table 5.2: Parameters used to calibrate the thermal module.

Parameter	Description	Values	Source
k_{frozen}	Thermal conductivity of frozen soil [W/m/K]	0.7, 1.7, 2.7	Kasper et al. (2023)
k_{unfrozen}	Thermal conductivity of unfrozen soil [W/m/K]	0.6, 1.05, 1.5	Kasper et al. (2023)
n_b	Water / ice content of soil [-]	0.45, 0.55, 0.65	Kasper et al. (2023)
$\alpha_{\text{surface flux}}$	Surface flux factor [-]	0.6, 0.8, 1.0	-

The soil temperature at deeper layers enters a relatively stable oscillation after approximately five years (Figure 5.6). To be conservative, we used a spin-up time of 10 years during the calibration to account for deeper soil layers. The thermal module is relatively quick and facilitates these simulation periods. We then extracted the predicted temperatures for the 17 different soil layers from the simulation results for the time period covered by the data (Figure 5.11a).

For each combination of parameter settings, we computed the Root Mean Square Error (RMSE) for each layer using the modelled and measured temperature data (Figure 5.17). We found the lowest RMSE for the following parameter values (corresponding to RunID 'cal_gt61' in Figure 5.17):

$$\begin{aligned} k_{\text{frozen}} &= 2.7 \text{ W/m/K}, \\ k_{\text{unfrozen}} &= 0.6 \text{ W/m/K}, \\ n_b &= 0.65, \\ \alpha_{\text{surface flux}} &= 1. \end{aligned}$$

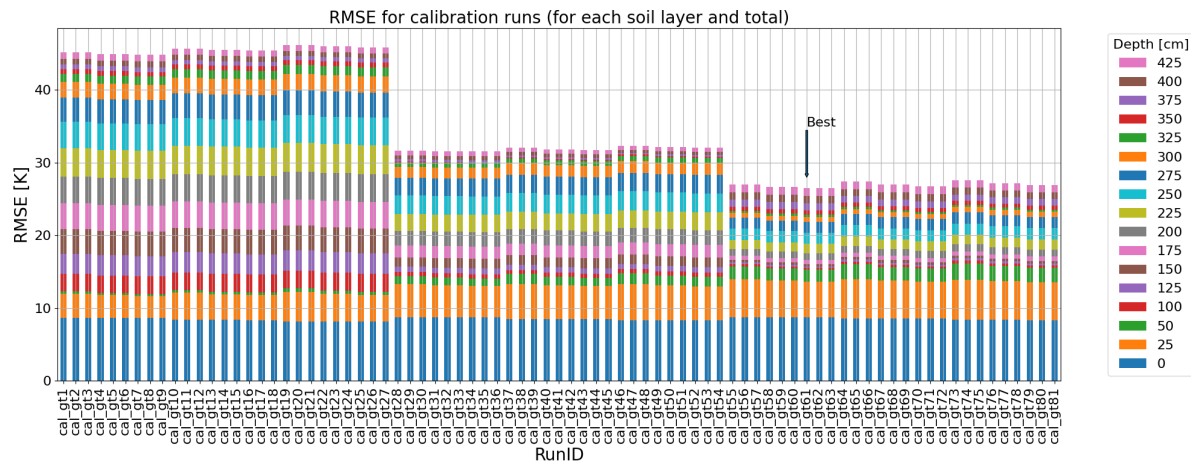


Figure 5.17: The Root Mean Square Error (RMSE) of each calibration run summed for all soil layers. The total height of each bar represents the total RMSE in Kelvin. We found the best RMSE for the simulation with RunID 'cal_gt61', annotated with 'best' in Figure 5.17.

The predicted temperature is plotted against the measured temperature in Figure 5.18.

The total RMSE from Figure 5.17 further shows three 'groups' of simulations:

- Group 1: cal_gt1 - cal_gt27
- Group 2: cal_gt28 - cal_gt54
- Group 3: cal_gt55 - cal_gt81

The differences in total RMSE within these groups are relatively small compared to differences in total RMSE between groups. These groups are characterized by a different thermal conductivity of frozen soil, where group 1, 2, and 3 (numbered in ascending order from left to right) have values of 0.7, 1.7, and 2.7 W/m/K for the thermal conductivity of frozen soil respectively.

For higher values of the thermal conductivity of frozen soils, the total RMSE decreases, mostly due to the reduced contribution of deeper soil layers. Deeper soil layers are more sensitive to changes in the thermal conductivity of frozen soil. This is likely caused by the deeper layers being frozen year-round and thus being more sensitive to changes in the frozen soil thermal conductivity.

5.3.2. Thermal Module Validation

Using the calibrated parameter settings (Section 5.3.1), we performed a validation simulation with the second ground temperature dataset (Section 5.2.4). This dataset contains soil temperature at four different layers for the year 2011.

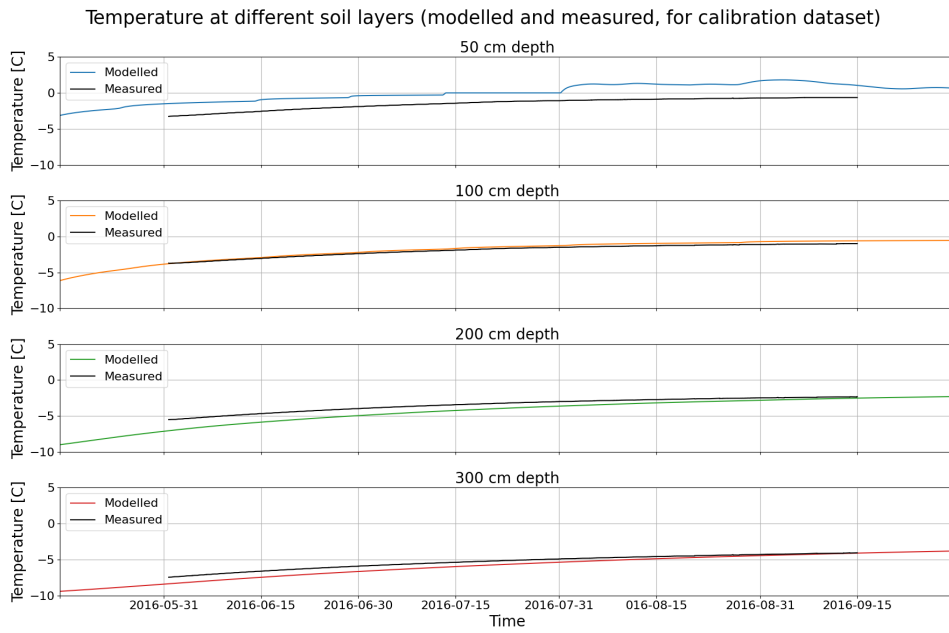


Figure 5.18: Modelled and measured temperature for different soil layers over time. The measured temperature comes from the calibration dataset.

Figures 5.19a, 5.19b, and 5.19c show a comparison between modelled and measured temperature over time, a direct comparison for each data point, and the RMSE respectively.

The model performed better for the upper soil layers (Figure 5.19). At greater depths, temperature was consistently under-predicted. This has three likely explanations:

- **Convergence of initial conditions**

The convergence of initial conditions may take considerably longer for deeper soil layers (Figure 5.6). For upper soil layers, hardly any change is noticeable after a year when modelling the same year repeatedly. This means that temperatures in the upper soil layer reached a stable oscillation much faster, whereas deeper soil layers required more time to adapt to the boundary conditions.

- **Heterogeneity soil**

Soil heterogeneity might explain the under-prediction of soil temperature at deeper layers. Currently, we assumed that soil properties are constant throughout the soil, i.e., we assumed the thermal conductivity, heat capacity, and ice content to be equal near the surface and at deeper layers. This means that the options for calibration are limited. For example, a higher frozen thermal conductivity results in a lower RMSE at deeper soil layers but a slightly higher RMSE for layers closer to the surface. This implies that the soil properties indeed vary over depth (Ravens et al., 2023). Therefore, the under-prediction of temperature for deeper layers might have resulted from an assumed soil homogeneity.

- **Heat conservation**

Since we used the finite difference method to discretize the enthalpy diffusion equation, heat conservation is not enforced. This could smoothen temperature differences between layers over time, leading to artificial diffusion of energy out of the system.

It is unlikely that the under-prediction of temperature for deeper layers relates to the boundary conditions. Temperature in the upper soil layers was predicted accurately (Figure 5.19a). The upper layers are more sensitive to the boundary conditions at the surface. If the surface boundary conditions would result in an under-prediction of temperature in deeper layers, this should also have been visible in upper soil layers, which is not the case.

The purpose of continuously modelling the soil temperatures was to obtain the thaw depth. A first-order estimate of the maximum thaw depth resulted in a value of 0.7 meters (Figure 5.20). Since the

prediction of the model is accurate up to a depth of at least 1 meter (Figure 5.19) with an error lower than 0.5 Kelvin, we assumed that we predict the thaw depth accurately, which is a prerequisite for moving on to the validation of the integrated thermo-morphological model.

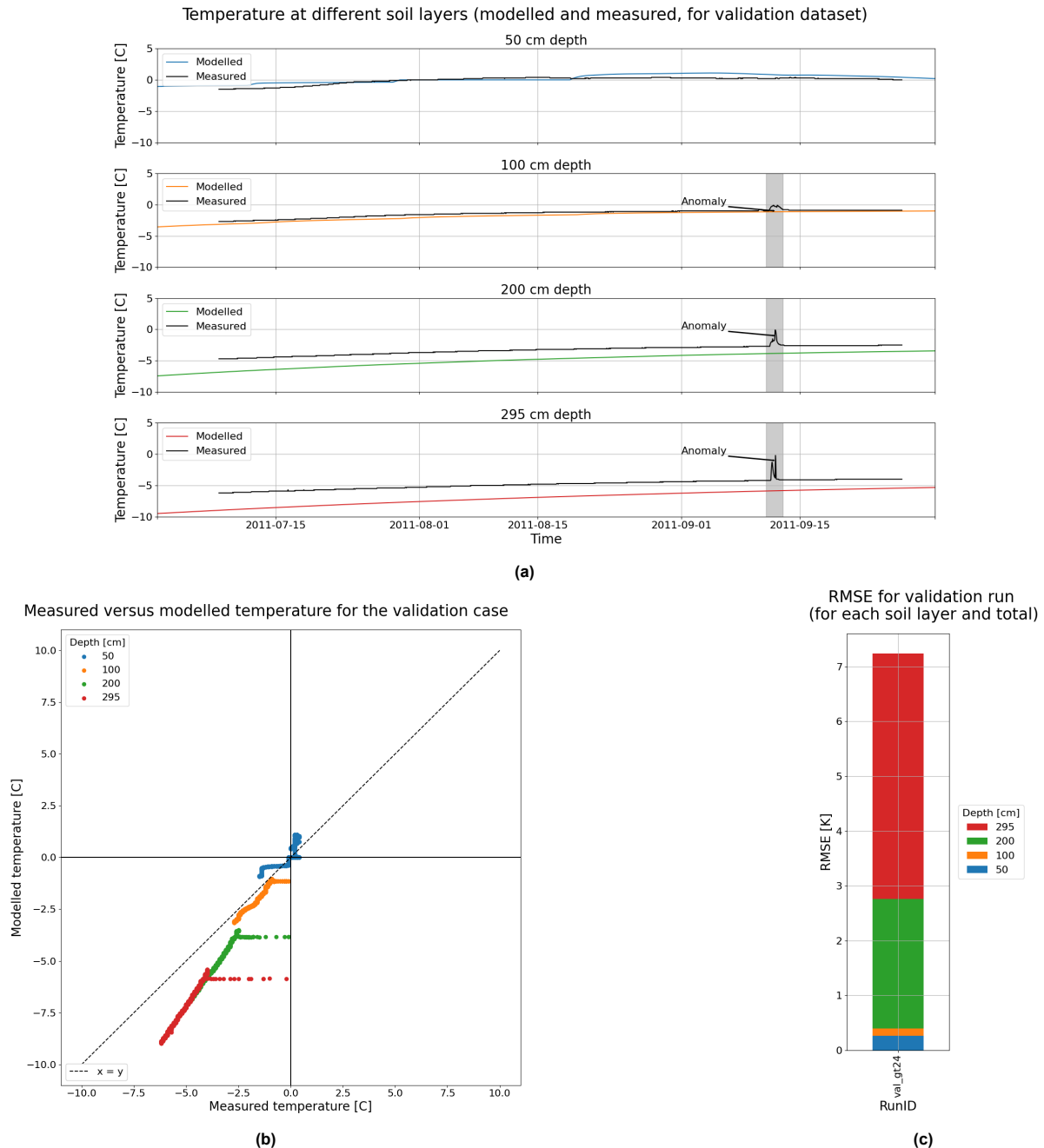


Figure 5.19: Modelled and measured temperature for different soil layers over time (5.19a), measured versus modelled temperature for different soil layers (5.19b), and RMSE of modelled temperature with respect to measured temperature for each soil layer (5.19c). Note that the measured temperature data contains an anomaly around 2011-09-12 (Figure 5.19a). This anomaly (highlighted in grey) is due to the measuring equipment being temporarily removed from the borehole for a data check.

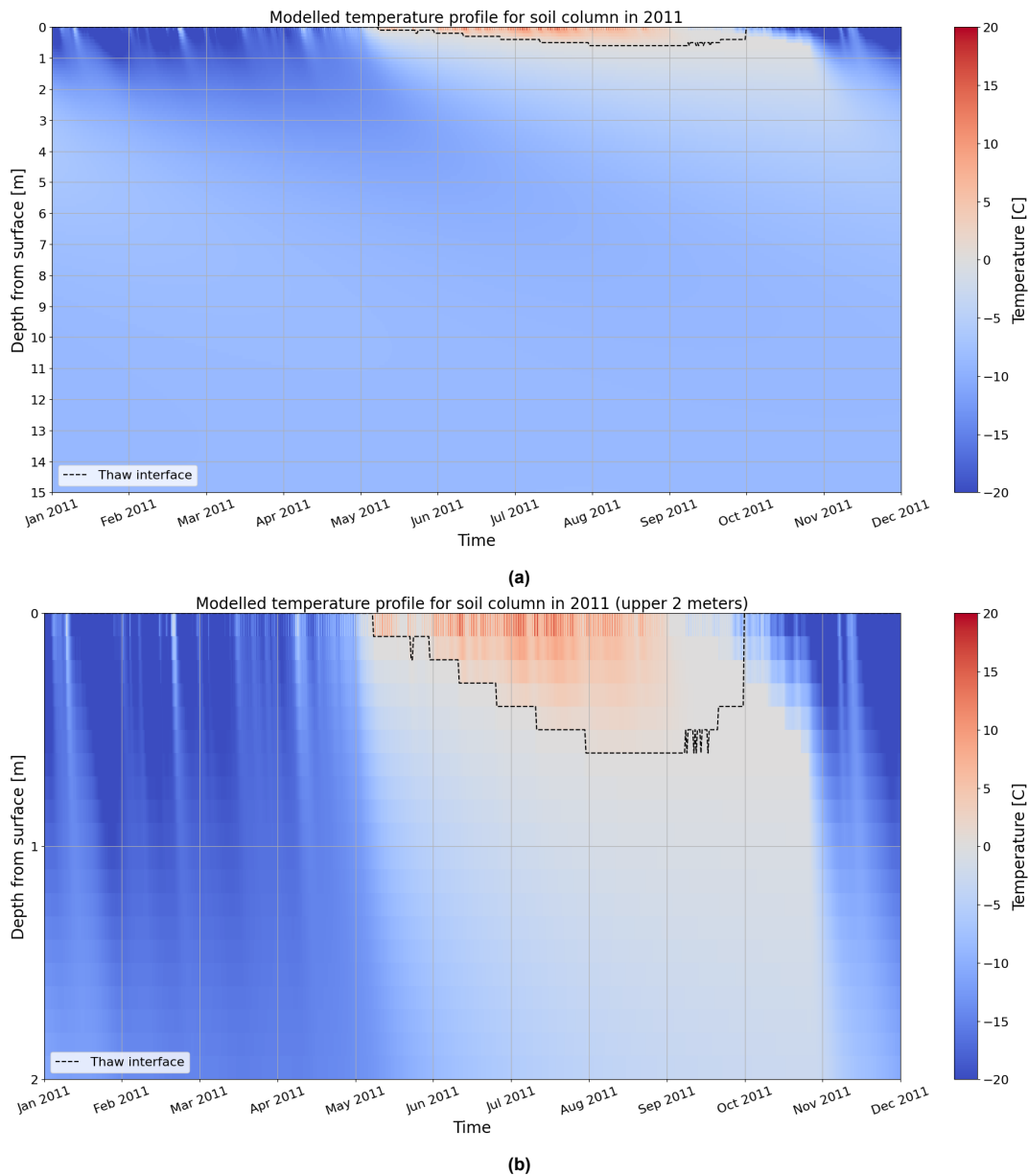


Figure 5.20: Complete temperature profile for validation simulation for the entire modelling depth (Figure 5.20a) and zoomed in to the upper two meters (Figure 5.20b). Both plots include the predicted thaw interface, for a d_{thaw} of 20 cm. We assumed a horizontal surface in the year 2011.

5.3.3. Thermo-morphological Model Calibration

To account for inaccurate initial conditions, we ran the model from the start of the year for each of the calibration/validation periods (Table 5.1). For example, the first period starts on August 2nd 2009, since that is the date of the first data point within that period. However, the starting date of the simulation was set to January 1st 2009.

The calibration of the integrated thermo-morphological model was done iteratively by adjusting the following (categorized) parameters (Section 5.2.3):

- **XBeach module**
 - critical dry slope
 - fac_{ua}
- **Thermal module**
 - d_{thaw}
 - N_{thermal}
- **Python wrapper**
 - $R_{2\%}$ -threshold
 - inter-storm XBeach activations

Table 5.3: List of parameters varied during calibration of the integrated thermo-morphological model, with respective values used. Not each combination of parameter values was tested.

Parameter	Description	Values
critical dry slope	Angle of repose for non-submerged material [-]	0.6; 1.0
fac_{ua}	XBeach calibration factor governing onshore transport [-]	0.0; 0.175; 0.225; 0.275; 0.325; 0.375; 0.425
$R_{2\%}$ -threshold	Threshold of predicted 2% run-up to activate XBeach [m]	0.7; 1.0
inter-storm XBeach activations	Interval with which XBeach is activated regardless of sea ice or storms [h]	12; 168
d_{thaw}	Depth that needs to be frozen before being treated as non-erodible [m]	0.10; 0.20; 0.30; 0.40
N_{thermal}	Number of nodes in 1D enthalpy models [1/meter]	10; 100

A huge parameter space can be generated based on the listed parameters alone. However, due to time constraints, an iterative approach was adopted instead of testing the full parameter space. An overview of parameter values for the different calibration runs is given in Table 5.3. We pre-calibrated the model based on calibration data and visualizations of the morphological evolution.

We mainly calibrated the model by adjusting XBeach parameters related to onshore transport through wave skewness and asymmetry (Section 4.2.3). We set the $R_{2\%}$ -threshold to 0.7 and 1.0 meters. We used the second period (i.e., high erosion followed by low erosion) for calibration (Figure 5.13).

For each calibration simulation, we computed the RMSE using the difference between the predicted bluff retreat and the measured bluff retreat (5.21). The lowest error is found for the following parameter values (corresponding to 'val_per2_2' in Figure 5.21):

$$\text{critical dry slope} = 0.6 \text{ [-]}$$

fac_{ua}	= 0.0 [-],
$R_{2\%}\text{-threshold}$	= 1.0 [m],
inter-storm XBeach activations	= 168 [h],
d_{thaw}	= 0.20 [m] (3 nodes with a distance between grid points of 10 cm corresponds to $(3 - 1) \times 10 \text{ cm} = 20 \text{ cm}$),
N_{thermal}	= 150 [-],

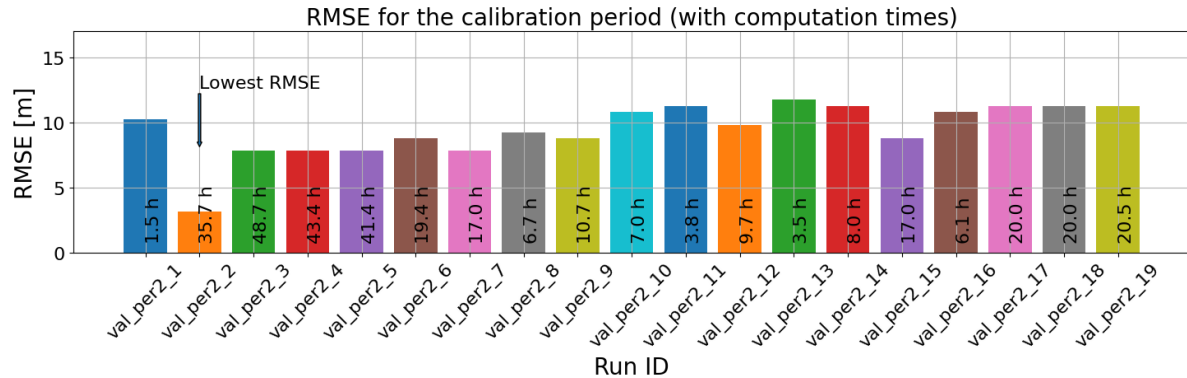


Figure 5.21: RMSE for each of the calibration simulations performed on period 2. We computed the RMSE from the difference between available data points and modelled points with the same time signature (excluding the first point of each period, as we used those as starting points of the simulation). The computation time is also included for each run.

Figure 5.22 plots the measured bluff retreat with the modelled bluff retreat. This modelled retreat uses the calibrated parameter values.

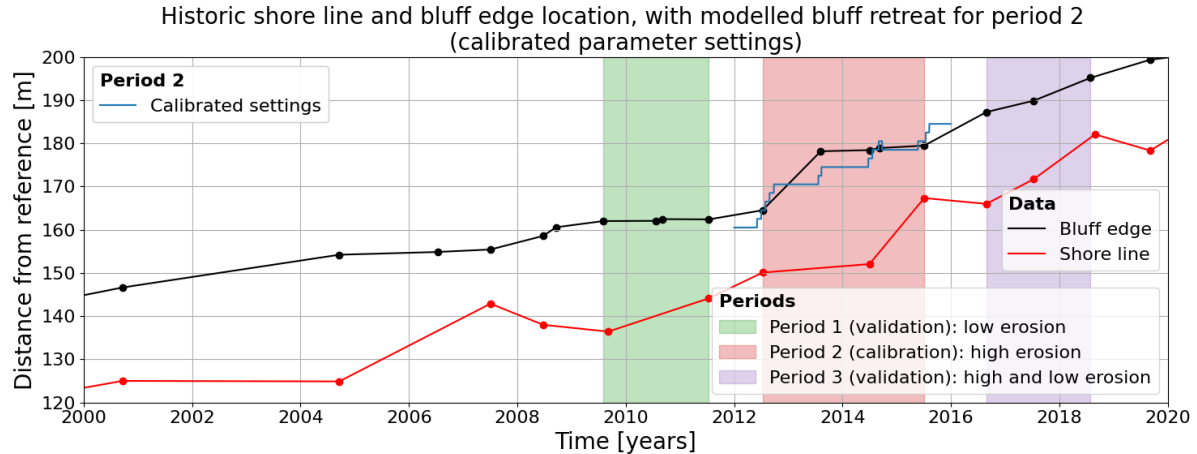


Figure 5.22: Bluff edge and shoreline erosion data plotted against modelled erosion. Three different periods are highlighted, which we used for calibration and validation. 'Zero' erosion occurs at the first measurement point within each period, after which the model diverges from observations. We obtained modelled erosion with the calibrated parameter settings ('val_per2_2' in Figure 5.21).

5.3.4. Thermo-morphological Model Validation

The calibration of the thermo-morphological model resulted in a set of parameters that minimized the RMSE for the calibration period, i.e., period 2. We validated these parameter values with periods 1 and 3. The calibration and validation results are plotted relative to measured values in Figure 5.23.

We found the lowest RMSE when using the lowest onshore transport settings in combination with a low $R_{2\%}$ -threshold. However, using these settings resulted in complete erosion of the beach until the bluff toe is located below the waterline (5.24).

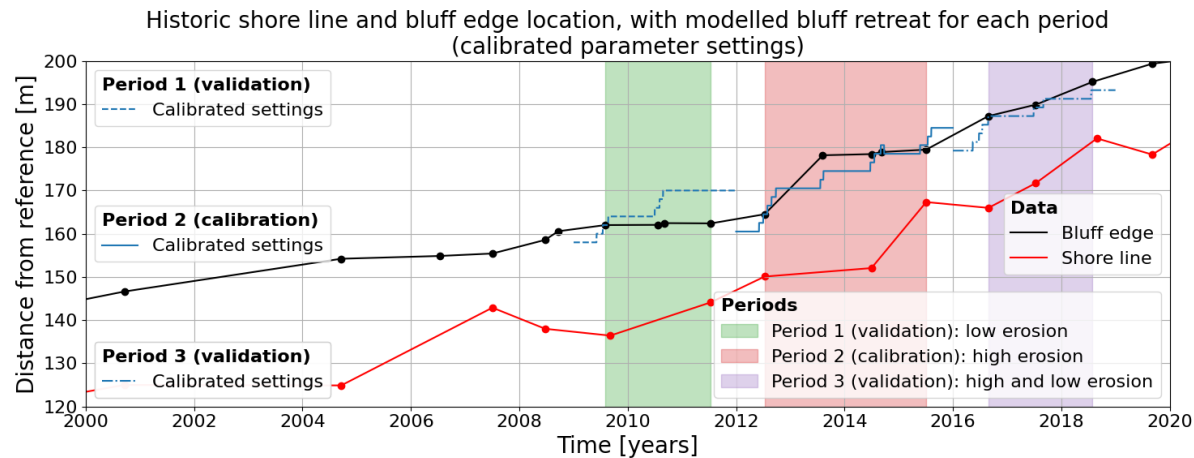


Figure 5.23: Bluff edge and shoreline erosion data plotted against modelled erosion. Three different periods are highlighted, which are used for calibration and validation. 'Zero' erosion occurs at the first measurement point within each period, after which the model diverges from observations.

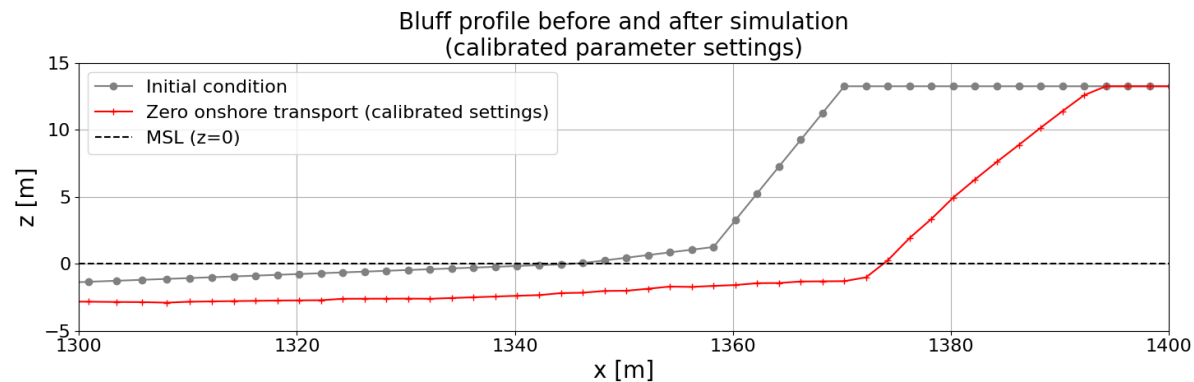


Figure 5.24: Initial and final bathymetric transect for the simulation of period 2. The calibrated settings result in complete erosion of the beach and the bluff toe is completely submerged after the simulation.

Therefore, we constructed a different set of parameter values to use during the sensitivity analysis (Section 5.4). These parameter values are:

critical dry slope	= 1.0 [-]
fac_{ua}	= 0.425 [-],
$R_{2\%}$ -threshold	= 1.0 [m],
inter-storm XBeach activations	= 168 [h],
d_{thaw}	= 0.20 [m] (3 nodes with a distance between grid points of 10 cm corresponds to $(3 - 1) \times 10 \text{ cm} = 20 \text{ cm}$),
N_{thermal}	= 150 [-],

We discuss the reasons behind choosing these values below. Complete overviews of the calibrated parameter settings and the settings proceeded with for the sensitivity analysis (also referred to as 'base' settings) are shown in Appendix F and Appendix G respectively.

Beach Erosion

The model systematically under-predicted erosion for the calibration period (Figure 5.23). Hence, increasing bluff erosion by reducing onshore transport resulted in a lower error. However, this increased erosion was facilitated by the disappearance of the beach.

In reality, a beach is present and the beach disappearing during the simulation is unrealistic. We can

obtain a first-order estimate of beach width by looking at the distance between the shoreline and the bluff edge. For a 10-meter-high bluff with a slope of 1:0.6, the beach width is equal to the distance between the shoreline and the bluff edge minus $10 / 0.6 \approx 17$ meters. In other words, a beach is present if the distance between the bluff edge and the shoreline is larger than approximately 17 meters, which is the case for most of the measurement period (Figure 5.23).

To retain the beach, onshore transport was artificially increased through fac_{ua} . However, that reduced erosion (either through reduced heat transfer directly from water into the bluff, or by reducing the number of XBeach activations). The model already under-predicted erosion for period 2, so reducing erosion further increased the error between the data and model predictions.

Even though increasing onshore transport gave a larger error, its larger onshore-directed transport resulted in the transect more accurately resembling a profile that might be expected, especially when we increased fac_{ua} to value higher than its default value of 0.175 (Figure 5.25).

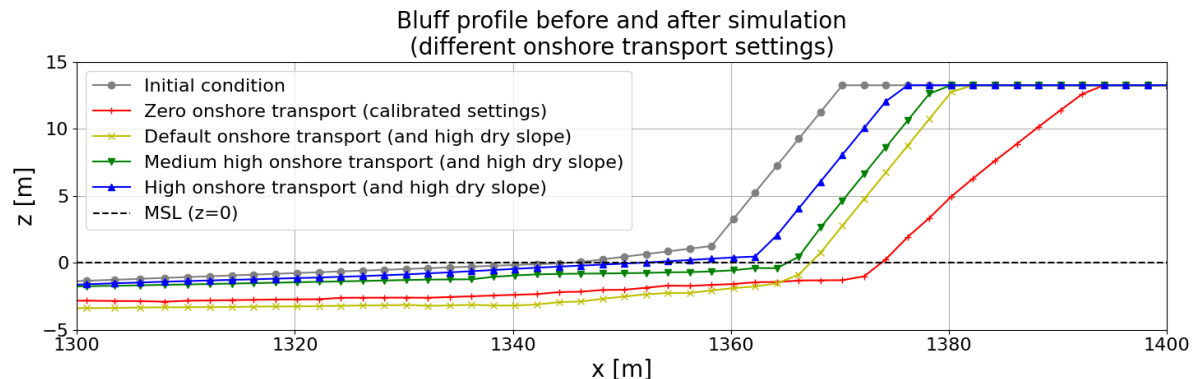


Figure 5.25: Bathymetric transect for simulations of period 2 with the same initial conditions and different onshore transport settings. XBeach's default onshore transport settings result in complete erosion of the beach.

Over-fitting of Data

We calibrated the model for the period 2012 - 2016. This period is characterized by relatively high bluff retreat. The model was able to reproduce these results because the calibrated model settings used an onshore transport factor of zero, leading to complete erosion of the beach. This allowed higher bluff retreat rates to be modelled, which was desirable during periods for which the data shows high erosion rates (e.g., periods 2 and 3 in Figure 5.23). This resulted in an over-prediction of erosion rates.

However the thermo-morphological model over-predicted erosion during the first validation period when using the calibrated model settings (Figure 5.23). Predictions were fairly consistent with the data, i.e., mostly no bluff retreat for 2009 - 2011, except for a large erosion event in 2010. This error likely occurred due to over-fitting of the available data.

A discrepancy visible occurred during period 2 in 2014 (Figure 5.23). In September of that year, the predicted bluff position first retreated and then advanced back in the offshore direction. The topography of the bluff shows no such bluff accretion (Figure 5.26). Hence, the bluff advancement was likely a result of the method used to determine the location of the bluff edge (Figure 5.15). This method is sensitive to gentler bluff face slopes, e.g., a value of 0.6.

Computation Times

The parametrization of $R_{2\%}$ uses the beach slope at the waterline to predict run-up and gives high values when the bluff touches the water. This resulted in XBeach being activated more often, and more bluff erosion, raising the question of whether or not XBeach is morphologically stable for the calibrated parameter settings (for which fac_{ua} is equal to zero).

Complete erosion of the beach resulted in a higher slope at the waterline (i.e., the bluff slope) and thus a higher expected 2% run-up and more XBeach activations. This was reflected by the fact that computation times can be up to five times as high for parameter settings with lower onshore transport (Figure 5.21).

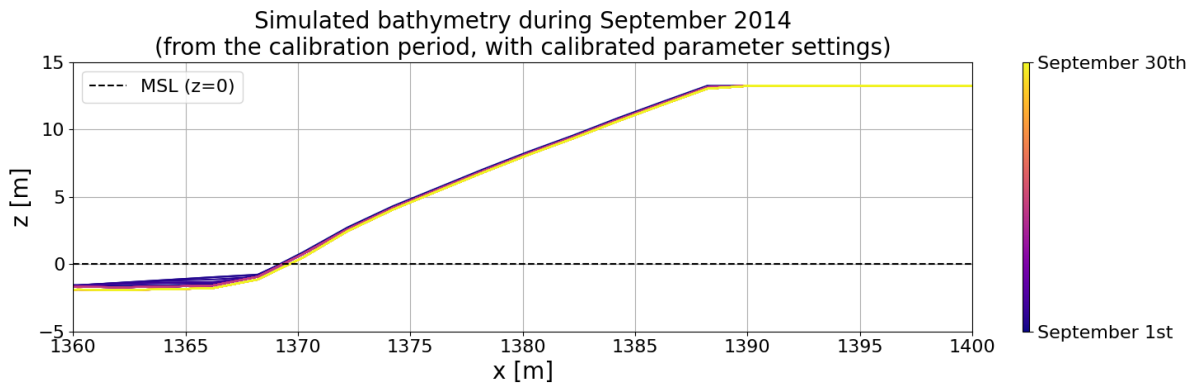


Figure 5.26: Modelled bathymetric transects for September 2014. We observed bluff retreat followed by bluff advancement (Figure 5.23), though this is not reflected by the simulated bathymetry.

Increasing onshore transport prevented the disappearance of the beach. The result was a lower slope at the waterline and less XBeach activations, i.e., shorter computation times.

Statistical Comparison of Different Settings

We plotted the model performance against the data for the calibrated parameter settings and the base settings in Figure 5.27a and Figure 5.27b respectively, and included some statistics based on the model fit. These statistics were obtained from a dataset with a limited size and should thus only be used to obtain a qualitative insight into model correlation and relative performance.

The base settings resulted in a worse fit with the data, which is visible through the higher values of the mean absolute error (MAE), the RMSE, and the lower value for the coefficient of determination (R^2). The base settings also resulted in a negative bias, i.e., an under-prediction of the bluff retreat. The Pearson correlation coefficient r shows that the model prediction and data are still moderately correlated (compared to the high correlation achieved with the calibrated model settings).

The calibrated parameter settings resulted in a lower error, bias, and correlation (Figure 5.27), even though the actual physics were captured better by using the base settings (Figure 5.25). The base parameter settings resulted in a larger error, which can mostly be explained by the large negative bias. There is still a moderate correlation between model prediction and measured bluff retreat, and we thus expected that the sensitivity analysis based on these settings still gave useful results.

Summary

The calibrated parameter settings resulted in complete beach erosion and large computation times. Additionally, these settings were obtained from a limited dataset. We decided to proceed with higher onshore transport for the sensitivity analysis in order to better represent the actual physics. Apart from a large erosion event in 2012, these settings resulted in accurate predictions of the bluff retreat for the calibration and validation periods (Figure 5.28). This erosion event is discussed further in Section 6.2.1.

Complete overviews of the calibrated parameter settings and the settings proceeded with in the sensitivity analysis (also referred to as 'base' settings) are provided in Appendix F and Appendix G respectively.

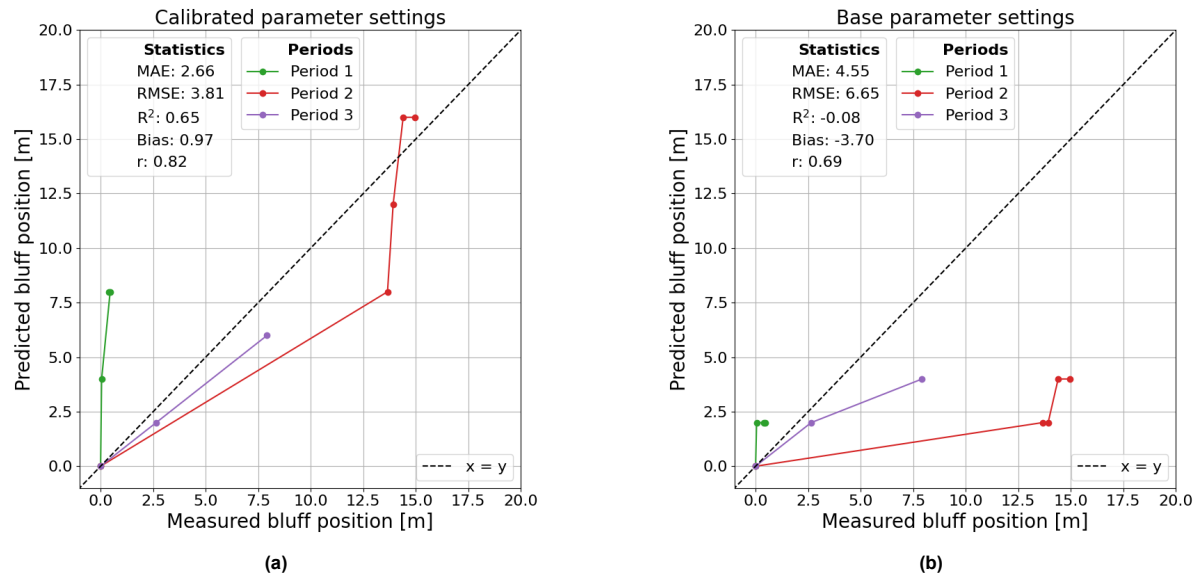


Figure 5.27: Measured and predicted location of bluff edge relative to the first measurement in each period. Perfect model predictions would be plotted exactly on the line $y = x$, which is also plotted. Figure 5.27a indicates how well the model prediction reflects the data for the 'best' parameter settings found during calibration. Figure 5.27b shows this for the 'base' parameter settings (used for the sensitivity analysis). Statistical metrics (Mean Absolute Error (MAE), Root Mean Square Error (RMSE), Coefficient of Determination (R^2), Bias, and Pearson Correlation Coefficient (r)) are also printed for both of these parameter settings.

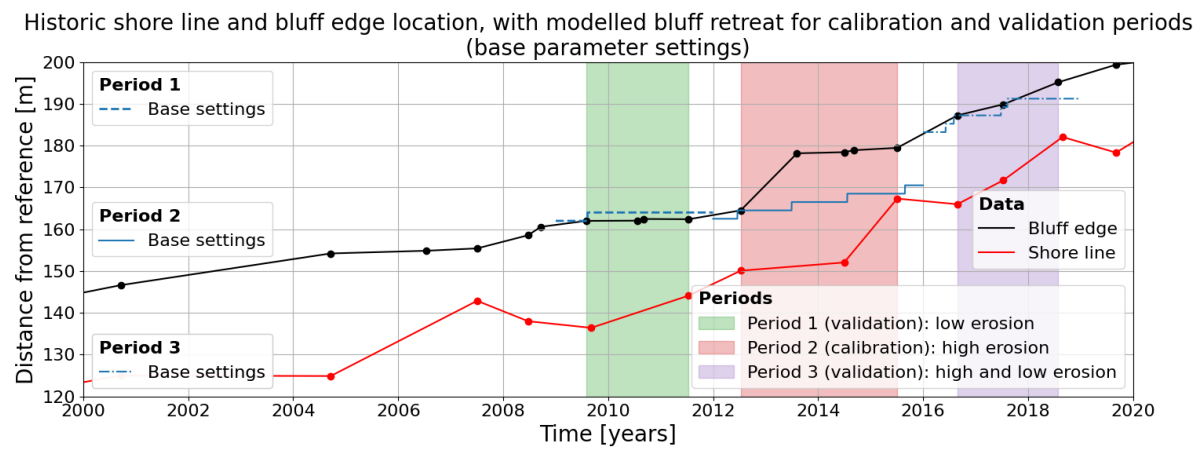


Figure 5.28: Predicted and measured bluff retreat for calibration and validation periods. The predicted bluff retreat uses the 'base' parameter settings (i.e., increased onshore transport). These settings lead to good predictions for the validation periods but underestimate the large bluff retreat for the calibration period (period 2) occurring in 2012.

5.4. Sensitivity Analysis

5.4.1. Description and Model Setup

To begin the sensitivity analysis, we performed a baseline simulation. We obtained the parameter settings for this baseline simulation through calibration and validation (Section 5.3.3 and 5.3.4). However, the calibrated model settings resulted in unrealistic beach erosion and were thus tweaked to reflect reality better. Exact model parameters for the baseline simulation are provided in Appendix G.

We performed a number of simulations with different parameter settings to compare against the baseline simulation. We computed erosion for the baseline simulation and for the simulations with different parameter settings. This allowed inter-comparison of the relative influence of varying model settings on the computed total erosion. The baseline run was performed for the period 2017-01-01 to 2019-01-01. This period had a substantial amount of bluff erosion (Figure 5.23) and is thus suitable for considering varying erosion rates by using varying parameter settings.

Running the baseline simulation took approximately two hours (for simulating a period of two years). A period longer than two years would result in too large computation times, which would be unfeasible for the sensitivity analysis in the current studies. For the baseline simulation, XBeach simulates $\sim 4.4\%$ of the entire simulations period but takes up $\sim 64\%$ of computation time. Computation time is discussed further in Appendix J.

Until this point in the thesis, we considered bluff retreat for calibration and validation of the thermo-morphological model. However, due to limitations of horizontal grid resolution, retreat could only occur in intervals of the grid spacing, i.e., about two meters. This made bluff retreat unsuitable as the dependent variable in the sensitivity analysis because the horizontal grid resolution was insufficient to detect subtle changes in the output.

A less discrete variable is the volume loss from the upper part of the bluff (ΔV_{ub}). XBeach simulates avalanching as a direct sediment exchange between grid cells if a critical slope is exceeded. This means that slumping effectively occurs by lowering the elevation of the grid cell that is located the highest in the bluff face. Once the critical slope is reached (i.e., the angle of repose or dry slope), the bed level of the next grid cell starts lowering and the bluff instantly retreats by two meters. The volume in the upper layer of the bluff is thus a more continuous variable than the total bluff retreat.

Specifically, we considered the upper five meters of the bluff (measured vertically downward from the top of the bluff) for volume loss. This threshold is larger than the critical slope times the grid spacing (i.e., $0.6 \times 2 = 1.2$ meters). However, the threshold does not reach the slump at the bluff toe, making it suitable for sensitivity analysis.

We computed the volume loss ΔV_{ub} by considering only the part of the domain that is higher than the bluff height minus the threshold of five meters. We computed the total volume present in that soil layer before and after a simulation through numerical integration using the composite trapezoidal rule. An example of a volume loss computation is visualized in Figure 5.29.

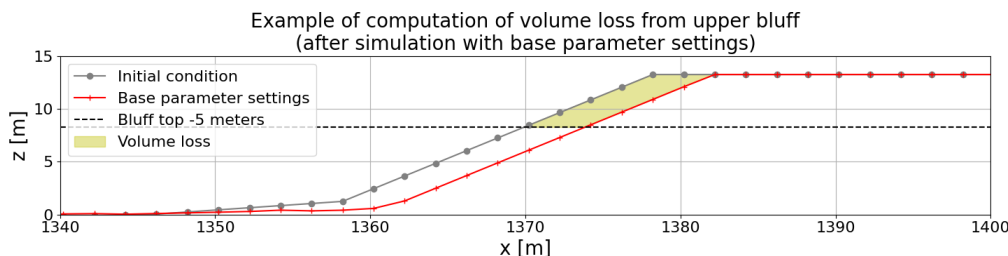


Figure 5.29: Visualization of how we computed volume loss. This example plots the initial topography and the output bathymetry for the baseline simulation, and the difference in volume for the upper 5 meters of bluff.

We considered three levels of sensitivity. These levels are:

- Level 1:** For the first level, we varied individual model parameters. We distinguished three categories: physical parameters, model (numerical) parameters, and bathymetry parameters. Physical parameters relate directly to the physical processes that are being modelled.

Table 5.4: Variations in parameters used for sensitivity analysis of the integrated thermo-morphological model. We varied most parameters by $\pm 20\%$, but there are exceptions (listed below).

Level	Sub-level	Standard variation	Exceptions (strategy)
1	Physical	20%	- Longshore transport gradient (± 0.01) - Melting temperature water ($\pm 1^\circ \text{K}$) - Latitude ($\pm 5^\circ$)
1	Model	20%	- Thaw threshold (± 1 node)
1	Bathymetry	20%	-
2	-	20%	- Water level ($\pm 0.1 \text{ m}$) - Sea temperature ($\pm 2^\circ \text{K}$) - Air temperature ($\pm 2^\circ \text{K}$)
3	-	-	- Thermal module (off) - Solar flux calculator (off)

These parameters include e.g., dry/wet slope, thermal conductivity and heat capacity of the soil. Identifying important physical parameters is the key towards advising which parameters are important to research more closely.

Model parameters relate to calibration factors and numerical parameters introduced in the thermo-morphological model, e.g., the interval with which XBeach is activated regardless of storms or sea ice, the number of surface nodes required to be thawed before being available for erosion, and the sea ice threshold.

Bathymetric parameters relate to the initial bed level of the modelled coastal transect. We used a schematized bathymetry, and bathymetric parameters relate to e.g., the schematized bluff height, beach slope, etc.

Level 2: For the second level, we considered different environmental drivers. This includes hydrodynamic forcing variables like waves and water levels, and thermodynamic forcing such as long- and shortwave radiation.

Level 3: For the third level, we assessed the relevance of the entire thermal model in predicting the morphological development of a permafrost coast. Additionally, we tested the impact of the solar flux calculator on upper bluff erosion.

We created other parameter settings based on the One-At-a-Time (OAT) method (Hamby, 1994). This is one of the simplest methods used in sensitivity analyses, as it varies a single parameter at a time relative to the baseline. We chose this method for its simplicity. Though nonlinear effects (i.e., compounding effects of varying multiple parameters at a time) were unaccounted for, this method provided straightforward first estimates of model sensitivity.

We tested the sensitivity of 43 parameter settings. We tested two values per parameter setting, one being lower and one being higher in comparison with the baseline simulation. We performed two additional simulations for level 3 of the sensitivity analysis, for which we disregarded the thermal module (Section 4.3) and the solar flux calculator (Section 4.3.5). Including the baseline simulation, we performed 89 simulations for this sensitivity analysis.

We attempted to use a consistent method for varying parameters for each (sub)level of the sensitivity analysis. For most parameters, we added (subtracted) twenty percent to (from) the default value in the baseline simulation. However, this strategy did not work for all parameters. For example, varying the melting temperature of water (273.15 Kelvin by default) by ten percent is highly unrealistic. Instead, we used a more realistic one percent variation. Table 5.4 provides an overview for each sub-level of how much each parameter is varied, with each exception listed. Exact parameter values are given in Figure 5.30.

The results of the three levels of sensitivity analysis are presented in the next section.

5.4.2. Results

This subsection presents the results of the sensitivity analysis. Figure 5.30 visualizes the model's total predicted erosion for different settings, ordered by total predicted erosion. Appendix H provides these same results but ordered by sub-level. We discuss the results for each level of the sensitivity analysis below.

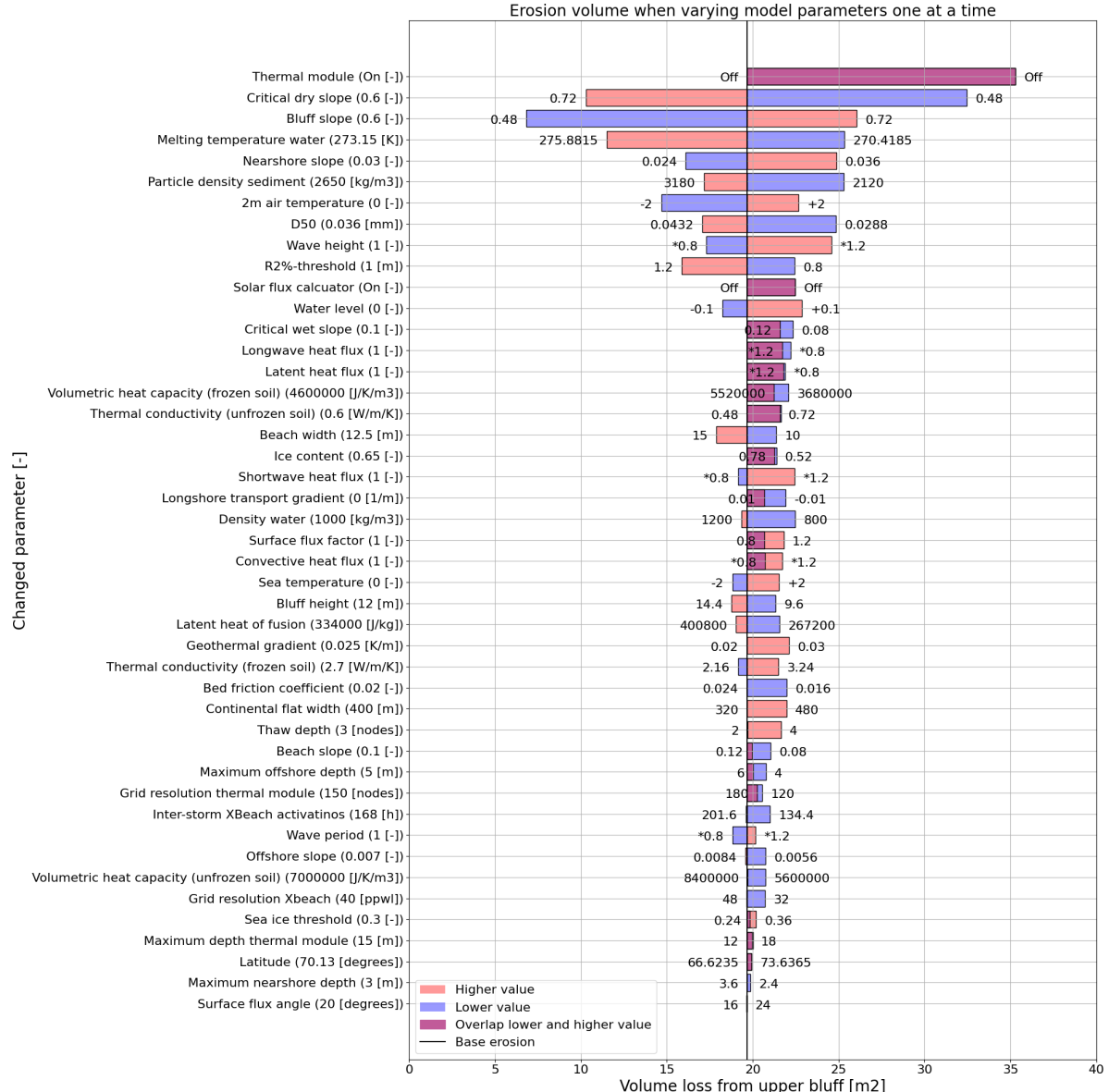


Figure 5.30: Results of the sensitivity analysis. Each bar represents the difference in volume loss from the upper bluff between the baseline simulation and simulations with different parameter settings, in descending order from most to least sensitive.

These parameter settings are either lower or higher relative to the base simulation. Parameter settings from the base simulation are shown next to their respective variable. We ordered the parameters by the sum of the absolute difference between the base simulation and the simulation with varied parameters.

Level 1: Individual Parameters

We distinguished three categories of individual parameters: physical parameters, model parameters, and bathymetry parameters.

Bathymetric parameters

Bathymetric parameters directly describe the initial bathymetry of the simulated transect. ΔV_{ub} was influenced most by the bluff slope, the nearshore slope, beach width, and bluff height (Figure 5.30). Decreasing the nearshore slope by 20% (and hence, widening the nearshore zone as the maximum nearshore depth remains constant) resulted in a similar decrease in ΔV_{ub} . Increasing the nearshore slope by that same percentage increased ΔV_{ub} by about 25%.

Though the erosion volume varies depending on the settings, the actual bluff retreat is similar for different initial conditions of the bluff (Figure 5.31). A 20% wider beach reduced ΔV_{ub} by a bit over 10%. Finally, a decrease in the height of the bluff resulted in an increase of ΔV_{ub} of over 10%. A higher bluff was slightly less vulnerable to erosion, which is consistent with Lantuit et al. (2012).

A wider beach and a lower nearshore slope (and thus wider nearshore) lead to a lower erosion volume (Figure 5.30). This is explained by the increased energy dissipation that resulted from the larger distance between the offshore wave generation and the bluff. Due to this increased energy dissipation, less erosion occurred and the run-up is generally lower. The latter means XBeach was activated less often, which further reduced ΔV_{ub} . Furthermore, an increased beach width meant that contact between the water and bluff was less frequent, which decreased ΔV_{ub} .

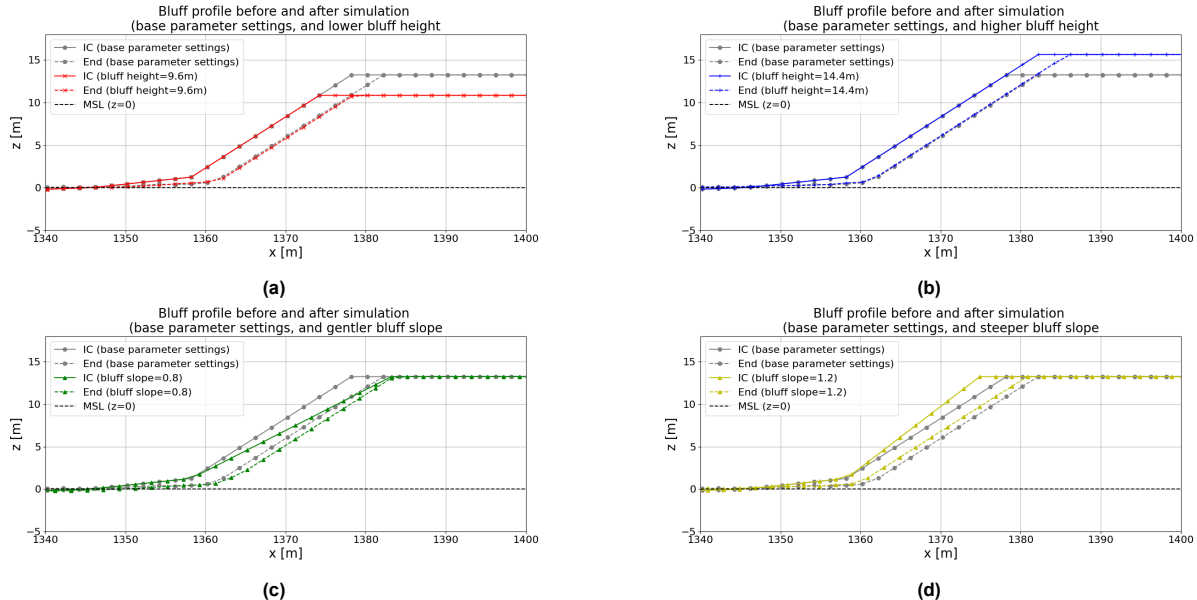


Figure 5.31: Pre- and post-simulation bathymetric transect for the baseline simulation and four other runs with different initial bluff geometry (i.e., different initial conditions for bed level): a lower and higher initial bluff height (Figure 5.31a and Figure 5.31b respectively, and a gentler and steeper initial bluff slope (Figure 5.31c and Figure 5.31d respectively).

Physical parameters

Physical parameters mainly relate to soil properties. The dry angle of repose of sediment had the largest influence on ΔV_{ub} (Figure 5.30). Increasing this critical dry slope resulted in a lower ΔV_{ub} . Other important soil properties are the particle density and the sediment diameter, and to a lesser extent the wet angle of repose, the soil's thermal conductivity, and ice content (Figure 5.30).

Both an increase and decrease in critical wet slope increased ΔV_{ub} , which indicates a local minimum. Decreasing the critical wet slope enhanced sediment transport in offshore direction by increasing avalanching in offshore direction, which increased ΔV_{ub} . The increase of ΔV_{ub} due to a higher critical wet slope can be explained by the run-up formulation used (Stockdon et al., 2006) to determine when XBeach is activated, i.e., when the predicted run-up exceeds the $R_{2\%}$ -threshold. This formulation uses the bed slope at the waterline, which depends on the critical wet slope. Increasing the critical wet

slope from 0.1 to 0.12 led to an increase in the number of XBeach activations, from 293 to 326. The decreased offshore directed avalanching (in case of a higher critical dry slope) was outweighed by the increased erosion due to the increased number of XBeach activations.

The values used for the volumetric heat capacity of frozen soil, the thermal conductivity of unfrozen soil, and the ground ice content by the baseline simulation also lead to local minima of ΔV_{ub} (Figure 5.30). The mechanisms through which changes in these parameters induced a local minimum of ΔV_{ub} are as follows:

- Increasing the volumetric heat capacity of frozen soil meant that frozen material took longer to heat up and cool down. This induced a delay in thawing at the start of summer but also delayed freezing in fall. The larger October storms gained more erosive potential due to a relative increase in active layer depth. Reducing the volumetric heat capacity effectively had the reverse effect, but increased the active layer depth during summer, leading to more erosive potential during the summer months.
- Increasing the thermal conductivity of unfrozen soil had a similar effect. A lower thermal conductivity in unfrozen soil (i.e., the upper soil layer / active layer) led to a delay in thawing and refreezing, which likely increased erosion during the fall months. Increasing the thermal conductivity deepened the active layer during the summer months, leading to an increase in ΔV_{ub} .
- Increasing the ground ice content led to a change in soil density, which directly influenced the soil's specific heat capacity. Its effects were therefore similar to changes in the volumetric heat capacity.

Additionally, increasing ice content increased the latent heat required to thaw the soil. This again led to a delay in thawing, but the increased storage of energy as latent heat also delayed the refreezing at the end of the season. Decreasing the ground ice content induced a deepening of the active layer during the season, leading to an expected increase in ΔV_{ub} . This effect was outweighed by the first process, as we do not observe a local minimum when varying the latent heat of fusion of water (Figure 5.30).

We found another local minimum of ΔV_{ub} for different values of the longshore transport gradient, though we did not perform sufficient analyses to discuss this further.

Due to the different approach we used for varying the melting temperature of water, comparing the effect of varying the melting temperature to other parameters is not possible. However, the effect of varying the melting temperature should not be understated. An increase in melting temperature led to less soil being thawed, the active layer depth being reduced, and ultimately a decrease in ΔV_{ub} . A decrease in melting temperature led to an increase ΔV_{ub} by deepening the active layer.

Increasing the latent heat of fusion (meaning more energy is needed during the thawing process) had the same effect as increasing the melting temperature, though to a lesser extent. Increasing the geothermal gradient slightly increased the heat flux at the bottom boundary, which induced a small increase in ΔV_{ub} .

The geometry of the bluff is an important factor for controlling erosion of the upper bluff (Figure 5.30). Small variations in the critical dry slope and the initial bluff slope induced large differences in erosion of the upper bluff. Part of the importance of these slopes is explained through the dependent variable that we used in the sensitivity analysis, i.e., volume loss from the upper five-meter-deep layer of the bluff (ΔV_{ub}).

If we reduced the critical dry slope, the initial slope would immediately exceed the critical slope, which led to immediate avalanching of material from the upper bluff to the bluff toe, which induced volume loss from the upper bluff. Similarly, if we increased the initial bluff slope, it would exceed the critical dry slope, again leading to avalanching and volume loss. Conversely, if we increased the critical dry slope, erosion of the bluff toe did not lead to immediate avalanching. In that case, more erosion of the bluff toe was required before avalanching started to occur, reducing the total erosion volume of the upper bluff (though not necessarily the total erosion of the entire bluff).

Model parameters

The $R_{2\%}$ -threshold, surface flux factor, and thaw threshold each affected ΔV_{ub} (Figure 5.30). Increasing

the $R_{2\%}$ -threshold led to fewer XBeach activations, which reduced erosion. Reducing the surface flux factor effectively reduced the surface heat flux for both incoming and outgoing fluxes. This means that thawing was slowed down during the warmer months, and refreezing was delayed into late fall. The active layer remained erodible during storms occurring later in the year, which enhanced erosion, similar to the effect seen with the (frozen) volumetric heat capacity, and the (unfrozen) thermal conductivity. Conversely, an enhanced surface heat flux due to an increased surface flux factor led to a deepening of the active layer during warmer months, deepening the active layer, and thereby enhancing erosion.

Furthermore, reducing the thaw threshold reduced erosion. Erosion was enhanced when fewer surface nodes were required to be frozen before the surface was treated as non-erodible. Specifically, increasing the number of nodes from three to four (thus increasing the threshold distance from 20 to 30 cm) resulted in an increase of ΔV_{ub} of approximately ten percent.

The model parameters are discussed further in Appendix I.

Level 2: Environmental Drivers

It is difficult to directly compare all environmental drivers due to the different strategies used to vary the water level, and sea- and air temperature (Table 5.4).

Varying the air temperature had a larger effect on the resulting ΔV_{ub} compared to the seawater temperature (Figure 5.30). An increase in air temperature of two degrees increased ΔV_{ub} by about 15%. Decreasing air temperature by that same amount had a larger effect, decreasing volume loss by approximately 25%. Variations in ΔV_{ub} due to changes in sea temperature were smaller. ΔV_{ub} was less sensitive to lower values of the sea temperature, but higher values did induce more erosion, likely due to increased convective heat transfer into the bluff during storm events.

In contrast with the solar radiation radiation flux which is effectively zero during the (polar) night, air temperature continuously affects the bluff through the convective heat flux at the surface. The surface ground layer reacts instantaneously to the air (and sea) temperature, as the convective flux is a function of the temperature difference at the interface of the ground and air (or sea).

The relative importance of the different surface heat fluxes on bluff erosion can be assessed (Figure 5.30). The largest control on volume loss is exerted by longwave radiation, followed by the latent heat flux, the shortwave heat flux, and the convective heat flux. The local minimum for the convective heat flux can be explained in the same way as the surface flux factor. An increase of the convective heat flux (both in and out of the soil) led to faster and deeper thawing in the warmer months, but also faster refreezing. A decrease of this flux led to a slower thawing in combination with a delayed refreeze.

The longwave and latent heat flux also show local minima with respect to the base simulation (Figure 5.30). Since these fluxes are mostly negative throughout the year, the explanation given for the convective heat flux does not apply here. This effect should be researched further.

Variations in wave period and wave height also led to small variations in eroded volume. Shorter wave periods resulted in less erosion and longer wave periods resulted in more erosion. 20% higher waves resulted in an increase of ΔV_{ub} of approximately 25%, and 20% lower waves resulted in a decrease of ΔV_{ub} by approximately 10%.

An increase in water level of 0.1 meters enhanced coastal erosion by approximately 15% (Figure 5.30). This can be attributed to three processes. Firstly, a higher water level increased run-up and thus increased the number of times the $R_{2\%}$ -threshold was exceeded, i.e., activating XBeach more often. This led to more erosion. Secondly, the higher water level allowed more wave energy to reach the coast, further increasing run-up and erosive forces on the beach. Thirdly, the increased run-up led to more convective heat transfer from water into the bluff. Since convective heat transfer from water into soil occurs on a shorter time scale in comparison to convective heat transfer from air into soil, a high run-up can lead to the rapid thawing of upper soil layers, making more sediments available for erosion in the lower bluff face.

Level 3: Thermal Module

Disregarding the thermal module resulted in an increase of ΔV_{ub} of almost 100%, (Figure 5.30). The thermal module restricted the erosion predicted by XBeach through the non-erodible layer. The budget of sediment available for erosion was lowered. Removing the thermal module resulted in higher

erosion rates, and a completely different post-simulation profile (Figure 5.32). Sediment eroded from the bluff was mainly deposited on the beach and accreted in the nearshore zone, resulting in a higher profile relative to the baseline simulation. Furthermore, disregarding the thermal module resulted in the formation of a higher and wider beach.

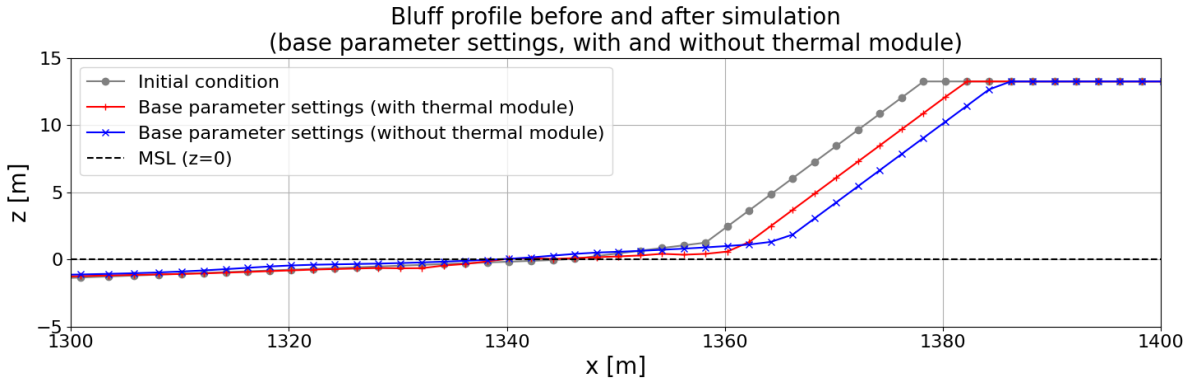


Figure 5.32: Transect showing the initial bed level and the post-simulation bed level for both the simulation with base parameter settings, with and without the thermal module.

To confirm that the thermal module restricts erosion and bluff erosion is increased when the thermal module is disregarded, the simulations done during calibration and validation of the integrated thermo-morphological model were repeated without the thermal module (Figure 5.33). When the thermal module was disregarded, the model systematically predicted a higher bluff retreat, though not as high as the results found using the calibrated parameter settings (Section 5.3.3).

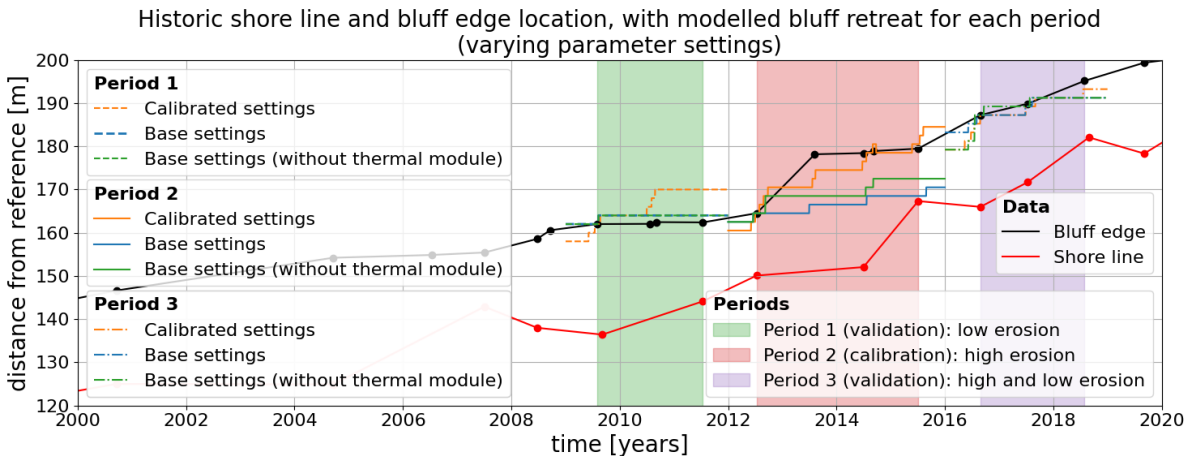


Figure 5.33: Timeseries of measured bluff and shoreline erosion used for calibration and validation of the thermo-morphological model. The three periods used for calibration and validation are highlighted. For these three periods, we performed model runs for the calibrated parameter settings (orange), the base parameter settings (blue), and the base parameter settings without the thermal module (green).

The model predicted less bluff retreat when the thermal module was active (Figure 5.33 and Figure 5.30). Additionally, the predicted erosion diminished with time without the thermal module (Figure 5.33). This is due to the wide beach that formed when the thermal module was not used (Figure 5.32). This beach formed over time and blocked most contact between the water and the bluff once wide enough.

The formation of the beach led to less frequent contact between the water and the bluff and thus a reduction in the predicted run-up. The $R_{2\%}$ was generally lower because there was no contact between the water and the bluff, which reduced the amount of XBeach activations. This effect was enhanced over time, as the beach formation could only occur when XBeach was active (i.e., during storms, when hydrodynamic conditions are generally erosive). As the beach formed, bluff erosion diminished, leading

to a predicted slowdown of bluff retreat for each of the periods used during calibration and validation (Figure 5.33).

The effect of the shortwave flux can be seen not only by directly adjusting the incoming solar radiation but also through the solar flux calculator. Disregarding the solar flux calculator resulted in approximately 15% more volume loss from the upper bluff. Disregarding this calculator means that the topography in the entire domain is assumed horizontal when computing the shortwave heat flux. In reality, parts of the domain were inclined, especially at the bluff. This effectively reduced the surface heat flux for a north-facing inclined surface when the sun is in the south, and increased the surface heat flux for the same surface when the sun is in the north. The bluff at Barter Island faces (approximately) northward at an incline of about 31°. The solar flux calculator has two main effects:

1. The bluff is covered in its own shadow around the sunset and sunrise of the polar night. The solar flux calculator takes this into account, and the influence of solar radiation on the thawing of the bluff face during spring is thus lowered by the solar flux calculator. As such, disregarding the solar flux calculator mainly leads to an increase in erosion, likely due to the early thawing of the bluff as well as delaying the refreezing at the end of the season due to an increase in shortwave surface heat flux around these times.
2. Additionally, during the polar day, solar radiation may come from the north and hit the bluff at an angle closer to perpendicular compared to the flat surface on top of the bluff. This means the solar radiation flux at the surface should be larger compared to a horizontal surface. The solar flux calculator increases the radiation flux in this case which should lead to a deepening of the active layer and a higher potential for erosion of the bluff. Conversely, disregarding the solar flux calculator should thus lead to less bluff erosion.

The first effect is dominant, as disregarding the solar flux calculator leads to an increase of ΔV_{ub} (Figure 5.30). This implies that the timing of thawing and freezing at the beginning and end of the season respectively were important in controlling erosion rates, which highlights the importance of storm timing (Ravens et al., 2023). This is discussed further in Section 6.1.3.

The exact effect of the solar flux calculator depends on latitude, bluff slope (i.e., critical dry slope), and bluff orientation. However, the result of varying these parameters with and without the solar flux calculator can not be assessed due to the method we used for this sensitivity analysis (i.e., One-At-a-Time). More simulations with different combinations of latitude, bluff slope, bluff orientation, and with/without solar flux calculator should be performed to obtain a better understanding of the influence of solar radiation on thermal denudation.

Summary

Of all tested parameters, the upper bluff erosion ΔV_{ub} predicted by the thermo-morphological model was most sensitive to changes in the following twelve parameters (in order of descending influence, with a short explanation, Figure 5.34):

- **Thermal module**

Disregarding the thermal module resulted in an almost 100% increase of volume eroded from the upper bluff (ΔV_{ub}). Without the thermal module, erosion was not constrained to the active layer and morphodynamic activity could occur for the entire soil depth.

- **Critical dry slope & Bluff slope**

The method of computation of ΔV_{ub} is sensitive to the dry slope and critical slope. Increasing the critical dry slope or decreasing the initial bluff slope resulted in more sediment that needed to be eroded from the bluff toe before avalanching could occur, which had an insulating effect on ΔV_{ub} . Conversely, decreasing the critical slope or increasing the initial bluff slope resulted in immediate avalanching at the onset of a simulation (i.e., avalanching as soon as the active layer thaws), resulting in an increase of ΔV_{ub} .

- **Melting temperature water**

Decreasing the melting temperature resulted in a deepening of the active layer (i.e., an increase of material available for erosion) which increased ΔV_{ub} . Decreasing the melting temperature resulted in less energy being required to thaw the soil and thus a deepening of the thaw depth, which facilitated more erosion.

- **Nearshore slope**

A decrease in nearshore slope effectively widened the nearshore (as the difference in depth remained the same) and thus increased the distance between the offshore boundary and the bluff. This increased distance led to more wave energy being dissipated before reaching the coast. An increase in nearshore slope had the opposite effect.

- **Particle density sediment & Mean sediment diameter (D50)**

An increased sediment particle density restricted erosive potential by requiring more wave energy to be eroded. A decrease in sediment particle density had the opposite effect. Similar results were observed when varying the mean sediment diameter.

- **2m air temperature**

Increasing the air temperature induced a higher convective heat flux into the top layer of the soil. As more energy was infused, the active layer deepened, which increased erosive potential. Furthermore, thawing occurred earlier in the year and refreezing occurred later, which widened the yearly window during which the surface soil layer was thawed. The chances of storms occurring within this window were higher, which also intensified erosion. In contrast, decreasing air temperature reduced the convective heat flux into the soil during thawing and accelerated refreezing, which reduced active layer depth and shortened the season during which erosion would occur, ultimately inducing less erosion.

- **Wave height**

Increasing the wave height led to more wave energy being transmitted to the coast which increased ΔV_{ub} . Additionally, higher wave heights were associated with a higher predicted run-up, i.e., a larger number of events during which the $R_{2\%}$ -threshold was exceeded and thus more XBeach activations, which also led to more erosion. Decreasing the offshore wave height had the opposite effect.

- **$R_{2\%}$ -threshold**

Decreasing the $R_{2\%}$ -threshold induced more XBeach activations and thus more erosion. Increasing the $R_{2\%}$ -threshold decreased the number of XBeach activations per simulation, which restricted erosion.

- **Solar flux calculator**

Disregarding the solar flux calculator increased the shortwave heat flux during the spring and fall months as the angle between the incoming rays of sunlight and the bluff was overestimated without the solar flux calculator. This accelerated thawing and delayed refreezing, which widened the yearly window during which erosion can occur. This resulted in a higher predicted ΔV_{ub} .

- **Water level**

A higher water level is associated with more wave energy being transferred to the coast and thus more coastal erosion. Furthermore, a higher water level facilitated convective heat transfer from the water directly into the bluff, which injected more energy into the soil and thus warms the soil. Finally, an increased water level leads to a higher predicted 2% run-up and thus more XBeach activations, which also increased ΔV_{ub} . This all led to an increase of ΔV_{ub} when we increased the water level. A decrease in water level had the opposite effect.

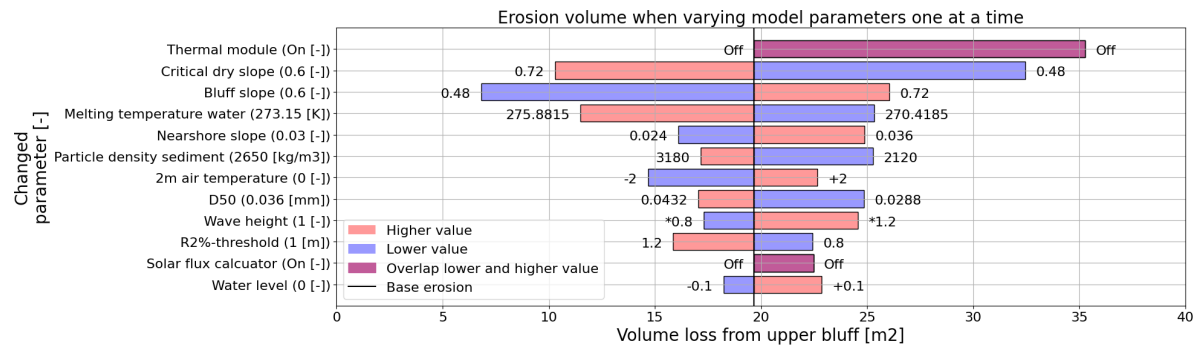


Figure 5.34: Results of the sensitivity analysis, for the top twelve most influential parameters (i.e., the parameters to which the thermo-morphological model is most sensitive with respect to bluff erosion). These parameters include the exceptions (i.e., deviations different than 20%, table 5.4), so comparisons for these should be done indirectly. Each bar shows the difference in volume loss from the upper bluff between the baseline simulation and simulations with different parameter settings, in descending order from most to least sensitive. These parameter settings are either lower or higher relative to the baseline simulation. Parameter settings from the baseline simulation are printed next to their respective variable on the left. We ordered the parameters by the sum of the absolute difference between the base simulation and the simulation with varied parameters.

6

Discussion

6.1. Climate Change

In the context of the sensitivity analysis performed in Section 5.4, we can relate climate change to four input parameters:

- Air temperature
- Sea temperature
- Water level
- Sea ice coverage

6.1.1. Air and Sea Temperature

Increases in air temperature, sea temperature, and water level are all directly associated with increased bluff erosion. Since global temperatures are expected to rise further in the future, especially in the Arctic (Ballinger et al., 2022; Chylek et al., 2022; Rantanen et al., 2022), we expect that the compounded effect of an increase in air- and sea temperature will enhance coastal erosion.

We performed three additional simulations to research the effect of air temperature on long-term (i.e., decadal) bluff erosion. Bluff erosion being larger for higher air temperatures is not only true on the time scale of single storms, but also shows long-term trends (Figure 6.1). Even though not all years result in additional erosion for higher temperatures (as erosion is still tightly coupled to specific storm timing, Section 6.1.3), increased air temperature does lead to additional bluff erosion on a decadal basis. The erosion even accelerates over time as the permafrost degrades and adjusts to the external heat forcing, which indicates that the system is out of balance.

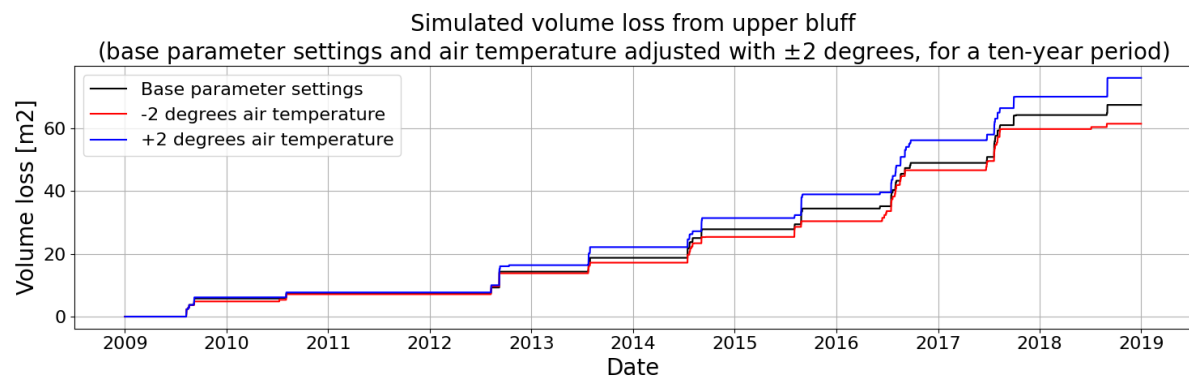


Figure 6.1: Volume loss from the upper bluff for three ten-year simulations. The first simulation employs the base parameter settings (Section 5.3.4), the second simulation adds two degrees to the air temperature, and the third simulation subtracts two degrees from the air temperature.

6.1.2. Relative Sea Level Rise

Increases in the relative sea level are associated with higher erosive potential due to more waves reaching the coast (Gibbs et al., 2019; Irrgang et al., 2022). Our sensitivity analysis reflects this, likely due to increased permafrost thawing as a result of convective heat transfer from water into the bluff, which is known to cause permafrost degradation (Sinitsyn et al., 2020; Kim et al., 2021). Furthermore, increases in relative sea level are associated with mostly thermal abrasion because more waves can reach the coast and contact between the seawater and bluff is more frequent (Gibbs et al., 2019). More frequent contact between the seawater and the bluff leads to higher erosion rates (Ravens and Peterson, 2021), which also explains the importance of the nearshore slope and beach width on the upper bluff erosion (Section 5.4.2).

Additionally, ice content is important for controlling bluff erosion (Figure 5.30). A high soil ice content means that thawing can lead to high subsidence (Günther et al., 2015; Lim et al., 2020). This thaw-induced subsidence is not included in the model, but its effect can be seen by artificially increasing the water level (i.e., increasing the relative sea level). Thaw-induced subsidence compounds with sea level rise to increase relative sea level rise, and we expect that this will further enhance coastal erosion (Horton et al., 2018).

6.1.3. Storm Intensity and Timing

The effect of single storms on the coastal morphology depends on two factors: storm intensity and storm timing.

Storm Intensity

Storm intensity relates to water level (Section 6.1), wave height, and wave period. The effect of wave height on bluff erosion (ΔV_{ub}) is larger than the effect of the wave period (Figure 5.30). This indicates that wave energy, which is proportional to the significant wave height H_s^2 and the energy period T_e (which itself is proportional to the wave period), is likely one of the main drivers of permafrost erosion, which agrees with the findings from Hume and Schalk (1967) and Gibbs et al. (2021).

Barter Island is likely subject to a combination of erosion mechanisms, i.e., thermal denudation and abrasion (Gibbs et al., 2021, Section 6.2.1). The latter is driven by the transmission of wave energy (Irrgang et al., 2022). However, the developed model does not account for thermal abrasion which might result in the erosive potential of wave power being underestimated, even though we found that variations in wave height already have a large effect on the magnitude of ΔV_{ub} .

The run-up parametrization by Stockdon et al. (2006) may partly explain the importance of the wave height and period. In this parametrization, the proportionality between predicted run-up and significant wave height is equal to the proportionality between predicted run-up and offshore wave length. Furthermore, the offshore wave length is quadratically proportional to the wave period. A first-order analysis shows that $R_{2\%} \sim \sqrt{H_s L_0} \sim \sqrt{H_s T^2} \sim \sqrt{H_s T}$. Run-up affects erosion by activating XBeach more often and increasing the convective heat transfer from the seawater into the bluff, which leads to increased thawing.

However, ΔV_{ub} is more sensitive to changes in the wave height compared to the wave period. Therefore, we expect that the wave power is dominant over the number of times XBeach is activated. To confirm this, a large number of different wave conditions should be used for hydrodynamic forcing in future research.

Storm Timing

We know that the timing of individual storms affects coastal erosion rates (Ravens et al., 2023). At the start of summer, a storm may have little effect on the coastal morphology due to the active layer still being frozen. Similarly, end-of-season storms occurring in fall also have little impact due to the refreezing of the active layer.

To research the effect of storm timing on coastal erosion, we performed two additional simulations: a simulation with a constant value of two degrees added to the air temperature, and a simulation for which we subtracted the same constant value from the air temperature (Figure 6.2). A (modelled) early-season storm occurring in late June of 2017 resulted in little bluff erosion relative to the storms occurring in July and August. Additionally, an end-of-season storm occurring in early October resulted

in relatively little to no erosion as well. This means that the bluff erosion is sensitive to storm timing, as most erosion occurs when the active layer is deepest (Brown et al., 2000; Nicolsky et al., 2017). Only storms occurring during the period within which the active layer is thawed led to erosion (Ravens et al., 2023).

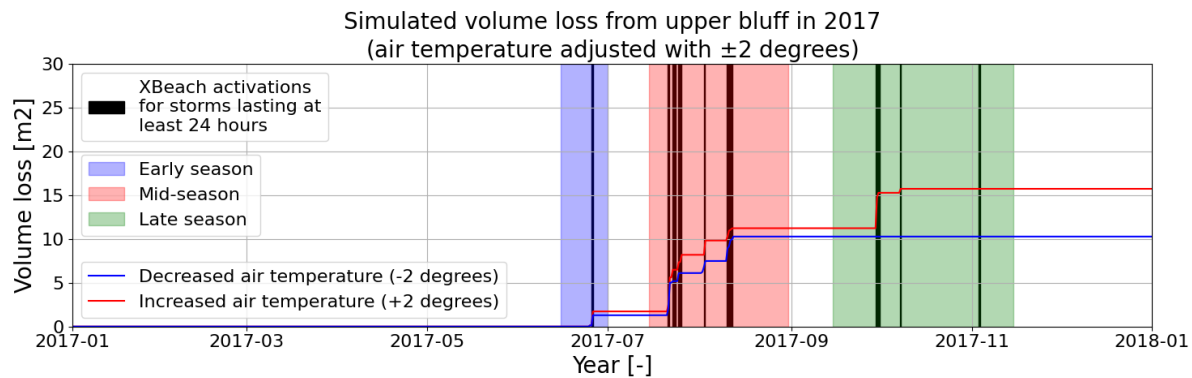


Figure 6.2: Volume loss from the upper bluff for two simulations. The first simulation adds two degrees to the air temperature, and the second simulation subtracts two degrees from the air temperature. We highlighted XBeach activations lasting 24 hours or longer (i.e., storms).

The window during which the active layer remained thawed was widened when an artificial temperature increase was added and narrowed when the air temperature was artificially reduced. If the active layer thawed earlier and refroze later in the season due to a temperature increase, both early- and late-season bluff erosion was intensified (Figure 6.2). Erosion volumes during the end-of-season storm in October 2017 and the early-season storm in July 2018 were both larger for the case with increased temperature when comparing to the simulation for which temperature was reduced. Especially the end-of-season storm resulted in much more erosion, which is in agreement with Ravens et al. (2023).

Soil properties such as thermal conductivity and ice content further control the active layer depth and the timing of thawing and refreezing (Section 5.4.2). For example, the difference in timing for refreezing of soil with an unfrozen thermal conductivity of 0.48 W/m/K versus an unfrozen thermal conductivity of 0.72 W/m/K is a few days (Figure 6.3). However, if a storm hits during this time, predicted erosion will be much larger if the soil is still thawed. The largest storms typically occur in the fall (Atkinson, 2005; Manson et al., 2005), so a small delay in refreeze may lead to a substantial increase in erosion (Ravens et al., 2023).

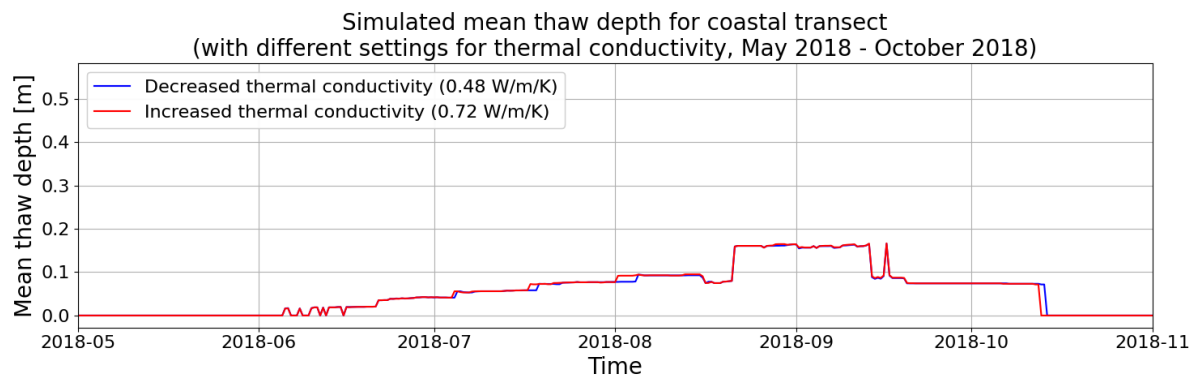


Figure 6.3: Simulated mean thaw depth for a coastal transect, for a simulation with a thermal conductivity of 0.48 W/m/K and for a simulation with a thermal conductivity of 0.72 W/m/K. The timing of complete freeze-up varies by a few days.

A deepening of the active layer due to global temperature increases will likely enhance erosion rates, which will compound with a widening of the annual window during which erosion can occur both due to the timing of thawing and freezing of the active layer (Günther et al., 2015; Lim et al., 2020) and the diminishing of yearly sea ice coverage (Barnhart et al., 2015; Box et al., 2019). The widening of this

annual window will also combine with an expected increase in storm intensity and frequency (Atkinson, 2005; Vermaire et al., 2013; Barnhart et al., 2014a; Thomson et al., 2016; Casas-Prat and Wang, 2020; Nielsen et al., 2020). This implies that the effects of climate change will further enhance erosion rates in the Arctic.

6.1.4. Future Perspectives and Societal Impact

Global warming is associated with permafrost degradation and accelerated coastal retreat in the Arctic (Irrgang et al., 2022). Without permafrost, morphological activity (i.e., erosion) is not constrained to the active layer, which facilitates increased erosion rates. The simulations that did not include the thermal module reflected this. However, these simulations also predicted a decrease in erosion rate over time as the eroded sediment ends up in the nearshore and forms a stable beach.

We do not expect this to be the case in the real world on the time scale predicted by the model (i.e., two years). Though the thermo-morphological model was able to maintain a stable beach through an artificial increase of onshore transport, it struggles with removing sediment from the nearshore. For one, the model does not currently include the bimodality that is typical for Arctic soil composition (Moore, 1961, Rex, 1964, Owens and McCann, 1970). All eroded sediment currently contributes to the sediment balance, whereas in reality the fines are transported offshore and do not contribute to the sediment balance (Rolph et al., 2022). Additionally, the single dimension (i.e., cross-shore) of the current model was not able to produce any alongshore gradient to help redistribute sediment.

For temperate coasts, we often assume that the nearshore profile will retain a constant form (Bruun, 1988). For this profile to retain its form, the bed is required to rise with the rising sea level (Bruun, 1962). Assuming that Arctic coasts are subject to similar long-term hydrodynamics and morphodynamics, we expect that the nearshore bed level will rise with the rising relative sea level. The required sediment will likely come from the beach and bluff, similar to how the shoreline supplies the sediment required to rise the bed with relative sea level rise for temperate coasts (Dean and Houston, 2016).

The warming air and sea temperatures in combination with the rising relative sea level and the diminishing sea ice in the Arctic will speed up this process of erosion and nearshore accretion (Figure 5.30). However, the bi-modality (Rolph et al., 2022) and excess ice content (O'Neill et al., 2023) of sediment means that the eroded volume is not equal to the accreted volume (Nairn et al., 1998). This increases the sediment volume that is required to be eroded to adapt to relative sea level rise. Erosion rates are likely to diminish once a stable equilibrium with a sufficiently high beach is achieved as predicted by the current model when we disregard the thermal module.

The developed model can be used to simulate a large number of coastal transects and obtain an estimate for the expected coastal retreat rate. However, not enough data on soil composition is available to obtain accurate predictions on a local scale. On a larger spatial scale, the model can be applied to obtain the estimated coastal retreat for specific coastal sections. Additionally, due to the model's (relatively) low computational cost, a large number of simulations can be performed to obtain a range of predictions for different possible soil properties, which can be used to add a probabilistic element to future predictions. These coastal retreat rates can inform the (probabilistically) mapping of permafrost degradation and potentially improve our predictive capability of carbon release along the Arctic coast (Vonk et al., 2012; Irrgang et al., 2022).

6.2. Generalizability of Thermo-morphological Model

6.2.1. Erosion Mechanism: Thermal Denudation and Thermal Abrasion

The developed thermo-morphological showed good skill in reproducing the measured coastal retreat for the validation periods. However, the model under-predicted bluff retreat for the calibration period. This is likely due to a thermal abrasion event that occurred in 2012 (Gibbs et al., 2021). There is proof of a thermal abrasion event occurring in 2008 as well (Ravens and Peterson, 2021), which coincides with a similar increase in bluff retreat rate (Figure 5.13b).

Since we calibrated the model to a period during which a thermal abrasion event occurred, the calibrated model settings do not capture the physics well (Section 5.3.4). These model settings are over-fitted to the calibration data and consistently result in high erosion, also when this is not reflected by the valida-

tion data. This is the result of low onshore transport during erosive conditions which causes the total erosion of the beach. This resulted in direct contact between the seawater and the bluff toe. Increasing onshore transport lets the model maintain a beach, though it leads to the model underestimating bluff retreat during the calibration period.

Even though yearly erosion rates are inherently tied to the timing of storms, thermal denudation is typically constrained by the slump volume available for erosion during a storm event. This makes thermal denudation more dependent on the surface heat flux and thus a long-term process. However, it is unclear to what extent the material available for erosion (i.e., the thaw slump) constrains bluff retreat and to what extent storm events govern the bluff erosion resulting from thermal denudation. In the developed model, avalanching does not occur without storm events because the bluff slope does not exceed the critical slope. Storm events are needed to remove slumped sediment, and to uncover deeper permafrost. However, more research using artificial storm events (i.e., hydrodynamic forcing conditions and storm timing) should be conducted to clarify the relative importance of storm events versus the thawing and slumping processes.

In contrast, thermal abrasion is tightly coupled with storm events. The process-based model developed for the current research was designed to model thermal denudation. In reality, Arctic coasts (such as Barter Island) can be subject to a combination of thermal denudation and thermal abrasion (Gibbs et al., 2021).

When more storms can occur within the annual window, the number of yearly storm events that result in direct contact between the water and the bluff increases (Ravens et al., 2023). This contact drives thermal abrasion (Ravens and Peterson, 2021, Ravens et al., 2023). Furthermore, if more storms can occur within this yearly window, the beach profile may change such that contact between the water and the bluff is more frequent.

Additionally, relative sea level rise is associated with more frequent contact between the seawater and the bluff (Gibbs et al., 2019), which enhances thermal abrasion (Ravens and Peterson, 2021). We agree with Gibbs et al. (2021) that a shift with respect to the dominant erosion mechanism may be possible. The relative importance of thermal abrasion with respect to thermal denudation may shift towards thermal abrasion (Gibbs et al., 2021), which may accelerate coastal retreat. Future studies should thus account for a combination of thermal denudation and thermal abrasion.

Explicitly accounting for a wave-cut niche in a permafrost bluff is not possible with a specialized model like XBeach without making significant changes in the source code. XBeach was developed to simulate hydro- and morphodynamics for temperate coastlines and uses a single bed level for each horizontal grid point (Roelvink et al., 2009). Numerically modelling the morphology of a wave-cut niche would require at least three vertical coordinates (i.e., bed, ceiling, and ground level above ceiling).

Empirical formulations such as Kobayashi (1985) could be used to keep track of niche properties without explicitly modelling the shear stresses in the bluff. Though thermal abrasion is event-driven (Ravens et al., 2023), predicting the exact moment it occurs is not necessary in the context of predicting long-term retreat rates, as long as the event occurs. Including a parametrization of thermal abrasion could enhance the predictive capability of the developed model, and it is worth researching to what extent the inclusion of a niche depth parametrization improves the model in future studies.

The model alternates the thermal module with the hydrodynamic module (i.e., XBeach) with intervals of one hour. This interval is chosen mostly based on data availability (e.g., from ERA5). However, it is unknown whether thermodynamically driven erosion of the bluff face during storms occurs on this timescale. It is recommended that the forcing data be interpolated to a finer temporal grid, and the coupling between the thermal and hydrodynamic modules be made tighter, to facilitate researching the influence of the coupling interval on bluff erosion. Since thermal denudation occurs on a longer time scale than thermal abrasion (which is more event-driven, Ravens et al., 2023), we expect that the modelling of thermal abrasion requires a relatively tighter coupling.

6.2.2. Missing Physical Parameters

Besides the coastal geometry and the resulting dominant erosion mechanism, Barter Island has a few site-specific physical parameters that may affect the generalizability of the developed model. These can

roughly be divided into two categories: sediment properties (e.g., particle density, mean diameter) and thermal properties of the soil (e.g., thermal conductivity, ice content). Though not entirely independent, these categories mostly influence the behavior of XBeach and the thermal module respectively.

We require suitable values for these parameters to be able to accurately simulate coastal transects for different locations. However, the environmental conditions in the Arctic in combination with the remote locations make data collection difficult. The presence of permafrost complicates large-scale measuring of soil properties and the harsh environment makes data collection strenuous, especially during winter.

Therefore, instead of using directly measured values for soil properties, we calibrated using some of the physical parameters with temperature data and coastal retreat data. Both modules should thus be re-calibrated and -validated when applying the thermo-morphological model to an unstudied site, as sediment properties and soil thermal properties are likely different.

Data on soil thermal properties is limited for most study sites, and large spatial variability on a local scale means that the recalibration of the thermal module is not straightforward. We recommend to calibrate the thermal module using the thermal conductivity and the ground ice content. Regardless of phase (i.e., solid or liquid), these parameters can vary over depth so using a depth-dependent distribution may provide better results (Ravens et al., 2023). Furthermore, the surface flux factor should be included to provide some control on the heat flux in and out of the soil.

Regarding the thermo-morphological model, knowledge of the critical dry slope, and the particle diameter and density should provide a good starting point for calibration (Figure 5.30). The influence of these parameters on ΔV_{ub} is much larger than that of other physical parameters. Further calibration can then be done using the XBeach factors that govern onshore transport as a result of shortwave asymmetry.

We used a critical dry slope of 0.6 for the base simulation because this value represents the measured profile well (Figure 5.7). This value is in agreement with Gibbs et al. (2019). However, as the bluff face thaws, meltwater is ejected from the bluff face and the soil may become unstable (Gibbs et al., 2019), leading to a lower critical slope. Therefore, using a lower critical slope may be beneficial to better represent the slumping process.

6.2.3. Schematization Challenges

Grid Dimensionality

Another strategy to improve model accuracy is to employ a higher-dimensional grid. This could be a two-dimensional vertical or horizontal grid or a fully three-dimensional grid. The benefit of a two-dimensional vertical grid is that employing a spatially varying grid size with spatially varying soil properties becomes much easier.

One of the difficulties of using a series of one-dimensional grids perpendicular to the ground surface is that the exact orientations and grid locations change after each morphological update. This restricts heat conservation and the implementation of spatially varying soil properties. In contrast, a spatially varying horizontal grid could benefit this model by being able to explicitly include wave direction, along-shore sediment transport, and spatial variability of soil properties in horizontal directions. Combining these two would result in a fully three-dimensional grid, which would have the best accuracy but come at the cost of a massive increase in computational costs.

An alternative could be to use a two-dimensional vertical grid and include an artificial longshore transport gradient through XBeach, which has the benefits of both a two-dimensional horizontal and vertical grid without the massive increase in the required computational resources.

We developed the thermo-morphological model for a one-dimensional transect and we assumed along-shore uniformity. We assumed that waves approached the coast perpendicularly, and we neglected any longshore sediment transport gradient. However, Figure 5.2 reveals features like barrier islands and spits typical to coasts with significant alongshore transport (gradients). This implies that longshore transport may play a non-negligible role in the morphological evolution of the Barter Island coastline, which is currently unaccounted for in the thermo-morphological model. We further discuss the relevance of alongshore variability and transport in Appendix K.

Resolution 1D Models

Especially near the soil surface boundary, large enthalpy gradients are present. These large gradients are an argument to employ a vertically varying spatial resolution. However, the ground temperature does not vary much at greater depths (Figure 5.20).

The thermo-morphological model showed skill in predicting bluff retreat even though the thermal module did not accurately reproduce measured temperatures at greater depths of, i.e., two meters or more (Figure 5.19). Therefore, the importance of accurately modelling ground temperature to a large depth is questionable as temperatures are still predicted accurately for the upper layers. The thaw depth does not extend deeper than 1 meter for the current study, similar to the results found by Ravens et al. (2023). However, a ground temperature distribution is required to obtain a thaw depth. Deeper soil layers can act as an additional heat sink (Matsumura and Yamazaki, 2012), thereby delaying the thawing of the surface.

Whether or not this heat sink is important on the time scale of thermal denudation should be researched by verifying that large variations in initial soil temperature of deeper layers indeed affect erosion rates. If this is not the case, we can safely omit the modelling of temperature for greater depths in the context of simulating the morphology of a thermal denudation-affected coastline.

Furthermore, this would imply that using a high resolution both near the surface and at greater depths might be a waste of computational resources. Instead, we recommend to increase the grid resolution near the surface and reduce grid resolution at greater depths. This would also allow for a better calibration of the thaw depth threshold, which governed at which thickness an ice sheet layered over a thawed soil would block erosion from occurring.

Currently, the additional computation time resulting from accurately modelling deeper layers is not an issue. However, employing a higher dimensional grid would increase computation time by modelling deeper layers. We discuss the trade-off of computation time and accurately modelling temperature for deeper soil layers further in Appendix J.

Heat Conservation

There are several ways to potentially improve the thermal module. Firstly, each one-dimensional enthalpy module currently employs a first-order-accurate finite difference method to discretise the enthalpy equation (Equations 4.2 and 4.3). However, higher-order methods exist which could provide more accurate results. More importantly, the finite difference method does not obey conservation laws. This might explain the under-prediction of soil temperature for deeper layers.

Alternatively, the finite volume method can be considered. Finite volume methods have been applied in various fields and could be beneficial in this application due to their ability to adhere to conservation laws like heat conservation (Eymard et al., 2000). Especially near the surface boundary, large enthalpy gradients are present, which are likely not described correctly when heat conservation is not enforced.

Enthalpy Formulation

We assumed isothermal phase change (Figure 4.3). The associated formulation is discontinuous (Equation 4.4), which manifests in the behavior of the one-dimensional thermal models.

A frozen grid cell cannot rise in temperature above the melting point without overcoming the barrier of latent heat. Since the thermal models are one-dimensional, a cell at the thaw interface blocks almost all heat transport to deeper layers, which delays thawing.

In reality, the interface between the solid and liquid phases is not as clear-cut. However, methods that account for a more realistic phase transition (e.g., Voller et al., 1987) quickly become too complex to apply on a large scale. Therefore, small-scale tests with more complex formulations should be conducted to compare with the discontinuous enthalpy formulation used in the current research to assess the accuracy of the current method. Further research into different formulations should be conducted to potentially find more suitable formulations.

6.2.4. Opportunities for Improved Calibration and Validation

We calibrated and validated the thermo-morphological model for a coastal setting with a narrow beach ($O(10)$ meters) with a moderately high bluff ($O(10)$ meters), an ice content of around 0.65, and bluff

retreat rates of $O(1 - 5)$ meter/year. The model was able to maintain the (geometric) beach properties (when the thermal module is active), indicating that it is morphologically stable for and applicable to similar coasts.

However, there is large variability in the Arctic regarding physical parameters like ice content and coastal geometry (Lantuit et al., 2012). Especially in the US Beaufort Sea area (where Barter Island is located), ice content and coastal change rates range between 0.05 to 0.60, and -10 to +12 meters per year (erosion and accretion respectively). Globally, bluff elevations can reach over 100 meters. Such extreme values were not tested for this research, and applying this model to such a coastline should be done with care.

Furthermore, high variability in soil properties like ice content means that the thermal module should be re-calibrated using local data for applications to different study sites. Additionally, further validation is required when applying this model to sites with significantly different coastal geometries. Finally, we developed the thermo-morphological model to reproduce the process of thermal denudation, and the model should not be applied in its current state to coastlines where thermal abrasion (Section 2.3) is the dominant erosion mechanism.

So far, Barter Island has been studied as one of the sites where thermal denudation occurs and which has sufficient data available (Gibbs et al., 2021). However, Barter Island is likely subject to a combination of erosion mechanisms, including thermal abrasion (Gibbs et al., 2019; Gibbs et al., 2021). We recommend that the model be validated for a different case study where it is known that thermal denudation is the prevailing erosion mechanism, e.g., Foggy Island Bay (Ravens et al., 2023).

Additionally, we validated the thermal module for a horizontal surface only. However, inclined surfaces are potentially more relevant in the context of thermal denudation, as the slumping process is governed by the active layer depth in an inclined coastal bluff. Timeseries of ground temperature do exist for coastal bluffs at Barter Island (Li Erikson, personal communication), and these timeseries provide an excellent opportunity for more extensive validation of the thermal module and the solar flux calculator.

Due to limited resources, the calibration and sensitivity analysis of the developed model did not include the full parameter space. We recommend that the calibration effort be extended with a larger set of parameter settings, and possibly applied to a different case study.

The sensitivity analysis can be extended by testing a more complete parameter space to include possible nonlinear effects that only occur when varying multiple parameters for a single simulation. For example, varying the latitude in combination with the bluff angle and the critical dry slope may enhance shortwave heat transfer in the coastal bluff (when the solar flux calculator is included). Similarly, we did not explicitly research the compounded effect of increasing the water level, and air- and sea temperatures in the same simulation. It is unrealistic to perform a sensitivity analysis of the full parameter space, but future research can include these kinds of engineered parameter combinations to obtain more insight in the specific coastal processes that ultimately govern thermal denudation.

7

Conclusions and Recommendations

7.1. Conclusions

Large sections of the world's coastline consist of permafrost, most of which are experiencing increasing erosion rates. The effects of climate change will likely further enhance erosion rates, and being able to quantitatively predict coastal erosion is required to facilitate policy-making and strategic coastal management (Irrgang et al., 2022). However, there is a lack of long-term predictive capability of morphodynamics for Arctic coastlines. This results in a knowledge gap regarding the coastal processes inducing permafrost erosion, and how these will change under the effects of climate change. This problem gave rise to the following main research questions:

How can the morphodynamics of permafrost coastlines be efficiently modelled at seasonal to yearly time scales to inform the analysis of climate change impacts?

Ravens et al. (2017) developed a process-based coupled thermal and coastal morphology model based on XBeach (Roelvink et al., 2009), called 'Arctic XBeach'. The current study decoupled this model and implemented a flexible Python wrapper to facilitate the analysis of longer periods (years to decades), which is a prerequisite for simulating the effects of climate change on Arctic morphology. Specifically, we developed the model to simulate the process of thermal denudation. We simulated thawing using a thermal module to predict which part of the domain was frozen and thus non-erodible, and we employed the XBeach model as a coastal morphodynamic and hydrodynamic model to simulate slumping and offshore transport. This allowed us to simulate the process of thermal denudation, which is the dominant erosion mechanism that leads to coastal bluff retreat at Barter Island.

We validated the thermal module using ground temperature data from Barter Island (Alaska). The thermal module showed good skill in predicting the ground temperature of upper soil layers. We further calibrated and validated the integrated model using bluff retreat data from Barter Island. The lack of data limited calibration, but the model was able to predict the correct order of magnitude of bluff retreat. However, the calibrated parameter settings that led to the best prediction of bluff retreat also resulted in beach erosion until the permafrost bluff toe was completely submerged. Different parameter settings allowed the retention of the beach but led to an under-prediction of bluff retreat, which we linked to an incident of thermal abrasion occurring that was not accounted for by the model. We developed the model to reproduce the process of thermal denudation, and the model showed good skill in predicting coastal retreat for coasts affected by thermal denudation, though it should not be applied in its current state to coastlines where thermal abrasion is the dominant erosion mechanism.

7.1.1. Key Findings

We performed a sensitivity study using the thermo-morphological model. From this study, we identified potential calibration parameters that exert large control on coastal bluff erosion. In case of a lack of data, physical constants such as the critical slope, soil thermal conductivity, and ground ice content should be used for calibration in future studies. Additionally, we introduced new parameters which we calibrated and are less site-variant (Appendix F).

We identified important environmental drivers of permafrost bluff erosion. These drivers are air temperature and (sea) water level. Increasing air temperature enhanced convective heat transfer between the bluff and the air, which increased the depth of the active layer and increased the sediment budget available for erosion. A higher water level led to an increase in bluff erosion by increasing convective heat transfer from water into the bluff and allowing more wave energy to reach the coast. Climate change is associated with both higher temperatures (especially in the Arctic) and higher water levels and is thus expected to enhance coastal erosion at Barter Island. Furthermore, we hypothesize that the changes in environmental drivers related to climate change may result in a relative shift in dominant erosion mechanism, from thermal denudation to thermal abrasion.

We showed that storm timing is an important factor in determining the erosive potential of any given storm. A storm that occurs in June before the coastal sediments are thawed has a limited effect on the coastal morphology. Similarly, storms occurring in late October after the refreezing of the soil also lead to limited erosion. Due to the effects of climate change, yearly sea ice coverage in the Arctic is declining. The widening of the annual window during which bluff erosion can occur will likely result in enhanced coastal erosion.

We found that bluff erosion is sensitive to the bluff slope and height, the nearshore slope, and the beach width. The model was able to maintain the (geometric) beach properties (when the thermal module was active), indicating that it is morphologically stable for and applicable to similar coasts. However, the large global variability in both coastal geometry and soil composition means that the model should be re-calibrated and validated before being applied to a different study site.

Though further calibration is required, the developed model can be used as a tool to research the quantitative effects of climate change on Arctic coastlines. From that, we will obtain a deeper understanding of how climate change affects the processes that ultimately lead to the erosion of permafrost bluffs. Furthermore, the rapid computation speeds mean the model can be applied to predict coastal erosion among larger regions, potentially benefiting the mapping of organic carbon released through permafrost degradation.

7.2. Recommendations

7.2.1. Model Improvements

Thermal Abrasion

We developed the thermo-morphological model to simulate thermal denudation and it currently does not include the thermal abrasion erosion mechanism (Section 2.3). The latter mechanism is associated with higher erosion rates (Ravens et al., 2023). In reality, Arctic coastlines are often subject to a combination of thermal denudation and thermal abrasion (e.g., Gibbs et al., 2021), and the relative importance can be assessed using the coarse sediment aerial density (Ravens and Peterson, 2021). In order to accurately predict long-term coastal retreat, the thermal abrasion process should be accounted for (Section 5.3.4).

Thermal abrasion can be included explicitly by modelling the shear stresses in the coastal bluff (e.g., Frederick et al., 2021). However, the associated computational costs severely limit simulation time. Instead, we propose that a parametrization of the thermo-erosional niche should be included (e.g., Kobayashi, 1985).

Thermal abrasion often occurs along ice wedges (Ravens et al., 2023), which are highly spatially variable on a local scale and difficult to measure for larger coastal sections. This makes the exact date and location of a block collapse hard to predict. Therefore, a parametrization that predicts an average coastal retreat based on the thermal abrasion mechanism, but does not rely on explicit block failure to occur, will still benefit the prediction of long-term (decadal) coastal retreat rates.

XBeach Threshold

The developed model alternates a thermal module with XBeach. For each simulated time step, the model performs a check to see if it should activate XBeach for the current time step. Whether XBeach is activated or not, is determined by the predicted 2% run-up through a threshold value. The predicted run-up is computed through the formulation by Stockdon et al. (2006), which uses the offshore wave

conditions and the nearshore bed slope to compute a prediction for the two-percent run-up. If this prediction is larger than some threshold value, XBeach is activated.

Considering the erosion mechanism of thermal denudation (i.e., sediments slump down from the bluff face and are removed from the bluff toe during storms), a logical threshold value would be the bluff toe. In that case, a consistent method to track the location of the toe over longer time periods should be applied, e.g., the second derivative method (Diamantidou et al., 2020; van IJzendoorn et al., 2021). We recommend that future studies implement the second derivative method to dynamically track the bluff toe and update the threshold used for the 2% run-up accordingly.

The sensitivity of the model to the run-up formulation can be assessed by using different combinations of wave conditions and determining the relative influence of wave height and wave period (Section 6.1.3). We recommend to try different formulations for the run-up and use different methods to determine the wet domain, to verify that the model is not overly sensitive to the current implementation.

Salinity

We did not account for salinity in the current implementation of the thermo-morphological model. However, its importance can be seen through three different variables:

- melting temperature water,
- latent heat of fusion,
- water density.

These three properties are different for saline water and fresh water. Specifically, the melting temperature is lower, the latent heat of fusion is lower, and the water density is higher, with the former two leading to increased bluff erosion (Figure 5.30).

Seawater comes into direct contact with the bluff during an event with a high total water level. The rapid convective heat transfer of water may then result in the rapid thawing of the lower bluff face and induce slumping. The saline seawater enhances this effect by reducing the melting temperature and the latent heat of fusion required for thawing. By adjusting the model parameters described above to reflect (exaggerated) saline conditions, we showed the importance of salinity on the retreat of the bluff.

Bi-modal Sediment

Arctic coastlines are often characterized by a bi-modality of sediment (Moore, 1961, Rex, 1964, Owens and McCann, 1970). The current model implementation only uses a single sediment fraction with a mean diameter of 0.036 millimeters, which corresponds with coarse silt. Mean sediment diameter exerts a large control on bluff erosion (Figure 5.30).

In reality, the fine sediment fraction is lost offshore during storms and does not significantly contribute to the nearshore sediment balance, whereas the larger sediment fraction does contribute to the sediment balance (Rolph et al., 2022). Furthermore, the current implementation does not account for the cohesive properties of fine sediment. It is recommended that future research studies determine the extent to which modelling bi-modal sediment is possible.

Subsidence

We found that a rise in water level will likely lead to an increase in bluff erosion (Irrgang et al., 2022), which indicates that thaw-induced subsidence may play a major role under the effects of global warming and sea level rise, and should be accounted for in future studies. To accurately model thaw-induced subsidence, a groundwater model should be established, which should account for both meltwater and rain/snow. Including snow may prove challenging, as it insulates the soil below, affects albedo, and leads to runoff that affects the critical slope of sediments in the bluff (Zhang, 2005).

Additionally, salt intrusion may lead to significant subsurface thawing (Guimond et al., 2021), which is a process not included here. Thawing of permafrost is known to cause subsidence, which effectively lowers the bluff height (or increases the relative sea level) which may result in higher bluff erosion rates (Figure 5.30). Lantuit et al. (2012) found similar results, with lower bluffs generally being subject to higher erosion rates. Simulating the subsidence resulting from thawing will improve the models ability to predict the coastal morphology.

7.2.2. Data Collection Priorities

To improve the model's predictive capability, reliable data should be collected on soil characteristics, coastal topography, and environmental drivers. Additionally, ground temperature measurements are key in defining initial conditions and calibrating/validating the thermal module. However, the environmental conditions in the Arctic in combination with the remote locations make data collection strenuous. The presence of permafrost complicates the large-scale measuring of soil properties and the harsh environment makes data collection strenuous, especially during winter.

Our research provides a first indication of which parameters are the most important to collect detailed data on (Figure 5.30). Regarding coastal characteristics, the bluff geometry and sediment diameter are the most important controls on bluff erosion. Though measuring soil properties is difficult on a large scale, soil samples can be taken and studied with relative ease. Particle density, sediment diameter, and ice content can each be derived from a soil sample. Furthermore, bluff geometry can be obtained with relatively simple instruments like a camera. Some larger scale features, e.g., beach width and coastline position, can be obtained through remote sensing (e.g., Gibbs et al., 2021). Due to the relative simplicity and low costs of measuring sediment properties and bluff characteristics, and their important role in coastal retreat, we recommend that these features be selected for data collection.

An added benefit of taking soil samples is that they can be used to assess the relative importance of different erosion mechanisms (i.e., thermal denudation and thermal abrasion, Section 2.3). Ravens and Peterson (2021) developed a method for predicting the dominant erosion mechanism based on the coarse sediment aerial density. The dominant erosion mechanism determines the coastal retreat rate to a large extent, and knowing which erosion mechanism prevails is key in determining which model should be employed to predict retreat rates.

7.2.3. Practical Applications

An advantage of using a one-dimensional shore-normal model is that its computations are relatively cheap in comparison with a multi-dimensional model. This means that the developed model can be used for large domains. Since the model is able to predict the order of magnitude of coastal erosion retreat, it will be beneficial to use this model to gain first-order estimates of coastal retreat among coastlines of larger regions. Additionally, rapid computations mean that a large number of simulations can be performed, which facilitates probabilistic research. This will benefit policy-making and climate research.

Currently, global climate models do not account for the carbon emissions that result from the erosion of a permafrost-affected coastline (Nielsen et al., 2022). Due to the model's ability to estimate the order of magnitude of coastal retreat, it may help map the release of organic carbon through permafrost degradation among Arctic coastlines, thereby improving future predictions of organic carbon release and benefiting the quality of global projections of climate change.

7.2.4. Future Research Directions

One of the main benefit of the current (process-based) model is that it facilitates the detailed investigation of different parts of the thermal denudation process. For example, the influence of the thaw slump on the temperature distribution within the permafrost bluff can be researched. The high relative temperature of the thaw slump (in combination with salt intrusion) may lead to additional thawing in the bluff face (Ferdinand Oberle, personal communication). This effect can be investigated using the developed model.

The developed thermo-morphological model shows good skill in predicting coastal bluff retreat on a time scale of three to four years while maintaining a low computational cost. It can thus be used to predict bluff retreat for a large number of coastal transects. This benefits the quantitative prediction of greenhouse gasses released through permafrost degradation (Vonk et al., 2012), which will improve the future predictions made by global climate models (Irrgang et al., 2022). The potential of this model for benefiting global climate models should be explored further in future research.

While we developed the thermo-morphological model to simulate the erosion of permafrost bluffs, other areas may also benefit from including soil temperature in coastal hydrodynamic models. Specifically, Hawkes et al. (2009) found that sand temperature influences the nesting behavior of sea turtles. The

thermal profiles of beaches are changing due to the effects of urbanization and global warming (Ariano-Sánchez et al., 2023). Although the specific relation between nest site selection and sand temperature is not well understood (Christiaanse et al., 2024), we know that sand temperature affects the primary sex distribution among hatchlings (Hawkes et al., 2009). Christiaanse et al. (2024) have identified potential breeding grounds on a global scale and using these breeding grounds as a starting point, more localized assessments can be done using the developed model.

References

- Abbott, B. W., & Jones, J. B. (2015). Permafrost collapse alters soil carbon stocks, respiration, CH₄, and N₂O in upland tundra. *Global Change Biology*, 21(12), 4570–4587. <https://doi.org/10.1111/gcb.13069> (cit. on p. 15).
- Ahmad, N., Bihs, H., Chella, M. A., Kamath, A., & Arntsen, □. A. (2019). CFD Modeling of Arctic Coastal Erosion due to Breaking Waves. *International Journal of Offshore and Polar Engineering*, 29(01), 33–41. <https://doi.org/10.17736/ijope.2019.ak31> (cit. on pp. 8, 16).
- Are, F., Reimnitz, E., Grigoriev, M., Hubberten, H.-W., & Rachold, V. (2008). The influence of cryogenic processes on the erosional Arctic shoreface. *Journal of Coastal Research*, 24(1), 110–121. <https://doi.org/10.2112/05-0573.1> (cit. on pp. 7, 8, 17).
- Ariano-Sánchez, D., Nesthus, A., Rosell, F., & Reinhardt, S. (2023). Developed black beaches - too hot to emerge? Factors affecting sand temperatures at nesting grounds of olive ridley sea turtles (*Lepidochelys olivacea*). *Climate Change Ecology*, 5, 100074. <https://doi.org/10.1016/j.ecochg.2023.100074> (cit. on p. 80).
- Aré, F. (2003). Shoreface of the Arctic seas – a natural laboratory for subsea permafrost dynamics (cit. on p. 8).
- Aré, F. E. (1988, January). Thermal abrasion of sea coasts (part I) [Archive Location: world Publisher: Taylor & Francis Group]. <https://doi.org/10.1080/10889378809377343> (cit. on p. 10).
- Atkinson, D. (2005). Observed storminess patterns and trends in the circum-Arctic coastal regime. *Geo-Marine Letters*, 25, 98–109. <https://doi.org/10.1007/s00367-004-0191-0> (cit. on pp. 1, 8, 70, 71).
- Ballinger, T. J., Overland, J. E., Wang, M., Walsh, J. E., Brettschneider, B., Thoman, R. L., Bhatt, U. S., Hanna, E., Hanssen-Bauer, I., & Kim, S. J. (2022). Surface Air Temperature. <https://doi.org/10.25923/13QM-2576> (cit. on pp. 13, 68).
- Baranskaya, A., Novikova, A., Shabanova, N., Belova, N., Maznev, S., Ogorodov, S., & Jones, B. M. (2021). The Role of Thermal Denudation in Erosion of Ice-Rich Permafrost Coasts in an Enclosed Bay (Gulf of Kruzenstern, Western Yamal, Russia). *Frontiers in Earth Science*, 8. Retrieved March 3, 2024, from <https://www.frontiersin.org/articles/10.3389/feart.2020.566227> (cit. on pp. 10, 13).
- Barnhart, K. R., Overeem, I., & Anderson, R. S. (2014a). The effect of changing sea ice on the physical vulnerability of Arctic coasts. *The Cryosphere*, 8(5), 1777–1799. <https://doi.org/10.5194/tc-8-1777-2014> (cit. on pp. 5, 7–9, 14, 17, 71).
- Barnhart, K., Miller, C., overeem, i., & Kay, J. (2015). Mapping the future expansion of Arctic open water. *Nature Climate Change*, 6. <https://doi.org/10.1038/nclimate2848> (cit. on pp. 14, 70).
- Barnhart, K. R., Anderson, R. S., Overeem, I., Wobus, C., Clow, G. D., & Urban, F. E. (2014b). Modeling erosion of ice-rich permafrost bluffs along the Alaskan Beaufort Sea coast. *Journal of Geophysical Research: Earth Surface*, 119(5), 1155–1179. <https://doi.org/10.1002/2013JF002845> (cit. on pp. 1, 10, 16, 18).
- Bauch, D., Hoelemann, J., Nikulina, A., Wegner, C., Janout, M., Timokhov, L., & Kassens, H. (2013). Correlation of river water and local sea-ice melting on the Laptev Sea shelf (Siberian Arctic). *Journal of Geophysical Research: Oceans*, 118, 550–561. <https://doi.org/10.1002/jgrc.20076> (cit. on p. 9).
- Bendixen, M., & Kroon, A. (2017). Conceptualizing delta forms and processes in Arctic coastal environments. *Earth Surface Processes and Landforms*, 42(8), 1227–1237. <https://doi.org/10.1002/esp.4097> (cit. on p. 9).
- Booij, N., Holthuijsen, L., & Ris, R. The "Swan" Wave Model for Shallow Water. en. In: In *Coastal Engineering 1996*. Orlando, Florida, United States: American Society of Civil Engineers, 1997, August, 668–676. ISBN: 978-0-7844-0242-9 978-0-7844-7951-3. <https://doi.org/10.1061/9780784402429.053> (cit. on p. 39).

- Box, J. E., Colgan, W. T., Christensen, T. R., Schmidt, N. M., Lund, M., Parmentier, F.-J. W., Brown, R., Bhatt, U. S., Euskirchen, E. S., Romanovsky, V. E., Walsh, J. E., Overland, J. E., Wang, M., Corell, R. W., Meier, W. N., Wouters, B., Mernild, S., Mård, J., Pawlak, J., & Olsen, M. S. (2019). Key indicators of Arctic climate change: 1971–2017 [Publisher: IOP Publishing]. *Environmental Research Letters*, 14(4), 045010. <https://doi.org/10.1088/1748-9326/aafc1b> (cit. on pp. 14, 70).
- Brady, M., & Leichenko, R. (2020). The impacts of coastal erosion on Alaska's North Slope communities: A co-production assessment of land use damages and risks. *Polar Geography*, 43, 1–21. <https://doi.org/10.1080/1088937X.2020.1755907> (cit. on pp. 1, 15).
- Brimmer, E. D. (2023). Changing Geopolitics in the Arctic (cit. on p. 15).
- Brown, J., Hinkel, K. M., & Nelson, F. E. (2000). The circumpolar active layer monitoring (calm) program: Research designs and initial results 1 [Publisher: Taylor & Francis Group]. *Polar Geography*. <https://doi.org/10.1080/10889370009377698> (cit. on pp. 8, 70).
- Bruun, P. (1962). Sea-Level Rise as a Cause of Shore Erosion. *Journal of the Waterways and Harbors Division*, 88(1), 117–130. <https://doi.org/10.1061/JWHEAU.0000252> (cit. on p. 71).
- Bruun, P. (1988). The bruun rule of erosion by sea-level rise: A discussion on large-scale two- and three-dimensional usages. *Journal of Coastal Research*, 4(4), 627–648. Retrieved January 10, 2025, from <http://www.jstor.org/stable/4297466> (cit. on p. 71).
- Buffo, J., Fritsch, L. J., & Murphy, J. L. (1972). DIRECT SOLAR RADIATION ON VARIOUS SLOPES FROM 0 TO 60 DEGREES NORTH LATITUDE. 142 (cit. on pp. 7, 30).
- Bull, D., Bristol, E., Brown, E., Choens, R., Connolly, C., Flanary, C., Frederick, J., Jones, B., Jones, C., Ward Jones, M., McClelland, J., Mota, A., & Tezaur, I. (2020, September). *Arctic Coastal Erosion: Modeling and Experimentation* (tech. rep. No. SAND–2020-10223, 1670531, 691093). <https://doi.org/10.2172/1670531> (cit. on pp. 1, 16, 18).
- Burkardt, J. (2012). Arctic XBeach: FD1D_heat_explicit. (Cit. on p. 27).
- C3S. (2018). ERA5 hourly data on single levels from 1940 to present. <https://doi.org/10.24381/CDS. ADBB2D47> (cit. on p. 117).
- Cao, B., Gruber, S., Zheng, D., & Li, X. (2020). The ERA5-Land soil temperature bias in permafrost regions [Publisher: Copernicus GmbH]. *The Cryosphere*, 14(8), 2581–2595. <https://doi.org/10.5194/tc-14-2581-2020> (cit. on p. 38).
- Carrión-Bertran, N., Falqués, A., Ribas, F., Calvete, D., de Swart, R., Durán, R., Marco-Peretó, C., Marcos, M., Amores, A., Toomey, T., Fernández-Mora, □., & Guillén, J. (2024). Role of the forcing sources in morphodynamic modelling of an embayed beach. *Earth Surface Dynamics*, 12(3), 819–839. <https://doi.org/10.5194/esurf-12-819-2024> (cit. on p. 101).
- Carvalho, K. S., & Wang, S. (2020). Sea surface temperature variability in the Arctic Ocean and its marginal seas in a changing climate: Patterns and mechanisms. *Global and Planetary Change*, 193, 103265. <https://doi.org/10.1016/j.gloplacha.2020.103265> (cit. on p. 13).
- Casas-Prat, M., Wang, X. L., & Swart, N. (2018). CMIP5-based global wave climate projections including the entire Arctic Ocean. *Ocean Modelling*, 123, 66–85. <https://doi.org/10.1016/j.ocemod.2017.12.003> (cit. on p. 17).
- Casas-Prat, M., & Wang, X. L. (2020). Projections of Extreme Ocean Waves in the Arctic and Potential Implications for Coastal Inundation and Erosion. *Journal of Geophysical Research: Oceans*, 125(8), e2019JC015745. <https://doi.org/10.1029/2019JC015745> (cit. on pp. 14, 71).
- Christiaanse, J. C., Antolínez, J. A. A., Luijendijk, A. P., Athanasiou, P., Duarte, C. M., & Aarninkhof, S. (2024). Distribution of global sea turtle nesting explained from regional-scale coastal characteristics [Publisher: Nature Publishing Group]. *Scientific Reports*, 14(1), 752. <https://doi.org/10.1038/s41598-023-50239-5> (cit. on p. 80).
- Chylek, P., Folland, C., Klett, J. D., Wang, M., Hengartner, N., Lesins, G., & Dubey, M. K. (2022). Annual Mean Arctic Amplification 1970–2020: Observed and Simulated by CMIP6 Climate Models. *Geophysical Research Letters*, 49(13), e2022GL099371. <https://doi.org/10.1029/2022GL099371> (cit. on pp. 13, 68).
- Coco, A., Currenti, G., Negro, C. D., & Russo, G. (2014). A Second Order Finite-Difference Ghost-Point Method for Elasticity Problems on Unbounded Domains with Applications to Volcanology. *Communications in Computational Physics*, 16(4), 983–1009. <https://doi.org/10.4208/cicp.210713.010414a> (cit. on p. 28).

- Couture, N. J., Irrgang, A., Pollard, W., Lantuit, H., & Fritz, M. (2018). Coastal Erosion of Permafrost Soils Along the Yukon Coastal Plain and Fluxes of Organic Carbon to the Canadian Beaufort Sea. *Journal of Geophysical Research: Biogeosciences*, 123(2), 406–422. <https://doi.org/10.1002/2017JG004166> (cit. on p. 15).
- Cox, D. T., Kobayashi, N., & Okayasu, A. (1996). Bottom shear stress in the surf zone. *Journal of Geophysical Research: Oceans*, 101(C6), 14337–14348. <https://doi.org/10.1029/96JC00942> (cit. on p. 30).
- Dawson, J., Johnston, M., & Stewart, E. (2017). The unintended consequences of regulatory complexity: The case of cruise tourism in Arctic Canada. *Marine Policy*, 76, 71–78. <https://doi.org/10.1016/j.marpol.2016.11.002> (cit. on p. 15).
- Dawson, T., Nimura, C., Lopez-Romero, E., Daire, M.-Y., & Jensen, A. M. (2018, January). *Public archaeology and climate change*. OXBOW BOOKS. (Cit. on p. 15).
- de Ridder, M. (2023). XBeach Python toolbox — XBeach toolbox 2023 documentation. Retrieved May 24, 2024, from <https://xbeach-toolbox.readthedocs.io/en/latest/index.html> (cit. on p. 26).
- Dean, R. G., & Houston, J. R. (2016). Determining shoreline response to sea level rise. *Coastal Engineering*, 114, 1–8. <https://doi.org/10.1016/j.coastaleng.2016.03.009> (cit. on p. 71).
- Dean, R., & Dalrymple, R. (2004). Coastal Processes With Engineering Applications. *Coastal Processes with Engineering Applications*, by Robert G. Dean and Robert A. Dalrymple, pp. 487. ISBN 0521602750. Cambridge, UK: Cambridge University Press, March 2004. (cit. on p. 16).
- Diamantidou, E., Santinelli, G., Stronkhorst, J., & Vries, S. (2020). An Automatic Procedure for Dune Foot Position Detection: Application to the Dutch Coast. *Journal of Coastal Research*, 36, 668. <https://doi.org/10.2112/JCOASTRES-D-19-00056.1> (cit. on p. 78).
- Dmitrenko, I. A., Kirillov, S. A., Tremblay, L. B., Kassens, H., Anisimov, O. A., Lavrov, S. A., Razumov, S. O., & Grigoriev, M. N. (2011). Recent changes in shelf hydrography in the Siberian Arctic: Potential for subsea permafrost instability. *Journal of Geophysical Research: Oceans*, 116(C10). <https://doi.org/10.1029/2011JC007218> (cit. on pp. 1, 13).
- Dobinski, W. (2011). Permafrost. *Earth-Science Reviews*, 108(3), 158–169. <https://doi.org/10.1016/j.earscirev.2011.06.007> (cit. on p. 5).
- Doré, G. (2004). Development and Validation of the Thaw-weakening Index. *International Journal of Pavement Engineering - INT J PAVEMENT ENG*, 5, 185–192. <https://doi.org/10.1080/10298430412331317464> (cit. on p. 5).
- Duffie, J. A., & Beckman, W. A. (2013). Solar Engineering of Thermal Processes (cit. on p. 30).
- Dunton, K. H., Schonberg, S. V., & Cooper, L. W. (2012). Food Web Structure of the Alaskan Nearshore Shelf and Estuarine Lagoons of the Beaufort Sea. *Estuaries and Coasts*, 35(2), 416–435. <https://doi.org/10.1007/s12237-012-9475-1> (cit. on p. 15).
- Dunton, K. H., Weingartner, T., & Carmack, E. C. (2006). The nearshore western Beaufort Sea ecosystem: Circulation and importance of terrestrial carbon in arctic coastal food webs. *Progress in Oceanography*, 71(2), 362–378. <https://doi.org/10.1016/j.pocean.2006.09.011> (cit. on p. 15).
- Eicken, H., Gradinger, R., Gaylord, A., Mahoney, A., Rigor, I., & Melling, H. (2005). Sediment transport by sea ice in the Chukchi and Beaufort Seas: Increasing importance due to changing ice conditions? *Deep Sea Research Part II: Topical Studies in Oceanography*, 52(24), 3281–3302. <https://doi.org/10.1016/j.dsrr.2005.10.006> (cit. on p. 9).
- Elfrink, B., & Baldock, T. (2002). Hydrodynamics and sediment transport in the swash zone: A review and perspectives. *Coastal Engineering*, 45(3), 149–167. [https://doi.org/10.1016/S0378-3839\(02\)00032-7](https://doi.org/10.1016/S0378-3839(02)00032-7) (cit. on p. 22).
- Enfield, D. B., & Allen, J. S. (1980). On the Structure and Dynamics of Monthly Mean Sea Level Anomalies along the Pacific Coast of North and South America [Section: Journal of Physical Oceanography]. Retrieved November 30, 2024, from https://journals.ametsoc.org/view/journals/phoc/10/4/1520-0485_1980_010_0557_otsado_2_0_co_2.xml (cit. on p. 39).
- Engelstad, A. C., Erikson, L., Reguero, B. G., Gibbs, A. E., & Nederhoff, K. (2023). Nearshore wave time-series along the coast of Alaska computed with a numerical wave model. <https://doi.org/10.5066/P931CSO9> (cit. on pp. 17, 20, 39, 117).
- Erikson, L., Gibbs, A. E., Richmond, B. M., Jones, B. M., Storlazzi, C. D., & Ohman, K. (2020a). Modeled 21st century storm surge, waves, and coastal flood hazards and supporting oceanographic and geological field data (2010 and 2011) for Arey and Barter Islands, Alaska and vicinity. <https://doi.org/10.5066/P9LGYO2Q> (cit. on pp. 33, 38, 41, 43).

- Erikson, L. H., Gibbs, A. E., Richmond, B. M., Storlazzi, C. D., Jones, B. M., & Ohman, K. (2020b). *Changing storm conditions in response to projected 21st century climate change and the potential impact on an arctic barrier island-lagoon system—A pilot study for Arey Island and Lagoon, eastern Arctic Alaska* (tech. rep. No. 2020-1142) (ISSN: 2331-1258 Publication Title: Open-File Report). U.S. Geological Survey. <https://doi.org/10.3133/ofr20201142> (cit. on pp. 36, 38, 40).
- Ermida, G. (2014). Strategic decisions of international oil companies: Arctic versus other regions. *Energy Strategy Reviews*, 2(3), 265–272. <https://doi.org/10.1016/j.esr.2013.11.004> (cit. on p. 15).
- ESA. (2019, July). Modelling tides in the Arctic Ocean. Retrieved March 30, 2024, from https://www.esa.int/Applications/Observing_the_Earth/FutureEO/CryoSat/Modelling_tides_in_the_Arctic_Ocean (cit. on p. 8).
- Eymard, R., Gallouët, T., & Herbin, R. Finite volume methods. In: In *Handbook of Numerical Analysis*. Vol. 7. Solution of Equation in \square (Part 3), Techniques of Scientific Computing (Part 3). Elsevier, 2000, January, pp. 713–1018. [https://doi.org/10.1016/S1570-8659\(00\)07005-8](https://doi.org/10.1016/S1570-8659(00)07005-8) (cit. on p. 74).
- Farquharson, L., Mann, D., Rittenour, T., Groves, P., Grosse, G., & Jones, B. (2018). Alaskan marine transgressions record out-of-phase Arctic Ocean glaciation during the last interglacial. *Geology*, 46(9), 783–786. <https://doi.org/10.1130/G40345.1> (cit. on pp. 8, 14).
- Fischer, H. B. (Ed.). (1979). *Mixing in inland and coastal waters*. Academic Press. (Cit. on p. 29).
- Frederick, J., Mota, A., Tezaur, I., & Bull, D. (2021). A thermo-mechanical terrestrial model of Arctic coastal erosion. *Journal of Computational and Applied Mathematics*, 397, 113533. <https://doi.org/10.1016/j.cam.2021.113533> (cit. on pp. 16, 77).
- Frederick, J. M., Thomas, M. A., Bull, D. L., Jones, C. A., & Roberts, J. D. (2016, September). *The Arctic Coastal Erosion Problem* (tech. rep. No. SAND2016-9762). Sandia National Lab. (SNL-NM), Albuquerque, NM (United States). <https://doi.org/10.2172/1431492> (cit. on pp. 7, 8, 16).
- Freeman, J., Baer, L., & Jung, G. (1957). The bathystrophic storm tide. *Journal of Marine Research*, 16(1). https://elischolar.library.yale.edu/journal_of_marine_research/878 (cit. on p. 16).
- French, H. M. (2007). *The Periglacial Environment* (3rd ed.). John Wiley & Sons. (Cit. on p. 10).
- French, H. M. (2017, December). *The Periglacial Environment* (4th ed.). John Wiley & Sons. (Cit. on p. 5).
- Friedlingstein, P., O'Sullivan, M., Jones, M. W., Andrew, R. M., Hauck, J., Olsen, A., Peters, G. P., Peters, W., Pongratz, J., Sitch, S., Le Quéré, C., Canadell, J. G., Ciais, P., Jackson, R. B., Alin, S., Aragão, L. E. O. C., Arneth, A., Arora, V., Bates, N. R., ... Zaehle, S. (2020). Global Carbon Budget 2020 [Publisher: Copernicus GmbH]. *Earth System Science Data*, 12(4), 3269–3340. <https://doi.org/10.5194/essd-12-3269-2020> (cit. on p. 15).
- Fritz, M., Vonk, J. E., & Lantuit, H. (2017). Collapsing Arctic coastlines [Publisher: Nature Publishing Group]. *Nature Climate Change*, 7(1), 6–7. <https://doi.org/10.1038/nclimate3188> (cit. on p. 1).
- Galappatti, G., & Vreugdenhil, C. B. (1985). A depth-integrated model for suspended sediment transport. *Journal of Hydraulic Research*, 23(4), 359–377. <https://doi.org/10.1080/00221688509499345> (cit. on p. 24).
- Gibbs, A., Richmond, B., Palaseanu-Lovejoy, M., Erikson, L., Jones, B., & Brock, J. (2013). Remote Sensing of the Arctic Coast of Alaska Using Airborne Lidar Data (cit. on pp. 10, 12).
- Gibbs, A. E., Erikson, L. H., Jones, B. M., Richmond, B. M., & Engelstad, A. C. (2021). Seven Decades of Coastal Change at Barter Island, Alaska: Exploring the Importance of Waves and Temperature on Erosion of Coastal Permafrost Bluffs. *Remote Sensing*, 13(21), 4420. <https://doi.org/10.3390/rs13214420> (cit. on pp. 33, 44, 45, 69, 71, 72, 75, 77, 79).
- Gibbs, A. E., Jones, B. M., & Richmond, B. M. (2020). A GIS compilation of vector shorelines and coastal bluff edge positions, and associated rate-of-change data for Barter Island, Alaska. <https://doi.org/10.5066/P9CRBC5I> (cit. on p. 43).
- Gibbs, A. E., Nolan, M., Richmond, B. M., Snyder, A. G., & Erikson, L. H. (2019). Assessing patterns of annual change to permafrost bluffs along the North Slope coast of Alaska using high-resolution imagery and elevation models. *Geomorphology*, 336, 152–164. <https://doi.org/10.1016/j.geomorph.2019.03.029> (cit. on pp. 6–8, 12, 14, 69, 72, 73, 75).
- Golubeva, E., Platov, G., Iakshina, D., & Kraineva, M. (2019). A simulated distribution of Siberian river runoff in the Arctic Ocean. *IOP Conference Series: Earth and Environmental Science*, 386(1), 012022. <https://doi.org/10.1088/1755-1315/386/1/012022> (cit. on p. 9).

- Gonzalez Martinez, K. J., Zona, D., Biggs, T., Bernabe, K., Sirivat, D., Tenorio, F., & Oechel, W. (2023). Environmental and vegetation control on active layer and soil temperature in an Arctic tundra ecosystem in Alaska [Publisher: Copernicus GmbH]. *Biogeosciences Discussions*, 1–31. <https://doi.org/10.5194/bg-2023-117> (cit. on p. 6).
- Gorokhovich, Y., Leiserowitz, A., & Dugan, D. (2014). Integrating Coastal Vulnerability and Community-Based Subsistence Resource Mapping in Northwest Alaska. *Journal of Coastal Research*, 293, 158–169. <https://doi.org/10.2112/JCOASTRES-D-13-00001.1> (cit. on p. 15).
- Grabowski, R. C., Droppo, I. G., & Wharton, G. (2011). Erodibility of cohesive sediment: The importance of sediment properties. *Earth-Science Reviews*, 105(3), 101–120. <https://doi.org/10.1016/j.earscirev.2011.01.008> (cit. on p. 6).
- Grosse, G., Harden, J., Turetsky, M., McGuire, A. D., Camill, P., Tarnocai, C., Frolking, S., Schuur, E. A. G., Jorgenson, T., Marchenko, S., Romanovsky, V., Wickland, K. P., French, N., Waldrop, M., Bourgeau-Chavez, L., & Striegl, R. G. (2011). Vulnerability of high-latitude soil organic carbon in North America to disturbance. *Journal of Geophysical Research: Biogeosciences*, 116(G4). <https://doi.org/10.1029/2010JG001507> (cit. on p. 11).
- Grosse, G., Schirrmeister, L., Siegert, C., Kunitsky, V. V., Slagoda, E. A., Andreev, A. A., & Dereviagyn, A. Y. (2007). Geological and geomorphological evolution of a sedimentary periglacial landscape in Northeast Siberia during the Late Quaternary. *Geomorphology*, 86(1), 25–51. <https://doi.org/10.1016/j.geomorph.2006.08.005> (cit. on p. 8).
- GSC. (2021). Coastline in the northwest territories erodes into the beaufort sea. rising sea levels and melting ice are worrying threats to infrastructure in the north, not just on the coasts, but in all communities where permafrost is thawing faster than usual, putting buildings in danger of collapse [Geological Survey of Canada]. Retrieved March 30, 2024, from <https://www.theglobeandmail.com/canada/article-the-big-thaw-what-arctic-communities-on-vanishing-permafrost-are-doing/> (cit. on p. 12).
- Guegan, E., & Christiansen, H. (2016). Seasonal Arctic Coastal Bluff Dynamics in Adventfjorden, Svalbard. *Permafrost and Periglacial Processes*, 28, n/a–n/a. <https://doi.org/10.1002/ppp.1891> (cit. on p. 10).
- Guimond, J. A., Mohammed, A. A., Walvoord, M. A., Bense, V. F., & Kurylyk, B. L. (2021). Salt-water Intrusion Intensifies Coastal Permafrost Thaw. *Geophysical Research Letters*, 48(19), e2021GL094776. <https://doi.org/10.1029/2021GL094776> (cit. on pp. 9, 78).
- Guégan, E. (2015). *Erosion of permafrost affected coasts: Rates, mechanisms and modelling* [Doctoral thesis]. NTNU [Accepted: 2016-01-05T12:17:52Z ISBN: 9788232613137 ISSN: 1503-8181]. Retrieved April 11, 2024, from <https://ntuopen.ntnu.no/ntnu-xmlui/handle/11250/2372616> (cit. on p. 16).
- Günther, F., Overduin, P. P., Sandakov, A. V., Grosse, G., & Grigoriev, M. N. (2013). Short- and long-term thermo-erosion of ice-rich permafrost coasts in the Laptev Sea region. *Biogeosciences*, 10(6), 4297–4318. <https://doi.org/10.5194/bg-10-4297-2013> (cit. on pp. 5, 13).
- Günther, F., Overduin, P. P., Yakshina, I. A., Opel, T., Baranskaya, A. V., & Grigoriev, M. N. (2015). Observing Muostakh disappear: Permafrost thaw subsidence and erosion of a ground-ice-rich island in response to arctic summer warming and sea ice reduction [Publisher: Copernicus GmbH]. *The Cryosphere*, 9(1), 151–178. <https://doi.org/10.5194/tc-9-151-2015> (cit. on pp. 1, 13, 69, 70).
- Günther, F., Overduin, P. P., Sandakov, A., Grosse, G., & Grigoriev, M. N. (2012). Thermo-erosion along the Yedoma coast of the Buor Khaya peninsula, Laptev Sea, East Siberia (K. M. Hinkel, Ed.) [Num Pages: 490 Place: Salekhard, Yamal-Nenets Autonomous District, Russia Publisher: The Northern Publisher, Salekhard, Russia]. *Proceedings of the Tenth International Conference on Permafrost, Volume 1: International Contributions*, 137–142. Retrieved March 30, 2024, from <https://epic.awi.de/id/eprint/30828/> (cit. on p. 9).
- Hamby, D. M. (1994). A review of techniques for parameter sensitivity analysis of environmental models. *Environmental Monitoring and Assessment*, 32(2), 135–154. <https://doi.org/10.1007/BF00547132> (cit. on p. 59).
- Harris, S. A., French, H. M., Heginbottom, J. A., Johnston, G. H., Ladanyi, B., Sego, D. C., & Everdingen, R. O. v. (1988). *Glossary of permafrost and related ground-ice terms*. (Cit. on pp. 5, 11).
- Hasselmann, K., Barnett, T. P., Bouws, E., Carlson, H., Cartwright, D. E., Enke, K., Ewing, J. A., Gienapp, H., Hasselmann, D. E., Kruseman, P., Meerburg, A., Müller, P., Olbers, D. J., Richter, K.,

- Sell, W., & Walden, H. (1973). Measurements of wind-wave growth and swell decay during the Joint North Sea Wave Project (JONSWAP) [Publisher: Deutches Hydrographisches Institut]. *Ergänzungsheft 8-12*. Retrieved June 7, 2024, from <https://repository.tudelft.nl/islandora/object/uuid%3Af204e188-13b9-49d8-a6dc-4fb7c20562fc> (cit. on p. 100).
- Hawkes, L., Broderick, A., Godfrey, M., & Godley, B. (2009). Climate change and marine turtles. *Endangered Species Research*, 7, 137–154. <https://doi.org/10.3354/esr00198> (cit. on pp. 79, 80).
- Hequette, A., & Barnes, P. W. (1990). Coastal retreat and shoreface profile variations in the Canadian Beaufort Sea. *Marine Geology*, 91(1), 113–132. [https://doi.org/10.1016/0025-3227\(90\)90136-8](https://doi.org/10.1016/0025-3227(90)90136-8) (cit. on p. 8).
- Hersbach, H., Bell, B., Berrisford, P., Hirahara, S., Horányi, A., Muñoz-Sabater, J., Nicolas, J., Peubey, C., Radu, R., Schepers, D., Simmons, A., Soci, C., Abdalla, S., Abellan, X., Balsamo, G., Bechtold, P., Biavati, G., Bidlot, J., Bonavita, M., ... Thépaut, J.-N. (2020). The ERA5 global reanalysis [eprint: <https://onlinelibrary.wiley.com/doi/pdf/10.1002/qj.3803>]. *Quarterly Journal of the Royal Meteorological Society*, 146(730), 1999–2049. <https://doi.org/10.1002/qj.3803> (cit. on p. 38).
- Hinzman, L. D., Kane, D. L., Gieck, R. E., & Everett, K. R. (1991). Hydrologic and thermal properties of the active layer in the Alaskan Arctic. *Cold Regions Science and Technology*, 19(2), 95–110. [https://doi.org/10.1016/0165-232X\(91\)90001-W](https://doi.org/10.1016/0165-232X(91)90001-W) (cit. on pp. 6, 32).
- Hjort, J., Karjalainen, O., Aalto, J., Westermann, S., Romanovsky, V. E., Nelson, F. E., Etzelmüller, B., & Luoto, M. (2018). Degrading permafrost puts Arctic infrastructure at risk by mid-century [Publisher: Nature Publishing Group]. *Nature Communications*, 9(1), 5147. <https://doi.org/10.1038/s41467-018-07557-4> (cit. on p. 15).
- Hjort, J., Streletskiy, D., Doré, G., Wu, Q., Bjella, K., & Luoto, M. (2022). Impacts of permafrost degradation on infrastructure [Publisher: Nature Publishing Group]. *Nature Reviews Earth & Environment*, 3(1), 24–38. <https://doi.org/10.1038/s43017-021-00247-8> (cit. on p. 15).
- Holland, P. R., Jenkins, A., & Holland, D. M. (2008). The Response of Ice Shelf Basal Melting to Variations in Ocean Temperature [Publisher: American Meteorological Society Section: Journal of Climate]. *Journal of Climate*, 21(11), 2558–2572. <https://doi.org/10.1175/2007JCLI1909.1> (cit. on p. 16).
- Hoonhout, B. (2015). Xbeach - stable. Retrieved July 6, 2024, from <https://xbeach.readthedocs.io/en/stable/> (cit. on p. 100).
- Hoque, M. A., & Pollard, W. H. (2009). Arctic coastal retreat through block failure [Publisher: NRC Research Press]. *Canadian Geotechnical Journal*, 46(10), 1103–1115. <https://doi.org/10.1139/T09-058> (cit. on pp. 1, 16, 18).
- Hoque, M. A., & Pollard, W. H. (2016). Stability of permafrost dominated coastal cliffs in the Arctic. *Polar Science*, 10(1), 79–88. <https://doi.org/10.1016/j.polar.2015.10.004> (cit. on p. 16).
- Horton, B. P., Kopp, R. E., Garner, A. J., Hay, C. C., Khan, N. S., Roy, K., & Shaw, T. A. (2018). Mapping Sea-Level Change in Time, Space, and Probability (cit. on pp. 8, 14, 69).
- Hu, H., & Argyropoulos, S. A. (1996). Mathematical modelling of solidification and melting: A review. *Modelling and Simulation in Materials Science and Engineering*, 4(4), 371–396. <https://doi.org/10.1088/0965-0393/4/4/004> (cit. on pp. 2, 3, 9, 16, 24).
- Hugelius, G., Strauss, J., Zubrzycki, S., Harden, J. W., Schuur, E. a. G., Ping, C.-L., Schirrmeyer, L., Grosse, G., Michaelson, G. J., Koven, C. D., O'Donnell, J. A., Elberling, B., Mishra, U., Camill, P., Yu, Z., Palmtag, J., & Kuhry, P. (2014). Estimated stocks of circumpolar permafrost carbon with quantified uncertainty ranges and identified data gaps [Publisher: Copernicus GmbH]. *Biogeosciences*, 11(23), 6573–6593. <https://doi.org/10.5194/bg-11-6573-2014> (cit. on p. 15).
- Hume, J. D., & Schalk, M. (1967). Shoreline Processes near Barrow, Alaska: A Comparison of the Normal and the Catastrophic [Number: 2]. *ARCTIC*, 20(2), 86–103. <https://doi.org/10.14430/arctic3285> (cit. on pp. 8, 69).
- Héquette, A., Desrosiers, M., & Barnes, P. (1995). Sea ice scouring on the inner shelf of the southeastern Canadian Beaufort Sea. *Marine Geology*, 128(3-4), 201–219. [https://doi.org/10.1016/0025-3227\(95\)00095-G](https://doi.org/10.1016/0025-3227(95)00095-G) (cit. on p. 9).
- Incropera, F. P., DeWitt, D. P., Bergman, T. L., & Lavine, A. S. (Eds.). (2013). *Introduction to heat transfer* (6. ed., internat. student version). Wiley. (Cit. on pp. 9, 24).

- Intergovernmental Panel On Climate Change (Ipcc). (2022, May). *The Ocean and Cryosphere in a Changing Climate: Special Report of the Intergovernmental Panel on Climate Change* (1st ed.). Cambridge University Press. <https://doi.org/10.1017/9781009157964> (cit. on p. 14).
- Irrgang, A. M., Bendixen, M., Farquharson, L. M., Baranskaya, A. V., Erikson, L. H., Gibbs, A. E., Ogorodov, S. A., Overduin, P. P., Lantuit, H., Grigoriev, M. N., & Jones, B. M. (2022). Drivers, dynamics and impacts of changing Arctic coasts. *Nature Reviews Earth & Environment*, 3(1), 39–54. <https://doi.org/10.1038/s43017-021-00232-1> (cit. on pp. 1, 8, 9, 13–15, 17, 18, 69, 71, 76, 78, 79).
- Irrgang, A. M., Lantuit, H., Gordon, R. R., Piskor, A., & Manson, G. K. (2019). Impacts of past and future coastal changes on the Yukon coast—threats for cultural sites, infrastructure, and travel routes [Publisher: NRC Research Press]. *Arctic Science*, 5(2), 107–126. <https://doi.org/10.1139/as-2017-0041> (cit. on pp. 1, 15).
- Islam, M. A., & Lubbad, R. (2022). A Process-Based Model for Arctic Coastal Erosion Driven by Thermodenudation and Thermoabrasion Combined and including Nearshore Morphodynamics. *Journal of Marine Science and Engineering*, 10(11), 1602. <https://doi.org/10.3390/jmse10111602> (cit. on pp. 1, 17, 18).
- Islam, M. A., Lubbad, R., & Afzal, M. S. (2020). A Probabilistic Model of Coastal Bluff-Top Erosion in High Latitudes Due to Thermoabrasion: A Case Study from Baydaratskaya Bay in the Kara Sea [Number: 3 Publisher: Multidisciplinary Digital Publishing Institute]. *Journal of Marine Science and Engineering*, 8(3), 169. <https://doi.org/10.3390/jmse8030169> (cit. on p. 16).
- ITCC. (2011). Fresh Water and Seawater Properties (cit. on p. 30).
- Jaskólski, M. (2021). Challenges and perspectives for human activity in Arctic coastal environments – a review of selected interactions and problems. *Miscellanea Geographica*, 25. <https://doi.org/10.2478/mgrsd-2020-0036> (cit. on p. 15).
- Jaskólski, M. W., Pawłowski, □., & Strzelecki, M. C. (2018). High Arctic coasts at risk—the case study of coastal zone development and degradation associated with climate changes and multidirectional human impacts in Longyearbyen (Adventfjorden, Svalbard). *Land Degradation & Development*, 29(8), 2514–2524. <https://doi.org/10.1002/lde.2974> (cit. on p. 15).
- Jin, Y., Chen, M., Yan, H., Wang, T., & Yang, J. (2023). Sea level variation in the Arctic Ocean since 1979 based on ORAS5 data [Publisher: Frontiers]. *Frontiers in Marine Science*, 10. <https://doi.org/10.3389/fmars.2023.1197456> (cit. on p. 14).
- Jones, B. (2017). A collapsed block of ice-rich permafrost sits in shoreline waters in drew point, alaska. [USGS]. Retrieved March 30, 2024, from <https://eos.org/articles/arctic-is-experiencing-a-warmer-new-normal-noaa-reports> (cit. on p. 10).
- Jones, B. M., Arp, C. D., Jorgenson, M. T., Hinkel, K. M., Schmutz, J. A., & Flint, P. L. (2009). Increase in the rate and uniformity of coastline erosion in Arctic Alaska. *Geophysical Research Letters*, 36(3). <https://doi.org/10.1029/2008GL036205> (cit. on p. 1).
- Jones, B. M., Irrgang, A. M., Farquharson, L. M., Lantuit, H., Whalen, D., Ogorodov, S., Grigoriev, M., Tweedie, C., Gibbs, A. E., Strzelecki, M. C., Baranskaya, A., Belova, N., Sinitsyn, A., Kroon, A., Maslakov, A., Vieira, G., Grosse, G., Overduin, P., Nitze, I., ... Romanovsky, V. E. (2020). Arctic Report Card 2020: Coastal Permafrost Erosion. <https://doi.org/10.25923/E47W-DW52> (cit. on p. 1).
- Jones, B. M., Farquharson, L. M., Baughman, C. A., Buzard, R. M., Arp, C. D., Grosse, G., Bull, D. L., Günther, F., Nitze, I., Urban, F., Kasper, J. L., Frederick, J. M., Thomas, M., Jones, C., Mota, A., Dallimore, S., Tweedie, C., Maio, C., Mann, D. H., ... Romanovsky, V. E. (2018). A decade of remotely sensed observations highlight complex processes linked to coastal permafrost bluff erosion in the Arctic. *Environmental Research Letters*, 13(11), 115001. <https://doi.org/10.1088/1748-9326/aae471> (cit. on p. 13).
- Jones, M. K. W., Pollard, W. H., & Jones, B. M. (2019). Rapid initialization of retrogressive thaw slumps in the Canadian high Arctic and their response to climate and terrain factors [Publisher: IOP Publishing]. *Environmental Research Letters*, 14(5), 055006. <https://doi.org/10.1088/1748-9326/ab12fd> (cit. on pp. 10, 11).
- Jonsson, I. G. (1966). WAVE BOUNDARY LAYERS AMD FRICTION FACTORS. *Coastal Engineering Proceedings*, (10), 9. <https://doi.org/10.9753/icce.v10.9> (cit. on p. 30).

- Jorgenson, M. T., & Brown, J. (2005). Classification of the Alaskan Beaufort Sea Coast and estimation of carbon and sediment inputs from coastal erosion. *Geo-Marine Letters*, 25(2), 69–80. <https://doi.org/10.1007/s00367-004-0188-8> (cit. on p. 6).
- Jorgenson, M. (2013). Thermokarst Terrains. *Treatise on Geomorphology*, 8, 313–324. <https://doi.org/10.1016/B978-0-12-374739-6.00215-3> (cit. on p. 12).
- Joyce, B. R., Pringle, W. J., Wirasaet, D., Westerink, J. J., Van der Westhuysen, A. J., Grumbine, R., & Feyen, J. (2019). High resolution modeling of western Alaskan tides and storm surge under varying sea ice conditions. *Ocean Modelling*, 141, 101421. <https://doi.org/10.1016/j.ocemod.2019.101421> (cit. on p. 14).
- Kanevskiy, M., Shur, Y., Jorgenson, M., Ping, C.-L., Michaelson, G., Fortier, D., Stephani, E., Dillon, M., & Tumskoy, V. (2013). Ground ice in the upper permafrost of the Beaufort Sea coast of Alaska. *Cold Regions Science and Technology*, 85, 56–70. <https://doi.org/10.1016/j.coldregions.2012.08.002> (cit. on p. 6).
- Kashiwase, H., Ohshima, K. I., Nihashi, S., & Eicken, H. (2017). Evidence for ice-ocean albedo feedback in the Arctic Ocean shifting to a seasonal ice zone [Publisher: Nature Publishing Group]. *Scientific Reports*, 7(1), 8170. <https://doi.org/10.1038/s41598-017-08467-z> (cit. on pp. 9, 14).
- Kasper, J., Erikson, L. H., Ravens, T., Bieniek, P., Engelstad, A. C., Nederhoff, K., Duvoy, P., Fisher, S., Brown, E. P., Man, Y., & Reguero, B. (2023). Central Beaufort Sea Wave and Hydrodynamic Modeling Study Report 1: Field measurements and model development. *Report 1: Field measurements and model development* (cit. on pp. 24, 30, 47, 96).
- Kattsov, V., Källén, E., Cattle, H., Christensen, J., Drange, H., Hanssen-Bauer, I., Jóhannesen, T., Karol, I., Räisänen, J., & Svensson, G. (2005). Future Climate Change: Modeling and Scenarios for the Arctic (cit. on p. 1).
- Kelley, A., Epstein, H., & Walker, D. Role of vegetation and climate in permafrost active layer depth in arctic tundra of northern Alaska and Canada. In: 2004. Retrieved June 11, 2024, from <https://www.semanticscholar.org/paper/Role-of-vegetation-and-climate-in-permafrost-active-Kelley-Epstein/1c6731718d0d41b7a6cfc0f25aff9ceecaf4bb6f> (cit. on p. 5).
- Kempama, E. W., Reimnitz, E., & Barnes, P. W. (1989). Sea ice sediment entrainment and rafting in the Arctic. *Journal of Sedimentary Research*, 59(2), 308–317. <https://doi.org/10.1306/212F8F80-2B24-11D7-8648000102C1865D> (cit. on p. 9).
- Kettridge, N., & Baird, A. (2008). Modelling soil temperatures in northern peatlands. *European Journal of Soil Science*, 59(2), 327–338. <https://doi.org/10.1111/j.1365-2389.2007.01000.x> (cit. on p. 117).
- Kim, J., Murphy, E., Nistor, I., Ferguson, S., & Provan, M. (2021). Numerical Analysis of Storm Surges on Canada's Western Arctic Coastline [Number: 3 Publisher: Multidisciplinary Digital Publishing Institute]. *Journal of Marine Science and Engineering*, 9(3), 326. <https://doi.org/10.3390/jmse9030326> (cit. on pp. 8, 69).
- Kobayashi, N., Vidrine, J. C., Nairn, R. B., & Solomon, S. M. (1999). Erosion of Frozen Cliffs Due to Storm Surge on Beaufort Sea Coast [Publisher: Coastal Education & Research Foundation, Inc.]. *Journal of Coastal Research*, 15(2), 332–344. Retrieved February 13, 2024, from <https://www.jstor.org/stable/4298946> (cit. on pp. 7, 16, 17, 29).
- Kobayashi, N. (1985). Formation of thermoerosional niches into frozen bluffs due to storm surges on the Beaufort Sea coast. *Journal of Geophysical Research: Oceans*, 90(C6), 11983–11988. <https://doi.org/10.1029/JC090iC06p11983> (cit. on pp. 10, 16, 72, 77).
- Kobayashi, N., & Aktan, D. (1986). Thermoerosion of Frozen Sediment Under Wave Action [Publisher: American Society of Civil Engineers]. *Journal of Waterway, Port, Coastal, and Ocean Engineering*, 112(1), 140–158. [https://doi.org/10.1061/\(ASCE\)0733-950X\(1986\)112:1\(140\)](https://doi.org/10.1061/(ASCE)0733-950X(1986)112:1(140)) (cit. on pp. 16, 30).
- Kobayashi, N., & Vidrine, J. C. (1995). *Combined Thermal-mechanical Erosion Processes Model*. University of Delaware, Center for Applied Coastal Research, Ocean Engineering Laboratory. (Cit. on p. 16).
- Kokelj, S. V., & Jorgenson, M. T. (2013). Advances in Thermokarst Research. *Permafrost and Periglacial Processes*, 24(2), 108–119. <https://doi.org/10.1002/ppp.1779> (cit. on p. 11).
- Komar, P. D. (1998). *Beach Processes and Sedimentation* [Google-Books-ID: DyJgQgAACAAJ]. Prentice Hall. (Cit. on p. 7).

- Kombiadou, K., Costas, S., & Roelvink, D. (2021). Simulating Destructive and Constructive Morphodynamic Processes in Steep Beaches [Number: 1 Publisher: Multidisciplinary Digital Publishing Institute]. *Journal of Marine Science and Engineering*, 9(1), 86. <https://doi.org/10.3390/jmse9010086> (cit. on p. 101).
- Korte, S., Gieschen, R., Stolle, J., & Goseberg, N. (2020). Physical Modelling of Arctic Coastlines—Progress and Limitations [Number: 8 Publisher: Multidisciplinary Digital Publishing Institute]. *Water*, 12(8), 2254. <https://doi.org/10.3390/w12082254> (cit. on p. 17).
- Kovacs, A., & Sodhi, D. S. (1980). Shore ice pile-up and ride-up: Field observations, models, theoretical analyses. *Cold Regions Science and Technology*, 2, 210–288. [https://doi.org/10.1016/0165-232X\(80\)90076-2](https://doi.org/10.1016/0165-232X(80)90076-2) (cit. on p. 9).
- Kroon, A., Abermann, J., Bendixen, M., Lund, M., Sigsgaard, C., Skov, K., & Hansen, B. U. (2017). Deltas, freshwater discharge, and waves along the Young Sound, NE Greenland. *Ambio*, 46(S1), 132–145. <https://doi.org/10.1007/s13280-016-0869-3> (cit. on p. 5).
- Kupilik, M., Ulgren, M., & Brunswick, D. (2020). Bayesian Parameter Estimation for Arctic Coastal Erosion Under the Effects of Climate Change. *IEEE Journal of Selected Topics in Applied Earth Observations and Remote Sensing*, 13, 3595–3604. <https://doi.org/10.1109/JSTARS.2020.3004291> (cit. on p. 17).
- Kuzin, V. I., Platov, G. A., & Golubeva, E. N. (2010). Influence that interannual variations in Siberian river discharge have on redistribution of freshwater fluxes in Arctic Ocean and North Atlantic. *Izvestiya, Atmospheric and Oceanic Physics*, 46(6), 770–783. <https://doi.org/10.1134/S0001433810060083> (cit. on p. 9).
- Kwok, R., Cunningham, G. F., Wensnahan, M., Rigor, I., Zwally, H. J., & Yi, D. (2022). Thinning and volume loss of the Arctic Ocean sea ice cover: 2003–2008. *Journal of Geophysical Research: Oceans*, 114(C7). <https://doi.org/10.1029/2009JC005312> (cit. on p. 13).
- Lambeck, K., Rouby, H., Purcell, A., Sun, Y., & Sambridge, M. (2014). Sea level and global ice volumes from the Last Glacial Maximum to the Holocene [Publisher: Proceedings of the National Academy of Sciences]. *Proceedings of the National Academy of Sciences*, 111(43), 15296–15303. <https://doi.org/10.1073/pnas.1411762111> (cit. on pp. 8, 14).
- Landauer, M., & Juhola, S. Loss and Damage in the Rapidly Changing Arctic (R. Mechler, L. M. Bouwer, T. Schinko, S. Surminski, & J. Linnerooth-Bayer, Eds.). en. In: *Loss and Damage from Climate Change: Concepts, Methods and Policy Options* (R. Mechler, L. M. Bouwer, T. Schinko, S. Surminski, & J. Linnerooth-Bayer, Eds.). Ed. by Mechler, R., Bouwer, L. M., Schinko, T., Surminski, S., & Linnerooth-Bayer, J. Cham: Springer International Publishing, 2019, pp. 425–447. ISBN: 978-3-319-72026-5. https://doi.org/10.1007/978-3-319-72026-5_18 (cit. on p. 15).
- Lantuit, H., Overduin, P. P., & Wetterich, S. (2013). Recent Progress Regarding Permafrost Coasts. *Permafrost and Periglacial Processes*, 24(2), 120–130. <https://doi.org/10.1002/ppp.1777> (cit. on pp. 1, 9, 12, 17).
- Lantuit, H., & Pollard, W. H. (2008). Fifty years of coastal erosion and retrogressive thaw slump activity on Herschel Island, southern Beaufort Sea, Yukon Territory, Canada. *Geomorphology*, 95(1), 84–102. <https://doi.org/10.1016/j.geomorph.2006.07.040> (cit. on pp. 11, 12).
- Lantuit, H., Atkinson, D., Paul Overduin, P., Grigoriev, M., Rachold, V., Grosse, G., & Hubberten, H.-W. (2011). Coastal erosion dynamics on the permafrost-dominated Bykovsky Peninsula, north Siberia, 1951–2006 [Publisher: Routledge]. *Polar Research*, 30(1), 7341. <https://doi.org/10.3402/polar.v30.07341> (cit. on p. 7).
- Lantuit, H., Overduin, P. P., Couture, N., Wetterich, S., Aré, F., Atkinson, D., Brown, J., Cherkashov, G., Drozdov, D., Forbes, D. L., Graves-Gaylord, A., Grigoriev, M., Hubberten, H.-W., Jordan, J., Jorgenson, T., Ødegård, R. S., Ogorodov, S., Pollard, W. H., Rachold, V., ... Vasiliev, A. (2012). The Arctic Coastal Dynamics Database: A New Classification Scheme and Statistics on Arctic Permafrost Coastlines. *Estuaries and Coasts*, 35(2), 383–400. <https://doi.org/10.1007/s12237-010-9362-6> (cit. on pp. 1, 5–7, 33, 61, 75, 78).
- Lim, M., Whalen, D., Martin, J., Mann, P. J., Hayes, S., Fraser, P., Berry, H. B., & Ouellette, D. (2020). Massive Ice Control on Permafrost Coast Erosion and Sensitivity. *Geophysical Research Letters*, 47(17), e2020GL087917. <https://doi.org/10.1029/2020GL087917> (cit. on pp. 1, 5, 13, 69, 70).
- Lowell, R. P., & Rona, P. A. TECTONICS | Hydrothermal Activity (R. C. Selley, L. R. M. Cocks, & I. R. Plimer, Eds.). In: *Encyclopedia of Geology* (R. C. Selley, L. R. M. Cocks, & I. R. Plimer, Eds.).

- Ed. by Selley, R. C., Cocks, L. R. M., & Plimer, I. R. Oxford: Elsevier, 2005, January, pp. 362–372. ISBN: 978-0-12-369396-9. <https://doi.org/10.1016/B0-12-369396-9/00126-X> (cit. on p. 28).
- Man, Y. (2023). THE EFFECT OF SNOW DEPOSITION ON SOIL TEMPERATURE PROFILE IN THE ARCTIC (cit. on p. 29).
- Manson, G. K., Solomon, S. M., Forbes, D. L., Atkinson, D. E., & Craymer, M. (2005). Spatial variability of factors influencing coastal change in the Western Canadian Arctic. *Geo-Marine Letters*, 25(2), 138–145. <https://doi.org/10.1007/s00367-004-0195-9> (cit. on pp. 8, 70).
- Manson, G., & Solomon, S. (2007). Past and Future Forcing of Beaufort Sea Coastal Change. *Atmosphere-ocean - ATMOS OCEAN*, 45, 107–122. <https://doi.org/10.3137/ao.450204> (cit. on p. 1).
- Manson, G. K., Davidson-Arnott, R. G. D., & Ollerhead, J. (2016). Attenuation of Wave Energy by Nearshore Sea Ice: Prince Edward Island, Canada [Publisher: Coastal Education and Research Foundation]. *Journal of Coastal Research*, 32(2), 253–263. <https://doi.org/10.2112/JCOASTRES-D-14-00207.1> (cit. on p. 9).
- Maslanik, J. A., Fowler, C., Stroeve, J., Drobot, S., Zwally, J., Yi, D., & Emery, W. (2007). A younger, thinner Arctic ice cover: Increased potential for rapid, extensive sea-ice loss. *Geophysical Research Letters*, 34(24). <https://doi.org/10.1029/2007GL032043> (cit. on p. 13).
- Matsumura, S., & Yamazaki, K. (2012). A longer climate memory carried by soil freeze–thaw processes in Siberia. *Environmental Research Letters*, 7(4), 045402. <https://doi.org/10.1088/1748-9326/7/4/045402> (cit. on pp. 74, 118).
- Meyssignac, B., & Cazenave, A. (2012). Sea level: A review of present-day and recent-past changes and variability. *Journal of Geodynamics*, 58, 96–109. <https://doi.org/10.1016/j.jog.2012.03.005> (cit. on p. 1).
- Miner, K. R., Turetsky, M. R., Malina, E., Bartsch, A., Tamminen, J., McGuire, A. D., Fix, A., Sweeney, C., Elder, C. D., & Miller, C. E. (2022). Permafrost carbon emissions in a changing Arctic [Publisher: Nature Publishing Group]. *Nature Reviews Earth & Environment*, 3(1), 55–67. <https://doi.org/10.1038/s43017-021-00230-3> (cit. on p. 15).
- Mioduszewski, J., Vavrus, S., & Wang, M. (2018). Diminishing Arctic Sea Ice Promotes Stronger Surface Winds [Publisher: American Meteorological Society Section: Journal of Climate]. *Journal of Climate*, 31(19), 8101–8119. <https://doi.org/10.1175/JCLI-D-18-0109.1> (cit. on p. 14).
- Moore, G. W. Sorting of beach sediment, northwestern alaska (T. B. Nolan, Ed.). In: *Geological survey research 1961, short papers in the geologic and hydrologic sciences, articles 147-292* (T. B. Nolan, Ed.). Ed. by Nolan, T. B. U.S. Geological Survey, 1961 (cit. on pp. 6, 71, 78).
- Mudryk, L. R., Dawson, J., Howell, S. E. L., Derksen, C., Zagon, T. A., & Brady, M. (2021). Impact of 1, 2 and 4 °C of global warming on ship navigation in the Canadian Arctic [Publisher: Nature Publishing Group]. *Nature Climate Change*, 11(8), 673–679. <https://doi.org/10.1038/s41558-021-01087-6> (cit. on p. 15).
- Nairn, R. B., Solomon, S., Kobayashi, N., & Virdrine, J. (1998). DEVELOPMENT AND TESTING OF A THERMAL-MECHANICAL NUMERICAL MODEL FOR PREDICTING ARCTIC SHORE EROSION PROCESSES (cit. on pp. 1, 11, 71, 120).
- Nairn, R. B., & Southgate, H. N. (1993). Deterministic profile modelling of nearshore processes. Part 2. Sediment transport and beach profile development. *Coastal Engineering*, 19(1), 57–96. [https://doi.org/10.1016/0378-3839\(93\)90019-5](https://doi.org/10.1016/0378-3839(93)90019-5) (cit. on p. 16).
- Nations Online Project. (2016). Retrieved March 25, 2024, from https://www.nationsonline.org/oneworld/map/USA/alaska_map.htm (cit. on p. 34).
- Nederhoff, K., Erikson, L., Engelstad, A., Bieniek, P., & Kasper, J. (2022). The effect of changing sea ice on wave climate trends along Alaska's central Beaufort Sea coast [Publisher: Copernicus GmbH]. *The Cryosphere*, 16(5), 1609–1629. <https://doi.org/10.5194/tc-16-1609-2022> (cit. on pp. 14, 20).
- Nicolsky, D. J., Romanovsky, V. E., Panda, S. K., Marchenko, S. S., & Muskett, R. R. (2017). Applicability of the ecosystem type approach to model permafrost dynamics across the Alaska North Slope. *Journal of Geophysical Research: Earth Surface*, 122(1), 50–75. <https://doi.org/10.1002/2016JF003852> (cit. on pp. 8, 17, 70).
- Nielsen, D. M., Dobrynin, M., Baehr, J., Razumov, S., & Grigoriev, M. (2020). Coastal Erosion Variability at the Southern Laptev Sea Linked to Winter Sea Ice and the Arctic Oscillation. *Geophysical*

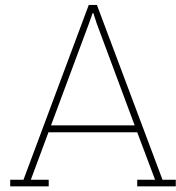
- Research Letters*, 47(5), e2019GL086876. <https://doi.org/10.1029/2019GL086876> (cit. on pp. 1, 14, 71).
- Nielsen, D. M., Pieper, P., Barkhordarian, A., Overduin, P., Ilyina, T., Brovkin, V., Baehr, J., & Dobrynin, M. (2022). Increase in Arctic coastal erosion and its sensitivity to warming in the twenty-first century. *Nature Climate Change*, 12(3), 263–270. <https://doi.org/10.1038/s41558-022-01281-0> (cit. on pp. 17, 79).
- Nielsen, P. (1992, July). *Coastal Bottom Boundary Layers and Sediment Transport* (Vol. 4). WORLD SCIENTIFIC. <https://doi.org/10.1142/1269> (cit. on p. 30).
- Nyland, K. E., Klene, A. E., Brown, J., Shiklomanov, N. I., Nelson, F. E., Streletskei, D. A., & Yoshikawa, K. (2017). Traditional Inupiat Ice Cellars (SIGIUAQ) in Barrow, Alaska: Characteristics, Temperature Monitoring, and Distribution [Publisher: Routledge]. *Geographical Review*, 107(1), 143–158. <https://doi.org/10.1111/j.1931-0846.2016.12204.x> (cit. on p. 15).
- Ogorodov, S., Baranskaya, A., Belova, N., Kamalov, A., Kuznetsov, D., Overduin, P., Shabanova, N., & Vergun, A. (2016). COASTAL DYNAMICS OF THE PECHORA AND KARA SEAS UNDER CHANGING CLIMATIC CONDITIONS AND HUMAN DISTURBANCES. *GEOGRAPHY, ENVIRONMENT, SUSTAINABILITY*, 9(3), 53–73. https://doi.org/10.15356/2071-9388_03v09_2016_04 (cit. on pp. 8, 9).
- Overduin, P. P., Schneider von Deimling, T., Miesner, F., Grigoriev, M. N., Ruppel, C., Vasiliev, A., Lantuit, H., Juhls, B., & Westermann, S. (2019). Submarine Permafrost Map in the Arctic Modeled Using 1-D Transient Heat Flux (SuPerMAP). *Journal of Geophysical Research: Oceans*, 124(6), 3490–3507. <https://doi.org/10.1029/2018JC014675> (cit. on p. 8).
- Overduin, P. P., Strzelecki, M. C., Grigoriev, M. N., Couture, N., Lantuit, H., St-Hilaire-Gravel, D., Günther, F., & Wetterich, S. (2014). Coastal changes in the Arctic. *Geological Society, London, Special Publications*, 388(1), 103–129. <https://doi.org/10.1144/SP388.13> (cit. on pp. 5, 33).
- Overduin, P. P., Westermann, S., Yoshikawa, K., Haberlau, T., Romanovsky, V., & Wetterich, S. (2012). Geolectric observations of the degradation of nearshore submarine permafrost at Barrow (Alaskan Beaufort Sea). *Journal of Geophysical Research: Earth Surface*, 117(F2). <https://doi.org/10.1029/2011JF002088> (cit. on p. 8).
- Overeem, I., Anderson, R. S., Wobus, C. W., Clow, G. D., Urban, F. E., & Matell, N. (2011). Sea ice loss enhances wave action at the Arctic coast. *Geophysical Research Letters*, 38(17). <https://doi.org/10.1029/2011GL048681> (cit. on pp. 1, 14, 17).
- Owens, E. H., & McCann, S. B. (1970). The role of ice in the arctic beach environment with special reference to Cape Ricketts, southwest Devon Island, Northwest Territories, Canada [Publisher: American Journal of Science]. *American Journal of Science*, 268(5), 397–414. <https://doi.org/10.2475/ajs.268.5.397> (cit. on pp. 6, 71, 78).
- O'Neill, H. B., Smith, S. L., Burn, C. R., Duchesne, C., & Zhang, Y. (2023). Widespread Permafrost Degradation and Thaw Subsidence in Northwest Canada. *Journal of Geophysical Research: Earth Surface*, 128(8), e2023JF007262. <https://doi.org/10.1029/2023JF007262> (cit. on pp. 6, 71).
- O'Rourke, M. (2017). Archaeological Site Vulnerability Modelling: The Influence of High Impact Storm Events on Models of Shoreline Erosion in the Western Canadian Arctic. *Open Archaeology*, 3, 1–16. <https://doi.org/10.1515/opar-2017-0001> (cit. on p. 15).
- Pacific Coastal and Marine Science Center. (2019). Alongshore view of barter island bluffs [USGS]. Retrieved March 30, 2024, from <https://www.usgs.gov/media/images/alongshore-view-barter-island-bluffs> (cit. on p. 11).
- Palaseanu-Lovejoy, M., Danielson, J., Thatcher, C., Foxgrover, A., Barnard, P., Brock, J., & Young, A. (2016). Automatic Delineation of Seaciff Limits using Lidar-derived High-resolution DEMs in Southern California. *Journal of Coastal Research*, 76 (10076), 162–173. <https://doi.org/10.2112/SI76-014> (cit. on pp. 45, 46).
- Panchang, V., & Kaihatu, J. M. (2018, June). *Advances In Coastal Hydraulics* [Google-Books-ID: BCpjD-wAAQBAJ]. World Scientific. (Cit. on pp. 11, 33).
- Penney, W. G., & Price, A. T. (1952). Part I. The diffraction theory of sea waves and the shelter afforded by breakwaters. *Philosophical Transactions of the Royal Society of London. Series A, Mathematical and Physical Sciences*, 244(882), 236–253. <https://doi.org/10.1098/rsta.1952.0003> (cit. on p. 7).

- Perovich, D., Meier, W., Tschudi, M., Hendricks, S., Petty, A. A., Divine, D., Farrell, S., Gerland, S., Haas, C., Kaleschke, L., Pavlova, O., Ricker, R., Tian-Kunze, X., Wood, K., & Webster, M. (2020). Arctic Report Card 2020: Sea Ice [Publisher: [object Object]]. <https://doi.org/10.25923/N170-9H57> (cit. on p. 13).
- Peterson, P. (2001). Fortran to Python Interface Generator with an Application to Aerospace Engineering (cit. on p. 21).
- Ping, C.-L., Michaelson, G. J., Guo, L., Jorgenson, M. T., Kanevskiy, M., Shur, Y., Dou, F., & Liang, J. (2011). Soil carbon and material fluxes across the eroding Alaska Beaufort Sea coastline. *Journal of Geophysical Research: Biogeosciences*, 116(G2). <https://doi.org/10.1029/2010JG001588> (cit. on pp. 8, 10).
- Radosavljevic, B., Lantuit, H., Pollard, W., Overduin, P., Couture, N., Sachs, T., Helm, V., & Fritz, M. (2016). Erosion and Flooding—Threats to Coastal Infrastructure in the Arctic: A Case Study from Herschel Island, Yukon Territory, Canada. *Estuaries and Coasts*, 39(4), 900–915. <https://doi.org/10.1007/s12237-015-0046-0> (cit. on pp. 1, 15).
- Ramage, J., Jungsberg, L., Wang, S., Westermann, S., Lantuit, H., & Heleniak, T. (2021). Population living on permafrost in the Arctic. *Population and Environment*, 43(1), 22–38. <https://doi.org/10.1007/s11111-020-00370-6> (cit. on p. 15).
- Rantanen, M., Karpeckho, A. Y., Lipponen, A., Nordling, K., Hyvärinen, O., Ruosteenoja, K., Vihma, T., & Laaksonen, A. (2022). The Arctic has warmed nearly four times faster than the globe since 1979 [Publisher: Nature Publishing Group]. *Communications Earth & Environment*, 3(1), 1–10. <https://doi.org/10.1038/s43247-022-00498-3> (cit. on pp. 13, 68).
- Ravens, T., & Ullgren, M. Arctic Coastal Geomorphic Change Modeling with Arctic Xbeach. In: In *Agu fall meeting abstracts*. 2020. 2020, December, C003-0009, C003–0009 (cit. on p. 11).
- Ravens, T., Jones, B., Zhang, J., Tweedie, C., Erikson, L., Gibbs, A., & Richmond, B. (2011). Arctic Coastal Erosion Modeling. *AGU Fall Meeting Abstracts*, 06 (cit. on pp. 11, 33).
- Ravens, T., Ullgren, M., Wilber, M., Hailu, G., & Peng, J. (2017). Arctic-capable coastal geomorphic change modeling with application to Barter Island, Alaska (cit. on pp. 1–3, 16–20, 28, 76, 96).
- Ravens, T. M., Jones, B. M., Zhang, J., Arp, C. D., & Schmutz, J. A. (2012). Process-Based Coastal Erosion Modeling for Drew Point, North Slope, Alaska. *Journal of Waterway, Port, Coastal, and Ocean Engineering*, 138(2), 122–130. [https://doi.org/10.1061/\(ASCE\)WW.1943-5460.0000106](https://doi.org/10.1061/(ASCE)WW.1943-5460.0000106) (cit. on pp. 2, 6, 16).
- Ravens, T. M., & Peterson, S. (2021). Geologic Controls on Erosion Mechanism on the Alaska Beaufort Coast. *Frontiers in Earth Science*, 9, 693824. <https://doi.org/10.3389/feart.2021.693824> (cit. on pp. 11, 33, 69, 71, 72, 77, 79).
- Ravens, T., Henke, M., & Ferreira, C. ARCTIC COASTAL STORMS, UNIQUE IN CHARACTER AND IMPACT. en. In: In *Coastal Sediments 2023*. New Orleans, LA, USA: WORLD SCIENTIFIC, 2023, April, 2434–2461. ISBN: 9789811279898 9789811275135. https://doi.org/10.1142/9789811275135_0223 (cit. on pp. 1, 7–11, 14, 17, 24, 30, 40, 49, 65, 69, 70, 72–75, 77, 96, 116, 119).
- Rawlinson, S. E. (1990). *Surficial geology and morphology of the Alaskan central Arctic coastal plain* [Ph.D.]. University of Alaska Fairbanks [ISBN: 9798207432595]. Retrieved March 25, 2024, from <https://www.proquest.com/docview/303836968/abstract/BD1CAF5868D14924PQ/1> (cit. on p. 6).
- Razumov, S. (2001). Modelling arctic seas coastal erosion in the changing climatic conditions. *Earth's Cryosphere*, 5(1), 53–60 (cit. on p. 10).
- Rearic, D. M., Barnes, P. W., & Reimnitz, E. (1990). Bulldozing and resuspension of shallow-shelf sediment by ice keels: Implications for Arctic sediment transport trajectories. *Marine Geology*, 91(1), 133–147. [https://doi.org/10.1016/0025-3227\(90\)90137-9](https://doi.org/10.1016/0025-3227(90)90137-9) (cit. on p. 9).
- Reed, C. W., Niedoroda, A. W., & Swift, D. J. (1999). Modeling sediment entrainment and transport processes limited by bed armoring. *Marine Geology*, 154(1-4), 143–154. [https://doi.org/10.1016/S0025-3227\(98\)00109-1](https://doi.org/10.1016/S0025-3227(98)00109-1) (cit. on p. 116).
- Reimnitz, E., Graves, S. M., & Barnes, P. W. (1988). *Beaufort Sea coastal erosion, sediment flux, shoreline evolution, and the erosional shelf profile* (tech. rep.). US Geological Survey. <https://doi.org/10.3133/i1182G> (cit. on p. 8).
- Rex, R. W. Arctic beaches: Barrow, alaska (R. L. Miller, Ed.). In: *Papers in marine geology* (R. L. Miller, Ed.). Ed. by Miller, R. L. 1964, 384–400 (cit. on pp. 6, 71, 78).

- Roelvink, D., Reniers, A., van Dongeren, A., van Thiel de Vries, J., McCall, R., & Lescinski, J. (2009). Modelling storm impacts on beaches, dunes and barrier islands. *Coastal Engineering*, 56(11), 1133–1152. <https://doi.org/10.1016/j.coastaleng.2009.08.006> (cit. on pp. 2, 3, 17, 23, 24, 40, 47, 72, 76, 100).
- Rolph, R., Overduin, P. P., Ravens, T., Lantuit, H., & Langer, M. (2022). ArcticBeach v1.0: A physics-based parameterization of pan-Arctic coastline erosion. *Frontiers in Earth Science*, 10, 962208. <https://doi.org/10.3389/feart.2022.962208> (cit. on pp. 1, 6, 7, 11, 16, 17, 71, 78).
- Russell-Head, D. S. (1980). The Melting of Free-Drifting Icebergs. *Annals of Glaciology*, 1, 119–122. <https://doi.org/10.3189/S0260305500017092> (cit. on p. 16).
- Sallenger, J. A. H. (2000). Storm Impact Scale for Barrier Islands. *Journal of Coastal Research*. Retrieved June 7, 2024, from <https://www.semanticscholar.org/paper/Storm-Impact-Scale-for-Barrier-Islands-Sallenger/eec42c765561e3adf07c2d7f7363fcb5097036c4> (cit. on p. 24).
- Sanuy, M., & Jiménez, J. A. (2019). Sensitivity of Storm-Induced Hazards in a Highly Curvilinear Coastline to Changing Storm Directions. The Tordera Delta Case (NW Mediterranean). *Water*, 11(4), 747. <https://doi.org/10.3390/w11040747> (cit. on p. 101).
- Schaefer, K., Elshorbany, Y., Jafarov, E., Schuster, P. F., Striegl, R. G., Wickland, K. P., & Sunderland, E. M. (2020). Potential impacts of mercury released from thawing permafrost [Publisher: Nature Publishing Group]. *Nature Communications*, 11(1), 4650. <https://doi.org/10.1038/s41467-020-18398-5> (cit. on p. 15).
- Schambach, L., Grilli, A. R., Grilli, S. T., Hashemi, M. R., & King, J. W. (2018). Assessing the impact of extreme storms on barrier beaches along the Atlantic coastline: Application to the southern Rhode Island coast. *Coastal Engineering*, 133, 26–42. <https://doi.org/10.1016/j.coastaleng.2017.12.004> (cit. on p. 101).
- Senechal, N., Coco, G., Bryan, K. R., & Holman, R. A. (2011). Wave runup during extreme storm conditions [eprint: <https://onlinelibrary.wiley.com/doi/pdf/10.1029/2010JC006819>]. *Journal of Geophysical Research: Oceans*, 116(C7). <https://doi.org/10.1029/2010JC006819> (cit. on p. 22).
- Shabanova, N., Ogorodov, S., Shabanov, P., & Baranskaya, A. (2018). HYDROMETEOROLOGICAL FORCING OF WESTERN RUSSIAN ARCTIC COASTAL DYNAMICS: XX-CENTURY HISTORY AND CURRENT STATE [Number: 1 Section: ENVIRONMENT]. *GEOGRAPHY, ENVIRONMENT, SUSTAINABILITY*, 11(1), 113–129. Retrieved March 30, 2024, from <https://ges.rgo.ru/jour/article/view/385/308> (cit. on pp. 8, 13).
- Shone, R. (2023). 1/3 we have just returned home from the northern edge of land, where we've been exploring some of the most northern caves on earth for science exploration. we have a lot to digest as we prepare to unveil our discoveries. in the meantime, here's a photograph, taken on this... [[@Greenland_caves, tweet]]. Retrieved March 30, 2024, from https://twitter.com/Greenland_Caves/status/1688541602090749952 (cit. on p. 13).
- Short, A. (1973, January). *Beach Dynamics and Nearshore Morphology of the Alaskan Arctic Coast*. [Doctor of Philosophy]. Louisiana State University and Agricultural & Mechanical College. https://doi.org/10.31390/gradschool_disstheses.2498 (cit. on pp. 7, 8).
- Sinitsyn, A. O., Guegan, E., Shabanova, N., Kokin, O., & Ogorodov, S. (2020). Fifty four years of coastal erosion and hydrometeorological parameters in the Varandey region, Barents Sea. *Coastal Engineering*, 157, 103610. <https://doi.org/10.1016/j.coastaleng.2019.103610> (cit. on pp. 5, 8, 69).
- Smith, L. C., & Stephenson, S. R. (2013). New Trans-Arctic shipping routes navigable by midcentury [Publisher: Proceedings of the National Academy of Sciences]. *Proceedings of the National Academy of Sciences*, 110(13), E1191–E1195. <https://doi.org/10.1073/pnas.1214212110> (cit. on p. 15).
- Smith, S. L., O'Neill, H. B., Isaksen, K., Noetzli, J., & Romanovsky, V. E. (2022). The changing thermal state of permafrost [Publisher: Springer Science and Business Media LLC]. *Nature reviews. Earth & environment*, 3(1), 10–23. <https://doi.org/10.1038/s43017-021-00240-1> (cit. on p. 5).
- Soulsby, R. (1997). *Dynamics of marine sands: A manual for practical applications* (1. publ.). Telford. (Cit. on p. 24).
- Southgate, H. N., & Nairn, R. B. (1993). Deterministic profile modelling of nearshore processes. Part 1. Waves and currents. *Coastal Engineering*, 19(1), 27–56. [https://doi.org/10.1016/0378-3839\(93\)90018-4](https://doi.org/10.1016/0378-3839(93)90018-4) (cit. on p. 16).

- Srinath, K. R. (2017). Python – The Fastest Growing Programming Language. *04*(12) (cit. on p. 21).
- Stephen, K. (2018). Societal Impacts of a Rapidly Changing Arctic. *Current Climate Change Reports*, *4*(3), 223–237. <https://doi.org/10.1007/s40641-018-0106-1> (cit. on p. 15).
- Stewart, E., Dawson, J., & Johnston, M. (2015). Risks and opportunities associated with change in the cruise tourism sector: Community perspectives from Arctic Canada. *The Polar Journal*, *5*, 1–25. <https://doi.org/10.1080/2154896X.2015.1082283> (cit. on p. 15).
- Stockdon, H. F., Holman, R. A., Howd, P. A., & Sallenger, A. H. (2006). Empirical parameterization of setup, swash, and runup. *Coastal Engineering*, *53*(7), 573–588. <https://doi.org/10.1016/j.coastaleng.2005.12.005> (cit. on pp. 22, 41, 61, 69, 77, 101).
- Tanski, G., Bröder, L., Wagner, D., Knoblauch, C., Lantuit, H., Beer, C., Sachs, T., Fritz, M., Tesi, T., Koch, B. P., Haghipour, N., Eglinton, T. I., Strauss, J., & Vonk, J. E. (2021). Permafrost Carbon and CO₂ Pathways Differ at Contrasting Coastal Erosion Sites in the Canadian Arctic [Publisher: Frontiers]. *Frontiers in Earth Science*, *9*. <https://doi.org/10.3389/feart.2021.630493> (cit. on p. 15).
- Terhaar, J., Lauerwald, R., Regnier, P., Gruber, N., & Bopp, L. (2021). Around one third of current Arctic Ocean primary production sustained by rivers and coastal erosion [Publisher: Nature Publishing Group]. *Nature Communications*, *12*(1), 169. <https://doi.org/10.1038/s41467-020-20470-z> (cit. on pp. 1, 15).
- Thomson, J., Fan, Y., Stammerjohn, S., Stopa, J., Rogers, W. E., Girard-Ardhuin, F., Ardhuin, F., Shen, H., Perrie, W., Shen, H., Ackley, S., Babanin, A., Liu, Q., Guest, P., Maksym, T., Wadhams, P., Fairall, C., Persson, O., Doble, M., ... Bidlot, J.-R. (2016). Emerging trends in the sea state of the Beaufort and Chukchi seas. *Ocean Modelling*, *105*, 1–12. <https://doi.org/10.1016/j.ocemod.2016.02.009> (cit. on pp. 8, 14, 71).
- Timmermans, M.-L., & Labe, Z. (2020). Arctic Report Card 2020: Sea Surface Temperature. <https://doi.org/10.25923/V0FS-M920> (cit. on pp. 1, 13).
- Turner, I. L., Leaman, C. K., Harley, M. D., Thran, M. C., David, D. R., Splinter, K. D., Matheen, N., Hansen, J. E., Cuttler, M. V. W., Greenslade, D. J. M., Zieger, S., & Lowe, R. J. (2024). A framework for national-scale coastal storm hazards early warning. *Coastal Engineering*, *192*, 104571. <https://doi.org/10.1016/j.coastaleng.2024.104571> (cit. on p. 117).
- USCB. (2020). 2020 united states census [United States Census Bureau]. <https://www.census.gov/> (cit. on p. 33).
- USGS. (1955). Retrieved March 25, 2024, from https://ngmdb.usgs.gov/img4/ht_icons/overlay/AK/AK_Barter%20Island%20A-5_354215_1955_63360_geo.jpg (cit. on p. 35).
- USGS. (2000). Geographic Names Information System. Retrieved March 23, 2024, from <https://edits.nationalmap.gov/apps/gaz-domestic/public/search/names/1398641> (cit. on p. 33).
- van IJzendoorn, C. O., de Vries, S., Hallin, C., & Hesp, P. A. (2021). Sea level rise outpaced by vertical dune toe translation on prograding coasts [Publisher: Nature Publishing Group]. *Scientific Reports*, *11*(1), 12792. <https://doi.org/10.1038/s41598-021-92150-x> (cit. on p. 78).
- Van Rijn, L. C. (1984). Sediment Transport, Part III: Bed forms and Alluvial Roughness. *Journal of Hydraulic Engineering*, *110*(12), 1733–1754. [https://doi.org/10.1061/\(ASCE\)0733-9429\(1984\)110:12\(1733\)](https://doi.org/10.1061/(ASCE)0733-9429(1984)110:12(1733)) (cit. on p. 24).
- Van Rijn, L. C. (2007). Unified View of Sediment Transport by Currents and Waves. I: Initiation of Motion, Bed Roughness, and Bed-Load Transport. *Journal of Hydraulic Engineering*, *133*(6), 649–667. [https://doi.org/10.1061/\(ASCE\)0733-9429\(2007\)133:6\(649\)](https://doi.org/10.1061/(ASCE)0733-9429(2007)133:6(649)) (cit. on p. 24).
- Van Thiel de Vries, J. S. M. (2009). Dune erosion during storm surges [Publisher: IOS Press]. Retrieved June 7, 2024, from <https://repository.tudelft.nl/islandora/object/uuid%3A885bf4b3-711e-41d4-98a4-67fc700461ff> (cit. on p. 24).
- Vasiliev, A., Kanevskiy, M., Cherkashov, G., & Vanshtein, B. (2005). Coastal dynamics at the Barents and Kara Sea key sites. *Geo-Marine Letters*, *25*(2-3), 110–120. <https://doi.org/10.1007/s00367-004-0192-z> (cit. on p. 9).
- Vermaire, J., Pisaric, M., Thienpont, J., Courtney Mustaphi, C., Kokelj, S., & Smol, J. (2013). Arctic climate warming and sea ice declines lead to increased storm surge activity. *Geophysical Research Letters*, *40*. <https://doi.org/10.1002/grl.50191> (cit. on pp. 14, 71).
- Voller, V., Cross, M., & Markatos, N. (1987). An Enthalpy Method for Convection-Diffusion Phase Change. *International Journal for Numerical Methods in Engineering*, Vol. 24, 271–284. <https://doi.org/10.1002/nme.1620240119> (cit. on p. 74).

- Vonk, J. E., Sánchez-García, L., van Dongen, B. E., Alling, V., Kosmach, D., Charkin, A., Semiletov, I. P., Dudarev, O. V., Shakhova, N., Roos, P., Eglington, T. I., Andersson, A., & Gustafsson, □. (2012). Activation of old carbon by erosion of coastal and subsea permafrost in Arctic Siberia [Publisher: Nature Publishing Group]. *Nature*, 489(7414), 137–140. <https://doi.org/10.1038/nature11392> (cit. on pp. 15, 71, 79).
- Wallace, K. (2019, July). Beyond Frozen. Retrieved April 19, 2024, from <https://projects.thestar.com/climate-change-canada/nunavut> (cit. on p. 6).
- Wegner, C., Bennett, K. E., Vernal, A. d., Forwick, M., Fritz, M., Heikkilä, M., Łacka, M., Lantuit, H., Laska, M., Moskalik, M., O'Regan, M., Pawłowska, J., Promińska, A., Rachold, V., Vonk, J. E., & Werner, K. (2015). Variability in transport of terrigenous material on the shelves and the deep Arctic Ocean during the Holocene. *Polar Research*. <https://doi.org/10.3402/polar.v34.24964> (cit. on p. 9).
- Wendler, G., & Kelley, J. (1988). On the Albedo of Snow in Antarctica: A Contribution to I.A.G.O. *Journal of Glaciology*, 34(116), 19–25. <https://doi.org/10.3189/S0022143000009011> (cit. on p. 9).
- Wendler, G., Moore, B., & Galloway, K. (2014). Strong Temperature Increase and Shrinking Sea Ice in Arctic Alaska. *The Open Atmospheric Science Journal*, 8(1), 7–15. <https://doi.org/10.2174/1874282301408010007> (cit. on p. 13).
- Westermann, S., Lüers, J., Langer, M., Piel, K., & Boike, J. (2009). The annual surface energy budget of a high-arctic permafrost site on Svalbard, Norway [Publisher: Copernicus GmbH]. *The Cryosphere*, 3(2), 245–263. <https://doi.org/10.5194/tc-3-245-2009> (cit. on p. 11).
- Whitehouse, P. L. (2018). Glacial isostatic adjustment modelling: Historical perspectives, recent advances, and future directions [Publisher: Copernicus GmbH]. *Earth Surface Dynamics*, 6(2), 401–429. <https://doi.org/10.5194/esurf-6-401-2018> (cit. on p. 8).
- Wobus, C., Anderson, R., Overeem, I., Matell, N., Clow, G., & Urban, F. (2011). Thermal erosion of a permafrost coastline: Improving process-based models using time-lapse photography. *Arctic, Antarctic, and Alpine Research*, 43(3), 474–484. <https://doi.org/10.1657/1938-4246-43.3.474> (cit. on p. 16).
- Woo, M.-k. (2012). *Permafrost Hydrology*. Springer. <https://doi.org/10.1007/978-3-642-23462-0> (cit. on p. 5).
- Yıldız, □. 1.15 Solar Energy (I. Dincer, Ed.). In: *Comprehensive Energy Systems* (I. Dincer, Ed.). Ed. by Dincer, I. Oxford: Elsevier, 2018, January, pp. 638–664. ISBN: 978-0-12-814925-6. <https://doi.org/10.1016/B978-0-12-809597-3.00117-6> (cit. on p. 31).
- Zhang, T., Stamnes, K., & Bowling, S. A. (1996). Impact of Clouds on Surface Radiative Fluxes and Snowmelt in the Arctic and Subarctic [Publisher: American Meteorological Society Section: Journal of Climate]. *Journal of Climate*, 9(9), 2110–2123. [https://doi.org/10.1175/1520-0442\(1996\)009<2110:IOCOSR>2.0.CO;2](https://doi.org/10.1175/1520-0442(1996)009<2110:IOCOSR>2.0.CO;2) (cit. on p. 9).
- Zhang, T. (2005). Influence of the seasonal snow cover on the ground thermal regime: An overview. *Reviews of Geophysics*, 43(4). <https://doi.org/10.1029/2004RG000157> (cit. on pp. 9, 10, 78).
- Zwieback, S., Kokelj, S. V., Günther, F., Boike, J., Grosse, G., & Hajnsek, I. (2018). Sub-seasonal thaw slump mass wasting is not consistently energy limited at the landscape scale [Publisher: Copernicus GmbH]. *The Cryosphere*, 12(2), 549–564. <https://doi.org/10.5194/tc-12-549-2018> (cit. on p. 12).



Differences with Arctic XBeach

We used Ravens et al. (2017) as a starting point for this study. The decoupling of the thermal module from XBeach brought some complications that required new modelling strategies. Additionally, we adopted some changes in methodology to account for processes not described by Ravens et al. (2017). Differences from the 'Arctic XBeach' model as described by Ravens et al. (2017) are described below.

- We added the Python wrapper to determine when XBeach should be activated based on the three criteria described in Section 4.1.1.
- We used enthalpy as the conserved quantity through the discretization of Equation 4.2 (Section 4.3.1). Previous work by Ravens et al. (2017), Ravens et al. (2023), and Kasper et al. (2023) facilitated this.
- The subsurface enthalpy was modelled using one-dimensional models perpendicular to the ground surface (Section 4.3.2). However, the dynamic updating of the morphology meant that these models could not realistically be expected to remain perpendicular to the ground surface. The horizontal grid was updated after each period of morphological change (i.e., subsequent activations of XBeach). Then, the model computed new locations for the perpendicular one-dimensional models. Enthalpy was interpolated to these new models based on distance from the old models.
- We added a new approach to compute the thaw depth from the ground enthalpy distribution. A minimum number of nodes at the surface end of each one-dimensional model is then prescribed that represents a minimum ice sheet thickness. This minimum thickness governs when the model considers the one-dimensional model as fully frozen (Section 4.3.4).
- We implemented a sub-grid time step in the thermal module to maintain a low CFL while not alternating the thermal and XBeach modules every few (simulated) seconds (Section 4.3.3).
- We computed the convective heat flux as a function of the difference between the surface temperature and the temperature of the external medium (water or air) dynamically from environmental drivers (Section 4.3.5).
- Similar to Ravens et al. (2017), a solar flux calculator was included in the model (Section 4.3.5). The solar flux calculator was dependent on three variables: time of day, day of year, and local surface angle. Due to the dynamic morphology, the local ground surface angle was subject to change during simulations. Therefore, the solar flux calculator updated the shortwave radiation flux for each grid cell dynamically based on the current local surface angle.

B

Thermo-morphological Model Flow Chart

Figure B.1 depicts a conceptual flow chart of the architecture of the thermo-morphological model. The developed thermo-morphological model consists of two parts: initialization and main loop.

Initialization

During initialization, key constants are set using the *config.yaml* file. This file contains all changeable run parameters. Firstly, temporal parameters are set. A temporal grid is generated based on the start and end times of the simulation, and the temporal resolution. For example, for a simulation of 1 day with a temporal resolution of 1 hour, 24 time steps are generated. Forcing data is loaded, a grid is generated, initial conditions are set (for both bathymetry, ground temperature, and ground enthalpy), soil property matrices are generated, and finally the solar flux calculator is precomputed. The solar flux calculator computes a factor for every day in a leap year for every whole angle between -90° and $+90^\circ$, generating a total of $180 \times 366 = 65880$ different factors. These factors are precomputed to avoid large computation times during the simulation.

Main Loop

After initialization, the main loop commences. The model loops through each time step determined during initialization. For each time step, the model first checks whether or not to generate output for that time step. The time steps for which to generate output are set from the start.

Then, it checks if XBeach should be activated this time step. If so, the erodible layer is determined, a params.txt file is generated, and XBeach is run. Then, the grid is updated to ensure all one-dimensional enthalpy models are still perpendicular to the surface, and enthalpy is interpolated from the old grid to the new grid.

After the XBeach module ends, the main loop continues on a temporal sub-grid. Since the thermal module is relatively fast, a sub-grid is employed. The thermal module loops through this sub-grid before continuing the main loop.

The first step of the sub-grid loop is the computation of the thermal boundary conditions, i.e., the surface heat flux. Firstly, the wet and dry domain are determined. Convective (also called sensible) heat fluxes are then computed. The latent heat flux and longwave radiation flux are each read from the forcing files. Finally, the solar flux is computed using the precomputed factors, and the solar radiation is read from a file.

Using the sum of all these heat fluxes, the temperature of the *ghost node* (artificial super-surface node) is determined, followed by the numerical update of enthalpy through the governing equations. Finally, the temperature is computed for each node, and the phase is determined from that. This process is repeated until the sub-grid finishes, after which the main loop continues.

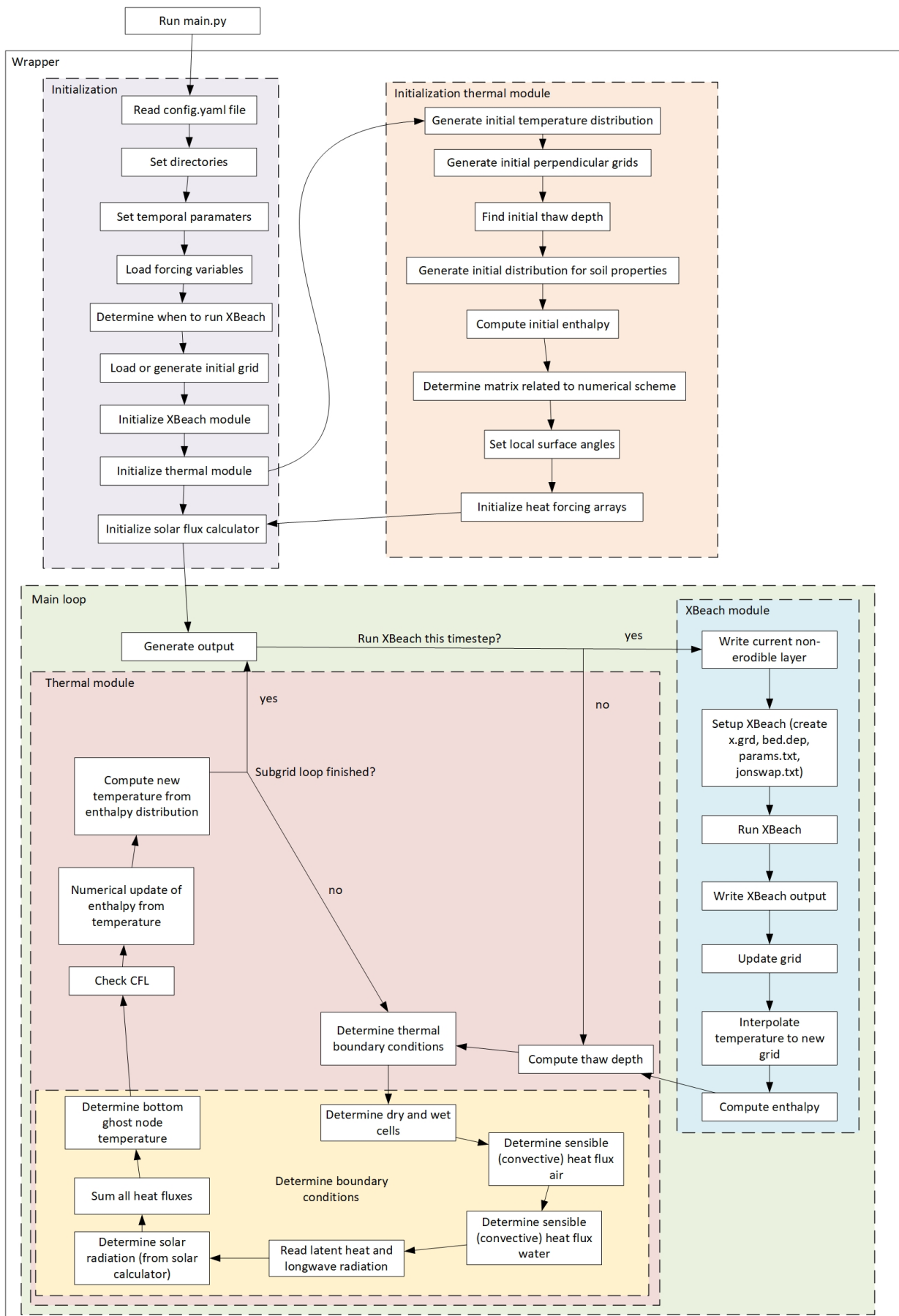
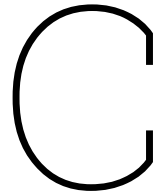


Figure B.1: Flow chart for the integrated thermo-morphological model.



Thermo-morphological Model Public Repository

We developed the thermo-morphological model for the current studies. The model is available publicly at:

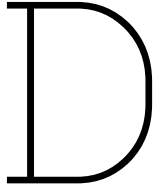
<https://github.com/khdebruijn/thermo-morphological-model>

This repository contains the final version of the thermo-morphological model used in this thesis. We calibrated and validated model settings.

We also provide a manual in the same repository. This manual contains an installation guide, usage guide, and helpful tips for post-processing. It is available at:

<https://github.com/khdebruijn/thermo-morphological-model/blob/main/manuals/manual.pdf>

Furthermore, the repository contains Jupyter Notebooks (.ipynb files) that we used to analyze results, create figures, etc.



Hydrodynamic Boundary Conditions

The current implementation of the XBeach module uses a JONSWAP spectrum (Hasselmann et al., 1973). This is done through a set of parameters which together describe a spectral wave boundary condition, which is used by XBeach to generate a random wave timeseries (Roelvink et al., 2009). A JONSWAP spectrum is described fully through the following parameters (Hooihout, 2015):

- H_{m0} : significant wave height of the wave spectrum [m],
- f_p : peak frequency of the wave spectrum [s^{-1}],
- γ : peak enhancement factor in the JONSWAP expression [-],
- s : directional spreading coefficient [-],
- D_p : main wave angle (i.e., direction of propagation) [$^\circ$],
- f_{nyq} : Nyquist frequency, (i.e., highest frequency used to generate the JONSWAP spectrum [s^{-1}]),
- Δf_j : step size frequency used to generate the JONSWAP spectrum [s^{-1}].

The random wave timeseries is used as forcing at the offshore boundary. To improve the modelling accuracy, a 'hotstart' is used in XBeach. This functionality uses output files from previous simulations to initialize an XBeach simulation. The advantage of the hotstart is that wave energy is present throughout the domain for the entire simulation, instead of needing the first time steps of the simulation to propagate from the offshore boundary to the coast, thus yielding more realistic results.

XBeach also includes the effects of wind in the model. It does so by including wind shear stress terms in the shallow water momentum equations for the entire computational domain. This requires wind speed and direction to be specified.

E

Challenge of Modelling Long-term Morphology

Problem description

The current model approach aims to reduce computational costs by only activating XBeach during periods when large morphological changes are expected. In practice, the model activates XBeach only during storms, with some inter-storm activations to allow for the slumping of thawed material from the bluff face. This means that the profile is only subject to storms; XBeach is not activated for the periods during which a stable beach is normally formed. This leads to the bathymetry resembling a storm profile. The beach may even erode completely (for default XBeach settings), resulting in the bluff toe being submerged. Without the beach, waves directly touch the bluff which induces higher erosion rates. Furthermore, alongshore transport is not included. This is the result of simulating in a single dimension. Ultimately, this methodology only includes short-term hydrodynamic and morphodynamic processes, i.e., storm and slumping events. Long-term processes are not modelled as XBeach is only activated to simulate the short-term processes. Long-term morphodynamic processes (i.e., rebuilding of the beach and alongshore transport) are underestimated, if not disregarded completely.

Considered solutions

Several solutions to this problem are possible. These mostly relate to re-attaching some equilibrium profile to the shoreline after a storm event. This equilibrium profile may be obtained from data or a parametrization. However, that changes the sediment balance. Additionally, bathymetric data on which to base an equilibrium profile is limited.

A different solution is to artificially induce onshore transport by adjusting the parameters that determine onshore transport related to wave asymmetry (Schambach et al., 2018; Sanuy and Jiménez, 2019; Kombiadou et al., 2021). By increasing the values of these parameters, onshore transport may be enhanced, which allows XBeach to more efficiently transport sediment onshore.

We also considered including an artificial longshore transport gradient (Appendix K).

Negative feedback loop

Additionally, the model formulation implicitly includes a negative feedback loop. The parametrization by Stockdon et al. (2006) is used to determine whether or not XBeach is activated (Section 4.1.1). This formulation uses the beach slope around the waterline. When the beach is eroded during large storm events, the waterline reaches the bluff. The slope around the waterline increases drastically, leading to a larger predicted run-up.

For lower waves and water levels (i.e., lower energy conditions), the model may now activate XBeach as the predicted run-up is higher and sooner exceeds the set threshold. Hence, XBeach is then activated for lower energy conditions. This negative feedback loop helps build up the beach after storms, which helps mitigate the problem of only activating XBeach during storms. However, further calibration is required as XBeach tends to overestimate erosion (Carrion-Bertran et al., 2024).

F

Calibrated Model Configuration

The complete configuration of the best calibration simulation is given below. These model settings were used to obtain the predicted bluff retreat for the second period shown in Figure 5.23.

```
1 # data parameters
2
3 data:
4   storm_data_path : 'database/ts_datasets/storms_engelstad.csv' # path to storm
5   ↵ dataset
6   forcing_data_path : 'database/ts_datasets/era5.csv' # path to forcing data
7   # initial_ground_temp_path : "database/ts_datasets/ground_temperature_erikson.csv"
8   ↵ # path to initial ground temperature
9   init_multi_linear_approx : True # when starting with era5 initial conditions for
10  ↵ soil temperature, 'init_multi_linear_approx' can be set to 'True' to use
11  ↵ multi-linear regression to make initial conditions more like erikson's measured
12  ↵ data
13
14 # model settings
15 model:
16   longitude : -143.7 # longitude of the study site
17   latitude : 70.13 # latitude of the study site
18   time_start : '01-01-2012' # DD-MM-YY starting time (if -1 take entire
19   ↵ dataset)
20   time_end : '01-01-2016' # DD-MM-YY stopping time (if -1 take entire
21   ↵ dataset)
22   timestep : 1 # size of time steps (in hours)
23   call_xbeach_inter : 168 # xbeach is called during inter-storm periods every X
24   ↵ (wrapper) time steps (default: 168, i.e. 1 week)
25   time_zone_diff : -8 # [hours] relative difference in hours with respect to UTC.
26   ↵ For Alaska equals -8.
27   repeat_sim : 1 # [-] number of times to repeat the simulation
28   spin_up_time : 1 # [years] spin up time of the thermal module, during which
29   ↵ no morphological update is performed (NOT USED YET, TO BE IMPLEMENTED)
30
31 # wrapper parameters:
32 wrapper:
33   sea_ice_threshold : 0.30 # Only run xbeach if sea ice fraction is below
34   ↵ threshold, otherwise assume all wave action attenuated
35   xb_threshold : 1.0 # [m + MSL] threshold value for total water level +
36   ↵ R2%
```

```

25    CFL_thermal          : 0.5      # maximum CFL for thermal module
26    CFL_xbeach           : 0.7      # maximum CFL for XBeach module
27
28 # bathymetry parameters
29 bathymetry:
30    xfile              : 'x.grd'    # file used for the grid (x-direction)
31    depfile             : 'bed.dep'   # file used for the bed
32    grid_orientation: 88.14 # [degrees], orientation of bluff face with respect to
   ↳ east (ccw). The current orientation is calculated in the
   ↳ 'generate_bathymetry.ipynb' notebook
33    ppwl               : 40        # number of points in the grid per wavelength. Default 20.
34    nx                  : 3         # number of points in initial grid. Set to 'None' if this
   ↳ should be based on ppwl.
35    with_nx             : False     # whether or not to use the number of points specified
   ↳ with nx
36
37 # schematized bathymetry parameters
38 with_schematized_bathymetry : True    # whether or not to generate a schematized
   ↳ bathymetry upon initialization
39    bluff_flat_length    : 100      # [m] length of the flat attached to the crest
   ↳ of the bluff
40    bluff_height          : 12       # [m] height of the bluff
41    bluff_slope            : 1        # [-] slope of the bluff, i.e., height/width
42    beach_width            : 12.5     # [m] width of the beach
43    beach_slope             : 0.1      # [-] slope of the beach, i.e., height/width
44    nearshore_max_depth    : 3        # [m] maximum depth of the nearshore
45    nearshore_slope          : 0.03     # [-] slope of the nearshore section, i.e.,
   ↳ height/width
46    offshore_max_depth     : 5        # [m] maximum offshore depth
47    offshore_slope          : 0.007    # [-] slope of the offshore section, i.e.,
   ↳ height/width
48    continental_flat_width : 400      # [m] width of the continental flat section
49    with_artificial          : True     # whether or not to extend to bathymetry with
   ↳ an artificial depth increase (if required by xbeach)
50    artificial_max_depth    : 10       # [m] maximum depth of the artificial section
   ↳ (wave heights in dataset are defined at a depth of 10m, so that value is
   ↳ recommended)
51    artificial_slope          : 0.02     # [-] slope of the artificial section, i.e.,
   ↳ height/width
52    N                      : 100      # number of points of each section
53    artificial_flat          : 60       # [m] length of flat section at the end of
   ↳ artificial slope
54
55 # xbeach parameters
56 xbeach:
57    # general settings
58    with_xbeach : True    # include the xbeach module in the model, default true
59    version      : '1.24'   # version of xbeach used
60
61    # physical processes:
62    with_wind      : False   # include wind in the xbeach model
63    with_ne_layer  : True    # if True include 'struct' (and thereby ne_layer) in XBeach
   ↳ computation
64
65    # grid settings
66    thetamin     : 0        # minimum angle

```

```

67      thetamax : 360 # maximum angle
68      dtheta   : 360 # bin width
69      thetanaut : 1 # for coordinate system
70
71      # hydrodynamics settings
72      wbctype : 'jons' # type of wave boundary condition
73      bcfile  : 'jonswap.txt' # file containing the bc specifications
74      rho_sea_water : 1025 # [kg/m3] density (sea) water
75
76      # sediment properties
77      dryslp    : 0.6 # [dz/dx] Critical avalanching slope above water (dz/dx and
78      #          ↳ dz/dy)
79      wetslp    : 0.1 # [dz/dx] Critical avalanching slope below water (dz/dx and
80      #          ↳ dz/dy)
81      D50       : 0.000036 # [m] mean grain size, value from Nando (personal
82      #          ↳ communication)
83      rho_solid  : 2650 # [kg/m3] density of sediment particles
84      bedfriccoef : 0.02 # [-] bed friction coefficient
85
86      # morphological parameters
87      lsgrad : 0.0 # [1/m] Factor to include longshore transport gradient in 1d
88      #          ↳ simulations; dsy/dy=lsgrad*sy; dimension 1/length scale of longshore gradients
89
90      # wave asymmetry factors
91      facSk: 0.0 # [-] Calibration factor time averaged flows due to wave skewness.
92      #          ↳ Default is 0.15.
93      facAs: 0.0 # [-] Calibration factor time averaged flows due to wave asymmetry.
94      #          ↳ Default is 0.20.
95      facua: 0.0 # [-] Calibration factor time averaged flows due to wave skewness and
96      #          ↳ asymmetry. Default is 0.175.
97
98      # parameters for writing the first storm
99      write_first_storms : 2 # [-] The first N number of storms to write. This doesn't
100     #          ↳ include intermediate XBeach runs
101     tintg_storms : 100 # [s] The output interval (only used if first storms are being
102     #          ↳ written)
103
104      # thermal moodel parameters
105      thermal:
106          # general
107          with_solar    : True # include shortwave solar radiation in thermal computation
108          #          ↳ step
109          with_longwave : True # include longwave radiation (incoming & outgoing) in
110          #          ↳ thermal computation step
111          with_latent   : True # include latent heat in thermal computation step
112          surface_flux_factor : 1 # [-] factor that multiplies with the total surface heat
113          #          ↳ flux, to account for reduced convective transport due to the peat layer
114          surface_flux_angle : 20 # [degrees] the threshold angle above which the
115          #          ↳ surface_flux_factor is not applied
116
117      # model properties
118      dt           : 36 # [s] time step used in the thermal model on the temporal
119      #          ↳ subgrid
120      grid_resolution : 150 # number of points for each 1D thermal model
121      max_depth      : 15 # [m], the maximum depth of the 1D thermal model

```

```

108 T_melt           : 273.15 # [K] Melting temperature at the interface of water/air
109   ↵ and bluff
110 grid_interpolation : "linear_interp_z" # method for interpolating to new grid. Can
111   ↵ be "linear_interp_with_nearest" or "linear_interp_z".
112 N_thaw_threshold: 3 # number of grid points that need to be frozen before being
113   ↵ counted as non-erodible surface

114
115 # solar flux calculator
116 with_solar_flux_calculator : True # include solar flux calculator in the
117   ↵ computation (if False, the every surface is treated as flat); requires
118   ↵ 'with_solar: True'
119 angle_min       : -89 # [degrees] minimum angle used in the solar flux calculator map
120 angle_max       : 89 # [degrees] maximum angle used in the solar flux calculator map
121 delta_angle     : 1 # [degrees] step size of angle used in the solar flux calculator
122   ↵ map
123 t_start         : '2000-01-01' # minimum date used in the solar flux calculator map
124 t_end           : '2001-01-01' # maximum date used in the solar flux calculator map
125
126 # guess for convective heat transfer from water
127 with_convective_transport_water_guess : True # include a guess of convective heat
128   ↵ transfer from water in thermal computation step. If False, a more sophisticated
129   ↵ computation is performed
130 hc_guess        : 500 # [W/m2/K], guess for the convective heat transfer coefficient from
131   ↵ water (from Kobayashi et al, 1999)

132
133 # water properties
134 MSL            : 0 # [m], water level relative to outputted local water level at
135   ↵ which is switched from wet to dry (positive means higher than output water
136   ↵ level)
137 L_water_ice    : 334000 # [J/kg] latent heat of fusion water-ice
138 rho_water      : 1000 # [kg/m3] water density
139 rho_ice         : 971 # [kg/m3] density ice
140
141 # soil properties
142 rho_soil        : "None" # [kg/m3] density soil, constant for frozen/unfrozen. If
143   ↵ "None", density is calculated as "nb * rho_water + (1-nb) * rho_particle".
144 rho_particle    : 2650 # [kg/m3] particle density of soil, only used if
145   ↵ "rho_soil = None"
146 nb_min          : 0.65 # [-] minimum ground ice content (Ravens et al, 2023:
147   ↵ 0.65 - 0.45)
148 nb_max          : 0.65 # [-] maximum ground ice content (Ravens et al, 2023:
149   ↵ 0.65 - 0.45)
150 nb_min_depth   : 1.5 # [m] end switch from max to min porosity (adapted from
151   ↵ Ravens, thermal model)
152 nb_max_depth   : 0.5 # [m] start switch from max to min porosity (adapted
153   ↵ from Ravens, thermal model)
154 c_soil_frozen   : 4600000 # [J/K/m3] volumetric heat capacity for frozen soil
155   ↵ (Ravens et al, 2023) (= specific heat capacity)
156 c_soil_unfrozen : 7000000 # [J/K/m3] volumetric heat capacity for unfrozen soil
157   ↵ (Ravens et al, 2023)
158 k_soil_frozen_min : 2.7 # [W/m/K] minimum thermal conductivity for frozen soil
159   ↵ (Ravens et al, 2023: 0.7 - 2.7)
160 k_soil_frozen_max : 2.7 # [W/m/K] maximum thermal conductivity for frozen soil
161   ↵ (Ravens et al, 2023: 0.7 - 2.7)
162 k_soil_unfrozen_min : 0.6 # [W/m/K] minimum thermal conductivity for unfrozen soil
163   ↵ (Ravens et al, 2023: 0.6 - 1.5)

```



```
189
190     "wind_velocity",
191     "wind_direction",
192 ]
193
194 save_ground_temp_layers: [0, 0.5, 1.0, 2.0, 2.95] # [m] depths at which ground
195   ↵ temperature is written separately to csv file
heat_fluxes: ['total_heat_flux[W/m2]', 'long_wave_radiation_flux[W/m2]',
195   ↵ 'solar_radiation_flux[W/m2]', 'latent_heat_flux[W/m2]',
195   ↵ 'convective_heat_flux[W/m2]']    # define heat fluxes to be used in memory
195   ↵ output
196
```



Base Configuration

The complete configuration of the base (proof-of-concept) run is given below. These model settings were used to perform the baseline run for the sensitivity analysis.

```
1 # data parameters
2 data:
3   storm_data_path : 'database/ts_datasets/storms_engelstad.csv' # path to storm
4   ↵ dataset
5   forcing_data_path : 'database/ts_datasets/era5.csv' # path to forcing data
6   # initial_ground_temp_path : "database/ts_datasets/ground_temperature_erikson.csv"
7   ↵ # path to initial ground temperature
8   init_multi_linear_approx : True # when starting with era5 initial conditions for
9   ↵ soil temperature, 'init_multi_linear_approx' can be set to 'True' to use
10  ↵ multi-linear regression to make initial conditions more like erikson's measured
11  ↵ data
12
13 # model settings
14 model:
15   longitude : -143.7 # longitude of the study site
16   latitude : 70.13 # latitude of the study site
17   time_start : '01-01-2017' # DD-MM-YY starting time (if -1 take entire
18   ↵ dataset)
19   time_end : '01-01-2019' # DD-MM-YY stopping time (if -1 take entire
20   ↵ dataset)
21   timestep : 1 # size of time steps (in hours)
22   call_xbeach_inter : 168 # xbeach is called during inter-storm periods every X
23   ↵ (wrapper) time steps (default: 168, i.e. 1 week)
24   time_zone_diff : -8 # [hours] relative difference in hours with respect to UTC.
25   ↵ For Alaska equals -8.
26   repeat_sim : 1 # [-] number of times to repeat the simulation
27   spin_up_time : 1 # [years] spin up time of the thermal module, during which
28   ↵ no morphological update is performed (NOT USED YET, TO BE IMPLEMENTED)
29
30 # wrapper parameters:
31 wrapper:
32   sea_ice_threshold : 0.30 # Only run xbeach if sea ice fraction is below
33   ↵ threshold, otherwise assume all wave action attenuated
34   xb_threshold : 1.0 # [m + MSL] threshold value for total water level +
35   ↵ R2%
36   CFL_thermal : 0.5 # maximum CFL for thermal module
```

```

25    CFL_xbeach           : 0.7      # maximum CFL for XBeach module
26
27 # bathymetry parameters
28 bathymetry:
29     xfile          : 'x.grd'    # file used for the grid (x-direction)
30     depfile        : 'bed.dep'   # file used for the bed
31     grid_orientation: 88.14    # [degrees], orientation of bluff face with respect to
      ↳ east (ccw). The current orientation is calculated in the
      ↳ 'generate_bathymetry.ipynb' notebook
32     ppwl           : 40        # number of points in the grid per wavelength. Default 20.
33     nx              : 3         # number of points in initial grid. Set to 'None' if this
      ↳ should be based on ppwl.
34     with_nx        : False     # whether or not to use the number of points specified
      ↳ with nx
35
36 # schematized bathymetry parameters
37     with_schematized_bathymetry : True    # whether or not to generate a schematized
      ↳ bathymetry upon initialization
38     bluff_flat_length       : 100     # [m] length of the flat attached to the crest
      ↳ of the bluff
39     bluff_height           : 12      # [m] height of the bluff
40     bluff_slope            : 1       # [-] slope of the bluff, i.e., height/width
41     beach_width            : 12.5    # [m] width of the beach
42     beach_slope             : 0.1     # [-] slope of the beach, i.e., height/width
43     nearshore_max_depth    : 3       # [m] maximum depth of the nearshore
44     nearshore_slope         : 0.03    # [-] slope of the nearshore section, i.e.,
      ↳ height/width
45     offshore_max_depth     : 5       # [m] maximum offshore depth
46     offshore_slope          : 0.007   # [-] slope of the offshore section, i.e.,
      ↳ height/width
47     continental_flat_width : 400    # [m] width of the continental flat section
48     with_artificial         : True    # whether or not to extend to bathymetry with
      ↳ an artificial depth increase (if required by xbeach)
49     artificial_max_depth   : 10      # [m] maximum depth of the artificial section
      ↳ (wave heights in dataset are defined at a depth of 10m, so that value is
      ↳ recommended)
50     artificial_slope        : 0.02    # [-] slope of the artificial section, i.e.,
      ↳ height/width
51     N                      : 100    # number of points of each section
52     artificial_flat         : 60      # [m] length of flat section at the end of
      ↳ artificial slope
53
54 # xbeach parameters
55 xbeach:
56     # general settings
57     with_xbeach : True    # include the xbeach module in the model, default true
58     version      : '1.24'   # version of xbeach used
59
60     # physical processes:
61     with_wind    : False   # include wind in the xbeach model
62     with_ne_layer: True    # if True include 'struct' (and thereby ne_layer) in XBeach
      ↳ computation
63
64     # grid settings
65     thetamin   : 0        # minimum angle
66     thetamax   : 360     # maximum angle

```

```

67 dtheta      : 360 # bin width
68 thetanaut : 1 # for coordinate system
69
70 # hydrodynamics settings
71 wbctype : 'jons' # type of wave boundary condition
72 bcfile  : 'jonswap.txt' # file containing the bc specifications
73 rho_sea_water : 1025 # [kg/m3] density (sea) water
74
75 # sediment properties
76 dryslp      : 1.0 # [dz/dx] Critical avalanching slope above water (dz/dx and
    #                  dz/dy)
77 wetslp      : 0.1 # [dz/dx] Critical avalanching slope below water (dz/dx and
    #                  dz/dy)
78 D50         : 0.000036 # [m] mean grain size, value from Nando (personal
    #                  communication)
79 rho_solid   : 2650 # [kg/m3] density of sediment particles
80 bedfriccoef : 0.02 # [-] bed friction coefficient
81
82 # morphological parameters
83 lsgrad : 0.0 # [1/m] Factor to include longshore transport gradient in 1d
    # simulations; dsy/dy=lsgrad*sy; dimension 1/length scale of longshore gradients
84
85 # wave asymmetry factors
86 facSk: 0.40 # [-] Calibration factor time averaged flows due to wave skewness.
    # Default is 0.15.
87 facAs: 0.45 # [-] Calibration factor time averaged flows due to wave asymmetry.
    # Default is 0.20.
88 facua: 0.425 # [-] Calibration factor time averaged flows due to wave skewness and
    # asymmetry. Default is 0.175.
89
90 # parameters for writing the first storm
91 write_first_storms : 2 # [-] The first N number of storms to write. This doesn't
    # include intermediate XBeach runs
92 tintg_storms : 100 # [s] The output interval (only used if first storms are being
    # written)
93
94 # thermal moodel parameters
95 thermal:
96     # general
97     with_solar      : True # include shortwave solar radiation in thermal computation
    # step
98     with_longwave : True # include longwave radiation (incoming & outgoing) in
    # thermal computation step
99     with_latent    : True # include latent heat in thermal computation step
100    surface_flux_factor : 1 # [-] factor that multiplies with the total surface heat
    # flux, to account for reduced convective transport due to the peat layer
101    surface_flux_angle : 20 # [degrees] the threshold angle above which the
    # surface_flux_factor is not applied
102
103    # model properties
104    dt             : 36 # [s] time step used in the thermal model on the temporal
    # subgrid
105    grid_resolution : 150 # number of points for each 1D thermal model
106    max_depth      : 15 # [m], the maximum depth of the 1D thermal model
107    T_melt         : 273.15 # [K] Melting temperature at the interface of water/air
    # and bluff

```

```

108 grid_interpolation : "linear_interp_z" # method for interpolating to new grid. Can
109   ↳ be "linear_interp_with_nearest" or "linear_interp_z".
110 N_thaw_threshold: 3 # number of grid points that need to be frozen before being
111   ↳ counted as non-erodible surface
112
113 # solar flux calculator
114 with_solar_flux_calculator : True # include solar flux calculator in the
115   ↳ computation (if False, the every surface is treated as flat); requires
116   ↳ 'with_solar: True'
117 angle_min : -89 # [degrees] minimum angle used in the solar flux calculator map
118 angle_max : 89 # [degrees] maximum angle used in the solar flux calculator map
119 delta_angle : 1 # [degrees] step size of angle used in the solar flux calculator
120   ↳ map
121 t_start : '2000-01-01' # minimum date used in the solar flux calculator map
122 t_end : '2001-01-01' # maximum date used in the solar flux calculator map
123
124 # guess for convective heat transfer from water
125 with_convective_transport_water_guess : True # include a guess of convective heat
126   ↳ transfer from water in thermal computation step. If False, a more sophisticated
127   ↳ computation is performed
128 hc_guess : 500 # [W/m2/K], guess for the convective heat transfer coefficient from
129   ↳ water (from Kobayashi et al, 1999)
130
131 # water properties
132 MSL : 0 # [m], water level relative to outputted local water level at
133   ↳ which is switched from wet to dry (positive means higher than output water
134   ↳ level)
135 L_water_ice : 334000 # [J/kg] latent heat of fusion water-ice
136 rho_water : 1000 # [kg/m3] water density
137 rho_ice : 971 # [kg/m3] density ice
138
139 # soil properties
140 rho_soil : "None" # [kg/m3] density soil, constant for frozen/unfrozen. If
141   ↳ "None", density is calculated as "nb * rho_water + (1-nb) * rho_particle".
142 rho_particle : 2650 # [kg/m3] particle density of soil, only used if
143   ↳ "rho_soil = None"
144 nb_min : 0.65 # [-] minimum ground ice content (Ravens et al, 2023:
145   ↳ 0.65 - 0.45)
146 nb_max : 0.65 # [-] maximum ground ice content (Ravens et al, 2023:
147   ↳ 0.65 - 0.45)
148 nb_min_depth : 1.5 # [m] end switch from max to min porosity (adapted from
149   ↳ Ravens, thermal model)
150 nb_max_depth : 0.5 # [m] start switch from max to min porosity (adapted
151   ↳ from Ravens, thermal model)
152 c_soil_frozen : 4600000 # [J/K/m3] volumetric heat capacity for frozen soil
153   ↳ (Ravens et al, 2023) (= specific heat capacity)
154 c_soil_unfrozen : 7000000 # [J/K/m3] volumetric heat capacity for unfrozen soil
155   ↳ (Ravens et al, 2023)
156 k_soil_frozen_min : 2.7 # [W/m/K] minimum thermal conductivity for frozen soil
157   ↳ (Ravens et al, 2023: 0.7 - 2.7)
158 k_soil_frozen_max : 2.7 # [W/m/K] maximum thermal conductivity for frozen soil
159   ↳ (Ravens et al, 2023: 0.7 - 2.7)
160 k_soil_unfrozen_min : 0.6 # [W/m/K] minimum thermal conductivity for unfrozen soil
161   ↳ (Ravens et al, 2023: 0.6 - 1.5)
162 k_soil_unfrozen_max : 0.6 # [W/m/K] maximum thermal conductivity for unfrozen soil
163   ↳ (Ravens et al, 2023: 0.6 - 1.5)

```

```

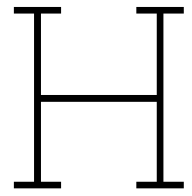
142 depth_constant_k      : 1 # [m] depth at which k reaches its maximum value. k
143   ↳ remains constant below this depth (Ravens, MATLAB script)
144 geothermal_gradient : 0.025 # [K/m] geothermal gradient, used as the boundary
145   ↳ condition at the bottom of each 1D model
146
147 # output
148 output:
149   output_res           : 12 # temporal resolution of output variables in hours
150     ↳ (i.e., model outputs given variable names every X hours)
151   use_default_output_path : False # If True, the model creates a subfolder in the
152     ↳ same folder as the configuration file, and stores all results there. If False,
153     ↳ the output_path variable is used and a subfolder with the run_id is created at
154     ↳ this location
155   output_path          : "P:/11210070-usgscoop-202324-arcticxb/runs/" #
156     ↳ "P:/11210070-usgscoop-202324-arcticxb/runs/" (absolute path to p-drive)
157   write_computation_time : True # If True, the model writes the computation time
158     ↳ between this output time and the last output time
159   output_vars           : [ # list of output variables
160     "timestamps",
161     "timestep_ids",
162     "timestep_output_ids",
163     "xbeach_times",
164
165     "xgr",
166     "zgr",
167     "angles",
168
169     "wave_height",
170     "run_up",
171     "storm_surge",
172     "wave_energy",
173     "radiation_stress_xx",
174     "radiation_stress_xy",
175     "radiation_stress_yy",
176     "mean_wave_angle",
177     "velocity_magnitude",
178     "orbital_velocity",
179
180     "thaw_depth",
181     "abs_xgr",
182     "abs_zgr",
183     "ground_temperature_distribution",
184     "ground_enthalpy_distribution",
185     "2m_temperature",
186     "sea_surface_temperature",
187
188     "solar_radiation_factor",
189     "solar_radiation_flux",

```

```

190     "wind_direction",
191 ]
192
193 save_ground_temp_layers: [0, 0.5, 1.0, 2.0, 2.95] # [m] depths at which ground
   → temperature is written separately to csv file
194 heat_fluxes: ['total_heat_flux[W/m2]', 'long_wave_radiation_flux[W/m2]',
   → 'solar_radiation_flux[W/m2]', 'latent_heat_flux[W/m2]',
   → 'convective_heat_flux[W/m2]'] # define heat fluxes to be used in memory
   → output
195
196 # used for sensitivity analysis of the hydrodynamic and thermodynamic drivers
197 sensitivity:
198 # hydrodynamics
199 term_water_level : 0 # [m] term added to the water level for the entire
   → simulation
200 factor_wave_height : 1 # [-] factor multiplied with the wave height for the
   → entire simulation
201 factor_wave_period : 1 # [-] factor multiplied with the wave height for the
   → entire simulation
202
203 # thermodynamics
204 factor_latent_heat_flux : 1 # [-] factor multiplied with the latent heat flux
   → for the entire simulation
205 factor_convective_heat_flux : 1 # [-] factor multiplied with the convective heat
   → flux (both submerged and above water) for the entire simulation
206 factor_longwave_heat_flux : 1 # [-] factor multiplied with the longwave heat
   → flux for the entire simulation
207 factor_shortwave_heat_flux : 1 # [-] factor multiplied with the shortwave heat
   → flux for the entire simulation
208 term_sea_temperature : 0 # [K] term added to the sea temperature for the
   → entire simulation
209 term_2m_air_temperature : 0 # [K] term added to the 2m air temperature for the
   → entire simulation

```



Ordered Sensitivity Analysis

Figure H.1 depicts the complete sensitivity analysis performed in Section 5.4 with all parameters, but categorized by (sub-)level. These levels are:

- **Level 1:** Individual model parameters
 - *sub-level 1:* Physical parameters
 - *sub-level 2:* Model parameters
 - *sub-level 3:* Bathymetric parameters
- **Level 2:** Environmental drivers
 - *sub-level 1:* Hydrodynamic forcing
 - *sub-level 2:* Thermodynamic forcing
- **Level 3:** Thermal module & solar flux calculator

Further explanation of each level is provided in Section 5.4.

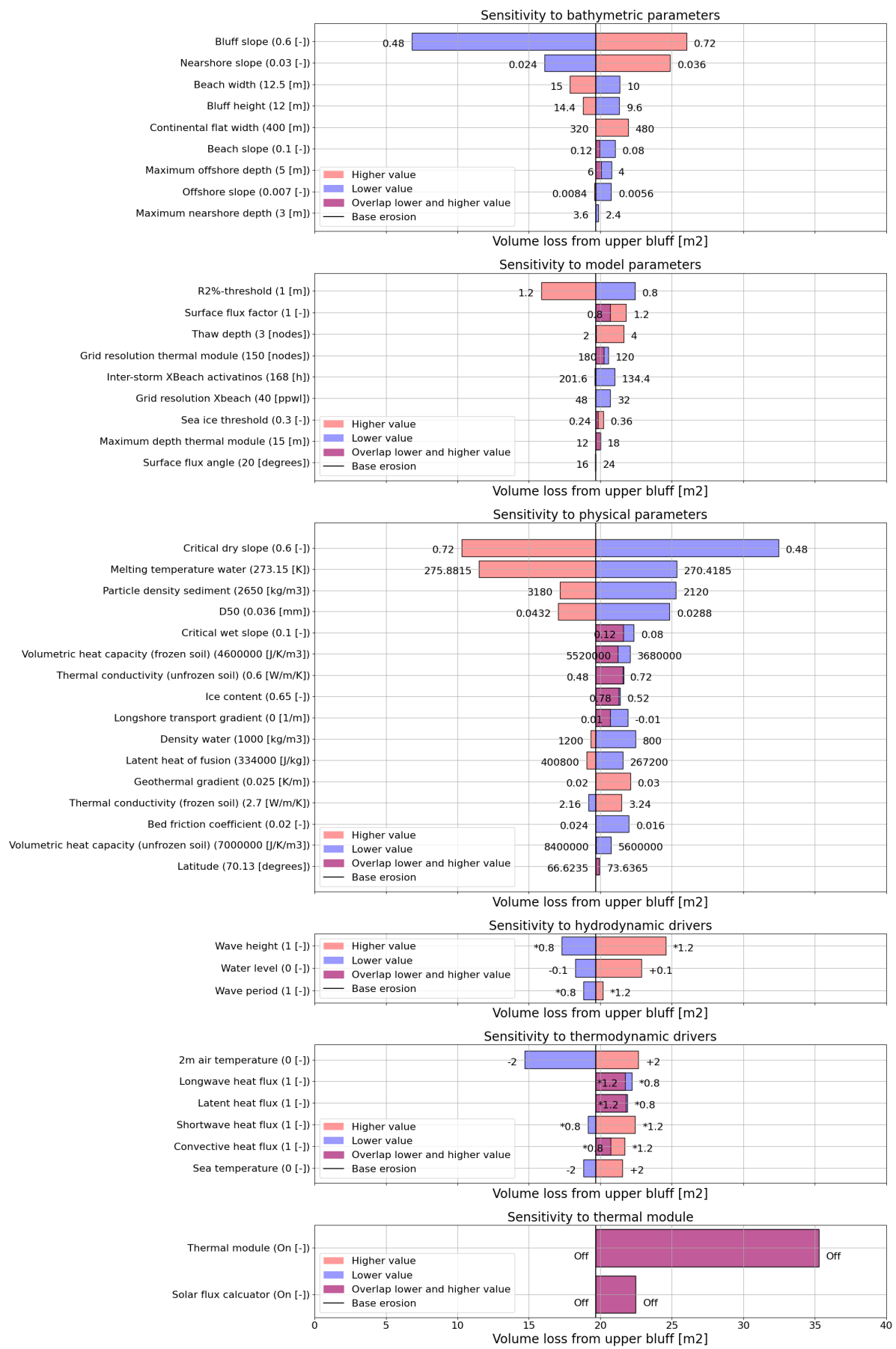


Figure H.1: Results of the sensitivity analysis. Each bar represents the difference in volume loss from the upper bluff between the baseline simulation and simulations with different parameter settings, in descending order from most to least sensitive.

These parameter settings are either lower or higher relative to the base simulation. Parameter settings from the base simulation are shown next to their respective variable. We ordered the parameters by the sum of the absolute difference between the base simulation and the simulation with varied parameters. This figure shows the same results as Figure 5.30 but is ordered by level and sub-level.

I

Discussion of New Numeric Parameters

The thermo-morphological model includes some newly introduced semi-physical parameters. We reflect on these parameters and their relative importance below.

- **Thaw threshold:**

The thaw threshold was used as a threshold value to determine the thickness a frozen layer must have before a non-frozen layer below it is treated as non-erodible. If no threshold is used, small periods of freezing temperatures (e.g., during the night) could lead to the freezing of only the surface nodes, leading to the entire domain being treated as non-erodible due to what can be viewed as a thin sheet of ice at the surface. Using a lower threshold value does not seem to affect erosion (Figure 5.30). This is unexpected, as a lower threshold value should result in a frozen soil surface being treated as non-erodible sooner, which should limit erosion. Conversely, a higher threshold results in a slight increase of ΔV_{ub} , as a frozen surface is less treated as non-erodible later (i.e., when more nodes are frozen) and therefore more available for erosion. If this parameter is continued to be used, it should be researched more in-depth to uncover the processes leading to this increase in erosion, especially since we did not find any similar approaches used previously. We did not find any literature that use a similar thaw threshold, though its effect can be compared to bed armoring (Reed et al., 1999), as the activity of the active layer is constrained by some threshold. In our application, this threshold depends on temperature of the upper layer, though in the case of bed armoring, this threshold (of motion) usually depends on sediment size.

- **Inter-storm XBeach activations:**

We used the number of inter-storm XBeach activations to determine with which interval XBeach is activated regardless of the presence of storms or sea ice. XBeach is used to perform the morphological update. The inter-storm activations were done to allow the slumping of sediments from the bluff face to occur. The process of slumping uncovers new material in the bluff face, which can then start to heat up through surface heat fluxes (Ravens et al., 2023). Increasing the number of inter-storm XBeach activations (i.e., reducing the interval) results in a tighter coupling of the thermal and XBeach modules, and results in additional computational resources being allocated to activating XBeach.

Figure 5.30 shows that a higher amount of inter-storm activations (i.e., lower interval) is associated with higher bluff erosion. A tighter coupling means more slumping events occur. When deeper soil layers are uncovered due to slumping, they receive more heat as the surface flux is generally higher than the conductive heat flux within the soil. This enhances the erosion process. A longer interval (i.e., looser coupling) does not result in less erosion, indicating that a minimum might have been found for values below 168 hours (i.e., 1 week).

- **$R_{2\%}$ -threshold:**

The 2% run-up threshold governs when XBeach is activated based on the run-up predicted from

wave conditions. Figure 5.30 shows that the value chosen for this threshold affects ΔV_{ub} . Generally, a lower threshold value leads to more XBeach activations and therefore more erosion. This is true as long as the number of XBeach activations is the bottleneck for bluff erosion. XBeach activations mainly induce bluff erosion if a slumping event is ready to occur, or if the total water level reaches the bluff toe, which can induce additional convective heat transfer from water into the bluff and thereby lead to additional bluff erosion. If the bluff face is already thawed, the water reaching the bluff toe can lead to a reduction in critical slope at the bluff toe, inducing avalanching of the entire bluff until it is stable under the current wet/dry conditions (i.e., the local slope is equal to the critical wet slope in the wet domain and equal to the critical dry slope in the dry domain). Turner et al. (2024) employed a similar threshold strategy in their early warning system for coastal hazards resulting from storms. They use a similar check to assess whether or not XBeach is activated, though their application does not require the modelling of long-term morphodynamic processes. They use a threshold value equal to the elevation of the dune toe, which we also recommend for future research (Section 7.2.1).

- **Sea ice threshold:**

The sea ice threshold was used to determine when storms would affect the coast. If the offshore sea ice coverage is higher than the predefined threshold, any waves are assumed to be fully attenuated such that the storm does not affect the coast. This threshold mostly depends on data availability and is less useful as a calibration parameter. Figure 5.30 showed little dependency on this threshold, because the timeseries used for the hydrodynamic forcing already includes sea ice, and does not provide any data when the sea ice coverage is larger than 30%.

The sea ice threshold can be used as a proxy for researching the influence of (changing) sea ice coverage. For instance, increasing the threshold effectively means more storms are included in the modelling process and the yearly window during which sea ice concentration is below the threshold is widened.

This threshold has been used in other studies of hydrodynamics in the Arctic (e.g., Engelstad et al., 2023). Furthermore, ERA5 employs a threshold of 30% for global climate datasets (C3S, 2018).

- **Surface flux factor & surface flux angle:**

The surface flux factor and surface flux angle were introduced as calibration factors for the solar flux calculator. There is a lack of measured data on shortwave solar radiation on Barter Island, which meant that the solar flux calculator had to be calibrated and validated implicitly through the modelling of the ground temperature for which there was data. This resulted in the factor being set to 1 (i.e., not being of further influence on the surface heat flux). Figure 5.30 shows that the solar flux calculator does influence bluff erosion rates. Additionally, the surface flux factor exerts some influence on ΔV_{ub} . However, the surface flux angle hardly does. This is likely due to their effect being non-linear and only relevant when both factors are varied at the same time. During calibration, we found the best model predictions for a surface flux factor of one and thus effectively omitted the factor entirely during the sensitivity analysis as varying the surface flux angle has no effect when the factor is set to one.

Additionally, the relevance of these two factors might also depend on the specific case study and we therefore recommend that these factors are still included during recalibration for other study sites where different values apply for latitude, bluff slope, and thickness of the insulating peat layer.

Kettridge and Baird (2008) employ a similar temperature model to simulate ground temperature using Neumann boundary conditions. Their results were promising, but they found that the surface heat flux (specifically in conditions where an insulating peat layer is present) requires further calibration. The surface flux factor and the surface flux angle facilitate this, though calibrating these factors requires testing with a more extensive parameter space than was used in this study.

J

Computation Times

We developed the thermo-morphological model to simulate periods of time in the order of years. This requires the model to be computationally efficient. As is often the case, a balance must be struck between efficiency and accuracy. Figure J.1 shows the cumulative computation time for the baseline simulation. Running the baseline simulation takes approximately two hours (for simulating a period of two years).

Computation time increases significantly during XBeach activations (Figure J.1). For the baseline simulation, XBeach simulates ~4.4% of the entire simulations period but takes up ~64% of computation time. The bottleneck for the total computation time is XBeach. The thermal module is continuously active for the entire simulation period. It is stable and relatively inexpensive with respect to computation time.

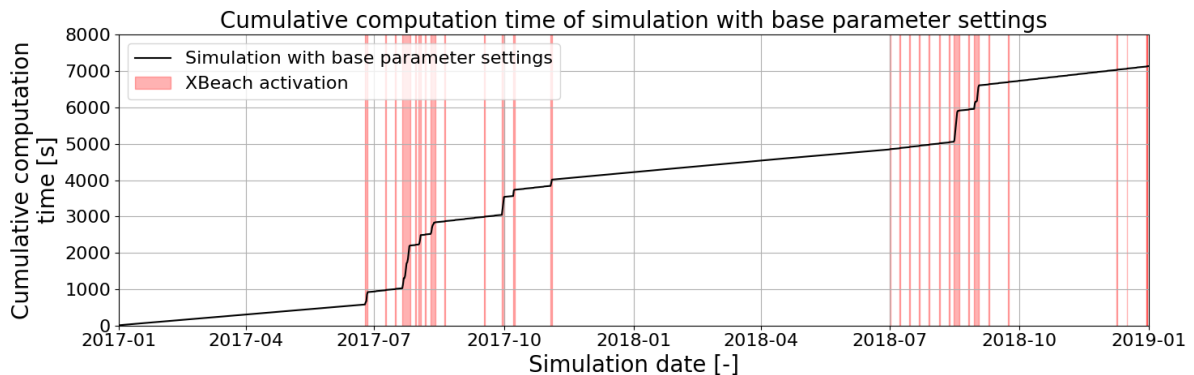


Figure J.1: Cumulative computation time (wall-clock time) for the baseline simulation of the sensitivity analysis. XBeach activations are highlighted. Computation time mostly depends on the number of XBeach activations, which depends on the $R_{2\%}$ -threshold. The computation time of the thermal module (i.e., outside of XBeach activations) is stable over time.

There is a trade-off between computation time and the $R_{2\%}$ -threshold used to determine when XBeach is activated (Section 5.4.1). We showed that the volume loss from the upper bluff (ΔV_{ub}) is sensitive to higher values of this threshold. When fewer storms are modelled, less erosion occurs. This indicates that the amount of erosion is not only constrained by the non-erodible layer. Rather, modelling additional storms results in additional convective heat transport into the soil, since convective heat transfer from water occurs faster than convective heat transfer from air.

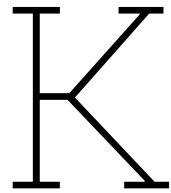
The bluff erosion is not as dependent on the depth or resolution of individual thermal models. A high thermal grid resolution is desirable close to the surface to accurately predict a thaw depth. However, the need to accurately model temperature (or rather, enthalpy) becomes lower at greater depths. The soil contains a 'memory' effect due to the slow response of (re)freezing soil to external heat forcing (Matsumura and Yamazaki, 2012), even though the soil temperature below ten meters depth hardly

varies during a single year (Figure 5.20). This raises the question of whether it is necessary to model ground temperature to larger depths, even though the active layer does not reach deeper than one meter.

Additionally, accurately modelling temperature at deeper layers might not be of interest in the context of modelling coastal morphology as most morphodynamic activity occurs close to the ground surface. However, modelling bluff erosion involves rapid erosion rates, potentially uncovering soil that was once buried beneath a large bluff, thus requiring a larger modelling depth to accurately model the temperature of this permafrost-affected soil. For reference, earlier work done by Ravens et al. (2023) models enthalpy to a depth of 10 meters. The modelling depth should always exceed the depth of the active layer, which can reach over 1 meter in permafrost bluffs (Ravens et al., 2023), not yet accounting for the erosion of the active layer and thus further deepening. Some computation time can be saved by reducing the thermal grid resolution or lowering the modelling depth, though Figure J.1 shows that most computation time comes from XBeach simulations.

This effect becomes stronger yet when a lower $R_{2\%}$ -threshold is chosen. Though the model is stable and performs well for longer periods (Figure 5.23), running these settings can take a long time (Figure 5.21). To make up for a lower $R_{2\%}$ -threshold, the modelled period can be shortened to keep computation times acceptable.

In that case, the spin-up time of the ground temperature model should be taken into account (Figure 5.6). A solution could be to simulate a spin-up period of a few months before the period of interest with only the thermal module active. Starting simulations during the winter before the research period will result in few XBeach activations due to sea ice coverage and thus only marginally increase computation time. Additionally, starting a simulation during winter will allow the thermal module some spin-up time, allowing at least the upper soil layers to adapt to environmental drivers.



Alongshore Transport

The model predicts that most eroded sediment is accreted in the nearshore zone. One of the basic assumptions leads to morphological updates (i.e., activations of XBeach) not occurring during generally accretive conditions. Therefore, it may not be accurate that most sediments end up in the nearshore zone as it leads to a flattening of the profile and makes the coast more dissipative.

Longshore transport affects the cross-shore sediment balance by acting as an additional sediment source or sink. In reality, a longshore transport gradient can e.g., remove any excess sediment from the nearshore (inject sediment into the system) and keep the profile stable.

The one-dimensional version of XBeach allows assessment of the influence of an alongshore sediment transport gradient by including a parameter that directly prescribes an artificial transport gradient. This parameter was included in the sensitivity analysis. Figure 5.30 shows that this parameter does affect bluff erosion (on the modelled time scale of two years), which implies that neglecting alongshore transport may have impacted results.

Therefore, an artificial alongshore transport gradient may help produce better modelling results. Due to the lack of accretive conditions, the model struggles with maintaining a stable beach. This is counteracted by artificially increasing the onshore transport. This leads to a flattening of the nearshore profile, as eroded sediment is not lost offshore (as should be the case for the eroded fine sediment, [Nairn et al. \(1998\)](#)).

A longshore transport gradient may provide a solution by artificially removing excess sediment from the system. The longshore transport gradient showed control on ΔV_{ub} in the sensitivity analysis, which means it could benefit simulations. Especially simulations spanning longer periods (i.e., more than two years) can benefit from further calibration using the artificial longshore transport gradient, as excess sediment builds up over longer periods of time. This opportunity should be explored.

Alongshore transport typically occurs on longer time scales. It is a continuous process that continues during low-energy conditions. However, longshore transport in our simulations can only occur while XBeach is activated (and the longshore transport gradient is enabled). Hence, the longshore transport gradient should be calibrated with the $R_{2\%}$ -threshold, to ensure that a suitable longshore transport gradient is applied for the number of storm events that are being modelled.